Dissertation

Submitted to the
Combined Faculty of Mathematics, Engineering
and Natural Science
University of Heidelberg, Germany
for the degree of
Doctor of Natural Sciences (Dr. rer. nat)

Presented by
Fabio Christopher Raith (M. Sc.)

Oral examination: December 3, 2021

Development of fluorogenic substrates for NAD(P)-Snifits enables the investigation of nicotinamide adenine dinucleotide metabolism in primary neurons

Examiners: Prof. Dr. Roland Krämer

Prof. Dr. Kai Johnsson

"*(…) Let the science speak. It is somewhat of a liberating feeling*."

Dr. Anthony S. Fauci

Abstract

The members of the cofactor family of nicotinamide adenine dinucleotides are involved in many biological processes. New insights about their role in health and disease have highlighted the need to measure these metabolites in live cells. Fluorescent biosensors have been proven to be valuable tools for metabolite measurements with subcellular resolution. Among them, the NAD(P)-Snifits have been developed to measure free NAD^+ levels and NADPH/$NADP^+$ ratios, respectively. The applicability of these FRET-based biosensors in physiological relevant model systems is limited by the permeability of the tetramethylrhodamine (TMR)-based FRET donor substrate and its SNAP-tag labelling.

In this work, fluorogenic FRET donor substrates were developed by manipulating the spirocyclization equilibrium of TMR. Their permeability and cellular SNAP-tag labelling outperformed early versions of these substrates, especially when they were derivatized with an optimized SPR inhibitor. Systematic characterization selected two FRET donor substrates that could also label the NAD(P)-Snifits in cultured primary neurons. Consequently, free subcellular NAD^+ levels and NADPH/$NADP^+$ ratios could be measured for the first time in primary neurons. These improvements allowed the comparison of free subcellular NAD^+ levels and NADPH/$NADP^+$ ratios between U2OS cells and primary neurons by FLIM-FRET measurements. Significant differences were revealed in free mitochondrial NAD^+ levels and NADPH/$NADP^+$ ratios, which could be the result of differences in oxidative phosphorylation activity and have not been described before.

In short, this work provides new tools for the quantification of NAD(P) metabolites in physiological relevant model system and thus help to gain new insights into their metabolism.

Zusammenfassung

Die Mitglieder der Cofaktor-Familie der Nicotinamidadenindinukleotide sind an vielen biologischen Prozessen beteiligt. Neue Erkenntnisse über ihre Rolle im Stoffwechsel und bei der Entstehung von Krankheiten haben die Notwendigkeit deutlich gemacht, diese Metaboliten in lebenden Zellen zu messen. Fluoreszierende Biosensoren haben sich als wertvolle Instrumente für Messungen von Metaboliten mit subzellulärer Auflösung erwiesen. Die NAD(P)-Snifits wurden für die Messungen von freien NAD^+ Gehältern bzw. NADPH/$NADP^+$ Verhältnissen entwickelt. Die Anwendbarkeit dieser FRET-basierten Biosensoren in physiologisch relevanten Modellsystemen ist durch die Permeabilität des Tetramethylrhodamin (TMR)-basierten Substrats für den FRET Donor und dessen SNAP-Tag Markierung begrenzt.

In dieser Arbeit wurden fluorogene Substrate für den FRET Donor durch Manipulation des Spirozyklisierungsgleichgewichtes von TMR entwickelt. Ihre Permeabilität und die zelluläre SNAP-Tag Markierung übertrafen frühere Versionen, insbesondere wenn sie mit einem optimierten SPR-Inhibitor derivatisiert wurden. Durch systematische Charakterisierung wurden zwei Substrate für den FRET Donor ausgewählt, die auch die NAD(P)-Snifits in kultivierten primären Neuronen markieren können. Dadurch konnten zum ersten Mal freie subzelluläre NAD^+ Gehälter und NADPH/$NADP^+$ Verhältnisse in primären Neuronen gemessen werden. Diese Verbesserungen ermöglichten den Vergleich der freien subzellulären NAD^+ Gehälter und NADPH/$NADP^+$ Verhältnisse zwischen U2OS Zellen und primären Neuronen mittels FLIM-FRET Messungen. Es wurden signifikante Unterschiede an freiem NAD^+ Gehältern und NADPH/$NADP^+$ Verhältnissen in den Mitochondrien festgestellt, die auf Unterschiede in der Aktivität der oxidativen Phosphorylierung zurückzuführen sein könnten und bisher nicht beschrieben wurden.

Zusammenfassend liefert diese Arbeit neue Werkzeuge für die Bestimmung von NAD(P) Metaboliten in physiologisch relevanten Modellsystemen und trägt somit zur Gewinnung von neuen Erkenntnissen über ihren Stoffwechsel bei.

Acknowledgements

First and foremost, I want to thank Prof. Dr. Kai Johnsson for the opportunity to conduct my PhD work in his group and for being my doctoral supervisor. I am very grateful for my interdisciplinary project, which has provided me with valuable skills and knowledge in organic chemistry, biochemistry, analytical chemistry and cell biology. He also has given me the scientific freedom to become independent and a better scientist. I highly appreciate his trust in my abilities and his encouragement, especially when I was struggling with my project. I want to thank Prof. Dr. Roland Krämer for being my first examiner and first supervisor. I also want to thank Jun.-Prof. Dr. Franziska Thomas and Prof. Dr. Joachim Spatz for being part of my examination committee.

I want to acknowledge our senior scientists Dr. Birgit Koch, Dr. Julien Hiblot and Dr. Richard Wombacher. Not only do they buffer lots of administrative duties, but also constantly provide scientific support. Our secretary Gwenaëlle Matthies has been really helpful in dealing with administrative duties and organizational matters. Ioannis Karagiannis has been indispensable for shipping and receiving samples. I also want to thank our technicians Andrea Bergner, Carmen Grosskurth, Bettina Réssy, Dominik Schmidt and Annette Herold for organizing the everyday lab life and providing us with chemicals, plasmids, proteins, etc.

Many previous and present members of Johnsson group have contributed to this work. Dr. Johannes Broichhagen has provided valuable advice in organic synthesis in the early stage of this project. Lars Hellweg has been the go-to person for discussing the NAD^+ metabolome and how to measure and manipulate it. Dr. Michelle Frei has been extremely helpful for setting-up FLIM-FRET measurements. Magnus Huppertz (aka the dude) has given valuable advice and support for establishing the NAD(P)-Snifits in primary neurons including protocols for infection, labelling and treatments. Jonas Wilhelm, Dr. Helen Farrants and Dr. Julien Hiblot have provided valuable advice for the *in vitro* characterization.

I am deeply grateful to everyone who was involved in establishing the NAD(P)-Snifits in primary neurons. From laborious cloning and AAV production to establishing

culturing conditions and the routinely neuron preparations: Dr. Julien Hiblot, Andrea Bergner, Annette Herold, Dr. Birgit Koch, Magnus Huppertz, Clara-Marie Gürth, Jasmine Hubrich, Victor Macarrón Palacios, Angel Rafael Cereceda Delgado and Dr. Elisa D'Este. I am grateful to Dr. Sebastian Fabritz, Tatjana Rudi and Juliana Kling from the mass spectrometry core facility at the MPImR for measuring HRMS data of my compounds and the collaboration on the NAD^+ measurements in cell lysate. I want to acknowledge Dr. Birgit Koch, Dr. Richard Wombacher, Lars Hellweg, Magnus Huppertz and Meike Amma for proofreading this thesis and their helpful suggestions.
I want to thank all my collaborators for their interest in our sensors and for the fruitful outcomes of the collaborations. They have definitely shaped my understanding of how to address biological questions. Prof. Dr. Joseph Baur, Dr. Timothy Luongo (University of Pennsylvania); Prof. Dr. Michael Hottiger, Dr. Ann-Katrin Hopp, Anka Güldenpfennig (University of Zurich) and Dr. Christiane Opitz, Dr. Tamara Prentzell, Sophie Seifert and Francisco Yanqui Rivera (DKFZ).
During my PhD, I had the privilege to work with some talented students: Leonie Kolmar, Carlo Walz and Estelle Bondeau. They all made significant contributions to the results presented in this thesis. I wish them all the best for their future.
I also want to acknowledge my former supervisors during my studies: Dr. Benjamin Williams, Dr. Edris Parsa, Dr. Johannes Broichhagen, Dr. Klaus Speck and Dr. Nina Hartrampf. Their supervision and training have prepared me well for my PhD.

I have really enjoyed the atmosphere in office 146 that I shared with Lars Hellweg and Konstantin Hinnah (aka the phage guy). The constant good mood made every working day enjoyable. I also want to thank some people who made my time in Johnsson group a pleasant one: Stefanie Kühn, Magnus Huppertz, Dr. Julien Hiblot, Dr. Michelle Frei, Dr. Helen Farrants, Lars Hellweg, Konstantin Hinnah, Nicolas Lardon, Nicole Mertes and Bettina Réssy.
Last but not least, my biggest thanks belong to Meike. Your constant support and encouragement has kept me going through rough and difficult times and without you, I would have never made it this far.

List of Abbreviations

Abbreviation	Meaning
AAV	adeno-associated virus
ACSF	artificial cerebrospinal fluid
ACMS	α-amino-β-carboxy muconate-ε-semialdehyde
ADP	adenosine diphosphate
ADPR	adenosine diphosphate ribose
AMPA	α-amino-3-hydroxy-5-methyl-4-isoxazolepropionic acid
ANOVA	analysis of variance
AP5	(2*R*)-amino-5-phosphonovaleric acid
aq. HCl	hydrochloric acid
AraC	arabinosylcytosin
ATP	adenosine triphosphate
a.u.	arbitrary unit
AXP	sum of ATP and ADP
BSA	bovine serum albumin
c_{50}	concentration at half-maximum sensor response
cADPR	cyclic adenosine diphosphate ribose
calc.	calculated
CD	cluster of differentiation
CFP	cyan fluorescent protein
CH_2Cl_2	dichloromethane
CI	confidence interval
CNQX	6-cyano-7-nitroquinoxaline-2,3-dione
CP	O^4-benzyl-2-chloro-6-aminopyrimidine
cp	circular permutated
CV	column volume
d	duplet (NMR)
d	day(s)
D	deuterium
D_{50}	dielectric constant at half-maximum absorbance
Da	Dalton
DAPI	4′,6-diamidino-2-phenylindole
DIPEA	*N*,*N*-diisopropylethylamine
DMAP	4-dimethylaminopyridine
DMEM	Dulbecco's modified Eagle's medium
DMF	*N*,*N*-dimethylformamide
DMSO	dimethyl sulfoxide
DNA	deoxyribonucleic acid
DTT	dithiothreitol
EC_{50}	effective drug concentration at half-maximal response
e.g.	example given
EDC	1-ethyl-3-(3-dimethylaminopropyl)carbodiimide
equiv.	equivalent(s)

ESI	electrospray ionization
EtOAc	ethyl acetate
EtOH	ethanol
f	femto
FA	formic acid
FACS	fluorescent activated cell sorting
FBS	fetal bovine serum
FCC	flash column chromatography
FDA	food and drug administration
FK866	(*E*)-*N*-[4-(1-benzoylpiperidin-4-yl)butyl]-3-(pyridin-3-yl) acrylamide
FLIM	fluorescence lifetime imaging
Fmoc	fluorenylmethoxycarbonyl
FP	fluorescent polarization (*in vitro* characterization)
FP(s)	fluorescent protein(s)
FPLC	fast protein liquid chromatography
FRET	Förster resonance energy transfer
g	gram(s)
g	gravity
G6DH	glucose-6-phosphate dehydrogenase
GFP	green fluorescent protein
Gln	glutamine
h	hour(s)
H_2	hydrogen
H_2O	water
H_2O_2	hydrogen peroxide
HBA(s)	hydrogen bond acceptor(s)
HBD(s)	hydrogen bond donor(s)
HBSS	Hanks' balanced salt solution
HEK	human embryonic kidney
HEPES	4-(2-hydroxyethyl)-1-piperazineethanesulfonic acid
HOBt	hydroxybenzotriazole
HPLC	high performance liquid chromatography
HR	high resolution
Hz	hertz
IC_{50}	inhibitor concentration at half-maximal reduction
IDH	isocitrate dehydrogenase
IDO	indoleamine 2,3-dioxygenase
i.e.	id est
iPS	induced pluripotent stem
IPTG	isopropyl β-D-1-thiogalactopyranoside
IS	internal standard
ITR	inverted terminal repeat
IUPAC	international union for pure and applied chemistry
JF	Janelia Fluor
J	coupling constant
k	kilo

K_2CO_3	potassium carbonate
$K_{50,\ app}$	ratio at half-maximum sensor saturation
KCl	potassium chloride
$K_{D,\ app}$	apparent affinity
L	liter(s)
LB	lysogeny broth
LC	liquid chromatography
logP	partition coefficient
LR	low resolution
M	mega
M	molar (concentration)
m	meter(s)
m	milli
m	multiplet (NMR)
MaP	Max Planck
MeCN	acetonitrile
ME	malic enzyme
mEGFP	monomeric enhanced green fluorescent protein
MeOH	methanol
min	minute(s)
mol	moles
mol%	percentages by moles
MRM	multiple reaction monitoring
MS	mass spectrometry
MS/MS	tandem mass spectrometry
MW	molecular weight
m/z	mass to charge ratio
N	number or replicates
n	nano
NA	nicotinic acid
NAAD	nicotinic acid adenine mononucleotide
Na_2SO_4	sodium sulfate
NAD(H)	nicotinamide adenosine dinucleotide (reduced)
NADK	NAD kinase
NADSYN	NAD synthetase
NADP(H)	nicotinamide adenosine dinucleotide phosphate (reduced)
$NaHCO_3$	sodium hydrogen carbonate
Nam	nicotinamide
NAMN	nicotinic acid mononucleotide
NAMPT	nicotinamide phosphoribosyltransferase
NaOH	sodium hydroxide
NAPRT	nicotinate phosphoribosyl transferase
NB	neurobasal
n.d.	not determined
NH_4OAc	ammonium acetate
Ni-NTA	nickel^{2+} ions coupled to nitrilotriacetic acid
NMDA	*N*-methyl-D-aspartate

NMN	nicotinamide mononucleotide
NMNAT	nicotinamide mononucleotide adenylyl transferases
NMR	nuclear magnetic resonance spectroscopy
norm.	normalized
NOX(s)	NADPH oxidase(s)
NP	normal phase
NR	nicotinamide riboside
NRK	nicotinamide riboside kinase
n.s.	not significant
OD	optical density
o.n.	overnight
p	pentet (NMR)
PARP	poly(ADP-ribose) polymerase
PBS	phosphate buffered saline
PCR	polymerase chain reaction
Pd/C	palladium on carbon
PDB	protein data bank
Pd_2dba_3	tris(dibenzylideneacetone)dipalladium(0)
PFA	paraformaldehyde
PGDH	15-hydroxyprostaglandin dehydrogenase
PMSF	phenylmethylsulfonyl fluoride
ppm	parts per million
PPP	pentose phosphate pathway
PPT	pyrazol-pyrrolo-triazine
PRPP	phosphoribosyl pyrophosphate
psi	pound per square inch
PyBOP	benzotriazol-1-yloxytripyrrolidinophosphonium hexafluorophosphate
q	quartet (NMR)
QRPT	quinolinate phosphoribosyl transferase
QY	quantum yield
R	ratio
R^2	coefficient of determination
r_{50}	ratio at half-maximum sensor response
R_f	retention factor
RNA	ribonucleic acid
ROI	region of interest
ROS	reactive oxygen species
RP	reverse phase
r.t.	room temperature
s	second(s)
s	singlet (NMR)
SARM1	sterile alpha and toll/interleukin-1 receptor motif-containing
SD	standard derivation
SDR	short-chain dehydrogenase/reducctase
SDS	sodium dodecyl sulfate
SEM	standard error of the mean

SERCA	sarcoplasmic/endoplasmic reticulum calcium ATPase
SiR	silicon rhodamine
siRNA	small interference RNA
SLC(s)	solute carrier(s)
SMX	sulfamethoxazole
Snifit	SNAP-tag-based indicator proteins with a fluorescent intramolecular tether
SPR	sepiapterin reductase
SPY	sulfapyridine
t	time
t	triplet (NMR)
TCA	tricarboxylic acid
TDO	tryptophan 2,3-dioxygenase
TFA	trifluoroacetic acid
THF	tetrahydrofuran
TICT	twisted-intramolecular charge transfer
TLC	thin layer chromatography
™	trade mark
TMR	tetramethylrhodamine
TPSA	topological polar surface area
t_R	retention time
Trp	tryptophan
TSTU	*N*,*N*,*N*′,*N*′-tetramethyl-*O*-(*N*-succinimidyl)uronium tetrafluoroborate
U2OS	human osteosarcoma
UPLC	ultra-performance liquid chromatography
UV	ultraviolet
V	volt(s)
Vis	visible
vol%	percentages by volume
WLL	white-liner laser
YFP	yellow fluorescent protein
ΔR	ratio change
°C	degree celsius
δ	chemical shift
ε	molar extinction coefficient
λ	wavelength
µ	micro
$\chi 2$	chi-square test to determine the goodness of fit
$\langle\tau\rangle$	amplitude weighted lifetime
®	registered
^{13}C	carbon-13

Table of Contents

Abstract VII
Zusammenfassung VIII
Acknowledgements IX
List of Abbreviations XI
1 Introduction 1
1.1 Methods to visualize cellular metabolism 1
1.1.1 Fluorescent biosensors 1
1.2 The cofactor family of nicotinamide adenine dinucleotides 5
1.2.1 Biosynthesis 5
1.2.2 Important NAD(P)(H) dependent processes 6
1.2.3 Implications of NAD(P)(H) in diseases 7
1.2.4 Methods to measure cellular NAD(P)(H) 8
1.2.5 Fluorescent biosensors for NAD(H) 8
1.2.6 Fluorescent biosensors for NADP(H) 9
1.2.6 Semisynthetic biosensors for free NADPH/$NADP^+$ and NAD^+ 10
2 Objectives 12
3 Results 13
3.1 Permeability of fluorescent substrates 13
3.2 JF dye-based FRET donor substrates 15
3.2.1 Synthesis 15
3.2.2 Characterization *in vitro* 17
3.2.3 Characterization in live cells 18
3.3 MaP dye-based FRET donor substrates 24
3.3.1 Design 24
3.3.2 Synthesis 26
3.3.3 Characterization *in vitro* 29
3.3.3 Characterization in live cells 32
3.3.4 Functionality of the NAD(P)-Snifits in live cells 36
3.3.5 Analyte buffering by NAD(P)-Snifits 38
3.3.6 FLIM-FRET measurements 39
3.3.7 FLIM-FRET measurements of the NAD-Snifit in live cells 40
3.3.8 FLIM-FRET measurements of the NADP-Snifit in live cells 44
3.3.9 Characterization in primary neurons 48
3.3.10 FLIM-FRET measurements of the NAD-Snifit in primary neurons 52
3.3.11 FLIM-FRET measurements of the NADP-Snifit in primary neurons 54

3.3.12 Subcellular NAD^+ levels and NADPH/NADP ratios in U2OS cells and primary neurons 56
3.3.13 Subcellular NAD^+ levels and neuronal activity 57
3.4 Identification of a mammalian mitochondrial NAD^+ transporter 59
3.5.1 Introduction 59
3.5.2 Outcome 60
3.5 Subcellular fluctuations of NAD^+ upon Nam and Trp starvation 62
3.6.1 Introduction 62
3.6.2 Preliminary outcome 62
4 Discussion 65
4.1 Substrate development 65
4.2 NAD(P)-Snifits *in vitro* 67
4.3 NAD(P)-Snifits in live cells 69
4.4 $NAD(P)^+$-Snifits in primary neurons 72
4.5 Subcellular differences between U2OS and primary neurons 74
4.6 NAD^+ transporter 77
4.7 Nam and Trp starvation 77
5 Summary and outlook 78
6 Experimental Procedure 81
6.1 Reproducibility and statistical analysis 81
6.2 Biochemical characterization 81
6.2.1 Spectral measurements 81
6.2.2 Determination of extinction coefficient 81
6.2.3 Determination of quantum yield 82
6.2.4 Water-dioxane titrations 82
6.2.5 Turn-on measurements 82
6.2.6 Labelling kinetics *in vitro* 82
6.2.7 Expression and purification of NAD(P) -Snifits 83
6.2.8 Labelling of NAD(P)-Snifits 83
6.2.9 Titrations of NAD(P)-Snifits 84
6.2.10 Cloning and production of AVVs 85
6.3 Live cell characterization 86
6.3.1 General remarks for mammalian cell culture 86
6.3.2 General remarks for rat primary hippocampal neurons 87
6.3.3 General remarks for confocal microscopy 87
6.3.4 General remarks for FLIM 88
6.3.5 General remarks for image analysis 89

6.3.6 General remarks for FACS measurements 89
6.3.7 Labelling conditions in U2OS cells 90
6.3.8 Titration of NAD(P)-Snifits with QM385 90
6.3.9 LC-MS/MS measurements of NAD^+ 90
6.3.10 Multiplexing of NAD-Snifit and Cal520 in primary neurons 92
6.3.11 SLC25A51 transfection screen 92
6.3.12 NAD^+ measurements: SLC25A51 92
6.3.13 NAD^+ measurements: Nam and Trp starvation 93
6.4 Chemical synthesis 94
General remarks 94
Diketone (16) 96
Triazane (18) 97
PPT (19) 98
C6-SMX (23) 99
Bisallyl-TMR (25) 100
Bisallyl-MaP1 (26) 101
Bisallyl-MaP555 (27) 102
MaP1 (28) 103
MaP555 (29) 104
MaP1-C6-SMX (30) 105
MaP555-C6-SMX (31) 106
CP-MaP1-C6-SMX (32) 107
CP-MaP555-C6-SMX (33) 108
MaP1-PPT (34) 109
MaP555-PPT (35) 110
CP-MaP1-PPT (36) 111
CP-MaP555-PPT (37) 112
Allyl-TMR (41) 113
Benzyl 4-sulfamoylbutanoate (39) 114
Allyl-benzyl-MaP3 (42) 115
Benzyl-MaP3 (43) 116
MaP3 (44) 117
MaP3-C6-SMX (45) 118
CP-MaP3-C6-SMX (46) 119
MaP3-PPT (47) 120
CP-MaP3-PPT (48) 121
7 Appendix 122

7.1 Protein sequences....122
7.1.1 SNAP-Halo (bacterial expression)....122
7.1.2 $NADP^+$-Snifit (bacterial expression)....122
7.1.3 NAD^+-Snifit (bacterial expression)....122
7.1.4 Cytosolic $NADP^+$-Snifit (mammalian expression)....123
7.1.5 Cytosolic NAD^+-Snifit (mammalian expression)....123
7.1.6 Nuclear $NADP^+$-Snifit (mammalian expression)....123
7.1.7 Nuclear NAD^+-Snifit (mammalian expression)....124
7.1.8 Mitochondrial $NADP^+$-Snifit (mammalian expression)....124
7.1.9 Mitochondrial NAD^+-Snifit (mammalian expression)....124
7.1.10 SNAP-mEGFP (mammalian expression)....125
7.1.11 Halo-mEGFP (mammalian expression)....125
7.1.12 SLC25A51 (mammalian expression)....125
7.1.13 SLC25A52 (mammalian expression)....125
7.2 NAD(P)-Snifits constructs....126
7.3 Key resource table....127
7.4 List of buffers....128
7.5 Analytical data....129
Diketone (16)....129
Triazine (18)....130
PPT (19)....131
C6-SMX (23)....132
Bisallyl-TMR (25)....133
Bisallyl-MaP1 (26)....134
MaP1 (28)....135
Bisallyl-MaP555 (27)....136
MaP555 (29)....137
MaP1-C6-SMX (30)....138
MaP555-C6-SMX (31)....139
CP-MaP1-C6-SMX (32)....140
CP-MaP555-C6-SMX (33)....141
MaP1-PPT (34)....142
MaP555-PPT (35)....143
CP-MaP1-PPT(36)....144
CP-MaP555-PPT (37)....145
Allyl-TMR (41)....146
Benzyl butanoate (39)....147

Allyl-benzyl-TMR (42) 148
Benzyl-MaP3 (43) 149
MaP3 (44) 150
MaP3-C6-SMX (45) 151
CP-MaP3-C6-SMX (46) 152
MaP3-PPT (47) 153
CP-MaP3-PPT (48) 154
8 References 155
9 List of Figures 163
10 List of Tables 165
11 List of Publications 166
12 Eidesstattliche Versicherung 167

1 Introduction

1.1 Methods to visualize cellular metabolism

Metabolic processes in cells are fast, dynamic and compartmentalized.[1] Ideally, a metabolite can be monitored in live cells with high spatial and temporal resolution.[2] However, this is not possible with traditional methods such as enzymatic assays or liquid chromatography coupled to mass spectrometry (LC-MS).[3]

The properties of fluorescence make it well suited for monitoring metabolites in live cells. Fluorescent molecules absorb and emit light in the nanosecond time range, making it ideal for fast changes.[4-5] Fluorescence microscopy also provides a high spatial precision, allowing the observation with subcellular resolution.

1.1.1 Fluorescent biosensors

According to the international union for pure and applied chemistry (IUPAC), a biosensor is defined as "*a device that uses specific biochemical reactions mediated by isolated enzymes, immunosystems, tissues, organelles or whole cells to detect chemical compounds usually by electrical, thermal or optical signals*".[6] Any fluorescent biosensor combines a sensing and reporting unit, thereby transforming the state of the metabolite (*e.g.* concentration) into a quantifiable read-out.[5] The majority of fluorescent biosensors have either an intensiometric or a ratiometric read-out. Intensiometric sensors change their fluorescent intensity upon metabolite fluctuation.[7] Values are expressed as change in fluorescent intensity with respect to basal levels ($\Delta F/F_0$). Ratiometric sensors are based on the Förster resonance energy transfer (FRET) between two fluorochromes (donor and acceptor).[8] Normally, a fluorochrome gets excited and relaxes back to the ground state while emitting a photon (**Figure 1A**). During FRET, non-radiative energy transfer from the excited state of the donor takes place and excites the acceptor (**Figure 1B**).[9] The FRET efficiency depends on the spectral overlap of donor and acceptor, the relative orientation of both dipoles and the distance between both fluorochromes.[10] Especially, the distance is an important measure to characterize FRET pairs, as the FRET efficiency is inversely proportional to the sixth power of the distance (**Equation 1**). For each combination of donor and

acceptor, a Förster radius (R_0) can be calculated, which corresponds to 50% FRET efficiency (**Equation 2** and **Figure 1C**).[11] Most FRET-based biosensors undergo a change in their FRET efficiency upon analyte fluctuation by changing the dipole orientation or the distance between the fluorochromes.[7] An additional read-out is fluorescent lifetime imaging (FLIM), which exploits changes in the lifetime of the fluorochrome upon analyte fluctuation.[4] The fluorescent lifetime is defined as the average time, in which a fluorochrome stays in the excited state. This results in a characteristic decay of a photon (**Figure 1D**).[12] As the lifetime is sensitive towards changes of the environment, it can be exploited for intensiometric or ratiometric sensors.

$$E = \frac{1}{1+\left(\frac{r}{R_0}\right)^6} \quad (\mathbf{1})$$

$$R_0 = 0.211 \cdot \sqrt[6]{\kappa^2 n^{-4} Q_D J(\lambda)} \quad (\mathbf{2})$$

E: FRET efficiency, r: distance between the fluorochromes, R_0: Förster radius, k: orientation factor, n: refraction index, QD: quantum yield of FRET donor, J: overlap integral.[13]

Fluorescent biosensors are either small synthetic molecules, fully genetically encoded proteins or hybrid versions thereof.[14]

Small fluorescent synthetic molecules are mainly based on organic dye scaffolds such as fluorescein, rhodamine or BODIPY.[15] They exhibit high brightness and photostability, but cannot be localized to any cellular compartment. [16] Popular examples are calcium indicators such as Fluo-3 or voltage indicators such as VoltageFluor 2.1 (**Figure 1E**).[17-18]

Fully genetically encoded biosensors are based on fluorescent proteins (FPs). They often have a lower brightness and photostability than synthetic molecules, but can be localized to any cellular compartment.[19] A prominent example is the genetically encoded calcium indicator GCaMP that is based on the green fluorescent protein (GFP) and the calcium sensing domain Cam/M13.[20] Cyan fluorescent protein (CFP) and yellow fluorescent protein (YFP) are commonly used as a FRET pair and serve as a scaffold for many biosensors (**Figure 1F**).[5]

Chemogenetic or semisynthetic biosensors combine the advantages of small molecules and genetically encoded sensors.[14] Such hybrid versions have substantially benefited from the development of self-labelling proteins (SPLs) such as

Halo-and SNAP-tag. These enzymes react irreversible with specific small molecule substrates and form a covalent bond.[21] The Halo-tag has a catalytic aspartate residue that attacks the chloroalkane substrate forming an ester bond (**Figure 1G**).[22] The SNAP-tag has a catalytic cysteine residue that attacks the benzylguanine substrate forming a thioether bond (**Figure 1H**).[23] This allows the specific labelling with fluorescent substrates and the protein part can be localized to any cellular compartment. One approach to exploit SLPs for biosensor design is the modification of a synthetic calcium indicator with the Halo-tag substrate, which transforms it into a localizable calcium indicator.[24] More elaborate chemogenetic biosensors are HaloCamP (Ca^{2+} indicator) and Voltron (voltage indicator). HaloCamP combines a circular permutated (cp) Halo-tag with the Cam sensing domain for Ca^{2+} and a complementing peptide. The intensity of the fluorophore bound to Halo-tag is increased upon Ca^{2+} binding (**Figure 1I**).[25] Voltron combines the Halo-tag with a voltage-sensitive rhodopsin. Depolarization results in quenching of the fluorescence of the Halo-tag bound fluorophore by rhodopsin (**Figure 1J**).[26]

SNAP-tag-based indicator proteins with a fluorescent intramolecular tether (Snifits) are a distinct class of chemogenetic biosensors.[27-28] They are also called semisynthetic and combine a fusion protein with small molecules. The fusion protein comprises the SNAP-tag, another self-labelling protein (*e.g.* Halo-tag) labelled with the FRET donor and a metabolite-binding protein.[29] The SNAP-tag is labelled with the FRET acceptor that is a small molecule fluorophore derivatized with an inhibitor of the binding protein. In the absence of the metabolite, the inhibitor binds to the binding protein and the Snifit is closed, resulting in a high FRET. The metabolite can displace the inhibitor and open the Snifit resulting in a low FRET. The change in FRET ratio is used as read-out (**Figure 1K**).[29-30]

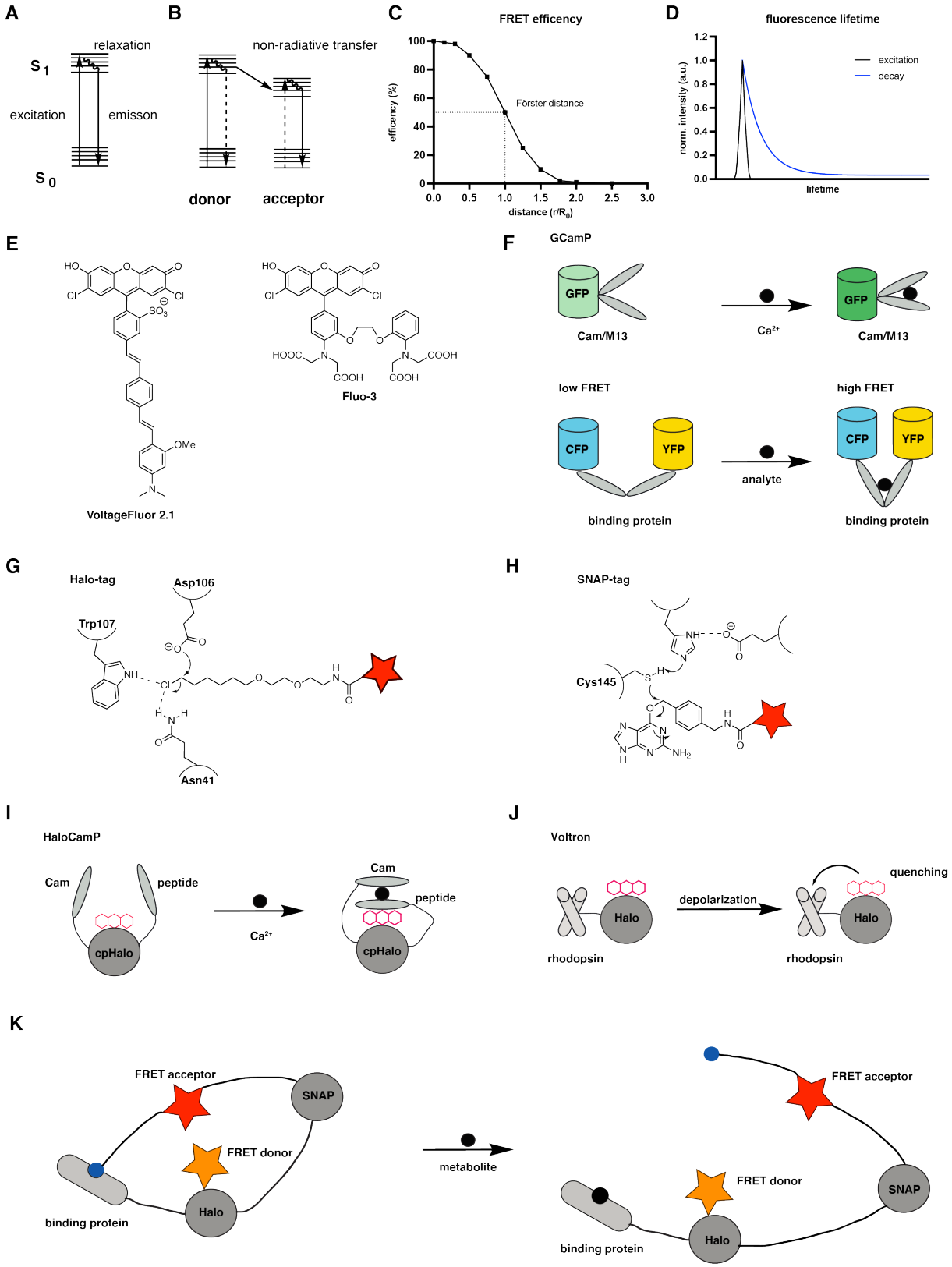

Figure 1: Fundamentals of fluorescent biosensors. A) simplified Jablonski diagram of excitation and emission. B) simplified Jablonski diagram of FRET. C) FRET efficiency as a function of distance between donor and acceptor. D) schematic representation of fluorescent decay after excitation. E) chemical structures of Voltage2.1 and Fluo3. F) schematic representation of GCamP and CYP/YFP based FRET biosensors. G) catalytic mechanisms of the Halo-tag. H) catalytic mechanisms of the SNAP-tag. I) schematic representation of HaloCamP. J) schematic representation of Voltron. K) schematic representation of the Snifit principle.

1.2 The cofactor family of nicotinamide adenine dinucleotides

Nicotinamide adenine dinucleotide (NAD^+) and its phosphorylated analog $NADP^+$ are central cofactors in cells together with their reduced forms NADH and NADPH.[31] Throughout this thesis, this cofactor family of will be abbreviated as NAD(P)(H).

1.2.1 Biosynthesis

NAD^+ and $NADP^+$ are non-cell permeable and cannot be taken up from diet.[32] There are three different pathways to synthesize NAD^+ from precursors that are taken up from diet. The Preiss-Handler pathway starts from nicotinic acid (NA), also known as vitamin B3.[33] The nicotinate phosphoribosyl transferase (NAPRT) builds up nicotinic acid mononucleotide (NAMN). Nicotinic amide mononucleotide adenylyltransferase (NMNAT)1–3 uses ATP to furnish the dinucleotide core of nicotinic acid adenine mononucleotide (NAAD).[34] The final step towards NAD^+ is a transamination by NAD^+ synthetase (NADSYN) using ATP and glutamine (**Figure 2A**).[35] NAD^+ can also be synthesized from tryptophan in the *de novo* pathway.[36] Indoleamine 2,3-dioxygenase (IDO) and tryptophan 2,3-dioxygenase (TDO) metabolize tryptophan to *N*-formylkynurenine. Subsequent enzymatic conversion results in α-amino-β-carboxy muconate-ε-semialdehyde (ACMS), which eventually cyclizes to quinolinic acid. The quinolinate phosphoribosyl transferase (QRPT) utilizes phosphoribosyl pyrophosphate (PRPP) to convert to quinolinic acid into NAMN.[33, 37] At this point, the *de novo* pathway follows the Preiss-Handler pathway (**Figure 2B**). The most important pathway in cultured cells is the salvage pathway, starting from nicotinamide riboside (NR) or nicotinamide (Nam), which is derived from NA.[38-39] NR is phosphorylated by nicotinamide riboside kinase (NRK)1–2 to yield nicotinamide mononucleotide (NMN) and NMNAT1–3 uses ATP to generate NAD^+.[40] Nam is converted to NMN by the nicotinamide phosphoribosyl transferase (NAMPT) using PRPP and ATP (**Figure 2C**).[38-39] NADH is generated from NAD^+ in redox reactions in the metabolism (*e.g.* during glycolysis or tricarboxylic acid (TCA) cycle).[32] $NADP^+$ is generated by the phosphorylation of NAD^+ catalyzed the NAD^+ kinase (NADK) (**Figure 2D**).[41] NADPH is generated from $NADP^+$ in the pentose phosphate pathway (PPP) or by isocitrate dehydrogenase (IDH) and malic enzyme (ME).[42-44]

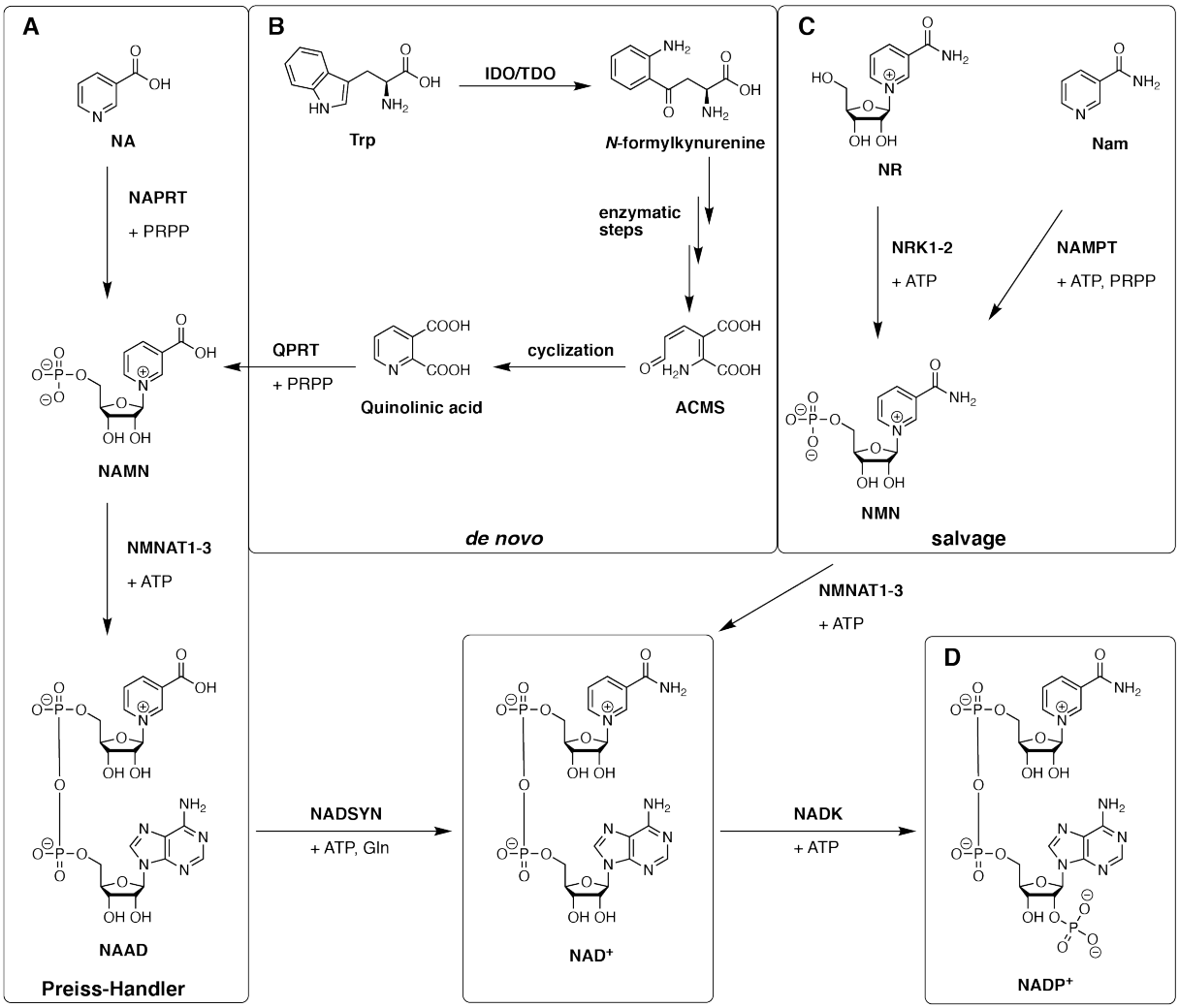

Figure 2: Biosynthesis of NAD+ and NADP+. A) Preiss-Handler pathway starting from NA. B) *de novo* pathway starting from tryptophan. C) salvage pathway starting from NR or Nam, respectively. D) phosphorylation of NAD+ by NADK to generate NADP+. Abbreviations: NA: nicotinic acid, NAPRT: nicotinate phosphoribosyl transferase, PRPP: phosphoribosyl pyrophosphate, NAMN: nicotinic acid mononucleotide, NMNAT: nicotinamide mononucleotide adenylyltransferase, ATP: adenosine triphosphate, NAAD: nicotinic acid adenine dinucleotide, NADSYN: NAD+ synthetase, Gln: glutamine, NADK: NAD+ kinase, Trp: tryptophan, IDO: indoleamine 2,3-dioxygenase, TDO: tryptophan 2,3-dioxygenase, ACMS: α-amino-β-carboxy muconate-ε-semialdehyde, QRPT: quinolinate phosphoribosyl transferase, NR: nicotinamide riboside, Nam: nicotinamide, NRK: nicotinamide riboside kinase, NAMPT: nicotinamide phosphoribosyl transferase, NMN: nicotinamide mononucleotide.

1.2.2 Important NAD(P)(H) dependent processes

NAD+ is involved in redox and non-redox processes and plays an essential role in energy metabolism.[45] NAD+ is an electron acceptor during glycolysis and TCA cycle and gets reduced to NADH.[32] NADH is then oxidized as part of the oxidative phosphorylation to produce ATP. In contrast, non-redox processes consume NAD+ and the remaining Nam is recycled to NAD+ by the salvage pathway (**Figure 2C**).[46] Poly-ADP-ribose polymerases (PARPs) are involved in the posttranslational modification of proteins with poly-ADP-ribose.[47] These modifications fulfill a plethora

of cellular functions such as energy metabolism, genome stability and transcription regulation.[48] In particular, PARP1 serves as a sensor for DNA damage.[49] Poly-ADP-ribosylation after DNA damage can consume up to 80% of cellular NAD^+ and PARP1 activity is crucial for cell survival and death.[33] Sirtuins are a class of enzymes that mainly deacetylate histones.[50] They are mainly involved in metabolic adaption to energy deficit during exercise, fasting or low glucose levels.[51-53] There is also evidence that sirtuins play a role in circadian rhythm.[54] Another important class of NAD^+-consuming enzymes are cluster of differentiation (CD) 38 and CD157.[55] Their product, cyclic ADP-ribose (cADPR) plays a role in Ca^{2+} signaling, cell cycle and immune response.[56-57]

NADPH is the main cellular form of $NADP^+$.[41] It provides electrons for defense against oxidative stress and reductive biosynthesis.[58] Glutathione is the major antioxidant in cells and gets oxidized by reactive oxidative species (ROS).[59] Glutathione is then regenerated by NADPH.[60] Importantly, NADPH is not only involved in detoxifying ROS, but also in their production.[61] NADPH oxidases (NOXs) are membrane-bound proteins that oxidize NADPH to $NADP^+$ with ROS as side product.[62] As part of the innate immune system, NOXs are involved in the defense against microorganisms.[63] ROS produced by NOXs play also a role in cellular signaling and gene expression.[64] Reductive biosynthesis comprises many important catabolic reactions such as fatty acid, cholesterol/steroid hormone and deoxynucleotide biosynthesis. NADPH donates the electrons to transform oxidized precursor to reduced products.[42]

1.2.3 Implications of NAD(P)(H) in diseases

Due to the involvement of NAD(P)(H) in a plethora of cellular processes, the onset of many diseases can be characterized by a decrease in $NAD(P)^+$ or a redox imbalance (*e.g.* changes in NAD(P)H/$NAD(P)^+$).[65] Such diseases includes diabetes, fatty liver, neurodegeneration and cancer.[66-70] Some drugs for cancer treatment directly interact with the NAD^+ metabolism. PARP1 inhibitor such as olaparib inhibit the repair of DNA damage in cancer cells induced by chemotherapy.[71] NMAPT is the rate-limiting enzyme in the NAD^+ biosynthesis and NMAPT inhibitors are currently in clinical trials.[72]

1.2.4 Methods to measure cellular NAD(P)(H)

The characteristics of NAD(P)(H) metabolism make cellular measurements challenging. The majority of NAD(P)(H) is bound to proteins (ca. 80%), but the concentration of the free form is much more relevant.[73] NAD(P)(H)-dependent processes are compartmentalized and their concentrations and ratios of reduced to oxidized form can differ.[74] Most methods are based on the measurements in cell lysate using enzymatic cycling assays, high performance liquid chromatography (HPLC) coupled to an ultraviolet (UV) detector or LC-MS/MS measurements. However, these methods do not offer spatial or temporal resolution and the observed values are highly dependent on the protocol, which hampers reproducibility and comparability.[75] In addition, the reduced forms of $NAD(P)^+$ are rather unstable due to oxidation during sample preparation and this degradation could lead to artefacts.[76] NADH and NADPH are autofluorescent and emit at 460 nm.[77] FLIM imaging can be used to measure free and protein-bound forms in live cells as they have different lifetimes.[78] However, separation of the lifetimes of NADH and NADPH in such experiments is not feasible, limiting the applicability of this approach. In contrast, fluorescent biosensors offer the possibility to measure free NAD(P)(H) in live cell with high spatial and temporal resolution.

1.2.5 Fluorescent biosensors for NAD(H)

Most of the fluorescent biosensors for NAD(H) are based on the combination of a circular permutated FP and a NAD(H) binding protein. cpVenus and FiNad are sensors for NAD^+ and combine a DNA ligase with cpVenus and cpYFP, respectively.[79-80] Both sensors are pH sensitive and also respond to high concentrations of NR, which limits their applicability for NR treatment. FiNad is also sensitive to ATP and ADP (termed AXP) and therefore reports on NAD^+/AXP ratios. Peredox, SoNar and Frex are sensors for NADH/NAD^+ ratios, NAD^+/NADH ratios and NADH levels, respectively.[81-83] They utilize the redox sensing repressors T- and B-Rex in combination with cpT-Sapphire or cpYFP. In contrast to these short wavelength responsive sensors, only sensor with emission > 550 nm the NAD-Snifit is the.[84] This sensor is discussed in more detail below (**Table 1**).

Table 1: Fluorescent biosensors for NAD(H).

sensor	cpVenus[79]	FiNad[80]	Peredox[81]	SoNar[82]	Frex[83]	NAD-Snifit[84]
metabolite	NAD^+	NAD^+/AXP	NADH/NAD^+	NAD^+/NADH	NADH	NAD^+
FP/dye	cpVenus	cpYPF/ mCherry	T-Sapphire mCherry	cpYPF	cpYPF	TMR/SiR
Read-out [nm]	ex. ratio λ_{ex}: 405/488 λ_{em}: 520	em. ratio λ_{ex}: 488 λ_{em}: 535	em. ratio λ_{ex}: 405 λ_{em}: 530	ex. ratio λ_{ex}: 405/488 λ_{em}: 530	ex. ratio λ_{ex}: 405/488 λ_{em}: 520	FRET ratio λ_{ex}: 550 λ_{em}: 570/670
Sensing	DNA ligase	DNA ligase	T-Rex	T-Rex	B-Rex	SPR
localization	cytosol nucleus mitochondria	cytosol	cytosol	cytosol	cytosol nucleus mitochondria	cytosol nucleus mitochondria
limitations	pH sensitive, short wavelengths, NMN/NR sensitive	pH sensitive, short wavelengths, NMN/NR sensitive, APX sensitive	short wavelengths	pH sensitive, short wavelengths	pH sensitive, short wavelengths	labelling with fluorescent substrates

1.2.6 Fluorescent biosensors for NADP(H)

iNAP is a sensor for NADPH levels, which is also based on the insertion of cpYFP into T-Rex (see SoNar).[85] Engineering of T-Rex shifted the specificity from NADH to NADPH, but this sensor also suffers from pH sensitivity. Apollo is a sensor for $NADP^+$ levels that is based on the fusion of two Cerulean FPs to the glucose-6-phosphate dehydrogenase (G6DH).[86] The read-out is a change in homoFRET between the two Cerulean FPs. The requirement to measure anisotropy limits the applicability of this sensor as anisotropy cannot be measured by most fluorescent microscopes. The NADP-Snifit is the only sensor to measure NADPH/$NADP^+$ ratios with emission > 550 nm and is discussed below (**Table 2**).[84]

Table 2: Fluorescent biosensors for NADP(H).

sensor	iNAP[85]	Apollo[86]	NADP-Snifit[84]
metabolite	NADPH	$NADP^+$	NADPH/$NADP^+$
FP/dye	cpYPF	Cerulean	TMR/SiR
Read-out [nm]	ex. ratio λ_{ex}: 405/488 λ_{em}: 530	homoFRET λ_{ex}: 405/488 λ_{em}: 520	FRET ratio λ_{ex}: 550 λ_{em}: 570/670
sensing	T-Rex	G6PD	SPR
localization	Cytosol mitochondria	cytosol	cytosol nucleus mitochondria
limitations	pH sensitive, short wavelengths	Complex set-up to measure, short wavelengths	labelling with fluorescent substrates

1.2.6 Semisynthetic biosensors for free NADPH/NADP$^+$ and NAD$^+$

Guided by the Snifit design described above, the Johnsson group has developed semisynthetic biosensors for free NADPH/NADP$^+$ ratios and free NAD$^+$ levels. These sensors are termed NADP-Snifit and NAD-Snifit, respectively.[84] The human sepiapterin reductase (SPR) was selected as metabolite-binding protein. The SPR catalyzes the reduction of sepiapterin to dihydrobiopterin using NADPH as cofactor. Previously it was shown that sulfa drugs such sulfapyridine (SPY) or sulfamethoxazole (SMX) can bind to SPR in the presence of NADP$^+$ (**Figure 3A**).[87] This interaction is exploited in the design of the FRET donor substrate CP-TMR-C6-SMX (also referred as intramolecular tether). π-stacking between NADP$^+$ and SMX ensures the selectivity of the NADP-Snifit. TMR is used as FRET donor and combined with silicon rhodamine (SiR) as FRET acceptor.[88] This red-shifted FRET pair has minimal spectral overlap and allows multiplexing with other commonly used fluorescent markers such as GFP or DAPI (**Figure 3B**).[89]

For the fusion protein part of the sensor, the SPR is combined with Halo- and SNAP-tag. The Halo-tag is labelled with Halo-SiR and the SNAP-tag is labelled with CP-TMR-C6-SMX. Both tags are separated by a proline 30 linker to reduce FRET efficiency in the open state. In the presence of NADP$^+$, there is a cooperative binding of TMR-C6-SMX and NADP$^+$ to the SPR. The binding brings the two fluorophores in close proximity and increases the FRET efficiency (**Figure 3C**). As NADPH and NADP$^+$ have similar concentrations in cells, both cofactors compete for the same binding site. Therefore, the NADP-Snifit reports on the ratio of free NADPH/NADP$^+$.[84, 90-91] Structure-guided engineering allowed the conversion of the NADP-Snifit into a NAD-Snifit. SPR belongs the superfamily of short-chain dehydrogenase/reductase (SDR) and all members have a characteristic Rossmann fold for binding of either NADP$^+$ or NAD$^+$.[92] NADP$^+$-binding enzymes such as SPR have two conserved arginine or lysine residues for the interaction with the 2′-phosphate and the adenine moiety of NADP$^+$. In contrast, NAD$^+$-binding enzymes such as 15-hydroxyprostaglandin dehydrogenase (PGDH) have two conserved arginine or lysine residues for the interaction with the 2′- and 3′-OH groups of NAD$^+$. Sequence and structure comparison of SPR and PGDH resulted in the insertion of the mutations A41D and R42W into the SPR.[93] These mutations switch the cofactor specificity to

NAD^+ and the sensor does not respond to physiological concentrations of $NADP^+$. NADH has a much lower concentration in cells than NAD^+, therefore the NAD-Snifit reports on free NAD^+ levels.[82, 84] The emission profile of the sensor depends on the metabolite concentration. At low metabolite concentrations, the sensor exhibits a high TMR and low FRET emission. Conversely, high metabolite concentrations result in a low TMR and high FRET emission (**Figure 3D**). Consequently, the ratio of FRET and TMR emission can be used as read-out (termed FRET ratio). This FRET ratio increases with rising analyte concentration (**Figure 3E**).

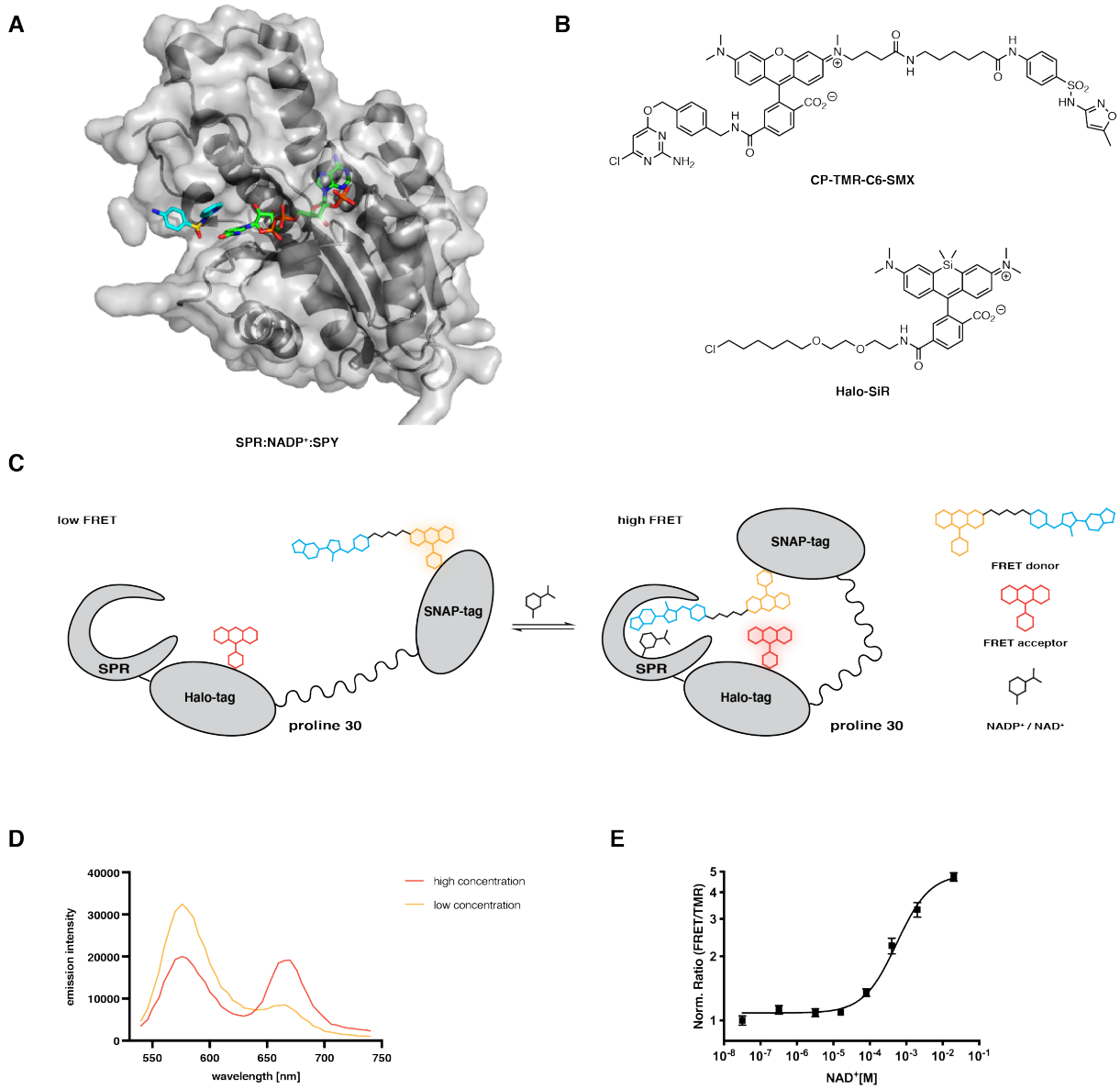

Figure 3: Design of NAD(P)-Snifits. A) selective binding of SPY to SPR in the presence of $NADP^+$ due to π-stacking interactions. SPY is shown in cyan and $NADP^+$ is shown in green (PDB: 4HWK). B) structures of CP-TMR-C6-SMX (FRET donor) and Halo-SiR (FRET acceptor). C) schematic representation of the NAD(P)-Snifit. The sensor is open in the absence of $NAD(P)^+$ (low FRET) and closed in the presence of $NAD(P)^+$ (high FRET). D) representative emission spectra of NAD-Snifit in presence of low or high NAD^+ concentrations. E) representative titration curve of FRET/TMR ratios against NAD^+ concentrations.

2 Objectives

In recent years, the importance of different cellular pools of the cofactors NAD(H) and NADP(H) has become apparent. Fluorescent biosensors have contributed to the gain of knowledge about these pools by subcellular measurements of these cofactors. However, due to various technical limitations they have been rarely used in more complex and physiological relevant model systems such as primary cells. The applicability of the NAD(P)-Snifit in such systems has been limited by the permeability of the FRET donor substrate CP-TMR-C6-SMX and its labelling performance of the SNAP-tag.

In this thesis, fluorogenic FRET donor substrates with improved permeability and SNAP-tag labelling were developed. More precisely, conversion of TMR into fluorogenic analogous and use of a more permeable inhibitor resulted in a small library of potential new FRET donor substrates. Characterization *in vitro* and in live cells selected the most suited substrates, which then were evaluated for their ability to label SNAP-tag in primary neurons. After successful labelling, the applicability of the resulting new NAD(P)-Snifits was be demonstrated in primary neurons.

3 Results

3.1 Permeability of fluorescent substrates

Improvement of intracellular SNAP-tag labelling with CP-TMR-C6-SMX required optimization of its cell permeability combined with a low unspecific background to obtain high signal to noise ratios. As of now, it is not fully understood how fluorescent molecules can pass the cell membrane. Based on structural similarities with known drugs and natural products, it was suggested that fluorescent molecules can be surrogate substrates for solute carriers (SLCs).[94] Fluorescein and Rhodamine123 are commonly used fluorophore scaffolds and have been described as substrates for several SLCs.[95-97] However, there has not been any systematic investigation of the whole human transportome (*i.e. the sum of membrane transporter and channels*) with different classes of fluorophores. Fluorescent substrates can also pass the cell membrane by passive diffusion.[98]

Criteria for the permeability of small molecules have emerged in medicinal chemistry about two decades ago.[99] Lipinski's rule of five defines parameters for ideal drug candidates: calculated lipophilicity < five (expressed as partition coefficient: logP), molecular weight < 500 Da, not more than five hydrogen bond donors (HBDs, *e.g.* sum of OH and NH) and not more than ten hydrogen bond acceptors (HBAs, *e.g.* sum of O and N).[100] These rules only apply for compounds that are not substrates for SLCs, however it is assumed that most compounds can be substrates for SLCs.[101-102] The rule of five concept has been evolved over time, also considering other physicochemical parameters such as polar surface area and number of rotational bonds.[103] The number of HBDs and calc. logP have emerged as the most important factors for cell permeability. Others such as molecular weight have become less important, which is evident by an increasing molecular weight of FDA approved oral drugs in recent years.[99]

CP-TMR-C6-SMX has six hydrogen bond donors and a calc. logP = 0.55, properties that are not well suited for cell permeability (**Figure 4A** and **Table 4**).[104] Rhodamine-based fluorophores such as TMR exist in an equilibrium between an open, fluorescent and a closed, non-fluorescent form (**Figure 4B**). Several studies have shown a higher permeability for the non-fluorescent spirolactone compared to the

fluorescent zwitterion.[88, 105-106] The spirolactone has a significant higher calc. logP than the zwitterion (2.84 vs. –2.74), which could explain the difference in permeability.[104] Motivated by this principle, several approaches have been developed to synthesize fluorescent probes that are mainly in the spirocyclic form. Binding to their intracellular targets should shift the equilibrium back to the open and fluorescent form. This so-called fluorogenic character combines improved permeability with low background staining.[107]

In the last years, two general strategies have emerged to shift the equilibrium of rhodamines towards the spirocyclic form. The group of Luke Lavis has developed the Janelia Fluor (JF) dyes by replacing the *N,N*-dimethyl amino moiety of the xanthene core with azetidines. Substitution of the azetidines with electron withdrawing substituents (*e.g.* fluorines) decreases the electron density of the xanthene core. This facilitates the attack of the carboxylic acid for the formation of the spirolactone (**Figure 4C**). For instance, the spirocyclic form of JF525 has a much higher calc. logP than the zwitterionic form (3.21 vs. –3.53).[104]

The group of Kai Johnsson has developed the Max Planck (MaP) dyes, a different strategy for fluorogenic rhodamines. Replacement of the *ortho*-carboxylic acid with sulfonamides bearing electron-donating substituents greatly improved the nucleophilicity. This also facilitated the formation of the spirolactam (**Figure 4D**). The spirocyclic form also has a higher calc. logP compared to zwitterionic form (*e.g.* MaP555: 2.83 vs. –2.41).[104]

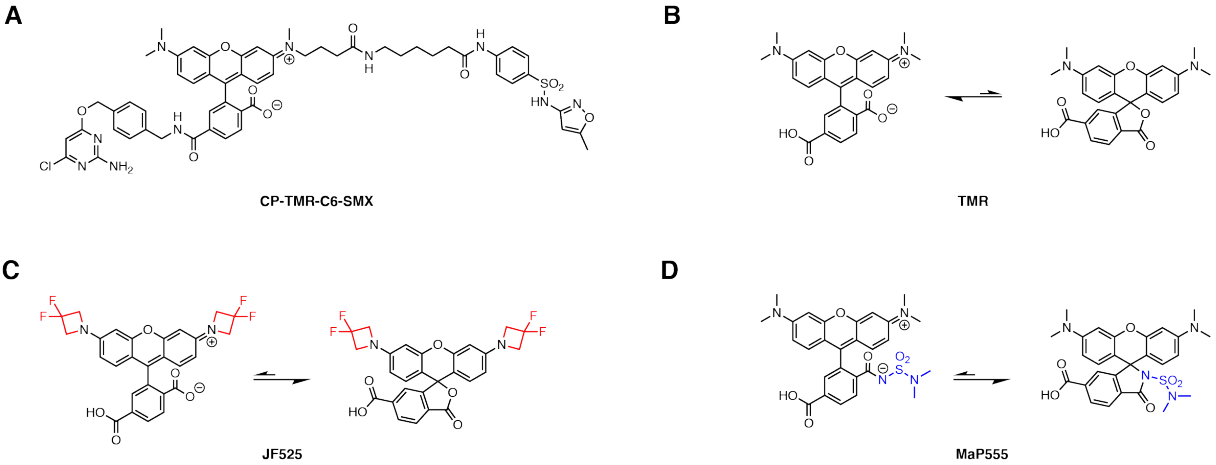

Figure 4: Spirocyclization equilibria of TMR derivatives. A) structure of CP-TMR-C6-SMX, B)–D) equilibria between zwitterionic and spirocyclic forms of TMR, JF525 and MaP555, respectively.

Both strategies allowed the transformation of TMR into highly fluorogenic and permeable fluorophores and were employed to improve the permeability of CP-TMR-C6-SMX.

3.2 JF dye-based FRET donor substrates

3.2.1 Synthesis

Following the JF dye strategy from the group of Luke Lavis, the FRET donor substrate CP-TMR-C6-SMX was redesigned (**Figure 5A**). The *N,N*-dimethyl amino moieties were replaced by 3,3-difluoroazetidine and 3-carboxylic acid azetidine. 3,3-difluoroazetidine was thought to improve permeability, while the C6-SMX moiety would be linked to 3-carboxylic acid azetidine *via* peptide coupling (**Figure 5B**). The newly designed FRET donor substrate was termed CP-Rhod540-C6-SMX. The open and spirocyclic form had a significant difference in their calc. logP (–1.12 vs. 6.43).[104] Azetidines also reduced the number of rotational bonds, while other physicochemical parameters remained unaffected (**Table 4**).

The synthesis of CP-Rhod540-C6-SMX started from the fluorescein bistriflate precursor **1** using exclusively the 6-regioisomer.[105-106] Two sequential Buchwald couplings were used to build an asymmetric substituted rhodamine scaffold. The first coupling step was more reproducible and easier to purify when the 3-carboxylic acid azetidine was coupled first. This was mainly due to the very similar polarities of **1** and 3,3-difluoroazetidine monotriflate. No separation could be achieved using column chromatography on silica with various solvent mixtures. Several attempts to improve the coupling step with 3-carboxylic acid azetidine did not succeed, despite using different conditions (time, temperature, base, catalyst and solvents). At best, the reaction only went to 50% completion and in addition to the 3-carboxylic acid azetidine monotriflate **3**, biscarboxylic acid azetidine and fluorescein were also obtained. Other conditions resulted in either lower substrate conversion, more side product formation or increased degradation of the starting material. It was then decided to continue this synthetic approach despite the low efficiency of the first step. The orthogonal protecting groups of the asymmetric substituted rhodamine **5** were then exploited to selectively

deprotect the aromatic carboxylic acid with TFA in CH_2Cl_2. Peptide coupling using TSTU was used to install the O^4-benzyl-2-chloro-6-aminopyrimidine (CP-NH_2) (**7**) for SNAP-tag labelling. Basic saponification of the methyl ester **8** and subsequent peptide coupling using TSTU gave rise to the new FRET donor CP-Rhod540-C6-SMX (**11**) (**Figure 5C**).

Figure 5: Design and synthesis of CP-Rhod540-C6-SMX. A) structure of CP-TMR-C6-SMX. B) structure of CP-Rhod540-C6-SMX. C) reagents and conditions: a) **2** (0.9 equiv.), Cs_2CO_3 (2.4 equiv.), XPhos (0.15 equiv.), Pd_2dba_3 (0.05 equiv.), 1,4-dioxane, 80 °C, 2 h; b) **4** (1.5 equiv.), Cs_2CO_3 (2.4 equiv.), XPhos (0.15 equiv.), Pd_2dba_3 (0.05 equiv.), 1,4-dioxane, 80 °C, 6 h; c) TFA (20% vol.), CH_2Cl_2, r.t., 4 h; d) **7** (1.2 equiv.), DIPEA (8.0 equiv.), TSTU (1.2 equiv.), DMSO, r.t., 4 h; e) NaOH (2.0 equiv.), THF/MeOH (2:1), r.t., 4 h; f) **10** (1.2 equiv.), DIPEA (8.0 equiv.), TSTU (1.2 equiv.), DMSO, r.t., 4 h.

3.2.2 Characterization *in vitro*

Spectral characterization of CP-Rhod540-C6-SMX revealed a blue-shift of ca. 15 nm in absorbance and emission compared to CP-TMR-C6-SMX (**Figure 6A** and **Table 3**). These observations were in agreement with data from the group of Luke Lavis, where also a blue-shift was observed when electron-withdrawing substituents were used. CP-Rhod540-C6-SMX was mainly closed in aqueous buffer, but became strongly fluorescent in ethanol containing 0.1% TFA (**Figure 6B**). The maximal extinction coefficient and quantum yield (QY) of CP-Rhod540-C6-SMX were determined in ethanol containing 0.1% TFA. The QY (0.76) was greatly improved compared to CP-TMR-C6-SMX (0.41), because the azetidines could not undergo the C-N bond rotation as the *N,N*-dimethyl moiety. This rotation results in transition induced charge transfer (TICT), which lowers the QY of CP-TMR-C6-SMX.[106] The extinction coefficient of CP-Rhod540-C6-SMX was higher compared to CP-TMR-C6-SMX, which was in agreement with previous data (**Table 3**).[106]

Table 3: Spectral properties of FRET donor substrates CP-TMR-C6-SMX and CP-Rhod540-C6-SMX. [a] PBS pH 7.4, [b] 0.1% TFA in EtOH.

FRET donor	λ_{ab} [nm]	λ_{em} [nm]	QY	ε (M^{-1})
CP-TMR-C6-SMX	555	580	0.41[a]	89,000[a]
CP-Rhod540-C6-SMX	540	562	0.76[b]	110,000[b]

The shift of the equilibrium towards the spirolactone was investigated with different mixtures of water and dioxane. These mixtures exhibited different dielectric constants and therefore mimic different polarities. CP-TMR-C6-SMX was mainly in the open form and fluorescent in all mixtures. In contrast, CP-Rhod540-C6-SMX only became fluorescent at higher dielectric constants, suggesting that it might be fluorogenic when used for protein labelling (**Figure 6C**). Purified NAD-Snifit was labelled with CP-Rhod540-C6-SMX/Halo-SiR or CP-TMR-C6-SMX/Halo-SiR and was titrated with NAD^+. NAD-Snifit labelled with CP-TMR-C6-SMX/Halo-SiR had a half-maximal sensor response concentration (c_{50}) of 973 µM (95% CI: 126–3361). In contrast, NAD-Snifit labelled with CP-Rhod540-C6-SMX/Halo-SiR had a much lower c_{50} of 109 µM (95% CI: 57–134) (**Figure 6D**).

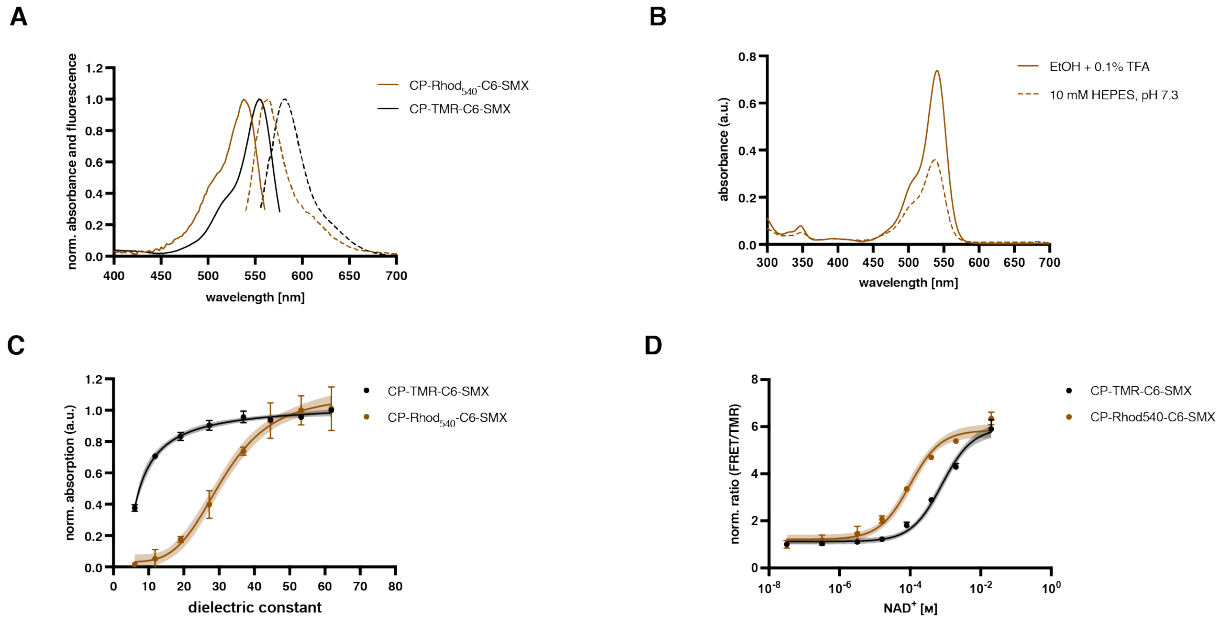

Figure 6: Characterization of CP-Rhod540-C6-SMX *in vitro*. A) normalized absorbance and emission spectra of CP-TMR-C6-SMX and CP-Rhod540-C6-SMX. B) absorbance spectra of CP-Rhod540-C6-SMX in HEPES buffer and EtOH + 0.1% TFA. C) normalized absorbance at 540 nm (CP-Rhod540-C6-SMX) and 550 nm (CP-TMR-C6-SMX) in water-dioxane mixtures as a function of dielectric constant. D) titration of purified NAD-Snifit labelled with CP-TMR-C6-SMX/Halo-SiR and CP-Rhod540-C6-SMX/Halo-SiR, respectively (37 °C). Data are shown as mean ± S.D and fit is shown with 95% CI.

3.2.3 Characterization in live cells

Intracellular SNAP-tag labelling with CP-Rhod540-C6-SMX was investigated in human osteosarcoma (U2OS) cells with an inducible NAD-Snifit. The sensor was expressed in the cytosol, nucleus or mitochondria and labelled with 500 nM of CP-Rhod540-C6-SMX or CP-TMR-C6-SMX. Live cell confocal imaging demonstrated that labelling with CP-Rhod540-C6-SMX resulted in a much brighter signal than CP-TMR-C6-SMX. In addition to an improved signal to noise ratio, no aggregations could be observed for labelling with CP-Rhod540-C6-SMX. Labelling of the NAD-Snifit in inner mitochondrial membrane with CP-TMR-C6-SMX resulted in bright aggregates (**Figure 7A, B**).

The response to changes in free NAD^+ was investigated by confocal microscopy using the cytosolic NAD-Snifit labelled with CP-TMR-C6-SMX/Halo-SiR or CP-Rhod540-C6-SMX/Halo-SiR. The potent NAMPT inhibitor FK866 was used to decrease cytosolic NAD^+. Resveratrol is believed to activate NMNAT1 to increase cytosolic NAD^+.[108-110] The SPR inhibitor QM385 was used as an internal control to artificially open the sensor by outcompeting the tethered ligand.[111] The NAD-Snifit labelled with CP-TMR-C6-SMX showed a response to FK866 (FRET ratio: 0.52,

95% CI: 0.49–0.53), QM385 (0.49, 95% CI: 0.46–0.52) and resveratrol (0.61, 95% CI: 0.57–0.64) compared to basal conditions (0.56, 95% CI: 0.53–0.59) (**Figure 7C**). In contrast, the NAD-Snifit labelled with CP-Rhod540-C6-SMX did not show a response to FK866 (0.09, 95% CI: 0.08–0.10), QM385 (0.09, 95% CI: 0.08–0.10) and resveratrol (0.09, 95% CI: 0.08–0.10) compared to basal conditions (0.09, 95% CI: 0.08–0.10) (**Figure 7D**). When comparing the ratios of cells labelled with CP-TMR-C6-SMX and CP-Rhod540-C6-SMX, much lower FRET ratios were observed for CP-Rhod540-C6-SMX. This indicated an almost fully open state of the sensor, resulting in a very low FRET efficiency. Such differences between CP-TMR-C6-SMX and CP-Rhod540-C6-SMX were not expected. *In vitro* titration demonstrated a response of the NAD-Snifit when labelled with CP-Rhod540-C6-SMX/Halo-SiR and the c_{50} appeared to be in a suitable range for cellular measurements.

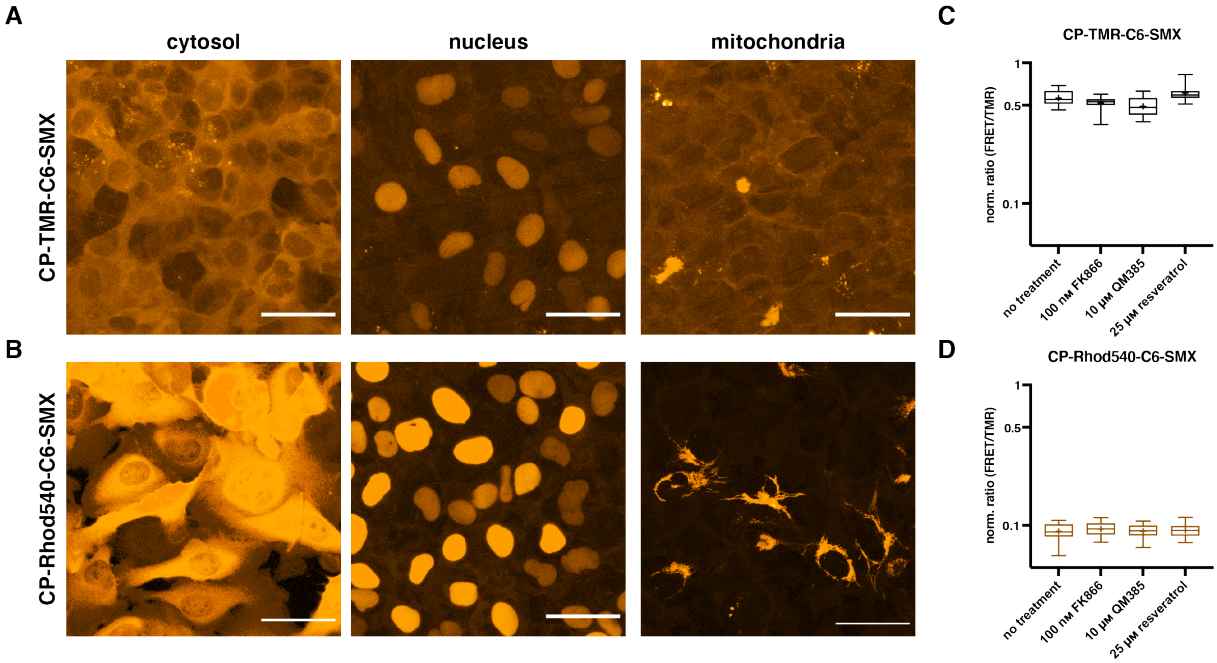

Figure 7: Labelling and response of NAD-Snifit in live cells. A) images of U2OS cells expressing the NAD-Snifit in cytosol, nucleus and mitochondria labelled with 500 nM CP-TMR-C6-SMX. B) images of U2OS cells expressing the NAD-Snifit in cytosol, nucleus and mitochondria labelled with 500 nM CP-Rhod540-C6-SMX. C) response of cytosolic NAD-Snifit in U2OS cells to pharmacological treatment labelled with CP-TMR-C6-SMX/Halo-SiR. D) response of cytosolic NAD-Snifit in U2OS cells to pharmacological treatment labelled with CP-Rhod540-C6-SMX/Halo-SiR. The box represents the 25th and 75th percentile and the whiskers are the minimum and maximum. The mean and median are indicated by a cross or line, respectively. $N = 50$ cells per condition.

The very low FRET ratios in live cells were further investigated by confocal microscopy. Upon excitation at 510 nm, emission spectra of the double labelled NAD-Snifit (*i.e.* NAD-Snifit was labelled with FRET donor substrate and Halo-SiR) were recorded. For CP-TMR-C6-SMX, the emission spectra showed a peak for FRET donor (570 nm) and FRET acceptor (650 nm) in the cytosol, nucleus and mitochondria. In contrast, CP-Rhod540-C6-SMX showed a peak for FRET donor (540 nm) in the cytosol, nucleus and mitochondria, but only a small peak for the FRET acceptor (650 nm) was observed. In addition, the emission peak for CP-Rhod540-C6-SMX was at 540 nm, which was blue-shifted by ca. 20 nm compared to spectral measurements of the free substrate in buffer (**Figure 8A**–**C**).

For a better comparison with *in vitro* data, cells expressing the cytosolic NAD-Snifit were labelled with CP-TMR-C6-SMX/Halo-SiR or CP-Rhod540-C6-SMX/Halo-SiR, lysed and the emission spectra were recorded on a plate reader. Similar to microscopy data, the spectrum of CP-TMR-C6-SMX showed a peak for FRET donor (575 nm) and FRET acceptor (650 nm) (**Figure 8D**). For CP-Rhod540-C6-SMX, only the peak for the FRET donor (543 nm) was observed. Direct excitation of SiR demonstrated labelling of the Halo-tag, making insufficient Halo-tag labelling less likely to be the reason for the low FRET signal (**Figure 8E**). These findings were in disagreement with *in vitro* data. In a systematic investigation to find the underlying issues, the DMSO stock of CP-Rhod540-C6-SMX was analyzed. The emission spectrum showed a broad peak (552 nm), which was neither consistent with the previously recorded spectra in buffer (560 nm) nor the emission spectrum from cell lysate (539 nm). The emission spectra from the DMSO stock was blue-shifted compared to previous measurements in buffer, but less shifted than the emission spectrum from cell lysate (**Figure 8F**).

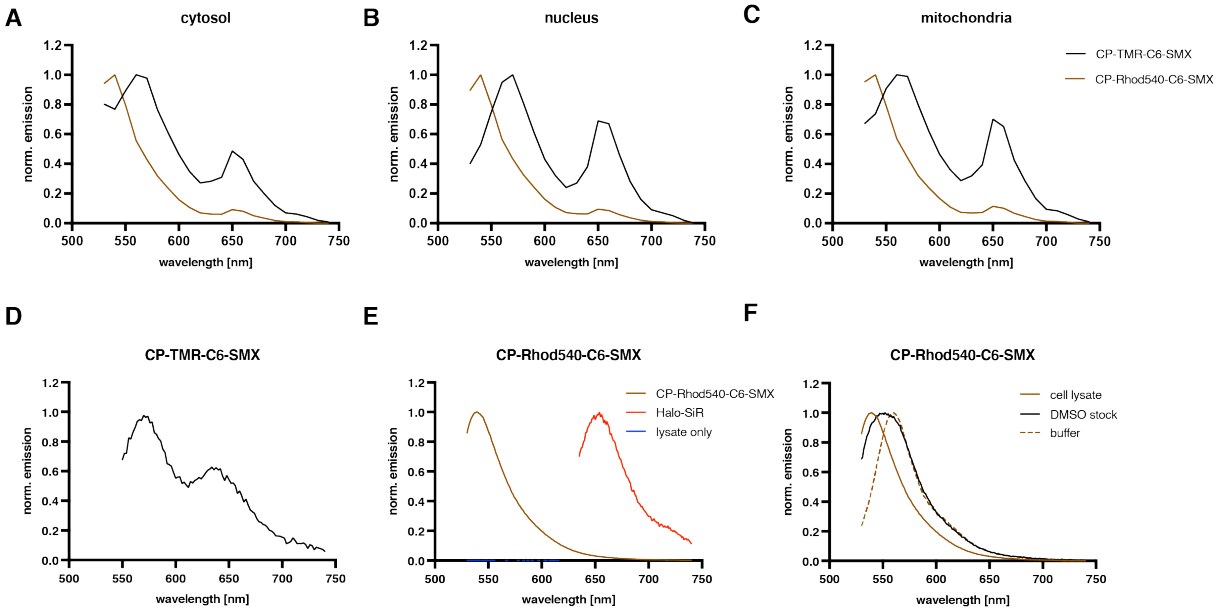

Figure 8: Characterization of NAD-Snifit in live cells. A)–C) emission spectra of NAD-Snifit labelled with CP-TMR-C6-SMX/Halo-SiR or CP-Rhod540-C6-SMX/Halo-SiR in cytosol, nucleus and mitochondria, respectively. D) emission spectra from lysate of cytosolic NAD-Snifit labelled with CP-TMR-C6-SMX and Halo-SiR. E) emission spectra from lysate of cytosolic NAD-Snifit labelled with CP-Rhod540-C6-SMX and Halo-SiR. F) comparison of different emission spectra of CP-Rhod540-C6-SMX.

For further investigation, the DMSO stock of CP-Rhod540-C6-SMX was analyzed by LC-MS. The UV-Vis chromatogram at 540 nm of CP-Rhod540-C6-SMX showed the product peak at $t_R = 2.56$ min with a corresponding mass to charge ratio (m/z) = 1129.32. In addition, a peak of a more polar impurity was detected at $t_R = 2.35$ min with a corresponding $m/z = 697.18$ (**Figure 9A**). The absorbance maximum of the impurity was at 520 nm (**Figure 9B**). Based on LC-MS analysis, around 20% of of CP-Rhod540-C6-SMX was degraded. In comparison, the UV-Vis chromatogram of CP-TMR-C6-SMX only showed minor impurities (**Figure 9C**). The DMSO stock of CP-Rhod540-C6-SMX was then subjected to high resolution mass spectrometry (HRMS) analysis. The existence of an impurity with a corresponding $m/z = 697.1722$ was confirmed and an additional impurity with a corresponding $m/z = 621.1644$ was detected (**Figure 9D**). The m/z of the impurities matched with degradation products of CP-Rhod540-C6-SMX, in which a ring opening of one or both azetidines took place. This would either result in the partially dealkylated rhodamine scaffold **12** or the fully dealkylated rhodamine 110 derivative **13** (**Figure 9E**). The dealkylation of the TMR core is known to blue-shift its spectral properties.[112] These findings could explain the blue-shift of the emission spectra of cells labelled with CP-Rhod540-C6-SMX. Both degradation products had a much lower molecular weight and less HBDs compared to CP-Rhod540-C6-SMX, which could lead to a better

permeability. This would result in a NAD-Snifit that was mainly labelled with the degradation products. As it did not have the SMX moiety, the NAD-Snifit would be non-functional, despite having a strong donor fluorescence. The DMSO stock of CP-Rhod540-C6-SMX was repurified by HPLC and the combined product fractions were neutralized with saturated bicarbonate solution before lyophilization. Cells expressing the cytosolic NAD-Snifit were labelled with repurified CP-Rhod540-C6-SMX and Halo-SiR, lysed and an emission spectrum was recorded on a plate reader. The spectrum showed a peak for the FRET donor (566 nm) and FRET acceptor (675 nm), which was not the case before. The emission of CP-Rhod540-C6-SMX now matched with the measurement in buffer and was not blue-shifted as before (**Figure 8F**). After the addition of QM385 to open the NAD-Snifit, the FRET signal was diminished. This indicated that the NAD-Snifit labelled with CP-Rhod540-C6-SMX would be functional (**Figure 9F**).

Subsequently, different storage conditions were investigated to avoid degradation. However, no differences were observed for the storage as powder or in dry DMSO (both –20 and –80 °C). As > 5% degradation was already sufficient to obtain a non-functional sensor, FRET donor substrates based on the JF dye strategy were not further investigated.

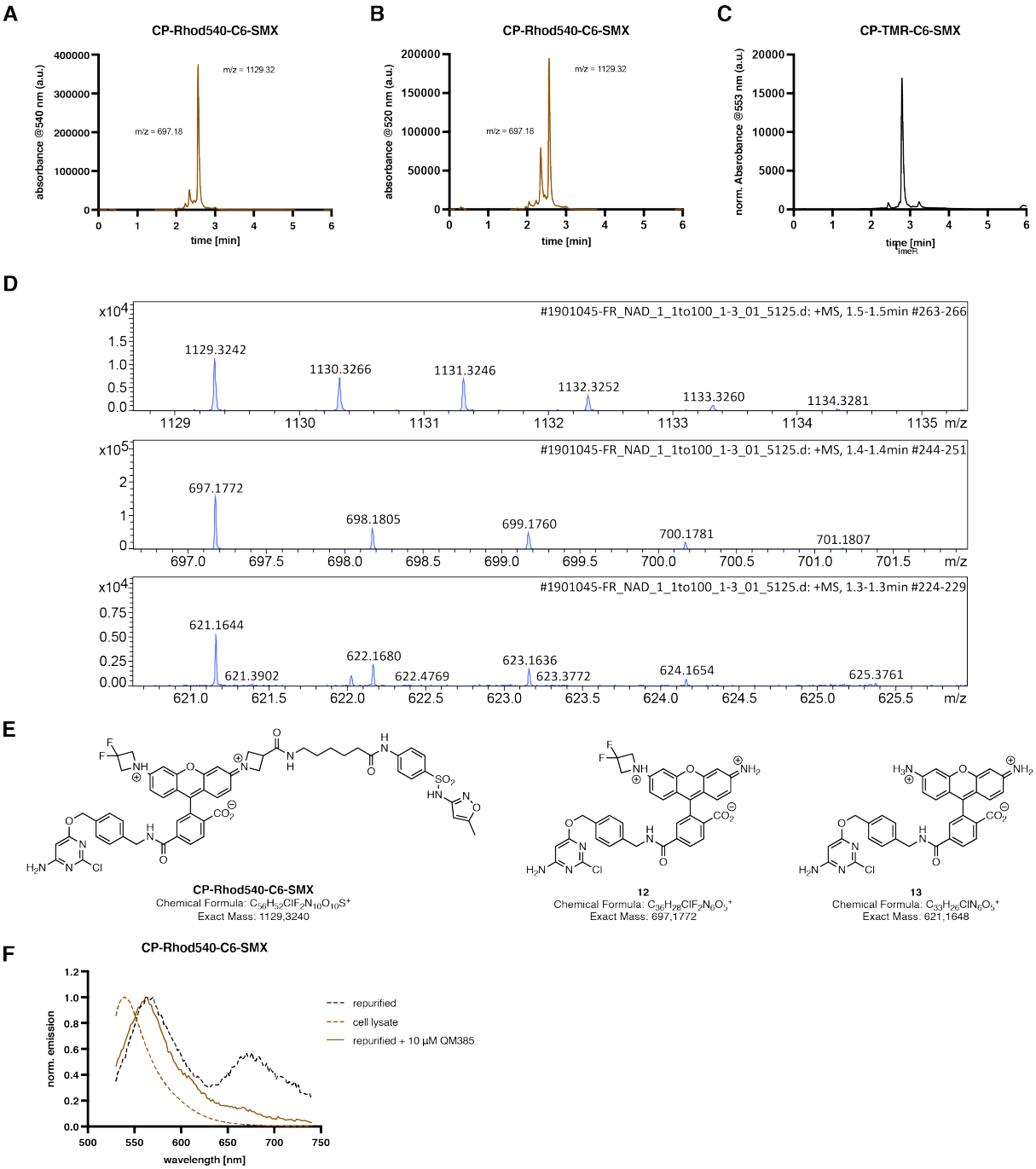

Figure 9: Investigation of CP-Rhod540-C6-SMX degradation. A) LC chromatrogram of CP-Rhod540-C6-SMX with absorbance at 540 nm. B) LC chromatrogram of CP-Rhod540-C6-SMX with absorbance at 520 nm. C) LC chromatrogram of CP-TMR-C6-SMX with absorbance at 553 nm. D) HRMS traces of CP-Rhod540-C6-SMX aliquot including degradation products. E) chemical structures of CP-Rhod540-C6-SMX and both dealkylated degradation products. F) emission spectra from lysate of cytosolic NAD-Snifit labelled with CP-Rhod540-C6-SMX and Halo-SiR.

3.3 MaP dye-based FRET donor substrates

3.3.1 Design

As the modification of CP-TMR-C6-SMX based on the JF dye strategy was not successful, the MaP dye strategy from the Johnsson lab utilizing sulfonamides was investigated. Based on previous data, two differently substituted sulfonamides were chosen to modify the TMR-C3-COOH scaffold. Methylsulfonamide (afterwards referred to as MaP1 derivatives) and *N,N*-dimethylsulfamide (afterwards referred to as MaP555 derivatives) effected the equilibrium between zwitterion and spirolactam to different extends.[113] This would allow tuning of the substrate to find a compromise between permeability and brightness, as fluorogenic substrates are more permeable, but also have a lower brightness. An additional approach was to modify TMR with a sulfonamide that was derivatized with an alkyl linker (afterwards referred to as MaP3 derivatives). One attractive feature of this approach would be to obtain a bifunctional and asymmetric molecule starting from a simple TMR as symmetric precursor (**Figure 10A**).

In addition, the inhibitor moiety of the FRET donor substrate could also influence its permeability. SMX has partial negative charge at physiological pH (pKa 5.7), which is not favorable for cell permeability.[114] Another potential drawback of SMX could be that it is an inhibitor of the bacterial dihydropteroate synthase and SPR was only classified as an off-target.[87, 115] The off-target binding is due to structural similarity between the respective enzyme substrates. Dihydropteroate synthase binds 6-hydroxymethyl-7,8-dihydropterin diphosphate (DHPP), while SPR binds sepiapterin and dihydrobiopterin (**Figure 10B**). Inhibition of dihydropteroate synthase with SMX does not require π-stacking interactions with $NADP^+$.[115] Therefore, π-stacking interactions between $NAD(P)^+$ and SMX inside SPR could result in a non-optimal affinity of the NAD(P)-Snifit. QM385 is a drug candidate for the inhibition of SPR and has been optimized for permeability and efficacy.[111] It was therefore considered as a template to design a more permeable inhibitor for the FRET donor substrates. Removal of the trifluoroethyl moiety would result in a pyrazol-pyrrolo-triazine (PPT) scaffold linked to a piperazine that could be exploited for peptide coupling (**Figure 10C**). SMX and other sulfa drugs such as SPY inhibit the SPR by the formation of a ternary complex between the inhibitor and $NADP^+$.[87] The x-ray structure of SPR with $NADP^+$

and QM385 showed the formation of a ternary complex as well, suggesting that π-stacking interactions should ensure the same selectivity as the SMX derivatives (**Figure 10D**).

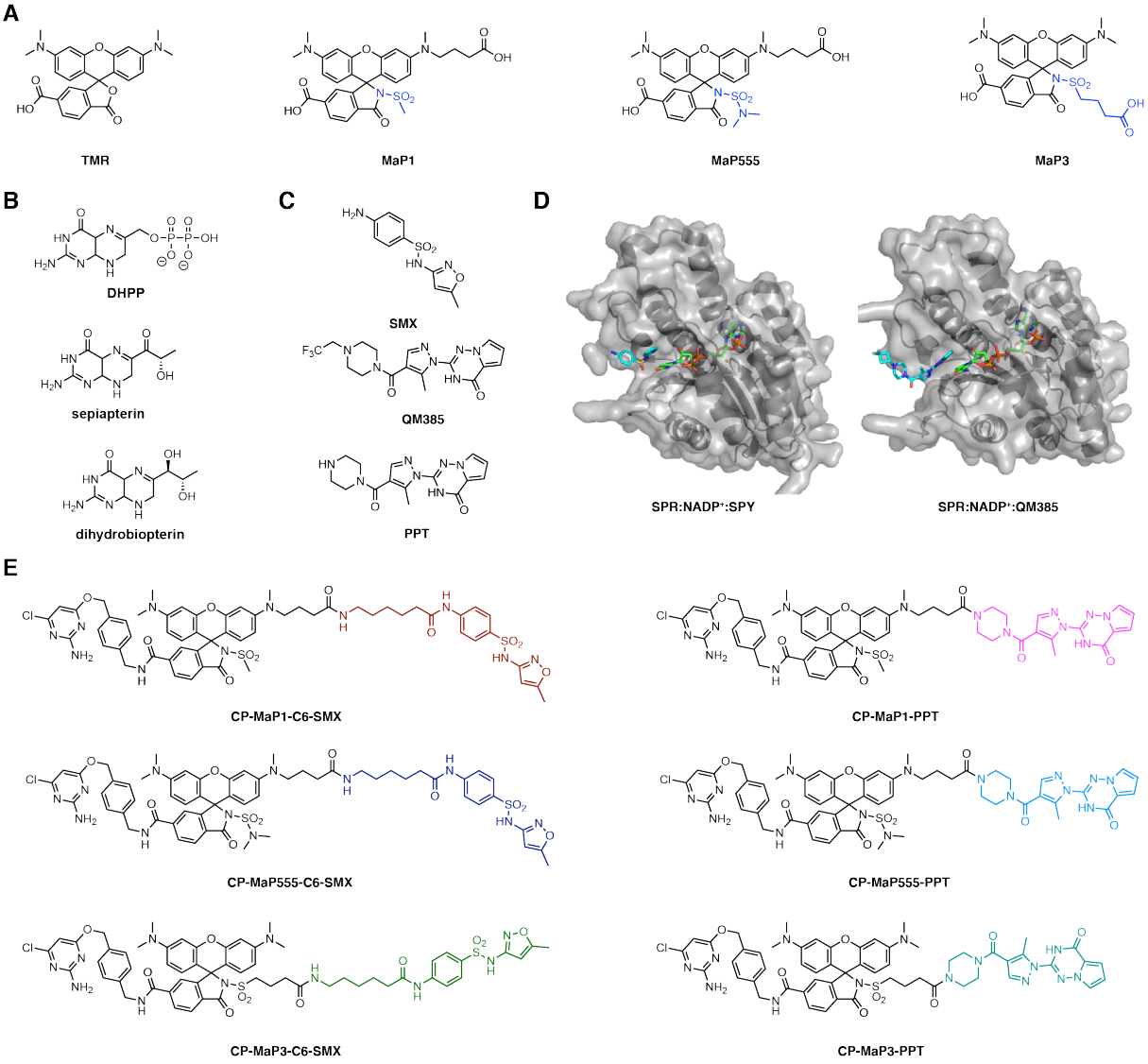

Figure 10: Design and rational of MaP dye-based FRET donor substrates. A) structures of TMR and TMR derived fluorophore scaffolds (MaP1, MaP555 and MaP3), where the *ortho*-carboxylic acid was converted into sulfonamides. B) stuctures of enzyme substrates: DHPP for dihydropteroate synthase and sepiapterin and dihydrobiopterin for SPR, respectively. C) stuctures of SPR inhibitors SMX, QM385 and PPT. D) x-ray structures of SPR with a complex of inhibitor and $NADP^+$. π-stacking interactions between sulfapyridine (SPY) and $NADP^+$ and QM385 and $NADP^+$ inside the binding pocket suggested the same binding mode. PDB:4HWK (SPY), structure of SPR with QM385 was obtained by Quartet Medicine and is not published. SPR is shown in grey, $NADP^+$ is shown in green and the inhibitors are shown in cyan. E) Structures new FRET donor substrates, where the *ortho*-carboxylic acid was converted into sulfonamides.

The modularity of the FRET donor substrate allowed the design of new substrates by combing MaP1, MaP555 and MaP3 with C6-SMX and PPT (**Figure 10E**). All new MaP dye-based FRET donor substrates had a significant difference in their calc. logP values between open and spirocyclic forms. CP-MaP1-PPT exhibited a relatively small

change in calc. logP compared to the other substrates. Using PPT as inhibitor reduced the numbers of hydrogen bond donors compared to C6-SMX (three vs. five). PPT substrates also had a lower polar surface area and less rotational bonds. These parameters indicated that PPT-based substrates could be more permeable than SMX-based substrates (**Table 4**).

Table 4: Key physicochemical properties of FRET donor substrates in the open[a] and spirocyclic[b] form, respectively. Properties were calculated with SwissADME.[104]

FRET donor	MW [Da]	calc. logP	HBDs	HBAs	TPSA [Å^2]	rot. bonds
CP-TMR-C6-SMX	1097.65	0.55[a]/6.43[b]	5[a]/5[b]	13[a]/13[b]	288.43[a]/270.92[b]	26[a]/25[b]
CP-Rhod540-C6-SMX	1129.32	–1.12[a]/6.41[b]	5[a]/5[b]	15[a]/15[b]	288.43[a]/270.92[b]	23[a]/22[b]
CP-MaP1-C6-SMX	1174.76	1.18[a]/4.72[b]	5[a]/5[b]	15[a]/14[b]	307.89[a]/307.45[b]	28[a]/26[b]
CP-MaP1-PPT	1135.66	2.97[a]/3.82[b]	3[a]/3[b]	14[a]/13[b]	277.71[a]/277.27[b]	20[a]/18[b]
CP-MaP555-C6-SMX	1203.13	2.43[a]/5.72[b]	5[a]/5[b]	16[a]/15[b]	311.13[a]/310.69[b]	29[a]/27[b]
CP-MaP555-PPT	1164.71	0.44[a]/6.08[b]	3[a]/3[b]	15[a]/14[b]	280.95[a]/280.51[b]	21[a]/19[b]
CP-MaP3-C6-SMX	1174.76	1.31[a]/5.06[b]	5[a]/5[b]	15[a]/14[b]	307.89[a]/307.45[b]	28[a]/26[b]
CP-MaP3-PPT	1135.66	1.00[a]/5.46[b]	3[a]/3[b]	14[a]/13[b]	277.71[a]/281.49[b]	20[a]/17[b]

3.3.2 Synthesis

The synthesis of PPT (**19**) started with the reaction of methyl acetoacetate **14** with *N,N*-dimethylformamide dimethyl acetal **15** to give enamine **16**. The pyrazole scaffold was furnished by first reacting triazine **17** with hydrazine followed by addition of enamine **16**. Saponification gave rise to **18**, which was coupled with an excess of piperazine to yield PPT (**19**). The synthesis of C6-SMX was performed as previously described.[84] Fmoc-protected 6-aminohexanoic acid **20** was coupled with SMX (**21**) followed by deprotection to yield C6-SMX (**23**) (**Figure 11**).

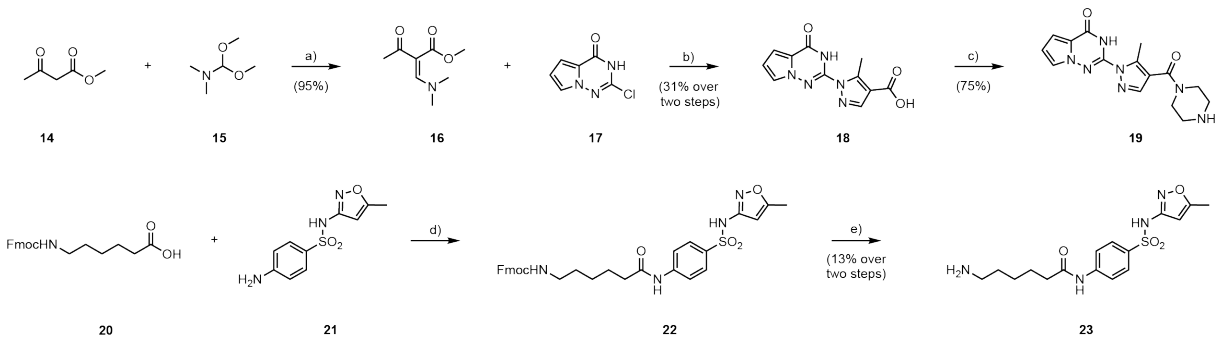

Figure 11: Synthesis of PPT and C6-SMX. Reagents and conditions: a) Dioxane, 80 °C; b) 1.) N_2H_4 (10.0 equiv.), EtOH, 50 °C, 72 h, 2.) AcOH (10.0 equiv.), **16** (1.1 equiv.), 50 °C; c) NaOH (3.0 equiv.) THF, r.t.; d) PyBOP (1.1 equiv.), piperazine (10.0 equiv.), DMF, 50 °C; e) EDC•HCl (2.0 equiv.), HOBt (2.0 equiv.), DIPEA (2.0 equiv.), DMF, r.t., piperidine (5 vol%), DMF, r.t..

The synthesis of MaP1 and MaP555 started with the bisallyl protection of TMR-C3-COOH (**24**). Several conditions were screened for the introduction of the sulfonamides. Originally, the *ortho*-carboxylic acid of TMR-C3-COOH (**24**) was converted to the corresponding acid chloride using $POCl_3$ in dichloromethane under reflux followed by addition of the respective sulfonamide.[113] However, these harsh conditions did not prove to be reproducible. An alternative to introduce the sulfonamides was the use of EDC and DMAP.[116] These mild conditions afforded **26** and **27** in good yield. Deprotection of both allyl groups gave rise to the optimized fluorophore scaffold **28** and **29** These molecules exhibited two carboxylic acids. For a selective coupling with C6-SMX (**22**) or PPT (**19**), the higher reactivity of the aliphatic carboxylic acid was exploited. **28** and **29** were coupled with C6-SMX or PPT to yield **30**, **31** and **34**, **35**, respectively. In the last step, they were coupled with CP-NH_2 (**7**) to give CP-MaP1-C6-SMX (**32**), CP-MaP1-PPT (**36**), CP-MaP555-C6-SMX (**33**) and CP-MaP555-PPT (**37**), respectively (**Figure 12**).

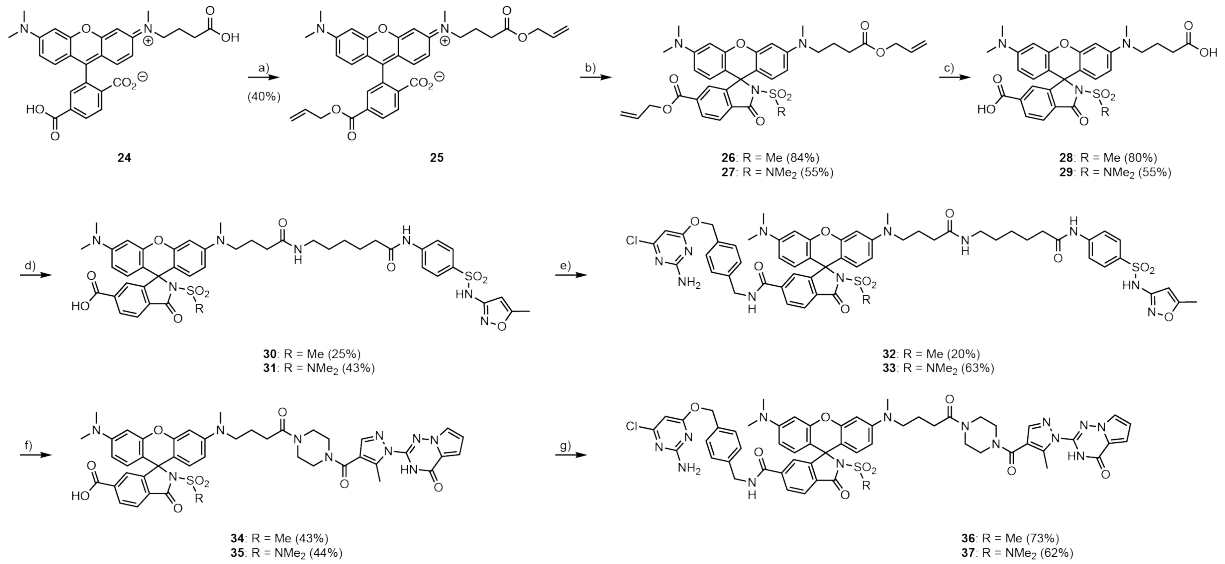

Figure 12: Synthesis of CP-MaP1-C6-SMX, CP-MaP1-PPT, CP-MaP555-C6-SMX and CP-MaP555-PPT. Reagents and conditions: a) Allylbromide (6.0 equiv.), NEt_3 (8.0 equiv.), K_2CO_3 (4.0 equiv.), DMF, 0 °C to r.t., o.n.; b) EDC•HCl (8.0 equiv.), methanesulfonamide or *N,N*-dimethylsulfamide (20.0 equiv.), DMAP (8.0 equiv.), CH_2Cl_2, 50 °C; c) 1,3-dimethylbarbituric acid (6.0 equiv.), $Pd(PPh_3)_4$ (1.0 equiv.), MeOH/CH_2Cl_2 (5:1), r.t.; d) **22** (1.2 equiv.), DIPEA (8.0 equiv.), TSTU (1.2 equiv.), DMSO, r.t., 6 h; e) **7** (1.2 equiv.), DIPEA (8.0 equiv.), TSTU (1.2 equiv.), DMSO, r.t., 6 h; f) **19** (1.2 equiv.), DIPEA (8.0 equiv.), PyBOP (1.1 equiv.), DMF, r.t., 6 h; g) **7** (1.2 equiv.), DIPEA (8.0 equiv.), TSTU (1.2 equiv.), DMSO, r.t., 6 h.

The synthesis of the MaP3 scaffold started with the benzyl protection of 4-sulfamoylbutyric acid **38** and allyl protection of TMR (**40**). Introduction of **39** was performed using EDC and DMAP. Subsequently, it was indented to exploit the orthogonal protection groups for selective coupling of the inhibitors and CP-NH_2. The

deprotection of the benzyl group with Pd/C and H_2 led to hydration of the allyl group to a propyl ester (even with short reaction times and at room temperature). The cleavage of the ester was neither possible under basic nor acidic conditions without degradation of the fluorophore. Next, it was attempted to first deprotect the allyl group and coupling with CP-NH_2 followed by deprotection of the benzyl group. However, Pd/C and H_2 reacted with the chloride moiety of CP. Therefore, the deprotection of **42** started with the removal of the allyl group followed by the benzyl group. Subsequently, the higher reactivity of the aliphatic carboxylic acid was exploited to first couple **43** with C6-SMX (**22**) and PPT (**19**). In the final step, **45** and **47** were coupled with CP-NH_2 (**7**) to yield CP-MaP3-C6-SMX (**46**) and CP-MaP3-PPT (**48**), respectively (**Figure 13**)

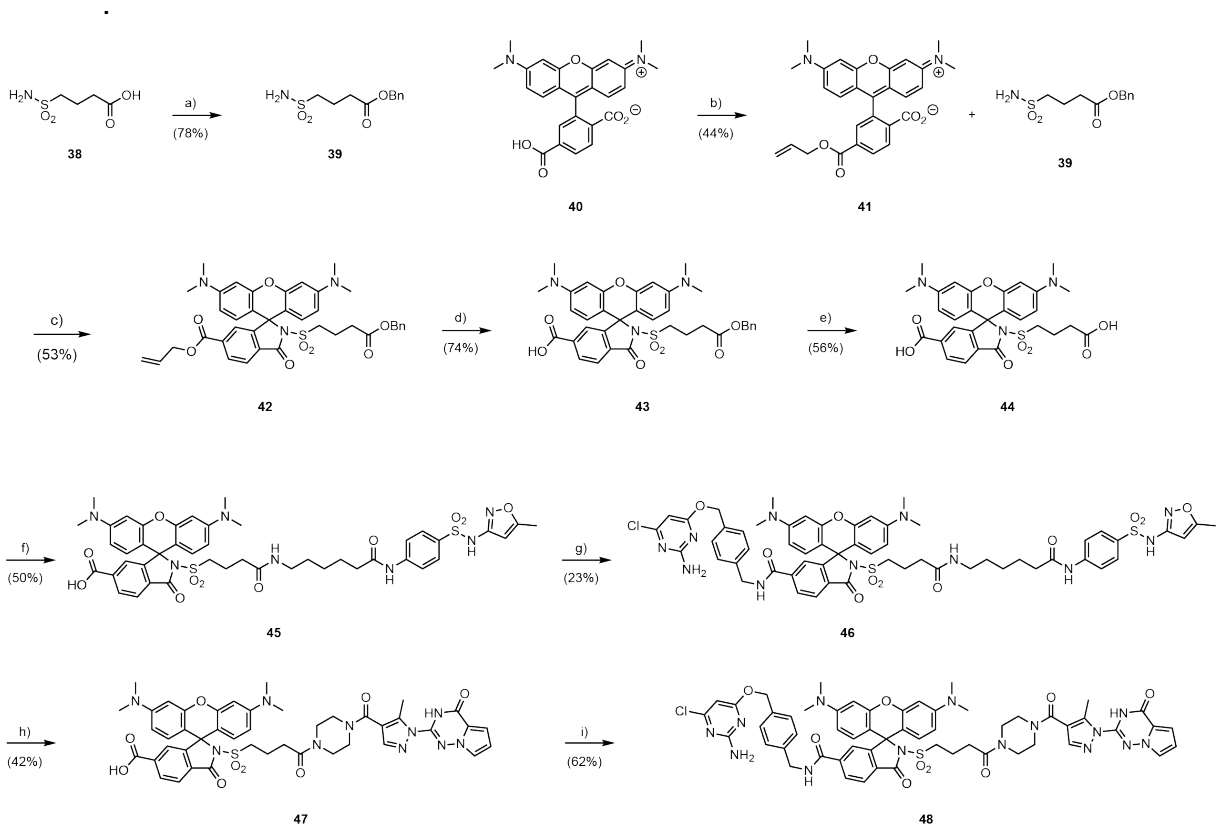

Figure 13: Synthesis of CP-MaP3-C6-SMX and CP-MaP3-PPT. Reagents and conditions: a) KI (0.3 equiv.), DIPEA (1.0 equiv.), benzyl bromide (1.0 equiv.), DMF, r.t., o.n.; b) allylbromide (3.0 equiv.), NEt_3 (8.0 equiv.), K_2CO_3 (2.0 equiv.), DMF, 0 °C to r.t., o.n.; c) EDC•HCl (8.0 equiv.), DMAP (8.0 equiv.), CH_2Cl_2, 50 °C; d) 1,3-dimethylbarbituric acid (6.0 equiv.), $Pd(PPh_3)_4$ (1.0 equiv.), MeOH/CH_2Cl_2 (5:1), r.t.; e) H_2, Pd/C (10 mol%), THF/MeOH (1:1), r.t., 12 h; f) **22** (1.2 equiv.), DIPEA (8.0 equiv.), TSTU (1.2 equiv.), DMSO, r.t., 6 h; g) **7**, DIPEA (8.0 equiv.), TSTU (1.2 equiv.), DMSO, r.t., 6 h; h) **19** (1.2 equiv.), DIPEA (8.0 equiv.), PyBOP (1.1 equiv.), DMF, r.t., 6 h; i) **7**, DIPEA (8.0 equiv.), TSTU (1.2 equiv.), DMSO, r.t., 6 h.

3.3.3 Characterization *in vitro*

The absorbance and emission spectra of the new FRET donor substrates were very similar to spectra obtained for CP-TMR-C6-SMX (**Table 5**). These results were in agreement with previous findings showing that introduction of sulfonamides do not affect the spectral properties compared to the parental rhodamine core (**Figure 14A**).[116] Titration of the new FRET donor substrates in different mixtures of water and dioxane demonstrated a clear shift towards the spirocyclic form. This was indicated by the D_{50} value representing the dielectric constant at half-maximum absorbance. CP-TMR-C6-SMX (8.4, 95% CI: 7.6–9.2) was fluorescent in all mixtures. CP-MaP1-C6-SMX (44.9, 95% CI: 43.7–46.2), CP-MaP1-PPT (43.4, 95% CI: 42.9–43.9), CP-MaP3-C6-SMX (44.8, 95% CI: 43.9–45.7) and CP-MaP3-PPT (44.5, 95% CI: 43.7–45.4) showed D_{50} values > 40 and could be considered as having a fluorogenic potential.[113] CP-MaP555-C6-SMX (53.1, 95% CI: 51.8–54.3) and CP-MaP555-PPT (53.2, 95% CI: 50.0–56.5) had even higher D_{50} values (**Figure 14B**). They also showed a significant higher turn-on after binding to the SNAP-tag than CP-TMR-C6-SMX (2.5, 95% CI: 2.4–2.6). Turn-on was expressed as fold-change in emission of substrate after SNAP labelling and substrate in aqueous buffer. CP-MaP1-C6-SMX (7.9, 95% CI: 7.1–8.6), CP-MaP1-PPT (7.4, 95% CI: 6.5–8.5), CP-MaP3-C6-SMX (9.8, 95% CI: 7.6–11.9) and CP-MaP3-PPT (9.6, 95% CI: 7.4–11.8) had a similar fold-change. CP-MaP555-C6-SMX (20.7, 95% CI: 18.0–23.3) and CP-MaP555-PPT (23.3, 95% CI: 22.8–23.9) showed an even higher turn-on, which was in agreement with differences in the D_{50} values. No overall difference between SMX and PPT substrates was observed (**Figure 14C**). MaP1 and MaP3 substrates gave equivalent results as their sulfonamides have both an alkyl substitution resulting in a similar nucleophilicity. The higher nucleophilicity of the *N,N*-dimethylsulfamide substituted MaP555 shifted the equilibrium even more to the spirocyclic form, which was in agreement with previous data.[113, 116]

Table 5: Spectroscopic data of FRET donor substrates and titration of purified NAD(P)-Snifits with NAD^+ or $NADPH/NADP^+$. Data are shown as mean ± SD. n.d. (not determined).

Substrate	λ_{ab} [nm]	λ_{em} [nm]	NAD^+: c_{50} [µM]	$NADPH/NADP^+$: r_{50}
CP-TMR-C6-SMX	554	579	923±182	14±3
CP-MaP1-C6-SMX	559	583	600±137	13±2
CP-MaP1-PPT	559	583	13±5	n.d.
CP-MaP555-C6-SMX	555	576	876±178	11±3
CP-MaP555-PPT	559	580	12±2	n.d.
CP-MaP3-C6-SMX	557	579	708±85	14±2
CP-MaP3-PPT	557	578	8±1	n.d.

SNAP-tag labelling kinetics with the new FRET donor substrates were comparable to those of CP-TMR-C6-SMX. Any potential differences in cellular labelling efficiency would thus less likely originate from differences in labelling kinetics (**Figure 14D**). Titration of purified NAD-Snifit with NAD^+ showed a significant shift in sensor response for PPT-based substrates compared to SMX-based substrates. Their c_{50} values were decreased 46–89-fold and independent from the fluorophore scaffold (**Figure 14E** and **Table 5**). Titration of purified NADP-Snifit with $NADPH/NADP^+$ showed a similar response for all SMX-based substrates (**Figure 14F** and **Table 5**). In contrast, titration curves for all PPT-based substrates could not be obtain. Titrations were performed with a total cofactor concentration of 100 µM. While SMX-based substrates were responsive under these conditions, all PPT-based substrates did not show a change in their ratio, presumably because the affinity for $NADP^+$ is too high and the difficulty to remove traces of $NADP^+$ even from pure NADPH.

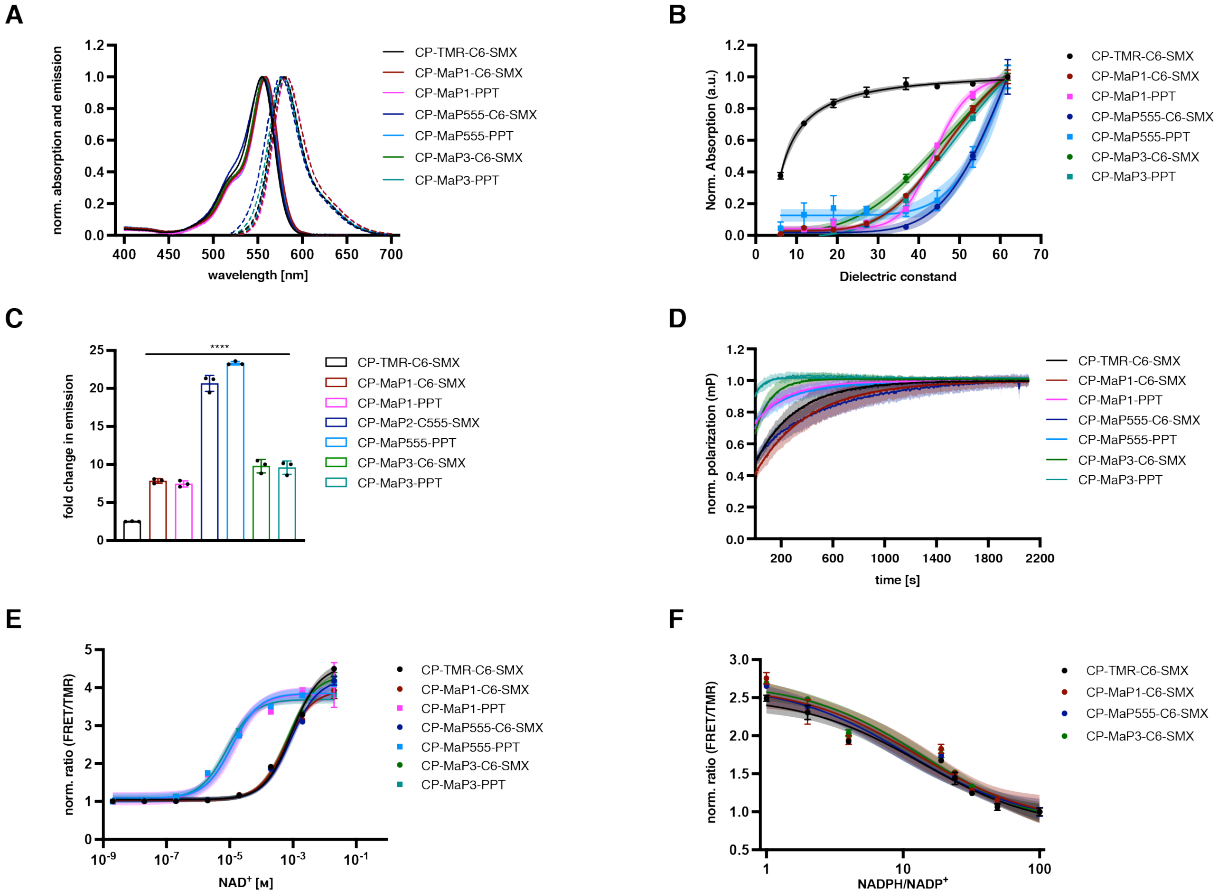

Figure 14: Characterization of MaP dye-based FRET donor substrates *in vitro*. A) normalized absorbance and emission spectra of new FRET donor substrates. B) normalized absorbance at 550 nm in water-dioxane mixtures as a function of dielectric constant. C) fold-change in emission upon SNAP-tag labelling compared to emission in buffer. D) labelling kinetics of purified NAD⁺ sensor with sensor substrates measured by fluorescence polarization. E) titration curve of purified NAD-Snifit labelled with sensor substrates and Halo-SiR. F) titration curve of purified NADP-Snifit labelled with sensor substrates and Halo-SiR. *N* = three independent experiments. Data are shown as mean ± SD and fit is shown with 95% CI. **** $p < 0.0001$ using a one-way ANOVA with Dunnett's multiple comparison test with respect to CP-TMR-C6-SMX.

3.3.3 Characterization in live cells

The labelling conditions for the new FRET donor substrates were determined in live cells. Previous conditions featured substrate concentrations of 1 µM and the use of 10 µM verapamil to increase intracellular substrate concentration.[84] In addition to high substrate concentrations, the efflux pump inhibitor verapamil is known to have off-target effects, which could affect metabolic measurements with the NAD(P)-Snifits.[117-118] U2OS cells expressing a cytosolic SNAP-mEGFP construct were used to determine the FRET donor substrate concentration for maximum intracellular SNAP-tag labelling. In FACS experiments, the ratio of TMR and GFP emission was used as a read-out for labelling efficiency. CP-MaP555-PPT showed a superior labelling compared to all other substrates and reached a plateau at 500 nM substrate concentration. The other substrates had a five to ten times lower TMR/GFP ratio and CP-MaP1-C6-SMX and CP-TMR-C6-SMX did not reach a plateau under these conditions (**Figure 15A**). Addition of 10 µM verapamil had no impact on MaP555 substrates, however CP-TMR-C6-SMX, CP-MaP1-C6-SMX and CP-MaP3-C6-SMX showed an up to five times increased labelling (**Figure 15B**). A similar approach was used to determine the optimal substrate concentration for Halo-SiR. U2OS cells expressing a cytosolic Halo-mEGFP construct were labelled with Halo-SiR and the ratio of SiR and GFP emission was used as a read-out. Labelling with Halo-SiR reached a plateau at 100–200 nM and the addition of verapamil had no effect (**Figure 15AC**). Based on these results, the following conditions were used for further labelling: 500 nM FRET donor substrates and 200 nM Halo-SiR.

U2OS cells expressing the NAD-Snifit in the cytosol, nucleus and mitochondria were labelled with 500 nM of the FRET donor substrates and analyzed by confocal microscopy. Similar to previous FACS data, CP-MaP555-C6-SMX (32,685, 95% CI: 30,085–35,285) and CP-MaP555-PPT (35,782, 95% CI: 32,206–35,285) showed higher fluorescent intensities in the cytosol compared to CP-TMR-C6-SMX (7,585, 95% CI: 6,967–8,203). CP-MaP3-C6-SMX did not show an improved fluorescent intensity (9,325, 95% CI: 8,754–9,716) compared to CP-TMR-C6-SMX (**Figure 15D**). CP-MaP555-C6-SMX (34,635, 95% CI: 31,426–37,844) and CP-MaP555-PPT (36,769, 95% CI: 33,409–40,129) also had higher fluorescence intensities in the nucleus compared to CP-TMR-C6-SMX (13,702, 95% CI: 12,673–14,731).

CP-MaP1-PPT (16,328, 95% CI: 14,718–17,938) and CP-MaP3-C6-SMX (16,604, 95% CI: 15,428–17,781) did not show increased fluorescence intensities compared to CP-TMR-C6-SMX (**Figure 15E**). Labelling in mitochondria gave comparable results. CP-MaP555-C6-SMX (27,353, 95% CI: 25,879–28,827) and CP-MaP555-PPT (32,308, 95% CI: 25,879–34,110) had higher fluorescence intensities compared to CP-TMR-C6-SMX (9,088, 95% CI: 8,632–9,544). CP-MaP3-C6-SMX did not show an improved intensity (8,891, 95% CI: 8,512–9,269) compared to CP-TMR-C6-SMX (**Figure 15F**).

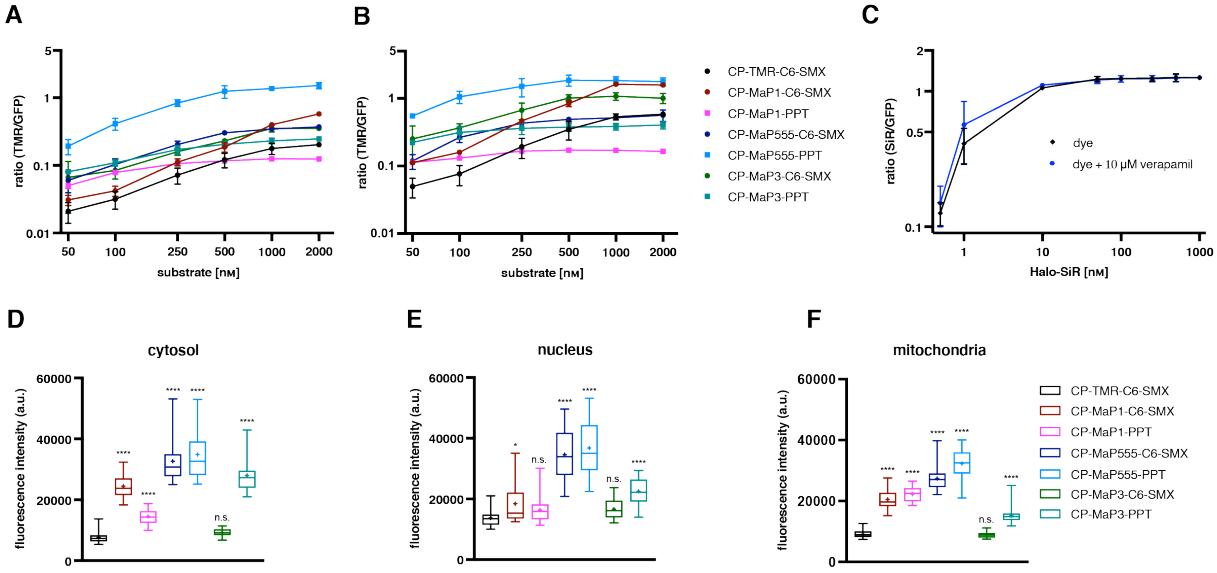

Figure 15: Determination of labelling conditions of MaP dye-based FRET donor substrates. A) FACS data of U2OS cells expressing a cytosolic SNAP-mEGFP labelled with sensor substrates for 14 h. B) FACS data of U2OS cells expressing SNAP-mEGFP labelled with sensor substrates in the presence of 10 µM verapamil. C) FACS data of U2OS cells expressing a cytosolic Halo-mEGFP labelled with Halo-SiR. D)–F) U2OS cells expressing the NAD-Snifit were single labelled with 500 nM of sensor substrates for 14 h and analyzed by confocal microscopy. *N* = three independent experiments for FACS experiments and data are shown as mean ± SD. *N* = 30 cells for confocal microscopy. The box represents the 25th and 75th percentile and the whiskers are the minimum and maximum. The mean and median are indicated by a cross or line, respectively. n.s. = not significant, **** $p < 0.0001$ using a one-way ANOVA with Dunnett's multiple comparison test with respect to CP-TMR-C6-SMX.

Confocal microscopy was also used to determine the labelling specificity of the new FRET donor substrates. CP-MaP555-C6-SMX and CP-MaP555-PPT did not only show the highest fluorescence intensities, but also had very high signal to noise ratios and gave very little unspecific staining in cells that did not express SNAP-tag. CP-MaP1-C6-SMX and CP-MaP1-PPT had improved signal to noise ratios compared to CP-TMR-C6-SMX. However, their fluorescence intensities were much lower than for both MaP555-based substrates. CP-MaP3-C6-SMX and CP-MaP3-PPT showed improved fluorescence intensities compared to CP-TMR-C6-SMX, but also exhibited much higher unspecific staining in non-expressing cells compared to CP-MaP555-C6-SMX and CP-MaP555-PPT (**Figure 16A–D**).

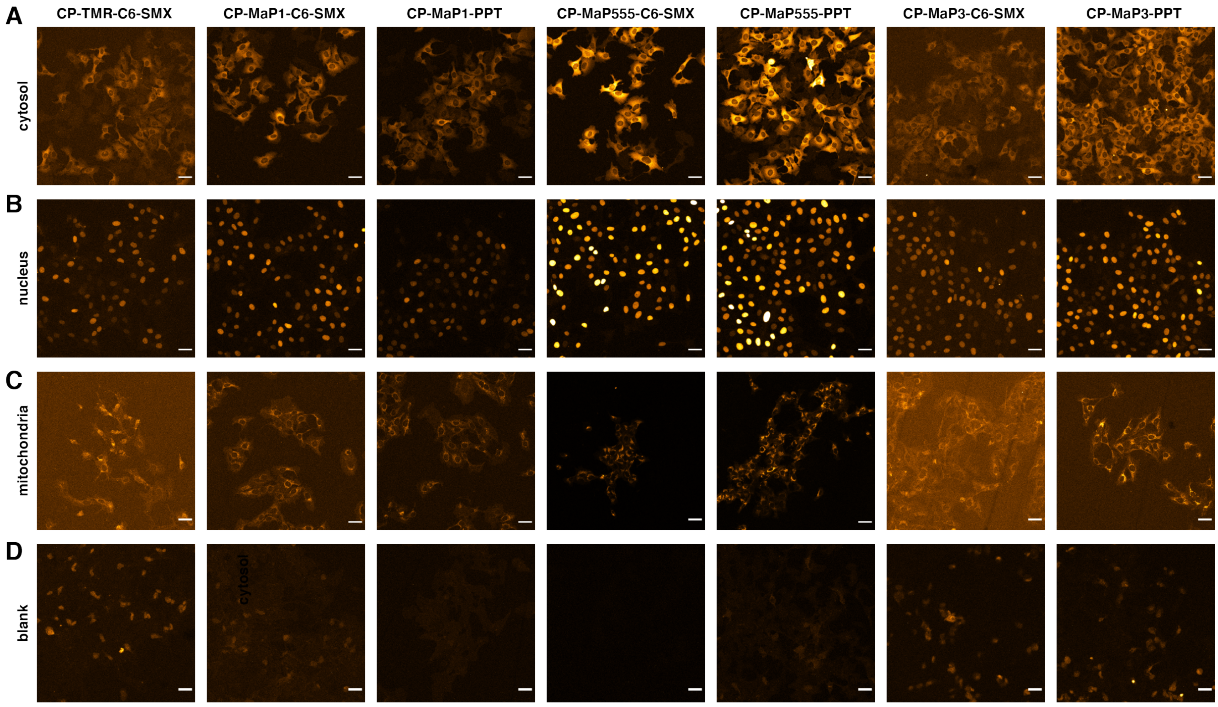

Figure 16: Live cell labelling with MaP dye-based FRET donor substrates. A)–C) confocal images of U2OS cells expressing the NAD^+ biosensor in the cytosol, nucleus or mitochondira. Cells were single labelled with 500 nM of sensor substrates. D) non-expressing U2OS cells were incubated with 500 nM of FRET donor substrates. Scale bar: 50 µm.

These labelling experiments demonstrated that CP-MaP555-C6-SMX and CP-MaP555-PPT exhibit the best labelling performance of the new FRET donor substrates. They also clearly outperformed CP-TMR-C6-SMX with respect to labelling efficiency and specificity. The substrate concentration could be reduced to 500 nM and addition of verapamil was not needed. Applying these conditions, CP-MaP555-C6-SMX and CP-MaP555-PPT had a very bright signal and high signal to noise ratios, which was especially evident in the mitochondria (**Figure 17A–C**).

After determination of the optimal substrate concentration, the minimal labelling time was determined. U2OS cells expressing a cytosolic SNAP-mEGFP construct were incubated with CP-TMR-C6-SMX, CP-MaP555-C6-SMX or CP-MaP555-PPT up to 12 h. Under these conditions, the ratio TMR/GFP reached a plateau after 10 h for cells labelled with CP-MaP555-C6-SMX or CP-MaP555-PPT, but not for cells labelled with CP-TMR-C6-SMX (**Figure 17D**). These data suggest that labelling with CP-MaP555-C6-SMX and CP-MaP555-PPT in live cells approaches completion after 10 h.

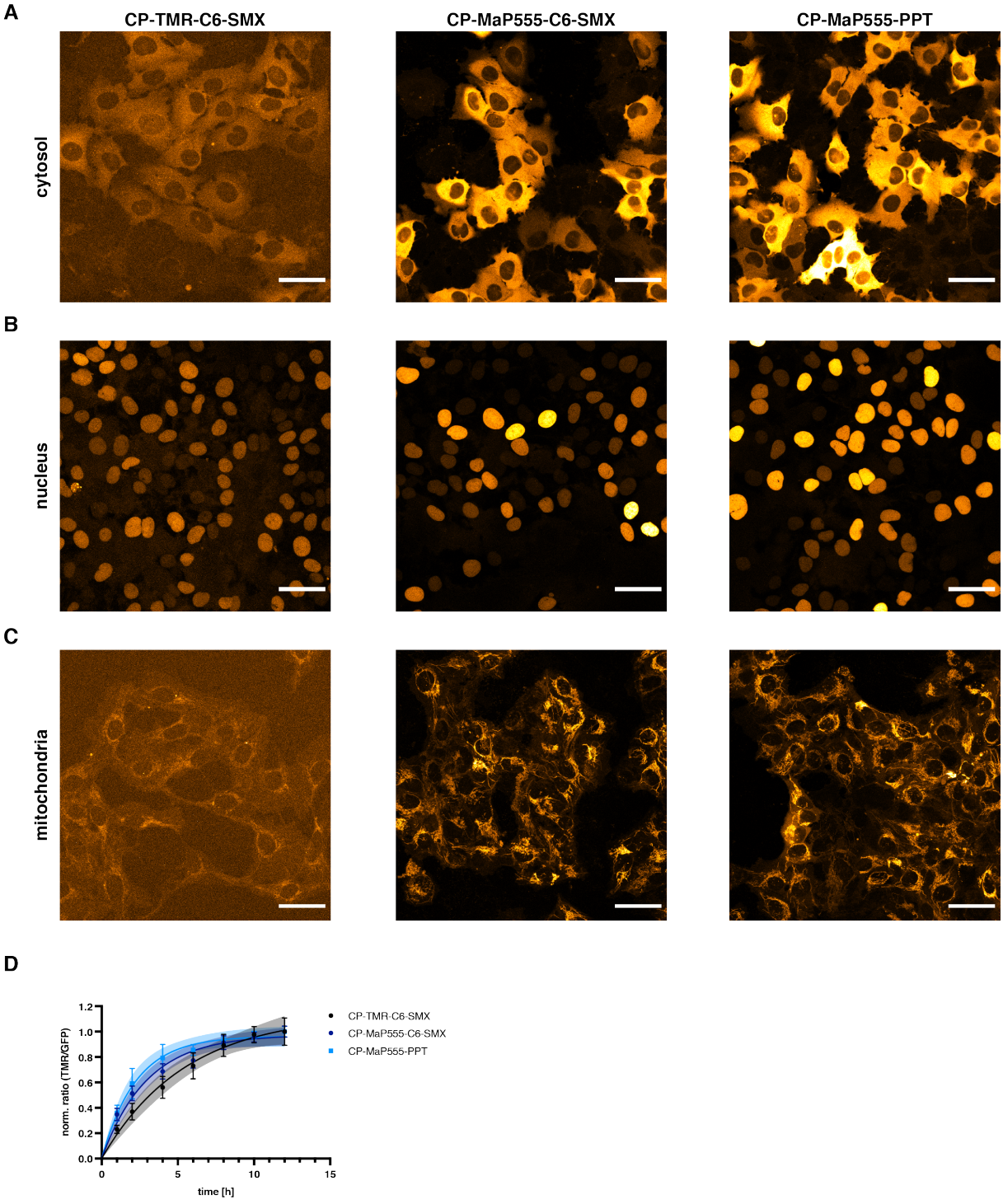

Figure 17: Benchmark of CP-TMR-C6-SMX with CP-MaP555-C6-SMX and CP-MaP555-PPT. A)–C) Confocal images of U2OS cells expressing the NAD-Snifit in the cytosol, nucleus or mitochondira. Cells were single labelled with 500 nM of FRET donor substrates. Scale bar: 50 µm. D) FACS data of U2OS cells expressing cytosolic SNAP-mEGFP and labelled with 500 nM of FRET donor substrates. Data are shown as mean ± SEM and fit is shown with 95% CI. *N* = three independent experiments.

3.3.4 Functionality of the NAD(P)-Snifits in live cells

The functionality of the NAD(P)-Snifits in cells labelled with CP-MaP555-C6-SMX and CP-MaP555-PPT was investigated. U2OS cells expressing an inducible NAD- or NADP-Snifit were labelled with CP-MaP555-C6-SMX or CP-MaP555-PPT and Halo-SiR. Subsequently, the cells were titrated with the SPR inhibitor QM385 to open the sensor in a dose-dependent manner, which was measured by FACS. Thereby, the NAD(P)-Snifit could be artificially opened by outcompeting the intramolecular tether. The change in FRET ratio (ΔR) between basal and fully open state and the half-maximum effective concentration (EC_{50}) of QM385 are indirect measures of the affinity of the NAD(P)-Snifits. In these titrations, the EC_{50} is defined as the QM385 concentration needed for 50% change in FRET ratio.

The ΔR was higher for the NAD-Snifit labelled with CP-MaP555-PPT/Halo-SiR compared to CP-MaP555-C6-SMX/Halo-SiR in the cytosol (58% vs. 181%), nucleus (59% vs. 135%) and mitochondria (86% vs. 102%), suggesting that the PPT ligand favors the closed state of the NAD-Snifit in cells. Also, the EC_{50} was higher for the NAD-Snifit labelled with CP-MaP555-PPT/Halo-SiR compared to CP-MaP555-C6-SMX/Halo-SiR in the cytosol (27 nM vs. 649 nM), nucleus (23 nM vs. 838 nM) and mitochondria (9 nM vs. 677 nM) (**Figure 18A** and **Table 6**). The differences in EC_{50} between NAD-Snifit labelled with CP-MaP555-PPT/Halo-SiR and CP-MaP555-C6-SMX/Halo-SiR are in agreement with the different response ranges in *in vitro* titrations.

Table 6: Titration of NAD-Snifit and NADP-Snifit with QM385 in U2OS cells. Data are shown as mean with 95% CI. *N* = three independent experiments.

NAD-Snifit	**cytosol**		**nucleus**		**mitochondria**	
	EC_{50} [nM]	ΔR (%)	EC_{50} [nM]	ΔR (%)	EC_{50} [nM]	ΔR (%)
CP-MaP555-C6-SMX	27 (7–46)	58 (36–79)	23 (6–40)	59 (39–79)	9 (5–13)	86 (31–108)
CP-MaP555-PPT	649 (484–813)	181 (141–220)	838 (651–2326)	135 (109–161)	677 (270–1626)	102 (92–112)
NADP-Snifit	**cytosol**		**nucleus**		**mitochondria**	
	EC_{50} [nM]	ΔR (%)	EC_{50} [nM]	ΔR (%)	EC_{50} [nM]	ΔR (%)
CP-MaP555-C6-SMX	25 (9–52)	61 (20–141)	37 (16–89)	50 (38–77)	28 (4–105)	41 (27–55)
CP-MaP555-PPT	708 (493–924)	170 (101–238)	421 (280–623)	168 (133–193)	1721 (210–3240)	70 (59–81)

The problems with the *in vitro* titration of the NADP-Snifit labelled with CP-MaP555-PPT/Halo-SiR were assumed to be of a technical nature. Therefore, the NADP-Snifit was also labelled with CP-MaP555-PPT/Halo-SiR in U2OS cells to investigate the cellular performance.

The results for the NADP-Snifit were similar to the NAD-Snifit. The ΔR was higher for the NADP-Snifit labelled with CP-MaP555-PPT/Halo-SiR compared to CP-MaP555-C6-SMX/Halo-SiR in the cytosol (61% vs. 170%), nucleus (50% vs. 168%) and mitochondria (41% vs. 70%). Also, the EC_{50} was higher for the NADP-Snifit labelled with CP-MaP555-PPT/Halo-SiR compared to CP-MaP555-C6-SMX/Halo-SiR in the cytosol (25 nM vs. 708 nM), nucleus (37 nM vs. 421 nM) and mitochondria (28 nM vs. 1721 nM) (**Figure 18B** and **Table 6**). These data suggested different response ranges higher for the NADP-Snifit labelled with CP-MaP555-C6-SMX and CP-MaP555-PPT.

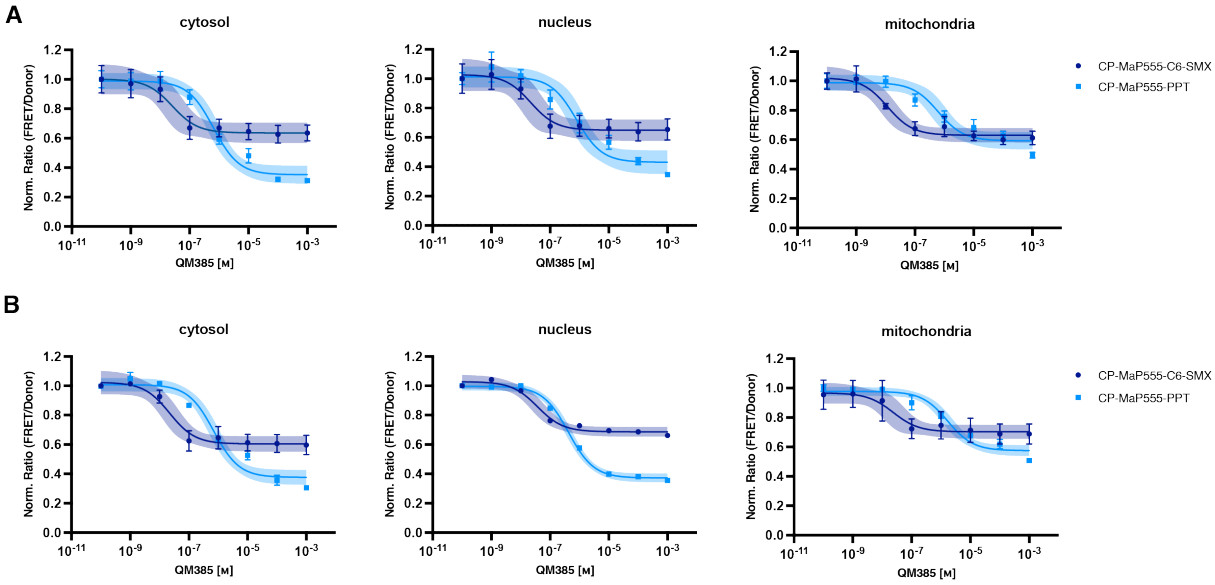

Figure 18: Artifical opeing of NAD(P)-Snifit in live cells. A) titration of NAD-Snifit in cytosol, nucleus and mitochondria with QM385. B) titration of NADP-Snifit in cytosol, nucleus and mitochondria with QM385. Data are shown as mean ± SEM and fit is shown with 95% CI. *N* = three independent experiments.

3.3.5 Analyte buffering by NAD(P)-Snifits

Applying a biosensor in a biological system (*e.g.* cells) can affect the concentration or behavior of the analyte and introduce a bias into the experiment. For instance, this has been shown for Ca^{2+} indicators, which could alter signaling patterns.[119] This raised the question whether expression and labelling of the NAD(P)-Snifit in cells could have an impact on $NAD(P)^+$.

To address this question, the total amounts of NAD^+ and $NADP^+$ in cell lysates after expression and labelling of the NAD(P)-Snifit were quantified. A sample preparation workflow and LC-MS/MS method was developed in collaboration with the mass spectrometry core facility at the MPImR. ^{13}C labelled yeast extract was used as internal standard (IS) to account for matrix effects and pipetting errors. $1 \cdot 10^6$ of U2OS cells (corresponded to one well in a six-well plate at 80% confluency) were sufficient for robust NAD^+ measurements and at least $3 \cdot 10^6$ of U2OS cells were needed for robust $NADP^+$ measurements. This was in agreement with lower concentrations reported for $NADP^+$.[58] As $NADP^+$ showed an unreproducible behavior during chromatography, only total NAD^+ measurements were pursued.

The NAD-Snifit was expressed and labelled in the cytosol, nucleus and mitochondria of U2OS cells. Cells were harvested and lysed with hot buffered ethanol (80 °C) in the presence of IS. NAD^+ was quantified in the supernatant whereby the protein content of the lysate was determined *via* Bradford assay and used for normalization (**Figure 19A**). Total NAD^+ in U2OS cells was found to be 1.38 µmol/mg protein (95% CI: 1.32–1.44). Expression of the NAD-Snifit and labelling with CP-MaP555-C6-SMX/Halo-SiR did not affect total NAD^+: cytosol (1.37 µmol/mg protein, 95% CI: 1.25–1.50), nucleus (1.38 µmol/mg protein, 95% CI: 1.15–1.61) and mitochondria (1.26 µmol/mg protein, 95% CI: 1.03–1.50). Labelling with CP-MaP555-PPT/Halo-SiR also had no effect on total NAD^+: cytosol (1.37 µmol/mg protein, 95% CI: 1.27–1.46), nucleus (1.39 µmol/mg protein, 95% CI: 1.30–1.49) and mitochondria (1.39 µmol/mg protein, 95% CI: 1.35–1.44). No difference between CP-MaP555-C6-SMX and CP-MaP555-PPT was observed, despite NAD-Snifits labelled with CP-MaP555-PPT were present in a more closed (NAD^+ bound) state (**Figure 19B, C**).

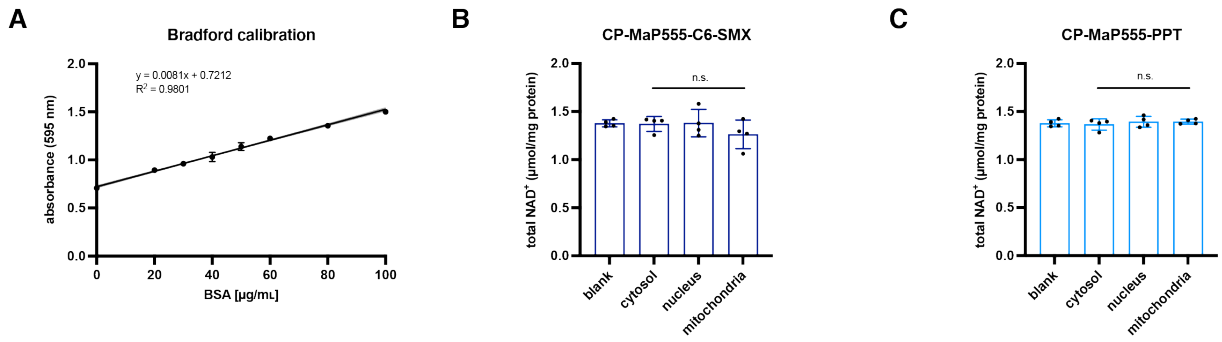

Figure 19: LC-MS/MS measurements of total NAD⁺ in lysates from U2OS cells. A) representative Bradford calibration curve to determine the protein content of cell lysates. B)–C) Measurements of total NAD⁺ in cell lysates of blank U2OS cells or cells expressing the NAD-Snifit in cytosol, nucleus or mitochondria. NAD-Snifit was labelled with CP-MaP555-C6-SMX/Halo-SiR or CP-MaP555-PPT/Halo-SiR. *N* = four independent experiments. Data are shown as mean ± SD. n.s. = not significant, using a one-way ANOVA with Dunnett's multiple comparison test with respect to blank cells

3.3.6 FLIM-FRET measurements

FRET measurements based on two-channel intensity imaging is susceptible to spectral bleed-through, pH, changes of excitation intensity and differences in probe concentration. FLIM-FRET measurements, which record the lifetime of the FRET donor are independent of the above-mentioned limitations. It has also been shown that FLIM-FRET is more accurate than intensity-based FRET.[120] This robust technique is therefore well suited to compare measurements between compartments, even across different cell types. As described in the introduction, a fluorophore has a characteristic fluorescence lifetime, which is the result of radiative and non-radiative decays of the excited state. If two fluorophores undergo FRET, the donor lifetime is shortened through energy transfer (non-radiative) to the acceptor.[10] In the case of the NAD(P)-Snifits, a shorter lifetime corresponds to a higher concentration of free NAD⁺ or a lower ratio of free NADPH/NADP⁺.

3.3.7 FLIM-FRET measurements of the NAD-Snifit in live cells

It was then tested whether the NAD-Snifit labelled with CP-MaP555-C6-SMX/Halo-SiR or CP-MaP555-PPT/Halo-SiR can be used to measure subcellular changes of NAD^+ levels in U2OS cells.

For CP-MaP555-C6-SMX labelling only, the donor only lifetime was similar in the cytosol (2.51 ns, 95% CI: 2.47–2.54) and mitochondria (2.53 ns, 95% CI: 2.47–2.59) compared to a slightly lower lifetime for the nucleus (2.47 ns, 95% CI: 2.37–2.57) (**Figure 20A**). Labelling with CP-MaP555-C6-SMX/Halo-SiR lowered the lifetimes in all compartments: cytosol (1.85 ns, 95% CI: 1.61–2.07), nucleus (1.81 ns, 95% CI: 1.74–1.87) and mitochondria (1.85 ns, 95% CI: 1.79–1.91). This change in lifetime indicated a partly closed NAD-Snifit under basal conditions (**Figure 20B**). Treatment with 100 µM QM385 fully opened the NAD-Snifit in all compartments similar to previous titrations with QM385 (**Figure 18A**). The resulting lifetimes were higher than for the basal levels: cytosol (2.33 ns, 95% CI: 2.29–2.37), nucleus (2.18 ns, 95% CI: 2.11–2.25) and mitochondria (2.29 ns, 95% CI: 2.23–2.35). As the fully open sensor still has a minimal FRET, the lifetimes were lower than for the donor only (**Figure 20C**). Basel levels of free NAD^+ were similar in cytosol (1.85 ns, 95% CI: 1.61–2.07), nucleus (1.81 ns, 95% CI: 1.74–1.87) and mitochondria (1.85 ns, 95% CI: 1.79–1.91) **Figure 20D**).

The response of the NAD-Snifit labelled with CP-MaP555-C6-SMX/Halo-SiR to subcellular changes of NAD^+ levels was tested in live U2OS cells. Treatment with the NAMPT inhibitor FK866 (100 nM) should deplete NAD^+ levels, while the biosynthetic precursor NR (1 mM) should boost NAD^+ levels.[109, 121] FK866 depleted free cytosolic NAD^+ level (2.33 ns, 95% CI: 2.29–2.37) compared to basal level (1.85 ns, 95% CI: 1.61–2.07), while NR led to an increase in free NAD^+ (1.55 ns, 95% CI: 1.41–1.69). The effect of FK866 was similar to QM385 treatment (2.33 ns, 95% CI: 2.29–2.37) (**Figure 20E**). Likewise, free nuclear NAD^+ levels were decreased upon FK866 treatment (2.19 ns, 95% CI: 2.11–2.29) compared to basal level (1.81 ns, 95% CI: 1.74–1.87), while NR led to an increase in free NAD^+ (1.59 ns, 95% CI: 1.44–1.46). The effect of FK866 was similar to QM385 treatment (2.18 ns, 95% CI: 2.11–2.25) (**Figure 20F**). Mitochondrial levels of free NAD^+ were also decreased upon FK866 treatment (2.10 ns, 95% CI: 1.94–2.21) compared to basal

level (1.85 ns, 95% CI: 1.79–1.91), while NR led to an increase in free NAD⁺ (1.62 ns, 95% CI: 1.51–1.73). The effect of FK866 was lower than QM385 treatment (2.29 ns, 95% CI: 2.23–2.35) (**Figure 20G**). These results indicated that the NAD-Snifit labelled with CP-MaP555-C6-SMX/Halo-SiR can be used to measure subcellular changes of NAD⁺ levels.

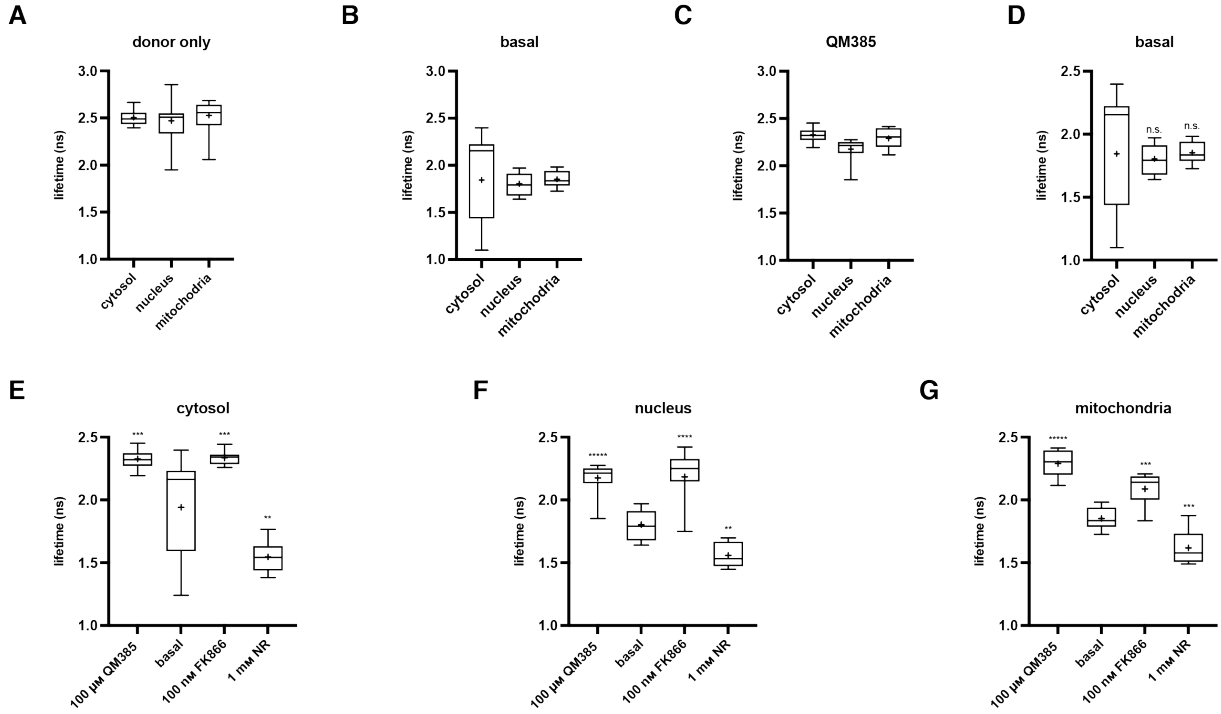

Figure 20: FLIM-FRET measurements of the NAD-Snifit labelled with CP-MaP555-C6-SMX/Halo-SiR in U2OS cells. A) donor only samples labelled with CP-MaP555-C6-SMX. B) subcellular basal levels of free NAD⁺. C) NAD-Snifit was fully opened by incubation with 100 µM QM385 for 1 h. D) comparison of subcellular basal levels of free NAD⁺. E) effect of pharmacological treatment on free cytosolic NAD⁺ levels. F) effect of pharmacological treatment on free nuclear NAD⁺ levels. G) effect of pharmacological treatment on free mitochondrial NAD⁺ levels. The box represents the 25th and 75th percentile and the whiskers are the minimum and maximum. The mean and median are indicated by a cross or line, respectively $N = 5–20$ cells. n.s. = not significant, ** $p < 0.01$, *** $p < 0.001$, **** $p < 0.0001$ using a one-way ANOVA with Dunnett's multiple comparison test with respect to basal conditions.

For CP-MaP555-PPT labelling only, the donor only lifetime was similar in the cytosol (2.45 ns, 95% CI: 2.41–2.49), nucleus (2.46 ns, 95% CI: 2.44–2.48) and mitochondria (2.46 ns, 95% CI: 2.43–2.49) (**Figure 21A**). Labelling with CP-MaP555-PPT/Halo-SiR lowered the lifetimes in all compartments: cytosol (1.56 ns, 95% CI: 1.51–1.61), nucleus (1.50 ns, 95% CI: 1.49–1.52) and mitochondria (1.46 ns, 95% CI: 1.40–1.52). This change in lifetime indicated a partly closed NAD-Snifit under basal conditions (**Figure 21B**). Treatment with 100 µM QM385 fully opened the NAD-Snifit in all compartments similar to previous titrations with QM385 (**Figure 18B**). The resulting lifetimes were higher than the basal level: cytosol (2.14 ns, 95% CI: 2.07–2.21), nucleus (1.97 ns, 95% CI: 1.95–2.00) and mitochondria (1.96 ns, 95% CI: 1.92–2.00). As the fully open sensor still has a minimal FRET, the lifetimes were lower than for the donor only (**Figure 21C**). Basel levels of free NAD^+ were higher in the nucleus (1.50 ns, 95% CI: 1.49–1.52) and mitochondria (1.46 ns, 95% CI: 1.40–1.52) than in the cytosol (1.56 ns, 95% CI: 1.51–1.61) (**Figure 21D**).

The response of the NAD-Snifit labelled with CP-MaP555-PPT/Halo-SiR to subcellular changes of NAD^+ levels was also tested in live U2OS cells. Treatment with the NAMPT inhibitor FK866 (100 nM) should deplete NAD^+ levels, while the biosynthetic precursor NR (1 mM) should boost NAD^+ levels.[109, 121] FK866 depleted free cytosolic NAD^+ levels (1.73 ns, 95% CI: 1.70–1.77) compared to basal level (1.56 ns, 95% CI: 1.51–1.61), while NR led to an increase in free NAD^+ (1.48 ns, 95% CI: 1.49–1.51). The effect of FK866 was lower than QM385 treatment (2.14 ns, 95% CI: 2.07–2.21) (**Figure 21E**). Likewise, free nuclear NAD^+ levels were decreased upon FK866 treatment (1.79 ns, 95% CI: 1.94–2.00) compared to basal level (1.50 ns, 95% CI: 1.49–1.52), while NR led to an increase in free NAD^+ (1.36 ns, 95% CI: 1.31–1.42). The effect of FK866 was lower than QM385 treatment (1.97 ns, 95% CI: 1.95–2.00) (**Figure 21F**). Mitochondrial levels of free NAD^+ were also decreased upon FK866 treatment (1.65 ns, 95% CI: 1.55–1.76) compared to basal level (1.46 ns, 95% CI: 1.40–1.52), while NR led to an increase in free NAD^+ (1.27 ns, 95% CI: 1.22–1.32). The effect of FK866 was lower than QM385 treatment (1.96 ns, 95% CI: 1.92–2.00) (**Figure 21G**). These results indicated that the NAD-Snifit labelled with CP-MaP555-PPT /Halo-SiR can also be used to measure subcellular changes of NAD^+ levels.

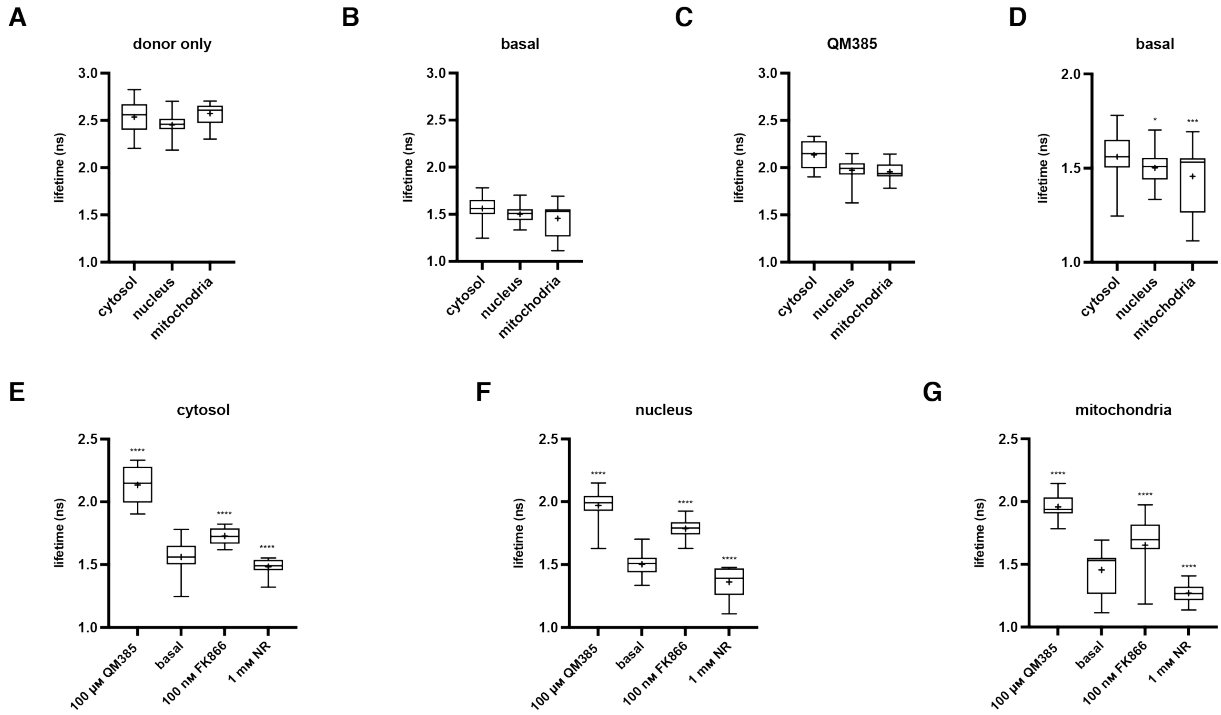

Figure 21: FLIM-FRET measurements of the NAD-Snifit labelled with CP-MaP555-PPT/Halo-SiR in U2OS cells. A) donor only samples labelled with CP-MaP555-C6-PPT. B) subcellular basal levels of free NAD^+. C) NAD-Snifit was fully opened by incubation with 100 µM QM385 for 1 h. D) comparison of subcellular basal levels of free NAD^+. E) effect of pharmacological treatment on free cytosolic NAD^+ levels. F) effect of pharmacological treatment on free nuclear NAD^+ levels. G) effect of pharmacological treatment on free mitochondrial NAD^+ levels. The box represents the 25th and 75th percentile and the whiskers are the minimum and maximum. The mean and median are indicated by a cross or line, respectively $N = 13–94$ cells. * $p < 0.05$, *** $p < 0.001$, **** $p < 0.0001$ using a one-way ANOVA with Dunnett's multiple comparison test with respect to basal conditions.

3.3.8 FLIM-FRET measurements of the NADP-Snifit in live cells

It was then tested whether the NADP-Snifit labelled with CP-MaP555-C6-SMX/Halo-SiR or CP-MaP555-PPT/Halo-SiR can be used to measure subcellular changes of NADPH/$NADP^+$ ratios in U2OS cells.

For CP-MaP555-C6-SMX labelling only, the donor only lifetimes were similar in the cytosol (2.64 ns, 95% CI: 2.55–2.74), nucleus (2.67 ns, 95% CI: 2.61–2.74) and mitochondria (2.60 ns, 95% CI: 2.55–2.64) (**Figure 22A**). Labelling with CP-MaP555-C6-SMX/Halo-SiR lowered the lifetimes in all compartments: cytosol (1.85 ns, 95% CI: 1.81–1.91), nucleus (1.98 ns, 95% CI: 1.92–2.05) and mitochondria (2.01 ns, 95% CI: 1.97–2.14). This change in lifetime indicated a partly closed NADP-Snifit under basal conditions (**Figure 22B**). Treatment with 100 µM QM385 fully opened the NADP-Snifit in all compartments similar to previous titrations with QM385 (**Figure 18B**). The resulting lifetimes were higher than the basal ratios: cytosol (2.33 ns, 95% CI: 2.26–2.39), nucleus (2.33 ns, 95% CI: 2.29–2.37) and mitochondria (2.37 ns, 95% CI: 2.28–2.46). As the fully open sensor still has a minimal FRET, the lifetimes were lower than for the donor only (**Figure 22C**). Basal ratios of free NADPH/$NADP^+$ were similar in cytosol (1.85 ns, 95% CI: 1.81–1.91) and nucleus (1.98 ns, 95% CI: 1.92–2.05). However, mitochondria showed higher free NADPH/$NADP^+$ ratios (2.01 ns, 95% CI: 1.97–2.14) (**Figure 22D**).

The response of the NADP-Snifit labelled with CP-MaP555-C6-SMX/Halo-SiR to subcellular changes of NADPH/$NADP^+$ ratios was tested in live U2OS cells. Treatment with the sarco-endoplasmic reticulum calcium transport ATPase (SERCA) inhibitor thapsigargin (1 µM) or H_2O_2 (1 mM) should induce oxidative stress.[122-124] Both treatments induced massive oxidative stress in the cytosol, indicated by a significantly lower free NADPH/$NADP^+$ ratio compared to basal ratios (1.85 ns, 95% CI: 1.81–1.91): thapsigargin (1.70 ns, 95% CI: 1.54–1.85) and H_2O_2 (1.57 ns, 95% CI: 1.46–1.68) (**Figure 22E**). Likewise, the free nuclear NADPH/$NADP^+$ ratio was also lowered by thapsigargin and H_2O_2 treatment compared to basal ratio (1.98 ns, 95% CI: 1.92–2.05): thapsigargin (1.83 ns, 95% CI: 1.78–1.88) and H_2O_2 (1.74 ns, 95% CI: 1.60–1.87) (**Figure 22F**). Free mitochondrial NADPH/$NADP^+$ ratios were also decreased upon thapsigargin and H_2O_2 treatment compared to basal ratio (2.01 ns, 95% CI: 1.97–2.14): thapsigargin (1.79 ns, 95% CI: 1.75–1.84) and H_2O_2 (1.56 ns,

95% CI: 1.47–1.65) (**Figure 22G**). These results indicated that the NADP-Snifit labelled with CP-MaP555-C6-SMX/Halo-SiR can be used to measure subcellular changes of NADPH/NADP$^+$ ratios.

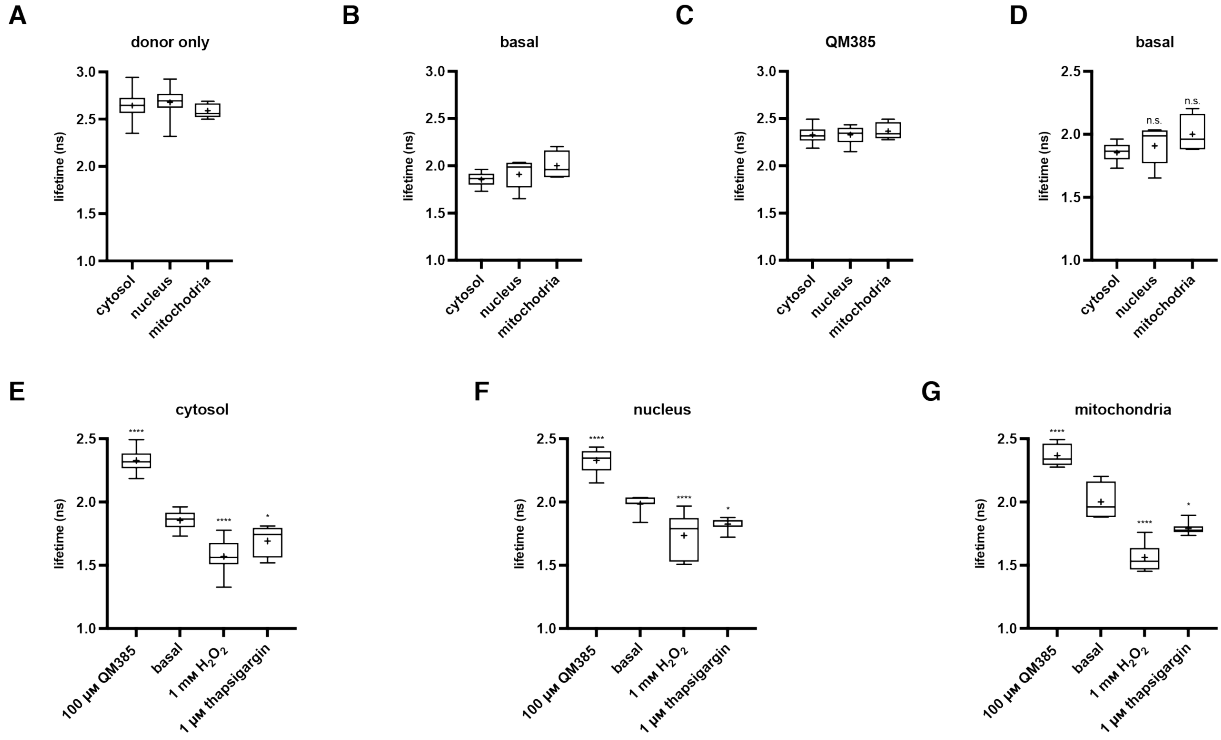

Figure 22: FLIM-FRET measurements by the NADP-Snifit labelled with CP-MaP555-C6-SMX/Halo-SiR in U2OS cells. A) donor only samples labelled with CP-MaP555-C6-SMX. B) subcellular basal ratios of free NADPH/NADP$^+$. C) NADP-Snifit was fully opened by incubation with 100 µM QM385 for 1 h. D) comparison of subcellular basal ratios of free NADPH/NADP$^+$. E) effect of pharmacological treatment on free cytosolic NADPH/NADP$^+$ ratios. F) effect of pharmacological treatment on free nuclear NADPH/NADP$^+$ ratios. G) effect of pharmacological treatment on free mitochondrial NADPH/NADP$^+$ ratios. The box represents the 25th and 75th percentile and the whiskers are the minimum and maximum. The mean and median are indicated by a cross or line, respectively $N = 5–20$ cells. n.s. = not significant, ** $p < 0.01$, *** $p < 0.001$, **** $p < 0.0001$ using a one-way ANOVA with Dunnett's multiple comparison test with respect to basal conditions.

For CP-MaP555-PPT labelling only, the donor only lifetimes were similar in the cytosol (2.41 ns, 95% CI: 2.35–2.48) and mitochondria (2.42 ns, 95% CI: 2.38–2.45) compared to the nucleus (2.34 ns, 95% CI: 2.32–2.36) (**Figure 23A**). Labelling with CP-MaP555-PPT/Halo-SiR lowered the lifetimes in all compartments: cytosol (1.53 ns, 95% CI: 1.48–1.57), nucleus (1.45 ns, 95% CI: 1.44–1.46) and mitochondria (1.81 ns, 95% CI: 1.72–1.91). This change in lifetime indicated a partly closed NADP-Snifit under basal conditions (**Figure 23B**). Treatment with 100 µM QM385 fully opened the NADP-Snifit in all compartments similar to previous titrations with QM385 (**Figure 18B**) The resulting lifetimes were higher than the basal ratios: cytosol (2.04 ns, 95% CI: 1.98–2.11), nucleus (1.89 ns, 95% CI: 1.88–1.91) and mitochondria (2.20 ns, 95% CI: 2.12–2.29). As the fully open sensor still has a minimal FRET, the lifetimes were lower than for the donor only (**Figure 23C**). Basal ratios of free NADPH/$NADP^+$ were lower in the nucleus (1.45 ns, 95% CI: 1.44–1.46) compared to the cytosol (1.53 ns, 95% CI: 1.48–1.57). However, mitochondria showed a significantly higher NADPH/$NADP^+$ ratio compared to the cytosol (1.81 ns, 95% CI: 1.72–1.91) (**Figure 23D**).

The response of the NADP-Snifit labelled with CP-MaP555-PPT/Halo-SiR to subcellular changes of NADPH/$NADP^+$ ratios was tested in live U2OS cells. Treatment with the SERCA inhibitor thapsigargin (1 µM) or H_2O_2 (1 mM) should induce oxidative stress.[122-124] Both treatments induced massive oxidative stress in the cytosol, indicated by a much lower free NADPH/$NADP^+$ ratio compared to basal ratio (1.53 ns, 95% CI: 1.48–1.57): thapsigargin (1.35 ns, 95% CI: 1.29–1.41) H_2O_2 (1.29 ns, 95% CI: 1.25–1.33) (**Figure 23E)** Likewise, free nuclear NADPH/$NADP^+$ ratio was also lowered by thapsigargin and H_2O_2 treatment compared to basal ratio (1.45 ns, 95% CI: 1.44–1.46): thapsigargin (1.37 ns, 95% CI: 1.35–1.40) and H_2O_2 (1.37 ns, 95% CI: 1.33–1.41) (**Figure 23F**). Free mitochondrial NADPH/$NADP^+$ ratios were also decreased upon thapsigargin and H_2O_2 treatment compared to basal ratio (1.81 ns, 95% CI: 1.72–1.91): thapsigargin (1.64 ns, 95% CI: 1.53–1.75) and H_2O_2 (1.57 ns, 95% CI: 1.48–1.66) (**Figure 23G**). These results indicated that the NADP-Snifit labelled with CP-MaP555-PPT/Halo-SiR can be used to measure subcellular changes of NADPH/$NADP^+$ ratios. They also showed that the NADP-Snifit was not fully closed at basal NADPH/$NADP^+$ ratios as the NADP-Snifit could respond to lower NADPH/$NADP^+$ ratios.

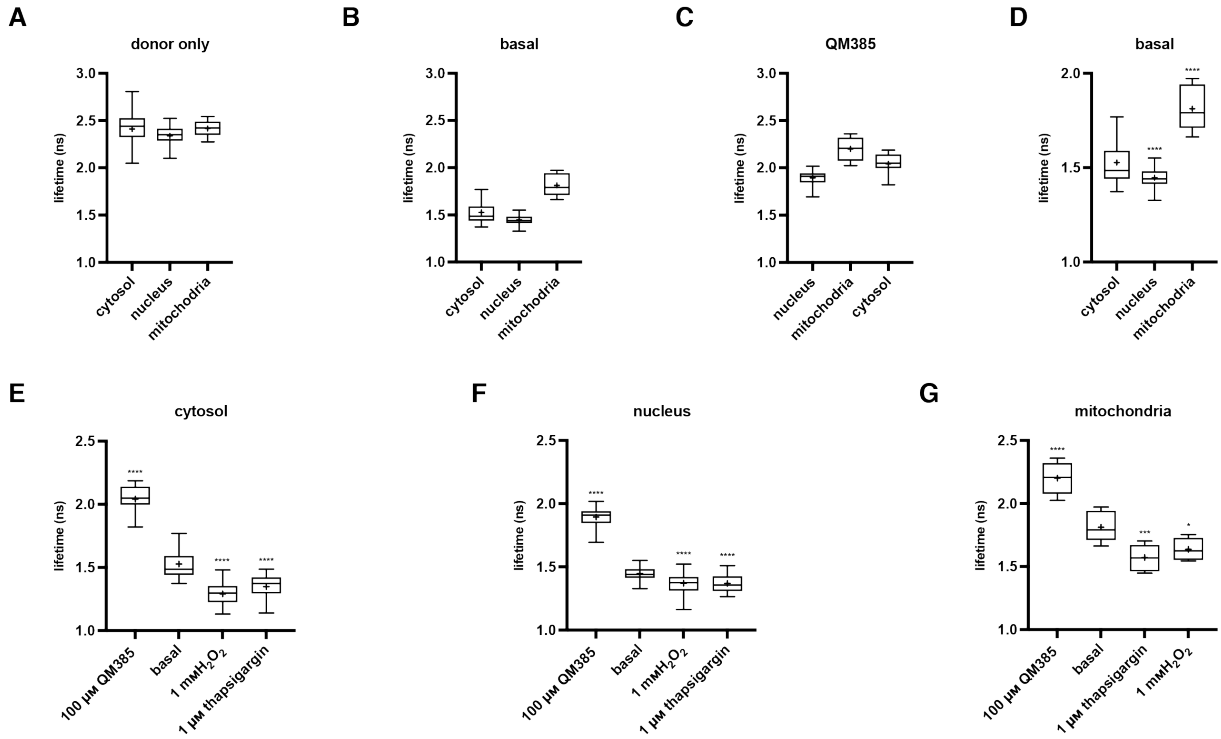

Figure 23: FLIM-FRET measurements by the NADP-Snifit labelled with CP-MaP555-PPT/Halo-SiR in U2OS cells. A) donor only samples labelled with CP-MaP555-C6-PPT. B) subcellular basal ratios of free NADPH/NADP+. C) NADP-Snifit was fully opened by incubation with 100 µM QM385 for 1 h. D) comparison of subcellular basal ratios of free NADPH/NADP+. E) effect of pharmacological treatment on free cytosolic NADPH/NADP+ ratios. F) effect of pharmacological treatment on free nuclear NADPH/NADP+ ratios. G) effect of pharmacological treatment on free mitochondrial NADPH/NADP+ ratios. The box represents the 25th and 75th percentile and the whiskers are the minimum and maximum. The mean and median are indicated by a cross or line, respectively $N = 5–25$ cells. * $p < 0.05$, *** $p < 0.001$, **** $p < 0.0001$ using a one-way ANOVA with Dunnett's multiple comparison test with respect to basal conditions.

3.3.9 Characterization in primary neurons

The final objective was to use the NAD(P)-Snifits in cultured primary neurons to investigate neuronal metabolism of NAD(P)(H). To this end, intracellular SNAP-tag labelling with CP-MaP555-C6-SMX and CP-MaP555-PPT was investigated. Rat hippocampal neurons (prepared in-house) were cultured in poly-L-ornithine and laminin-coated 24-well imaging plates. No arabinosylcytosine (AraC) was added to remove proliferating glial cells. AraC treatment has been shown to reduce the quality and robustness of the culture and might also affect neuronal function.[125] After being cultured for nine days, the neurons were infected with AAVs for the expression of cytosolic SNAP-mEGFP or Halo-mEGFP constructs. After 13 days, the neurons were labelled with different concentrations of CP-MaP555-C6-SMX, CP-MaP555-PPT or Halo-SiR for 14 h to determine the optimal substrate concentrations. A sufficient signal (ratio TMR/mEGFP) was only observed for 500 nM of CP-MaP555-C6-SMX (0.86, 95% CI: 0.83–0.89). 125 nM (0.31, 95% CI: 0.30–0.34) and 250 nM (0.35, 95% CI: 0.32–0.37) resulted in a very weak TMR signal (**Figure 24A**). In contrast, 125 nM of CP-MaP555-PPT (1.51, 95% CI: 1.46–1.58) already had a higher ratio than 500 nM of CP-MaP555-C6-SMX. Similar to U2OS cells, CP-MaP555-PPT reached a plateau at 500 nM (1.96, 95% CI: 1.94–1.99) (**Figure 24B**). These results indicated a much better permeability of CP-MaP555-PPT compared to CP-MaP555-C6-SMX, which could be explained by a higher calc. logP and less HBDs. Halo-SiR already reached a plateau at 50–100 nM (**Figure 24C**). 500 nM of CP-MaP555-C6-SMX or CP-MaP555-PPT and 200 nM of Halo-SiR were subsequently used for labelling in neurons. SNAP-tag labelling with CP-MaP555-C6-SMX co-localized well with the mEGFP signal and showed no aggregations (**Figure 24D**). CP-MaP555-PPT also co-localized well with the mEGFP signal and did not aggregate. In agreement with the previous substrate titration, CP-MaP555-PPT gave a much brighter signal (**Figure 24E**).

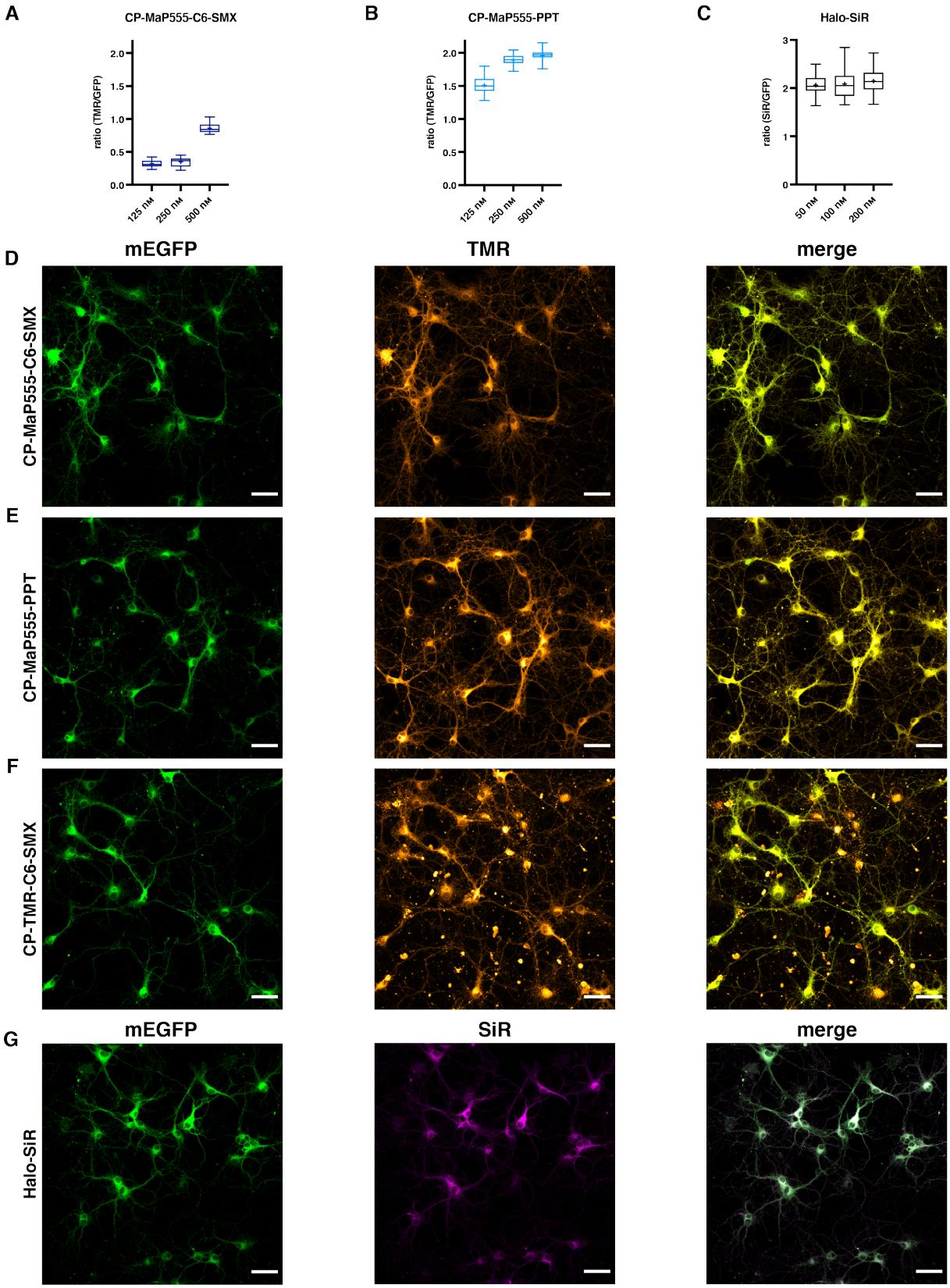

Figure 24: Labelling of SNAP- and Halo-tag in primary neurons. A)–B) quantification of hippocampal neurons expressing a cytosolic SNAP-mEGFP labelled with different concentrations of CP-MaP555-C6-SMX and CP-MaP555-PPT. C) quantification of hippocampal neurons expressing a cytosolic Halo-mEGFP labelled with different concentrations of Halo-SiR. D)–F) confocal images of hippocampal neurons expressing a cytosolic SNAP-mEGFP labelled either with 500 nM of CP-MaP555-C6-SMX, CP-MaP555-PPT or CP-TMR-C6-SMX. G) confocal images of hippocampal neurons expressing a cytosolic Halo-mEGFP labelled with 200 nM Halo-SiR. The box represents the 25th and 75th percentile and the whiskers are the minimum and maximum. The mean and median are indicated by a cross or line, respectively $N = 30$ cells. Scale bar: 50 µm.

In contrast, CP-TMR-C6-SMX showed strong aggregation combined with unspecific signal and did not co-localized well with the mEGFP signal. This indicated low cell permeability of CP-TMR-C6-SMX. The low solubility of CP-TMR-C6-SMX in aqueous media led to aggregates, which were brighter than the specific SNAP-tag labelling. Therefore, CP-TMR-C6-SMX was not found to be a suitable substrate for SNAP-tag labelling in neurons (**Figure 24F**). Halo-tag labelling with Halo-SiR gave a strong signal that overlapped well with the mEGFP signal and did show no aggregation (**Figure 24G**).

After successful AAV infection and expression of SNAP-mEGFP, cultured hippocampal neurons were infected with AAVs for the expression of the NAD-Snifit in cytosol, nucleus and mitochondria. Labelling with CP-MaP555-C6-SMX and CP-MaP555-PPT showed a bright and specific signal in the respective compartments and no aggregation (**Figure 25A, B**).

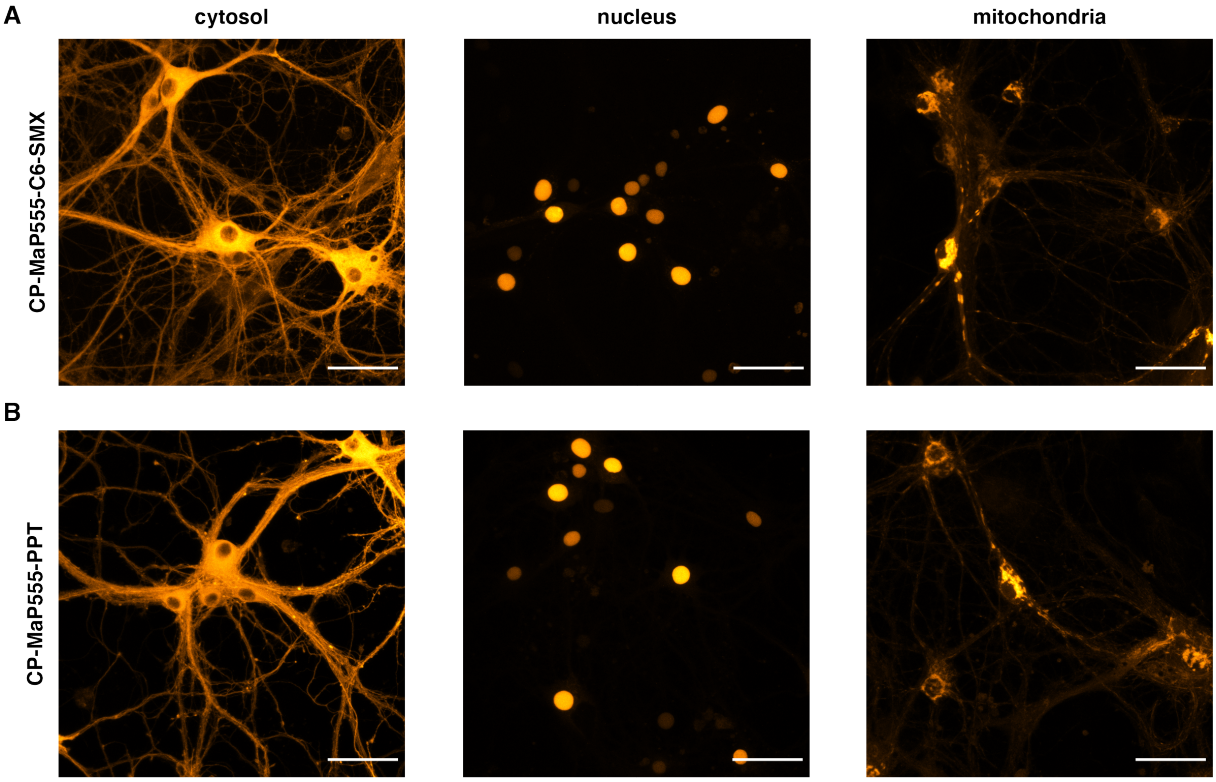

Figure 25: Labelling of NAD-Snifit in primary neurons. A) NAD-Snifit expressed in cytosol, nucleus or mitocchondria was single lablled with 500 nM CP-MaP555-C6-SMX. B) NAD-Snifit expressed in cytosol, nucleus or mitocchondria was single lablled with 500 nM CP-MaP555-PPT. Scale bar: 50 µm.

In the experiments described so far, images of labelled neurons were taken in artificial cerebrospinal fluid (ACSF) buffer after one washing step using the same buffer. However, neurons can only be maintained in AFCS for a few hours as this buffer does

not support cell survival.[126] This is a major limitation for the application of the NAD(P)-Snifit in more complex experiments (*e.g.* time course). The protocol was adapted to do a no-wash labelling and neurons were cultured in phenol-red free neurobasal medium. The FRET donor substrates were added in phenol-red free neurobasal medium (1:2000 dilution). After labelling, any remaining fluorescent substrate was further diluted twice. These conditions were evaluated by comparing the intensities of the labelled cytosolic NAD-Snifit with the unspecific signal from neurons not expressing the NAD-Snifit. CP-MaP555-C6-SMX only showed a 3.8-fold (95% CI: 3.5–4.2) difference of signal over background (**Figure 26A, B**). In contrast, CP-MaP555-PPT had a 14.4-fold (95% CI: 12.9–15.9) difference of signal over background (**Figure 26C, D**). The combination of a low signal over background and low overall signal made CP-MaP555-C6-SMX not ideal for no-wash SNAP-tag labelling in hippocampal neurons. Therefore, experiments in neurons were only performed with CP-MaP555-PPT. Previous substrate titrations showed that labelling with 500 nM of CP-MaP555-PPT approaches saturation (**Figure 24A, B**). Therefore, high cellular concentrations of non-bound CP-MaP555-PPT are unlikely, which could bind to endogenous SPR.

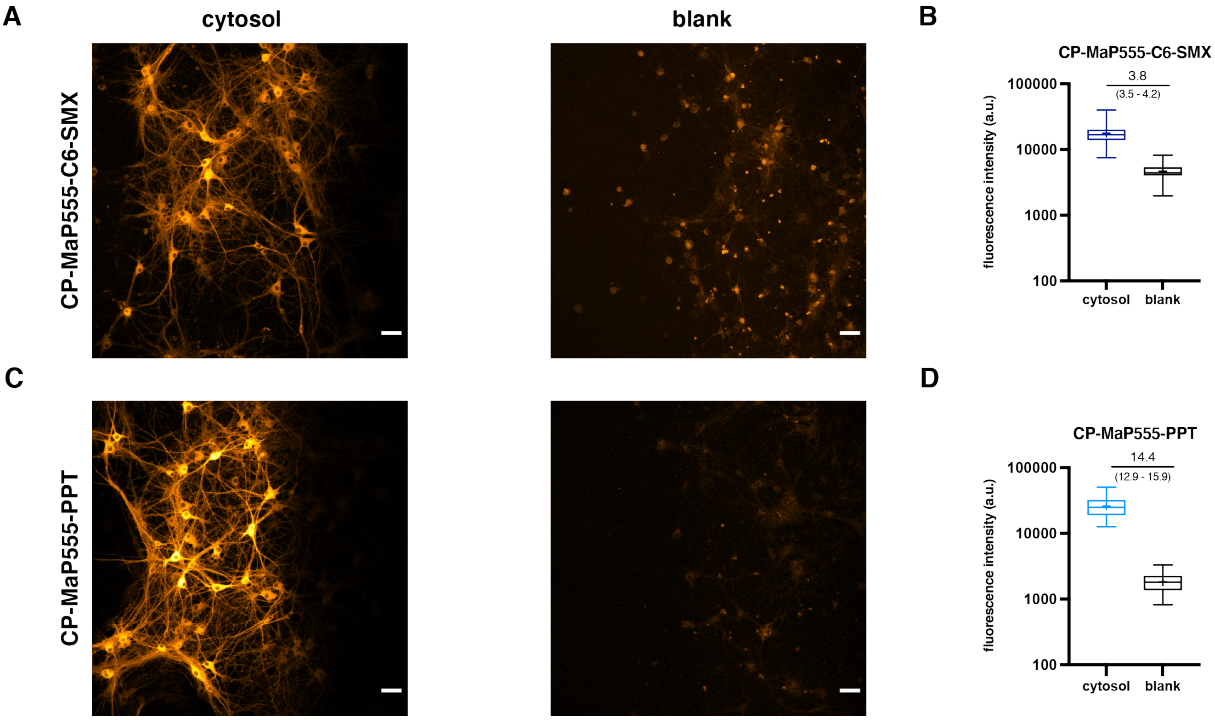

Figure 26: No wash labelling in primary neurons. A)–B) neurons expressing the cytosolic NAD-Snifit or blank neurons were incubated with 500 nM CP-MaP555-C6-SMX and their signal intensities are quantified C)–D) neurons expressing the cytosolic NAD-Snifit or neurons cells were incubated with 500 nM CP-MaP555-PPT and their signal intensities are quantified. The box represents the 25th and 75th percentile and the whiskers are the minimum and maximum. The mean and median are indicated by a cross or line, respectively $N = 50$ cells. The fold-difference between specific and unspecific labelling is reported with 95% CI. Scale bar: 50 µm.

3.3.10 FLIM-FRET measurements of the NAD-Snifit in primary neurons

It was then tested whether the NAD-Snifit labelled with CP-MaP555-PPT/Halo-SiR can be used to measure subcellular changes of NAD^+ levels in primary neurons.

The donor only lifetimes were similar in the cytosol (2.56 ns, 95% CI: 2.52–2.60) and nucleus (2.52 ns, 95% CI: 2.49–2.55) and slightly higher in mitochondria (2.60 ns, 95% CI: 2.57–2.63) (**Figure 27A**). Labelling with CP-MaP555-PPT/Halo-SiR lowered the lifetimes in all compartments: cytosol (1.57 ns, 95% CI: 1.55–1.59), nucleus (1.38 ns, 95% CI: 1.36–1.40) and mitochondria (1.81 ns, 95% CI: 1.79–1.83). This change in lifetime indicated a partly closed NAD-Snifit under basal conditions (**Figure 27B**). Treatment with 100 µM QM385 fully opened the NAD-Snifit in all compartments similar to previous results from U2OS cells (**Figure 18A**). The resulting lifetimes were higher than the basal levels: cytosol (2.14 ns, 95% CI: 2.12–2.17), nucleus (1.92 ns, 95% CI: 1.90–1.94) and mitochondria (2.14 ns, 95% CI: 2.12–2.17). As the fully open sensor still has a minimal FRET, the lifetimes were lower than for the donor only (**Figure 27C**). Nuclear basal levels of free NAD^+ (1.38 ns, 95% CI: 1.36–1.40) were significantly higher than cytosolic levels (1.60 ns, 95% CI: 1.58-1.61). Mitochondrial basal levels of free NAD^+ (11.83 ns, 95% CI: 1.77–1.89) were much lower than cytosolic levels (**Figure 27D**).

The response of the NAD-Snifit labelled with CP-MaP555-PPT/Halo-SiR to subcellular changes of NAD^+ levels was tested in live primary neurons. Similar to U2OS cells, treatment with the NAMPT inhibitor FK866 (100 nM) should deplete NAD^+ levels, while the biosynthetic precursor NR (1 mM) should boost NAD^+ levels.[109, 121]. FK866 depleted free cytosolic NAD^+ levels (1.92 ns, 95% CI: 1.86–1.96) compared to basal levels (1.60 ns, 95% CI: 1.58–1.61), while NR led to an increase in free NAD^+ (1.47 ns, 95% CI: 1.43–1.51). The effect of FK866 was lower than QM385 treatment (2.14 ns, 95% CI: 2.12–2.17) (**Figure 27E**). Likewise, free nuclear NAD^+ levels were decreased upon FK866 treatment (1.73 ns, 95% CI: 1.71–1.76) compared to basal levels (1.38 ns, 95% CI: 1.36–1.40), while NR led to an increase in free NAD^+ (1.28 ns, 95% CI: 1.27–1.30). The effect of FK866 was lower than QM385 treatment (1.92 ns, 95% CI: 1.90–1.94) (**Figure 27F**). Mitochondrial levels of free NAD^+ were also decreased upon FK866 treatment (1.93 ns, 95% CI: 1.90–1.95) compared to basal

level (1.81 ns, 95% CI: 1.79–1.83), while NR led to an increase in free NAD^+ (1.56 ns, 95% CI: 1.50–1.62). The effect of FK866 was lower than QM385 treatment (2.14 ns, 95% CI: 2.12–2.17) (**Figure 27G**). These results indicated that the NAD-Snifit labelled with CP-MaP555-PPT /Halo-SiR can also be used to measure subcellular changes of NAD^+ levels in primary neurons.

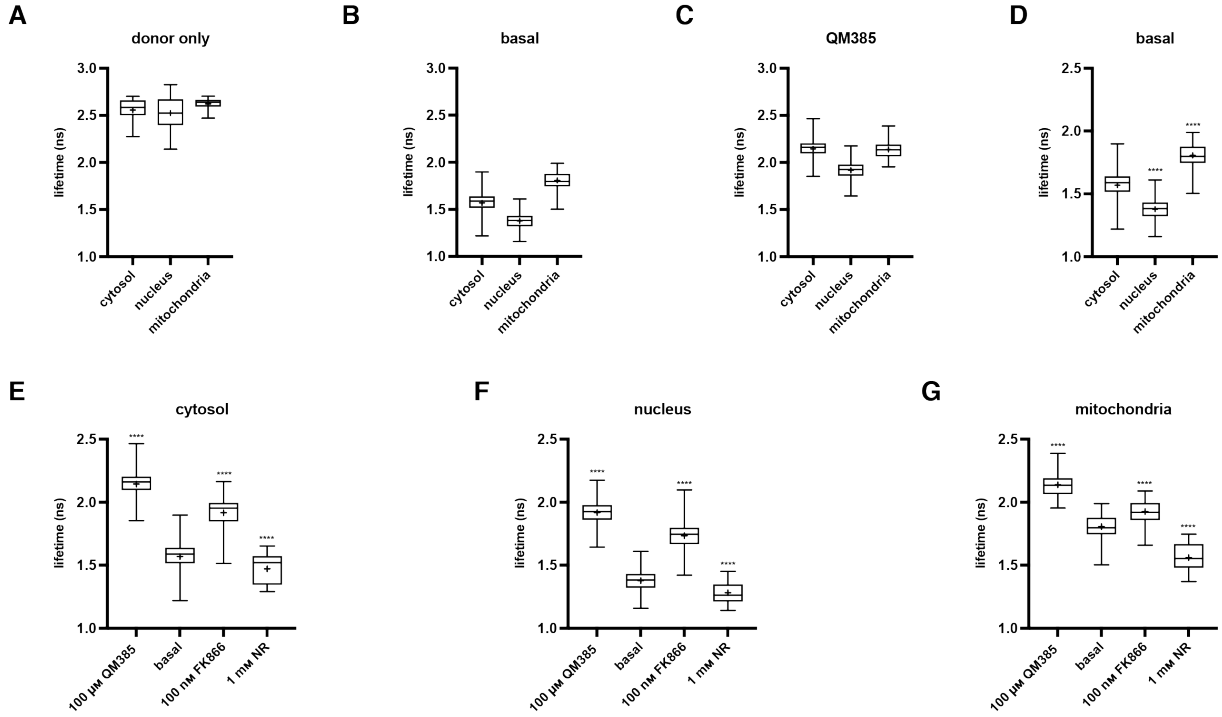

Figure 27: FLIM-FRET measurements of the NAD-Snifit labelled with CP-MaP555-PPT/Halo-SiR in primary neurons. A) donor only samples labelled with CP-MaP555-PPT. B) subcellular basal levels of free NAD^+. C) NAD-Snifit was fully opened by incubation with 100 µM QM385 for 1 h. D) comparison of subcellular basal levels of free NAD^+. E) effect of pharmacological treatment on free cytosolic NAD^+ levels. F) effect of pharmacological treatment on free nuclear NAD^+ levels. G) effect of pharmacological treatment on free mitochondrial NAD^+ levels. The box represents the 25th and 75th percentile and the whiskers are the minimum and maximum. The mean and median are indicated by a cross or line, respectively $N = 50–100$ cells per condition from three independent experiments. n.s. = not significant, *** $p < 0.001$, **** $p < 0.0001$ using a one-way ANOVA with Dunnett's multiple comparison test with respect to basal conditions

3.3.11 FLIM-FRET measurements of the NADP-Snifit in primary neurons

It was then tested whether the NADP-Snifit labelled with CP-MaP555-PPT/Halo-SiR can be used to measure subcellular changes of NADPH/$NADP^+$ ratios in primary neurons.

The donor only (lifetime was higher in the cytosol (2.85 ns, 95% CI: 2.55–2.62) compared to rather similar lifetimes for nucleus (2.44 ns, 95% CI: 2.42-2.46) and mitochondria (2.46 ns, 95% CI: 2.41–2.51) (**Figure 28A**). Labelling with CP-MaP555-PPT/Halo-SiR lowered the lifetimes in all compartments: cytosol (1.69 ns, 95% CI: 1.67–1.71), nucleus (1.73 ns, 95% CI: 1.70–1.76) and mitochondria (1.52 ns, 95% CI: 1.48–1.57). This change in lifetime indicated a partly closed NADP-Snifit under basal conditions (**Figure 28B**). Treatment with 100 µM QM385 fully opened the NADP-Snifit in all compartments similar to previous results from U2OS cells (**Figure 18B**). The resulting lifetimes were higher than the basal ratios: cytosol (2.16 ns, 95% CI: 2.14–2.18), nucleus (1.95 ns, 95% CI: 1.93–1.97) and mitochondria (2.15 ns, 95% CI: 2.13–2.18). As the fully open sensor still has a minimal FRET, the lifetimes were lower than for the donor only (**Figure 28C**). Basal ratios of free NADPH/$NADP^+$ were similar in cytosol (1.69 ns, 95% CI: 1.67–1.71) and nucleus (1.73 ns, 95% CI: 1.70–1.76). However, mitochondria had a more oxidizing environment, which was evident by a lower free NADPH/$NADP^+$ ratio (1.52 ns, 95% CI: 1.48–1.57) (**Figure 28D**).

The response of the NADP-Snifit labelled with CP-MaP555-PPT/Halo-SiR to subcellular changes of NADPH/$NADP^+$ ratios was tested in live primary neurons. Similar to U2OS cells, treatment with the SERCA inhibitor thapsigargin (1 µM) or H_2O_2 (1 mM) should induce oxidative stress.[122-124] Both treatments induced oxidative stress in the cytosol, indicated by much lower free NADPH/$NADP^+$ ratios compared to basal level (1.69 ns, 95% CI: 1.67–1.71): thapsigargin (1.45 ns, 95% CI: 1.41–1.49) and H_2O_2 (1.33 ns, 95% CI: 1.30–1.35) (**Figure 28E**). Likewise, free nuclear NADPH/$NADP^+$ ratios were also lowered by thapsigargin and H_2O_2 treatment compared to basal ratio (1.73 ns, 95% CI: 1.70–1.76): thapsigargin (1.48 ns, 95% CI: 1.45–1.51) and H_2O_2 (1.36 ns, 95% CI: 1.35–1.38) (**Figure 28F**). Conversely, by thapsigargin and H_2O_2 treatment increased free mitochondrial NADPH/$NADP^+$ ratios compared to basal ratio (1.52 ns, 95% CI: 1.48–1.57): thapsigargin (1.71 ns,

95% CI: 1.67–1.74) and H_2O_2 (1.68 ns, 95% CI: 1.61–1.74) (**Figure 28G**). These results indicated that the NADP-Snifit labelled with CP-MaP555-PPT/Halo-SiR can be used to measure subcellular changes of NADPH/NADP$^+$ ratios in primary neurons.

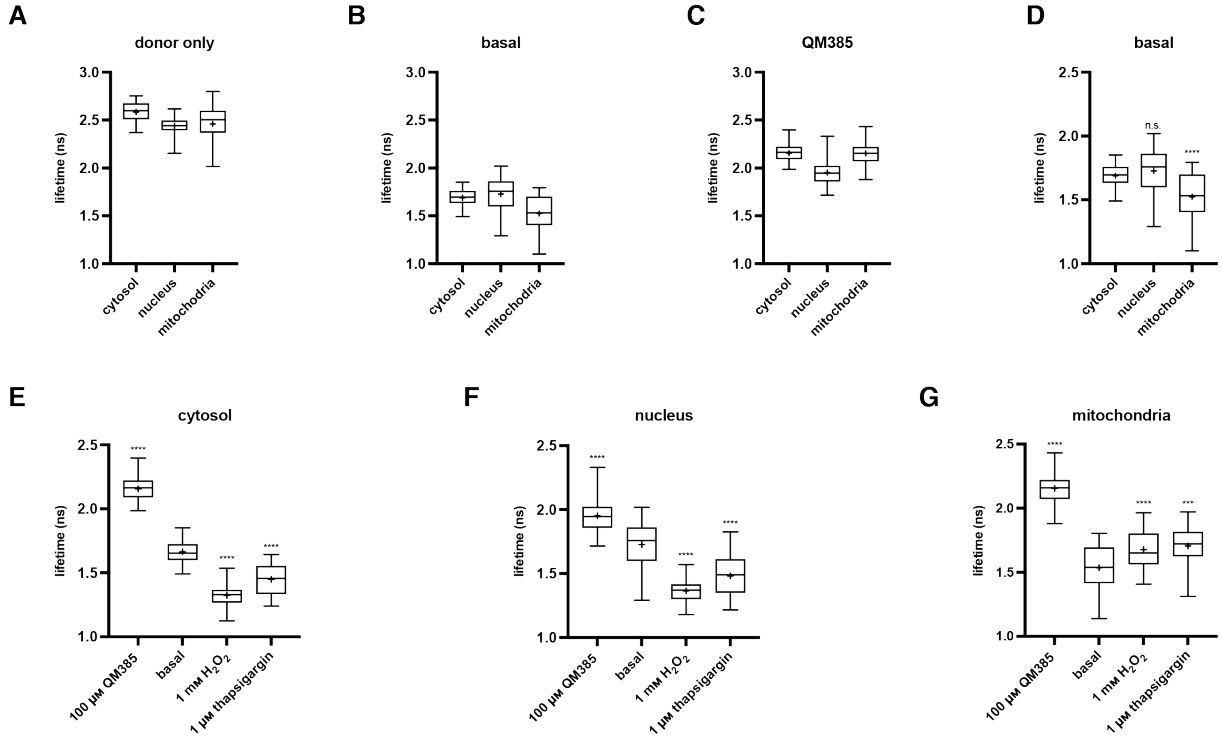

Figure 28: FLIM-FRET measurements of the NADP-Snifit labelled with CP-MaP555-PPT/Halo-SiR in primary neurons. A) donor only samples labelled with CP-MaP555-PPT. B) subcellular basal ratios of free NADPH/NADP$^+$. C) NADP-Snifit was fully opened by incubation with 100 µM QM385 for 1 h. D) comparison of subcellular basal ratios of free NADPH/NADP$^+$. E) effect of pharmacological treatment on free cytosolic NADPH/NADP$^+$ ratios. F) effect of pharmacological treatment on free nuclear NADPH/NADP$^+$ ratios. G) effect of pharmacological treatment on free mitochondrial NADPH/NADP$^+$ ratios. The box represents the 25th and 75th percentile and the whiskers are the minimum and maximum. The mean and median are indicated by a cross or line, respectively $N = 50–100$ cells per condition from three independent experiments. n.s. = not significant, *** $p < 0.001$, **** $p < 0.0001$ using a one-way ANOVA with Dunnett's multiple comparison test with respect to basal conditions.

3.3.12 Subcellular NAD+ levels and NADPH/NADP ratios in U2OS cells and primary neurons

Its independence from the intracellular sensor concentration makes FLIM-FRET ideal for the comparison of subcellular basal NAD+ levels and NADPH/NADP+ ratios in U2OS cells and cultured primary hippocampal neurons. The general assumption is that the cellular environment of the NAD(P)-Snifit is the same in U2OS cells and cultured primary hippocampal neurons. Differences in lifetimes should be only due to differences in NAD+ levels and NADPH/NADP+ ratios.

No differences could be observed for cytosolic free NAD+ levels between primary neurons (1.57 ns, 95% CI: 1.55–1.59) and U2OS (1.56 ns, 95% CI: 1.51–1.61). In contrast, nuclear free NAD+ level was higher in hippocampal neurons (1.38 ns, 95% CI: 1.36–1.40) than in U2OS cells (1.50 ns, 95% CI: 1.49–1.52). U2OS cells (1.46 ns, 95% CI: 1.40–1.52) had much higher level of mitochondrial free NAD+ compared to hippocampal neurons (1.81 ns, 95% CI: 1.79–1.83) (**Figure 29A**).

Primary neurons (1.69 ns, 95% CI: 1.67–1.71) had a higher cytosolic NADPH/NADP+ ratio than U2OS cells (1.53 ns, 95% CI: 1.48–1.57). Nuclear NADPH/NADP+ ratio was also more reducing in primary neurons (1.73 ns, 95% CI: 1.70–1.76) than U2OS cells (1.45 ns, 95% CI: 1.44–1.46). In contrast, mitochondria (1.52 ns, 95% CI: 1.48–1.57) were much more oxidizing in primary neurons than in U2OS cells (1.81 ns, 95% CI: 1.72–1.91) (**Figure 29B**).

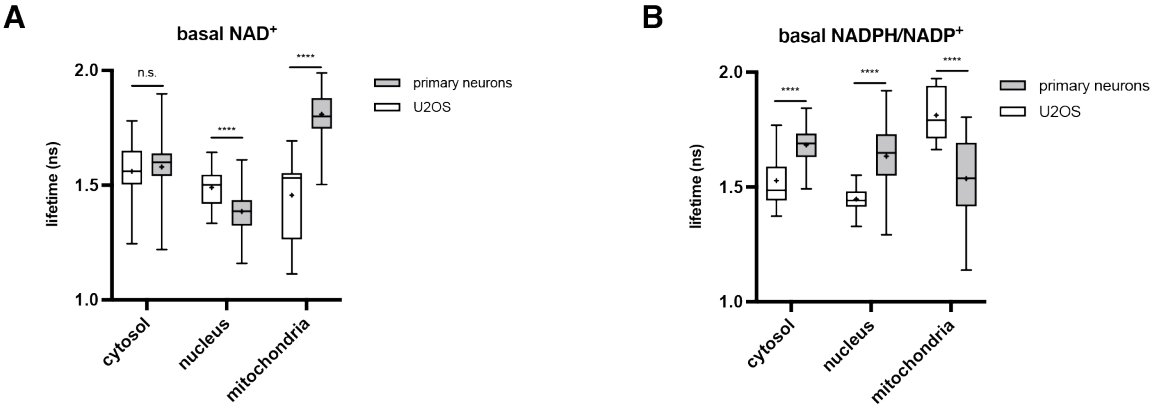

Figure 29: Comparison of subcellular NAD+ levels and NADPH/NADP+ ratios in U2OS cells and primary neurons. A) basal subcellular lifetimes of NAD-Snifit. B) basal subcellular lifetimes of NADP-Snifit. The box represents the 25th and 75th percentile and the whiskers are the minimum and maximum. The mean and median are indicated by a cross or line, respectively. *N* = 30–80 cells per condition. n.s. = not significant, **** $p < 0.0001$ using an unpaired *t*-test

3.3.13 Subcellular NAD^+ levels and neuronal activity

The combination of two biosensors or one biosensor with a fluorescent marker can be a powerful approach to monitor several biological activities in the same cell at once. The ability of multiplexing was demonstrated by combining the NAD-Snifit with the synthetic calcium indicator Cal520 in cultured hippocampal neurons. Total neuronal NAD^+ has been shown to be depleted upon excessive stimulation with glutamate.[127] The NAD-Snifit was expressed in the cytosol, nucleus and mitochondria in primary neurons and labelled with CP-MaP555-PPT and Halo-SiR. Cells were incubated with 1 µM Cal520 for 1 h and neuronal activity was recorded with FLIM. Using a scan rate of 600 MHz, the Falcon FLIM setup from Leica was able to record spontaneous neuronal activity (**Figure 30A**). A temporal resolution of 400 ns was sufficient for single Ca^{2+} waves. Neuronal stimulation was achieved by activation of *N*-methyl-D-aspartate (NMDA) receptors using 10 µM glutamate and 2.5 µM glycine.[128] Incubation for 1 h with these agonists of ionotropic glutamate receptors increased neuronal activity (**Figure 30B**). Incubation for 1 h with 25 µM (2*R*)-2-amino-5-phosphonovaleric acid (AP5) and 10 µM 6-cyano-7-nitroquinoxaline-2,3-dione (CNQX) blocks NMDA and α-amino-3-hydroxy-5-methyl-4-isoxazolepropionic acid (AMPA) receptors, respectively.[129-130] This treatment almost completely abolished neuronal activity (**Figure 30C**). Neuronal stimulation decreased cytosolic NAD^+ (1.71 ns, 95% CI: 1.67–1.76), while synaptic inhibition had no effect on cytosolic NAD^+ (1.56 ns, 95% CI: 1.53–1.59) compared to basal level (1.53 ns, 95% CI: 1.48–1.57) (**Figure 30D**). Conversely, nuclear NAD^+ was increased upon stimulation (1.27 ns, 95% CI: 1.24–1.30). Also, synaptic inhibition had no effect on nuclear NAD^+ levels (1.37 ns, 95% CI: 1.34–1.39) compared to basal level (1.39 ns, 95% CI: 1.37–1.42) (**Figure 30E**). Mitochondrial NAD^+ was also decreased upon stimulation (1.91 ns, 95% CI: 1.89–1.94) and synaptic inhibition led to a significant increase in mitochondrial NAD^+ (1.73 ns, 95% CI: 1.68–1.79) compared to basal level (1.84 ns, 95% CI: 1.82–1.87) (**Figure 30F**). The decrease in cytosolic NAD^+ upon stimulation could be explained by metabolic adaption to an increased ATP demand. Stimulation leads to an increased glycolytic activity in neurons that affects the cytosolic NADH/NAD^+ ratio by the reduction of NAD^+ to NADH.[131] Changes in mitochondrial NAD^+ could also originate from metabolic adaption of the NADH/NAD^+ ratio. Increased

ATP demand upon stimulation could lead to an higher activity of oxidative phosphorylation, which would affect the mitochondrial NADH/NAD+ ratio by the reduction of NAD+ to NADH.[132] Conversely, synaptic inhibition would decrease the ATP demand by oxidative phosphorylation and affect the mitochondrial NADH/NAD+ ratio by a lower reduction rate of NAD+ to NADH (**Figure 35C, D**).

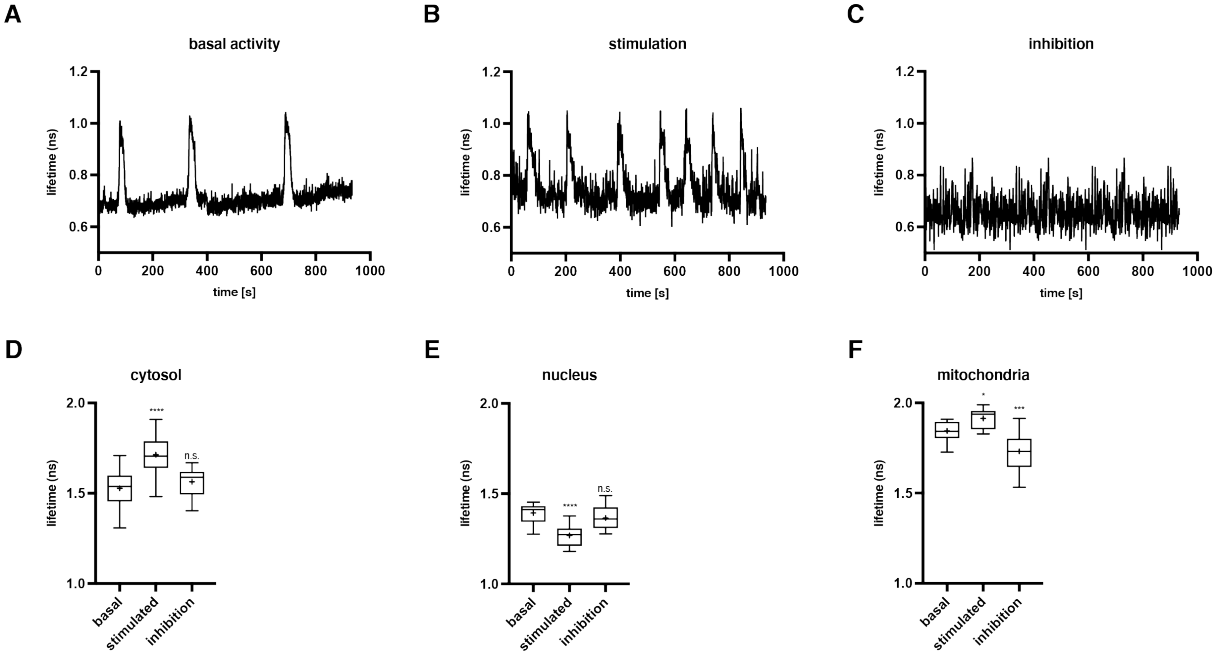

Figure 30: Subcellular levels of NAD+ and neuronal activity. A)–C) neuronal activity recorded with Cal520 using FLIM for basal activity, upon stimulation with 10 µM glutamate and 2.5 µM glycine or upon synaptic inhibition with 25 µM AP5 and 10 µM CNQX, respectively. D)–F) NAD+ levels upon stimulation and synaptic inhibition in the cytosol, nucleus and mitochondria after 1 h treatment. The box represents the 25th and 75th percentile and the whiskers are the minimum and maximum. The mean and median are indicated by a cross or line, respectively *N* = 50 cells per condition. n.s. = not significant, * $p < 0.05$, *** $p < 0.001$, **** $p < 0.0001$ using a one-way ANOVA with Dunnett's multiple comparison test with respect to basal conditions.

3.4 Identification of a mammalian mitochondrial NAD+ transporter

This project was part of a collaboration with the group of Joseph Baur (University of Pennsylvania) and has been published.[133] Knock-down experiments shown below were performed by Timothy Luongo, University of Pennsylvania. As these experiments have been performed before the improved FRET donor substrates were available, CP-TMR-C6-SMX was used.

3.5.1 Introduction

Mitochondria harbor most of the NAD^+ in a cell (roughly 40–70% of the total cellular NAD^+), which is used to maintain crucial processes such as the TCA cycle and oxidative phosphorylation.[134-135] Mitochondrial NAD^+ homeostasis is a prerequisite for sufficient ATP production and depletion of mitochondrial NAD^+ leads to apoptosis.[136] Despite intensive research on NAD^+ metabolism, the origin of the mammalian mitochondrial NAD^+ pool has not been discovered. In contrast, plants and yeast have NAD^+-transporters in the mitochondrial matrix.[135, 137] A mammalian homolog of these has not been identified so far. The existence of NMNAT3 (mitochondrial isoform of NMNAT) could suggest that mitochondria take up NMN, which is then converted into NAD^+.[138] NAMPT, the key enzyme of salvage pathway, co-purifies with liver mitochondria, but is not found in the mitochondria of multiple mammalian cell lines.[139-140] Isolated mitochondria were unable to produce NAD^+ from exogenous NMN or nicotinamide. However, isolated mitochondria were able to take up isotopically labelled NAD^+ from the cytosol. These results suggest the existence of a mammalian NAD^+ transporter.[141]

The Baur lab speculated that SLC25A51 could be a potential candidate for a mammalian mitochondrial NAD^+ transporter. The corresponding gene emerged to be essential in genome-wide screens.[142-143] SLC25A51 belongs to the mitochondrial carrier family, but no substrate has been assigned. In their preliminary data, overexpression of SLC25A51 and its paralog SLC25A52 increased mitochondrial NAD^+. The effect was similar to heterologous overexpression of Ndt1 (mitochondrial NAD^+ transporter in yeast). Conversely, knockdown of SLC25A51 resulted in a decrease of mitochondrial NAD^+.[133]

3.5.2 Outcome

The effect of overexpressing SLC25A51 on free mitochondrial NAD^+ was investigated using the NAD^+ biosensor in U2OS cells. First, the transfection conditions for a FLAG-tag fused construct of SLC25A51 were optimized. Expression of the mitochondrial NAD-Snifit was induced by doxycycline. After 24 h, the cells were transfected with different ratios of Fugene6 and DNA. The transfection efficiency and expression levels of SLC25A51 were investigated by confocal microscopy. The NAD-Snifit was labelled with Halo-CPY and SLC25A51 was stained with an anti-FLAG antibody, which was stained with a Alexa647 antibody. Ratios (Fugene6 to DNA) of 3:1 and 4:1 gave lower transfection efficiencies than 1.5:1 and 6:1.

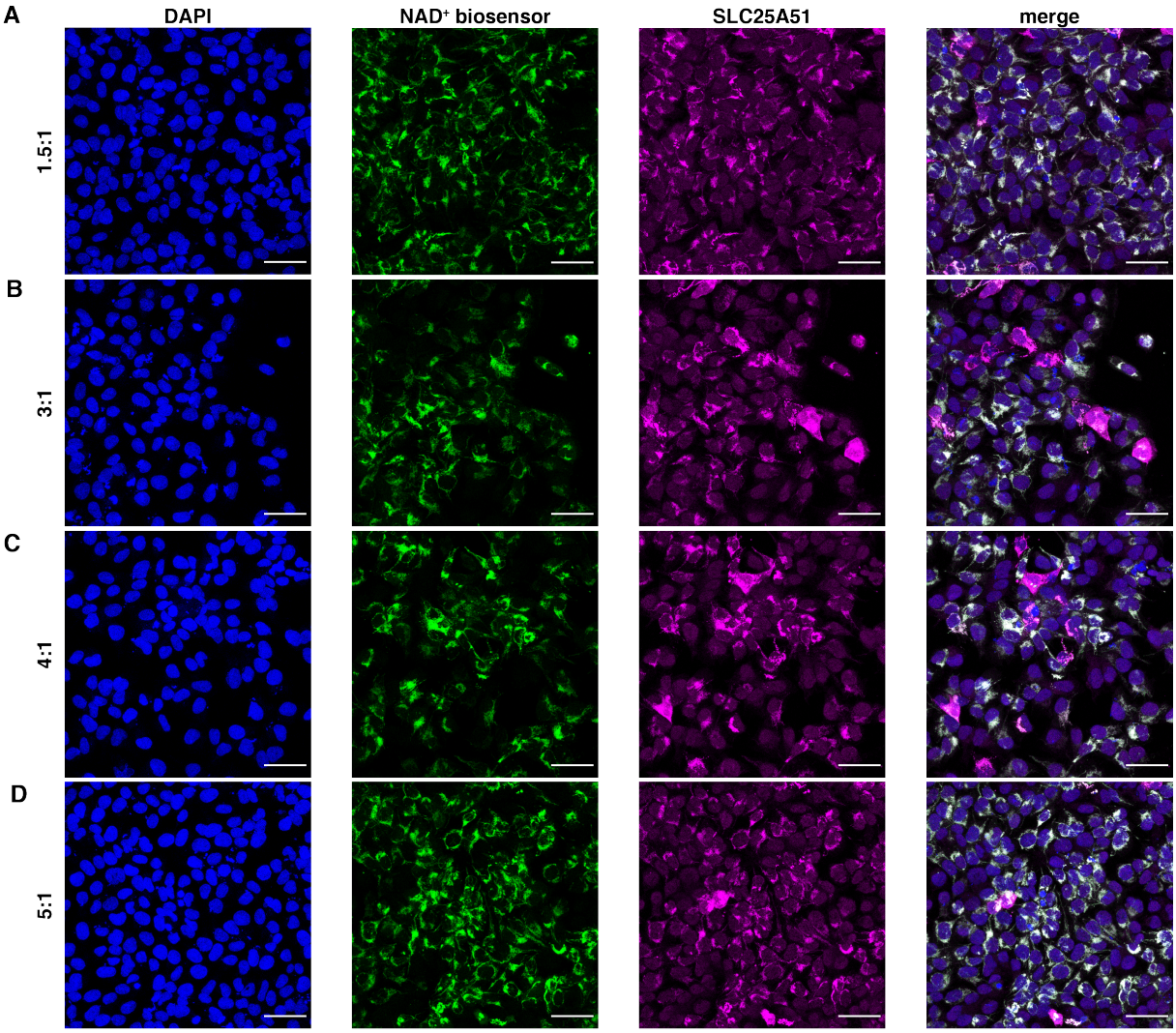

Figure 31: Transfection screen for SLC25A51 using different ratios of Fugene6 reagent to DNA. Nuclei were stained with DAPI, mitochondrial NAD-Snifit was labelled with Halo-CPY and SLC25A51 was stained with anti-FLAG antibody (primary) and Alexa647-antobody (secondary). A) 1.5:1. B) 3:1 C) 4:1. D) 5:1. Scale bar: 50 µm.

In addition, 3:1 and 4:1 resulted in expression artefacts, whereas 1.5:1 and 6:1 gave a more homogenous expression with 1.5:1 having the best results (**Figure 31A–D**). The

optimized transfection conditions were used to determine the workflow of the experiment. Initially, expression of the mitochondrial NAD-Snifit was induced for 24 h followed by transfection with SLC25A51 for 24 h. The NAD-Snifit was labelled with CP-TMR-C6-SMX (500 nM) and Halo-SiR (200 nM) for 16 h. However, employing these conditions did not show a significant change in mitochondrial NAD^+ compared to the non-treated control.

Next, the workflow was changed and expression was induced for 24 h. The NAD-Snifit was labelled with CP-TMR-C6-SMX (500 nM) and Halo-SiR (200 nM) for 16 h and SLC25A51 or SLC25A52 were transfected. 24 h after transfection, mitochondrial NAD^+ levels were analyzed with FACS. Overexpression of SLC25A51 significantly increased mitochondrial NAD^+ levels (1.16, 95% CI: 1.12–1.20) compared to the non-treated control (1.02, 95% CI: 0.93–1.11). Importantly, using an empty pcDNA5 plasmid vector as mock control, no significant increase in mitochondrial NAD^+ levels was observed (1.04, 95% CI: 1.01–1.06) (**Figure 32A**). Similar, overexpression of SLC25A52 also significantly increased mitochondrial NAD^+ levels (1.12, 95% CI: 1.09–1.15) compared to the non-treated control (1.01, 95% CI: 0.95–1.06). The mock control also did not affect mitochondrial NAD^+ levels (1.04, 95% CI: 1.03–1.06) (**Figure 32B**). Conversely, siRNA knock-down of SLC25A51 resulted in a significant decrease of increased mitochondrial NAD^+ levels (0.82, 95% CI: 0.76–0.89) compared to non-treated cells (1.00, 95% CI: 0.94–1.06). Using a scrambled siRNA as mock control had no effect on mitochondrial NAD^+ levels (1.04, 95% CI: 1.03–1.05) (**Figure 32C**). These results indicated important roles of SLC25A51 and SLC25A52 in establishing the mitochondrial NAD^+ pool in mammalian cells.

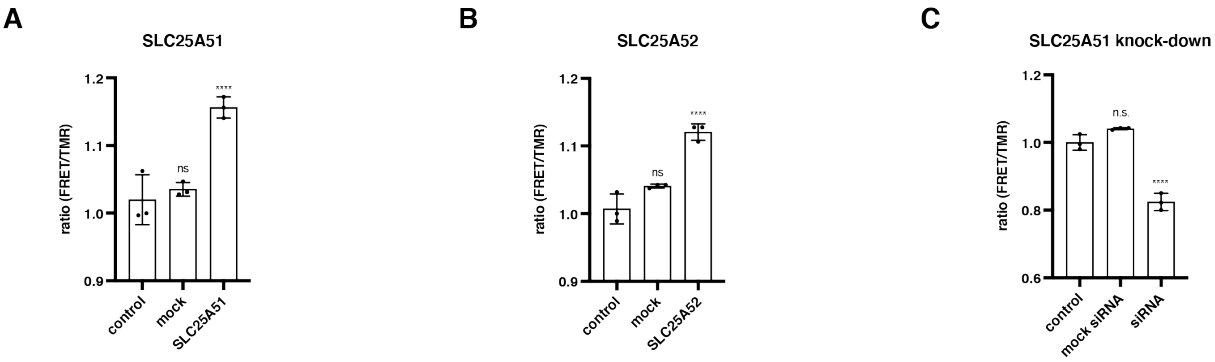

Figure 32: Measurements of mitochondrial NAD^+ levels. A) mitochondrial NAD^+ levels upon overexpression of SLC25A51. B) mitochondrial NAD^+ level upon overexpression of SLC25A52. C) mitochondrial NAD^+ level upon knock-down of SLC25A51. *N* = three biological experiments. Data are shown as mean ± SD. n.s. = not significant, **** $p < 0.0001$ using a one-way ANOVA with Dunnett's multiple comparison test with respect to control conditions.

3.5 Subcellular fluctuations of NAD^+ upon Nam and Trp starvation

This project was part of an ongoing collaboration with the group of Christiane Opitz (German Cancer Research Center, Heidelberg).

3.6.1 Introduction

The Opitz lab is interested in the role Trp in brain cancer metabolism and is specifically looking into the link between Trp and NAD^+ biosynthesis. They observed that Trp depletion in the medium had no effect on NAD^+ levels or even caused an increased in NAD^+ levels (cell type dependent), whereas Nam depletion significantly lowered NAD^+ levels. The decrease in NAD^+ upon both, Trp and Nam depletion was smaller than for Nam only. This observation led to the hypothesis that Trp depletion could compensate the effect of Nam depletion. To further elucidate mechanistic details, information about the subcellular NAD^+ pools are necessary. As they only have measured NAD^+ in cell lysate with a cycling assay, they wanted to apply the NAD-Snifit to gain subcellular insights.

3.6.2 Preliminary outcome

U2OS cells with an inducible NAD-Snifit were cultured in normal cell culture medium before seeded in 6 wells in customized media (prepared by Opitz lab): normal media, Nam-free, Trp-free and Nam/Trp-free. After 24 h, the cells showed a normal morphology in all conditions. No effect on proliferation was observed for Nam-free (compared to control). However, cells in Trp-free conditions did not proliferate and the cells showed a change in morphology. The cells appeared to be bigger and oblong. The same trend could be observed for culturing for 72 h (**Figure 33A**). The Opitz lab also observed changes in morphology and proliferation upon depletion of Trp.

After culturing for 72 h, the cells were seeded in 24-well plates and the NAD-Snifit expression was induced for 24 h. After labelling with CP-MaP555-PPT and Halo-SiR for 14 h, the cells were analyzed by FACS. Nam depletion resulted in a strong decrease of cytosolic NAD^+ (0.47, 95% CI: 0.46–0.48) compared to control conditions (0.91, 95% CI: 0.84–0.97), whereas Trp depletion had no significant effect on NAD^+ (0.86, 95% CI: 0.79–0.94). Nam/Trp depletion also significantly reduced cytosolic NAD^+ (0.66, 95% CI: 0.62–0.72), but to a much lower extent than Nam depletion (**Figure 33B**). Nuclear NAD^+ was also strongly reduced upon Nam depletion (0.57, 95% CI: 0.50–0.64) compared to control conditions (1.18, 95% CI: 1.16–1.21) and Trp depletion also led to a small decrease (1.05, 95% CI: 0.99–1.11). Nam/Trp depletion reduced nuclear NAD^+ (0.76, 95% CI: 0.63–0.88), but not as much as Nam depletion only (**Figure 33C**). Mitochondrial NAD^+ also showed a strong decrease upon Nam depletion (0.53, 95% CI: 0.51–0.55) compared control conditions (0.74, 95% CI: 0.71–0.76). The extent of decrease was less than for cytosol and nucleus. In contrast, Trp depletion led to an increase in mitochondrial NAD^+ (0.88, 95% CI: 0.86–0.90). Nam/Trp depletion also increased mitochondrial NAD^+ (0.81, 95% CI: 0.77–0.86), but to a lower extent than only Trp depletion (**Figure 33D**). These preliminary experiments showed that the NAD-Snifit was able to monitor changes in NAD^+ upon different culturing conditions. Interesting subcellular effects could be observed, however, the data are too preliminary to draw any biological conclusion.

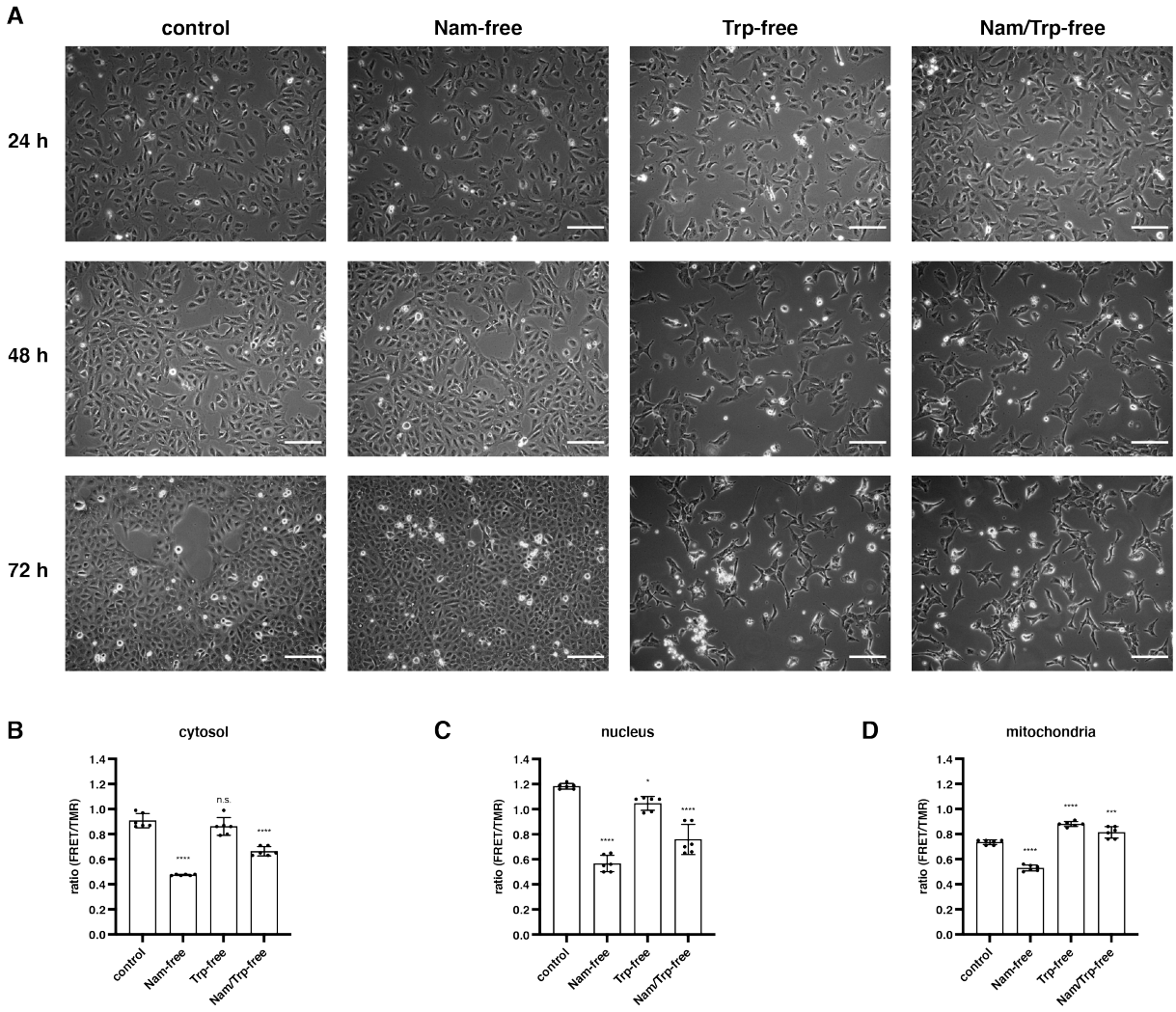

Figure 33: Subcellular NAD^+ levels upon Nam and Trp starvation. A) representative images of U2OS cells expressing the NAD-Snifit cultured in different media for 72 h. Scale bar: 50 µm. B)–D) subcellular NAD^+ levels in U2OS cells measured with NAD-Snifit upon being cultured in different media. *N* = six, three biological replicates performed in technical duplicates. Data are shown as mean ± SD. n.s. = not significant, * $p < 0.05$, *** $p < 0.001$, **** $p < 0.0001$ using a one-way ANOVA with Dunnett's multiple comparison test with respect to control conditions

4 Discussion

4.1 Substrate development

The JF dye strategy was successfully applied to convert CP-TMR-C6-SMX, a substrate for labelling the NAD(P)-Snifits, into the fluorogenic CP-Rhod540-C6-SMX. Even though this FRET donor substrate features improved brightness and cellular labelling, it also has certain limitations. The current synthesis is not elegant as the first Buchwald coupling is low yielding. The fluorescein bistriflate precursor **1** is easily accessible by synthetic means, however an asymmetric precursor would be more suited, but also synthetically much more challenging. Another drawback is the 15 nm blue-shift in absorbance and emission compared to the properties of the classical TMR scaffold. Many instruments such microscopes use spectral filters for excitation and emission. These filters are classically suited for GFP and TMR and the spectral properties CP-Rhod540-C6-SMX are between these channels. Non-optimal filter settings could result in a low signal and might influence the FRET ratio.

In addition, CP-Rhod540-C6-SMX was instable in DMSO or as powder. The degradation products are most likely the result of a ring-opening of the azetidines. Such ring-openings have observed in the presence of Lewis acids, nucleophiles or irradiation.[144-146] There are recent literature examples that the ring strain of azetidines can also negatively affect their stability. Aryl azetidines such **49** can undergo an acid-mediated intramolecular ring-opening. Nucleophilic attack of the amide group and loss of dimethylamine would lead to a lactone intermediate **50** that would undergo a rearrangement to lactam **51** (**Figure 34A**).[147] It has also been shown that azetidine containing molecules can be degraded by nucleophiles under acidic conditions. G334089 (**52**) is the S-enantiomer of the free fatty acid receptor 2 antagonist GLP0974. In acidic conditions, protonation of the azetidine nitrogen and subsequent attack of nucleophiles was observed, which resulted in intermediate **53** (**Figure 34B**).[148] A similar degradation mechanism could be possible for CP-Rhod540-C6-SMX. Protonation of the azetidine nitrogen would be followed by the attack of a nucleophile (e.g. H_2O), would lead to intermediate **55**. Further steps would lead to the observed degradation product **12** (**Figure 34C**). As neutralization after HPLC purification did not improve the long-term stability, one could speculate that 3-carboxylic acid azetidine

has an inherent reactivity. Introduction of a linker between the azetidine and the carboxylic acid could reduce the reactivity. However, ring-opening of 3,3-difluoroazetidine was also observed, which makes the JF dye strategy rather unattractive to pursue in this context. Such degradation problems have not been reported for other azetidine modified rhodamines. However, these fluorescent probes do not have their azetidines derivatized with a functional moiety, thus degradation would only lead to a change in spectral properties.

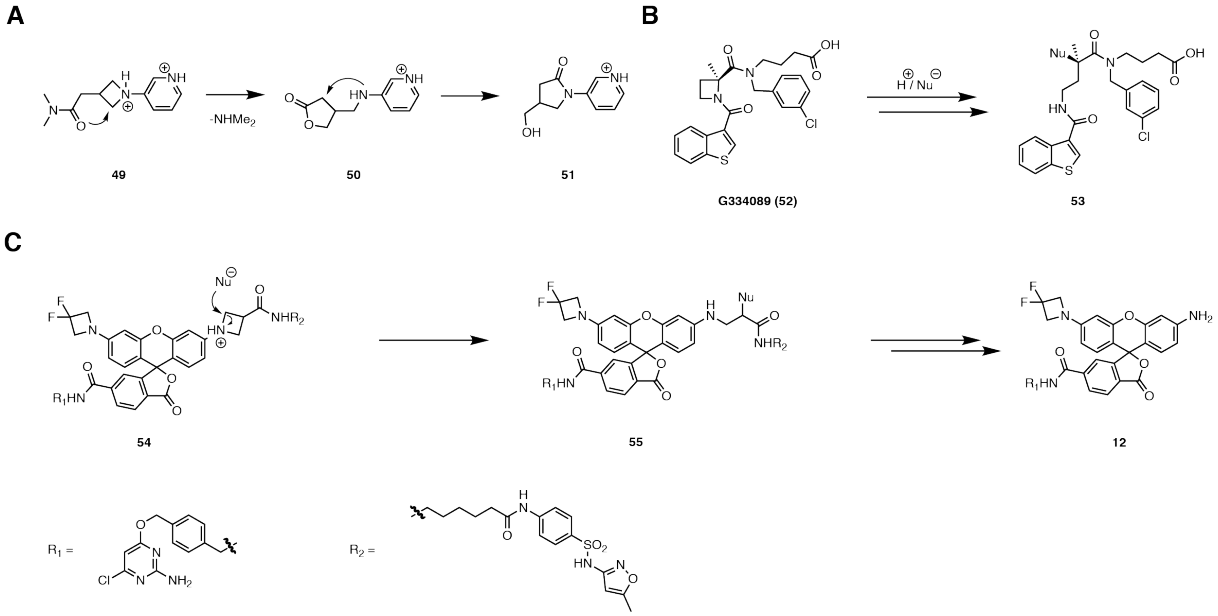

Figure 34: Degradation pathways of azetidine containing molecules. A) ring-opening via an acid-mediated intramolecular route. B) ring-opening via an acid-mediated nucleophilic attack. C) possible degradation mechanism for CP-Rhod540-C6-SMX.

The MaP dye strategy allowed the design of FRET donor substrates with tunable fluorogenicity. The modified fluorophore scaffolds are readily accessible from TMR-C3-COOH or TMR. The synthetic routes could be optimized by orthogonal protecting groups for the aromatic carboxylic and aliphatic acids. The physicochemical parameters of the FRET donor substrates are even more suited for cell permeability when using PPT as inhibitor compared to SMX. PPT-based FRET donor substrates have less HBDs and rotational bonds and a lower topological polar surface area compared to the corresponding SMX-based FRET donor substrates. In contrast, the calc. logP is increased for PPT substrates.

4.2 NAD(P)-Snifits *in vitro*

The new FRET donor substrates differ in their fluorogenic potential, which can be explained by the different electron-donating effects of the substituents of the sulfonamides. The alkyl substituents of MaP1 and MaP3 have a lower electron-donating effect than the *N,N*-dimethyl substituents of MaP555. This results in a higher nucleophilicity of the sulfonamide moiety of MaP555, which shifts the spirocyclization equilibrium strongly towards to the spirocyclic form. A high propensity for the spirocyclic form is key for a high permeability and specific labelling.[105-106, 113, 116]

In vitro titrations with NAD^+ demonstrate different response ranges for SMX- and PPT-based FRET donor substrates. This can be explained by a higher affinity of PPT to SPR in the presence of NAD^+ compared to SMX.

In vitro titrations of the NADP-Snifit labelled with SMX-based FRET donor substrates showed no differences between CP-TMR-C6-SMX and the MaP dye versions. However, such titrations were not successful for the NADP-Snifit labelled with PPT-based FRET donor substrates. The NADP-Snifit was always closed, even at very high NADPH/$NADP^+$ ratios (> 60). The hypothesis was that either the purification of commercial NADPH *via* anion exchange chromatography was not sufficient or NADPH partly oxidized again immediately after purification. Absorbance measurements of purified NADPH at 260 nm and 340 nm gave A_{260}/A_{340} ratios of 2.40–2.46. A pure NADPH sample has a A_{260}/A_{340} ratio of 2.32, but this ratio was never reached during the purification.[149] Determination of $NADP^+$ content in purified NADPH with **Equation 5** indicated 3–5% impurity. Originally, the NADPH/NADP titrations were performed with a total cofactor concentration of 100 µM and 20 nM NADP-Snifit. Lowering the total cofactor concentration to 1 µM could not solve this issue. Even 1 µM NADPH would then contain 30–50 nM $NADP^+$, which is higher than the concentration of the NADP-Snifit (20 nM). Considering the high affinity of PPT to SPR in the presence of $NADP^+$, which could be deduced from a very low nanomolar IC_{50} value for the parental QM385, one could assume that the NADP-Snifit is fully saturated under these conditions.[150] Therefore, it can be assumed that the problems with NADPH/$NADP^+$ titrations are most likely of a technical nature. Different strategies to overcome these technical limitation are currently under investigation. Degassing of the buffers used for

NADPH purification and for NADPH/$NADP^+$ titration could reduce the possibility of NADPH oxidation. Supplementation of the buffers with ascorbic acid could also prevent NADPH oxidation, because ascorbic acid has a higher redox potential (58 mV) compared NADPH (–400 mV).[33, 151] Increasing the NADP-Snifit concentration (up to 1 µM) could also be an option to decrease its sensitivity towards $NADP^+$ impurities.

4.3 NAD(P)-Snifits in live cells

Most of the new FRET donor substrates based on the MaP dye strategy show an improved labelling of the SNAP-tag in U2OS cells. Among them, CP-MaP555-C6-SMX and CP-MaP555-PPT outperform all other FRET donor substrates. Both substrates do not require the addition of verapamil and the labelling concentration can be reduced to 500 nM (previously 1 µM). This indicates a superior cell permeability of the MaP555 scaffold. The highly fluorogenic character of CP-MaP555-C6-SMX and CP-MaP555-PPT results in a high signal to noise in live cells and reduced artifacts due to unspecific background staining. Additionally, fluorescent imaging can be performed under no-wash conditions and with lower laser power, the latter reduces phototoxicity and bleaching.

Expression and labelling of the NAD-Snifit in U2OS cells does not affect total NAD^+ levels based on LC-MS/MS measurements in cell lysate. These data give no information whether the equilibrium between free and protein-bound NAD^+ is affected. One way to investigate this equilibrium would be to measure the lifetime of NAD(P)H, which is different for the free and protein-bound form. However, only the reduced form can be measured and the discrimination of NADH and NADPH lifetimes is very challenging.[77]

The highly potent SPR inhibitor QM385 is a valuable control compound for cellular applications of the NAD(P)-Snifits. It offers the possibility to open the sensor by outcompeting the intramolecular tether. In contrast to other sensors, the Snifit design allows this control, which can be used for different purposes. Treatment with QM385 can demonstrate that the NAD(P)-Snifits are functional, which has been very important in the case of CP-Rhod540-C6-SMX. The difference between basal and fully open state (ΔR) informs about how closed the NAD(P)-Snifits are. It allows to estimate the ability of the NAD(P)-Snifits to detect decreasing NAD^+ levels or increasing $NADPH/NADP^+$ ratios. ΔR depends on the affinity of the NAD(P)-Snifits towards NAD^+ and $NADPH/NADP^+$. In these experiments, the differences in affinity can also be estimated by the EC_{50} values of QM385. It is defined as the QM385 concentration needed for 50% change in FRET ratio. Comparison of EC_{50} values for the NAD-Snifit

labelled with CP-MaP555-C6-SMX and CP-MaP555-PPT shows a 24–75-fold higher EC_{50} values for CP-MaP555-PPT. The difference between CP-MaP555-C6-SMX and CP-MaP555-PPT is in agreement with the 73-fold lower c_{50} for CP-MaP555-PPT in *in vitro* titrations.

The conclusion of the problems with the *in vitro* titration of the NADP-Snifit labelled with CP-MaP555-PPT was that the issue is most likely of a technical nature. It was then decided to still test this combination live U2OS cells. If the conclusion was true, NADP-Snifit labelled with CP-MaP555-PPT would respond to treatments the similar to the NADP-Snifit labelled with CP-MaP555-C6-SMX.

The NADP-Snifit labelled with CP-MaP555-PPT responds to titrations with QM385 similar to the NADP-Snifit labelled with CP-MaP555-C6-SMX. This indicates that the NADP-Snifit is functional when using CP-MaP555-PPT. The differences between CP-MaP555-C6-SMX and CP-MaP555-PPT are in agreement with a higher affinity of PPT to SPR compared to SMX.

The NAD-Snifit is functional in live cells using the new FRET donor substrates CP-MaP555-C6-SMX and CP-MaP555-PPT. The subcellular response to treatment with FK866 and NR could be observed with CP-MaP555-C6-SMX and CP-MaP555-PPT. It should be noted that response of the NAD-Snifit labelled with CP-MaP555-C6-SMX to treatment with FK866 and QM385 is very similar, suggesting that NAD-Snifit is almost fully open upon FK866 treatment. This makes the NAD-Snifit labelled with CP-MaP555-PPT more attractive for measuring a decrease in NAD^+.

In these experiments, it is easier to deplete NAD^+ with FK866 than to induce an increase with NR. FK866 is a potent NAMPT inhibitor, the key enzyme of the salvage pathway, which is the most important part of NAD^+ biosynthesis.[109] U2OS cells are cultured in high-glucose DMEM that contains 33 µM Nam as biosynthetic precursor to fuel the salvage pathway.[152] Under these conditions, a drastic boost in free NAD^+ levels is unlikely by NR treatment. Increased free NAD^+ levels also affect the NADH/NAD^+ ratios, which could affect the activity of oxidative phosphorylation.[153] NR has been shown to efficiently rescue phenotypes that involve decreased NAD^+ levels.[154-155] These points again indicate that NR treatment might not be suited to significantly boost free NAD^+ levels under normal cell culture conditions. To better compare the response of the sensor labelled with CP-MaP555-C6-SMX and

CP-MaP555-PPT, U2OS cells could be cultured in Nam-free media. NR treatment could be used to replenish subcellular NAD^+ pools. Such conditions could also be employed to screen for novel biosynthetic precursors.

The NADP-Snifit is also functional in live cells using the new FRET donor substrates CP-MaP555-C6-SMX and CP-MaP555-PPT. The subcellular response to oxidative stress (induced by thapsigargin or H_2O_2) could be observed with CP-MaP555-C6-SMX and CP-MaP555-PPT. Importantly, the NADP-Snifit labelled with CP-MaP555-PPT was not fully closed at basal NADPH/$NADP^+$ ratios, but was more closed in response to oxidative stress. It showed a similar response as the NADP-Snifit labelled with CP-MaP555-C6-SMX. This suggests that the NADP-Snifit labelled with CP-MaP555-PPT also responds to changes of NADPH/$NADP^+$ ratios. Such observations also support the assumption that the problems with *in vitro* titrations are of a technical nature. Due to its presumably affinity towards higher NADPH/$NADP^+$ ratios, CP-MaP555-PPT might be more suited for the use in reducing environments (*e.g.* mitochondria of U2OS cells).

4.4 NAD(P)$^+$-Snifits in primary neurons

The improved permeability of CP-MaP555-C6-SMX and CP-MaP555-PPT allows labelling of the SNAP-tag in primary neurons without aggregation. Substrate titrations show a much better labelling for CP-MaP555-PPT than CP-MaP555-C6-SMX, indicating a much better permeability. By comparison, the older FRET donor substrate CP-TMR-C6-SMX shows strong aggregation, unspecific signal and a poor colocalization with the cytosolic mEGFP signal. These differences in neuronal SNAP-tag labelling highlight the significant improvements of CP-MaP555-C6-SMX and CP-MaP555-PPT with respect to live cell applications. Halo-tag labelling with Halo-SiR is straightforward in primary neurons and has been previously demonstrated.[156-157]

Optimal conditions for cultured primary neurons avoid changing the medium as primary neurons constantly secrete growth factors and nutrients that can be taken up again. Also, long-term or time-course measurements with the NAD(P)$^+$-Snifits cannot be performed in ACSF buffer.[126] These facts require the development of a no-wash labelling procedure for the NAD(P)$^+$-Snifits. In addition to the signal intensity of the labelled NAD$^+$-Snifit, the unspecific signal of non-expressing neurons is a relevant factor to determine the signal over background. Consistent with previous data, CP-MaP555-PPT has a much higher signal intensity than CP-MaP555-C6-SMX. Together with a higher brightens, CP-MaP555-PPT also has much less background signal than CP-MaP555-C6-SMX. This results in a higher signal over background for CP-MaP555-PPT, making it much more suited for the application in primary neurons.

The NAD-Snifit is fully functional in the cytosol, nucleus and mitochondria of primary neurons using CP-MaP555-PPT/Halo-SiR and responds to changes in subcellular free NAD$^+$ induced by treatment with FK866 or NR. This is the first time that subcellular free NAD$^+$ levels are measured in live primary neurons. The NAD-Snifit also reveals distinct differences in basal subcellular free NAD$^+$. The nuclear levels of free NAD$^+$ are found to be higher than in the cytosol. The significantly lower levels of free NAD$^+$ in mitochondria could be explained by subcellular differences in the free NADH/NAD$^+$ ratio.[158] Neurons mainly use oxidative phosphorylation for ATP production and their

mitochondria have a higher NADH concentration when oxidative phosphorylation takes place (**Figure 35B**).[159]

The NADP-Snifit is also fully functional in the cytosol, nucleus and mitochondria of primary neurons using CP-MaP555-PPT/Halo-SiR and responds to changes in subcellular free NADPH/$NADP^+$ ratio induced by treatment with H_2O_2 or thapsigargin. This is the first time that subcellular free NADPH/$NADP^+$ ratios are measured in live primary neurons. The NADP-Snifit also reveals differences in basal free NADPH/$NADP^+$ ratios between compartments. While cytosol and nucleus have similar redox states, the mitochondria have a significant lower NADPH/$NADP^+$ ratio. This could be explained by ATP production via oxidative phosphorylation as this pathway is the major source of mitochondrial ROS (**Figure 35B**).[160]

Both, H_2O_2 or thapsigargin induce strong oxidative stress and deplete cytosolic and nuclear NADPH, resulting in a low free NADPH/$NADP^+$ ratio. In contrast, the induction of oxidative stress with H_2O_2 or thapsigargin results in a higher free mitochondrial NADPH/$NADP^+$ ratio. This could be explained by metabolic adaption of the mitochondria. While neurons normally use oxidative phosphorylation for ATP production, short-term demand for NADPH as reducing equivalents could be more relevant than ATP demand.[161] Under normal conditions, NAD^+ is reduced to NADH during the TCA cycle and NADH is then subjected to oxidative phosphorylation.[162] Mitochondria can also convert NADH to NADPH using the nicotinamide nucleotide transhydrogenase.[163] Intermediates of the TCA cycle can also serve as substrates for NADPH producing enzymes such as ME or IDH2.[164-165] A different explanation could be that neurons normally metabolize glucose *via* glycolysis and pentose phosphate pathway (PPP). During oxidative stress, glucose could be completely metabolized *via* PPP to generate NADPH. Consequently, no glycolytic products could fuel the TCA cycle, resulting in lower activity of the oxidative phosphorylation and subsequent mitochondrial ROS production.[166-167] Such metabolic adaption could explain the higher mitochondrial NADPH/$NADP^+$ ratio upon oxidative stress.

4.5 Subcellular differences between U2OS and primary neurons

The applicability of the NAD(P)-Snifits in primary neurons allowed for the first time a direct comparison of their free NAD^+ levels and NADPH/$NAPD^+$ ratio with a commonly used human osteosarcoma cell line (U2OS) using FLIM-FRET. The subcellular comparison highlights significant and so far unknown differences between U2OS cells and primary neurons. The main differences are much higher levels of free NAD^+ and a higher NADPH/$NAPD^+$ ratio in the mitochondria of U2OS cells compared to primary neurons. In addition, the cytosol and nucleus are much more reducing in primary neurons compared to U2OS cells.

These differences could be explained by the metabolic characteristics of U2OS cells and primary neurons. Typical for cancer cells are the constant proliferation and high ATP demand.[168] This is required for fast growth and proliferation. This ATP demand is covered by aerobic glycolysis, where glucose is metabolized to pyruvate and then lactate, while only a minimal activity of the oxidative phosphorylation is observed.[169] This phenomenon is also known as the Warburg effect and the high glycolytic activity results in a high ROS level in cytosol and nucleus.[170-171] Conversely, the low activity of the oxidative phosphorylation leads to lower ROS level in the mitochondria.[172] This would also lead to lower NADH level compared to cells using oxidative phosphorylation as a substantial fraction of the mitochondrial NAD^+ could be reduced.[173] This could be an explanation for the higher mitochondrial NAD^+ level compared to primary neurons (**Figure 35A**).

In contrast, 14 d old cultured primary neurons are fully differentiated and are non-proliferating cells.[174] During differentiation, a metabolic shift takes place and primary neurons almost exclusively use oxidative phosphorylation for ATP production.[175] This involves a low glycolytic activity and the uptake of lactate. Lactate is metabolized to pyruvate, which fuels the TCA cycle, where NADH is generated. This could result in a higher NADH/NAD^+ ratio, which would explain the lower levels of free NAD^+ compared to U2OS cells.[173] As oxidative phosphorylation is the major soured source of mitochondrial ROS, this could also be an explanation for the more oxidizing environment of mitochondria in primary neurons compared to U2OS cells

(**Figure 35B**).[160] In support of this hypothesis are the changes in neuronal mitochondrial NAD^+ levels upon pharmacological stimulation or inhibition. Stimulation has been shown to increase oxidative phosphorylation and additionally activate glycolysis.[131-132] Activation of glycolysis increases the cytosolic NADH/NAD^+ ratio, which is in line with lower free cytosolic NAD^+ levels measured with the NAD^+-Snifit. An increased activity in oxidative phosphorylation should increase the mitochondrial NADH/NAD^+ ratio. Accordingly, lower free mitochondrial NAD^+ levels were measured (**Figure 35C**). Synaptic inhibition decreases the neuronal ATP demand, which results in a lower activity of oxidative phosphorylation. A measured increase in free mitochondrial NAD^+ levels is in line with a decreased mitochondrial NADH/NAD^+ ratio (**Figure 35D**). The measurements of neuronal subcellular NADPH/$NADP^+$ ratios upon pharmacological stimulation or inhibition could further strengthen the hypothesis.

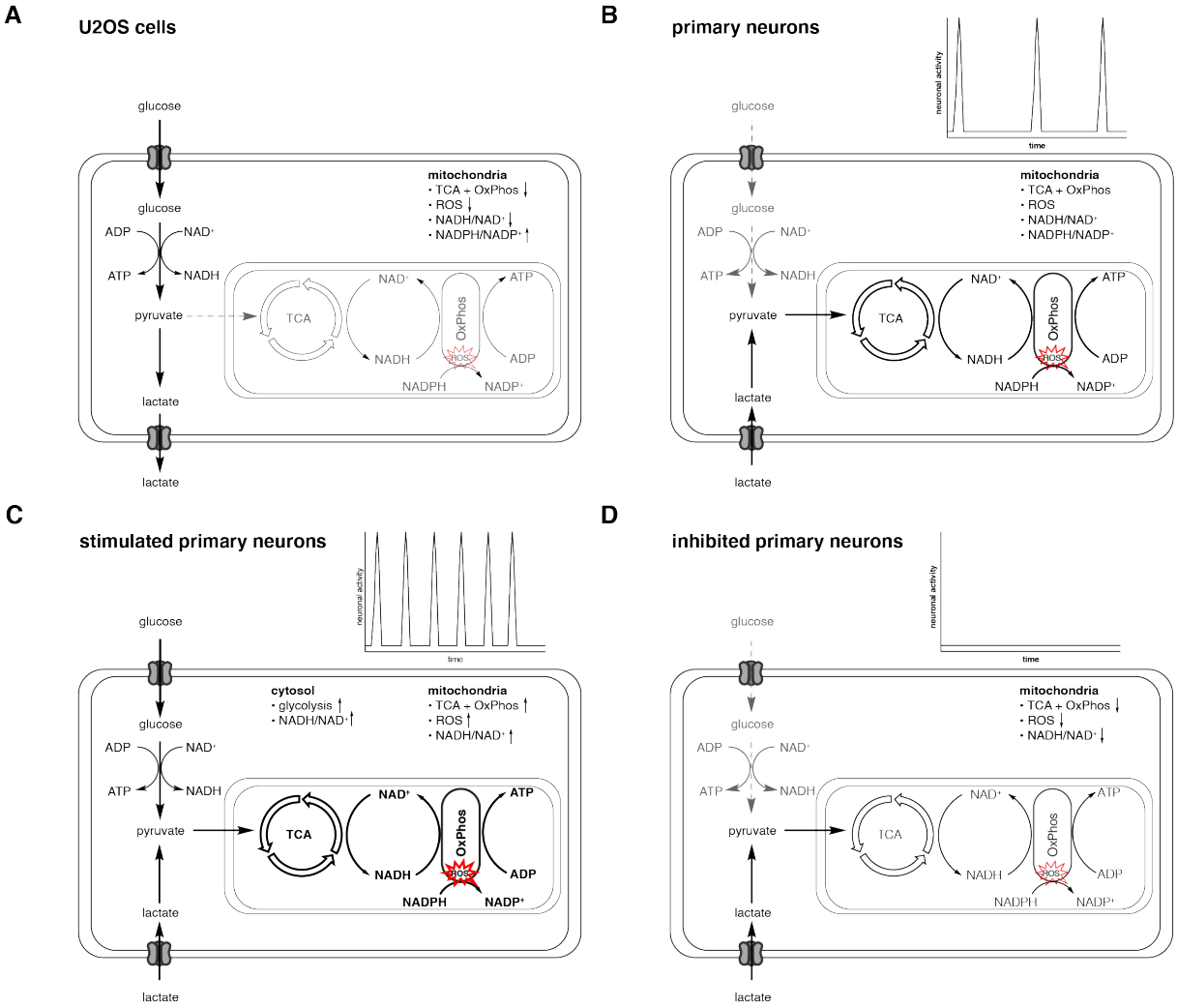

Figure 35: Major pathways for energy production in cancer cells and primary neurons. A) U2OS cells have a high glycolytic activity and only minimal oxidative phosphorylation compared to primary neurons (Warburg effect). B) primary neurons with spontaneous activity mainly utilize pyruvate for oxidative phosphorylation. C) stimulated primary neurons have an upregulated oxidative phosphorylation and an additional glycolytic activity. D) inhibited primary neurons have a lower rate of oxidative phosphorylation.

The hypothesis that differences in mitochondrial metabolism account for the differences in mitochondrial free NAD^+ levels and NADPH/$NADP^+$ ratios could be tested by selective inhibition of TCA cycle or complex I of the respiratory chain. Inhibition of key enzymes of the TCA cycle such as aconitase or IDH would inhibit the reduction of NAD^+ to NADH and should result in higher levels of free NAD^+.[176] Blocking complex I of the respiratory chain with rotenone would inhibit the oxidation of NADH to NAD^+ and should result in lower levels of free NAD^+.[176] Both treatments would inhibit the respiratory chain before ROS are generated and should therefore result in a higher NADPH/$NADP^+$ ratio.[177] As oxidative phosphorylation is much more relevant in primary neurons, a stronger effect of these treatment could be expected in primary neurons compared to U2OS cells. The hypothesis could also be tested by applying the NAD(P)-Snifits in astrocytes. These are a diverse class of neural cells and play an important role in nutrient homeostasis and neurotransmitter recycling.[178] They are part of a neural network and exchange metabolites with neurons (e.g. lactate shuttle). In contrast to neurons, astrocytes mainly utilize glycolysis for ATP production.[179] Therefore, if the hypothesis would be correct, a similar difference in mitochondrial free NAD^+ levels and NADPH/$NADP^+$ ratios could be expected between primary neurons and astrocytes. Applying the NAD(P)$^+$-Snifits in a co-culture of primary neurons and astrocytes would generate new insights into this symbiotic relationship. In particular, differences between resting and stimulated neural cultures could be very interesting.

There are also fluorescent biosensors for NADH/NAD^+ ratio, NADH, $NADP^+$ and NADPH that could be used to investigate mitochondrial NAD(P)(H) metabolism in U2OS cells and primary neurons. However, Peredox and SoNar can only be used to measure cytosolic NADH/NAD^+ ratios, which limits their applicability for investigating mitochondrial NADH/NAD^+ ratios.[81-82] Frex is a fluorescent NADH biosensor that can be used in mitochondria. Its pH sensitivity requires careful corrections and could also limit the accuracy. iNap is a fluorescent biosensor that reports on NADPH and can be used in mitochondria.[85] This sensor could be used to compare free mitochondrial NADPH levels in U2OS cells and primary neurons.

4.6 NAD^+ transporter

The question how the mammalian mitochondrial NAD^+ pool is established has been unsolved for decades. In recent years, evidence has emerged indicating that mammalian cells have a NAD^+ transporter for the mitochondria similar to plants or yeast.[79, 141] This hypothesis is in line with hundreds of orphan SLCs, where neither functions or substrates are known.[180] The Baur lab uses different methods to identify and characterize SLC25A51 and SLC25A52. Among these methods, the NAD-Snifit demonstrates the benefit of subcellular measurements in live cells. Such successful contributions help to establish the NAD(P)-Snifits as standard research methods. Independently, two other research groups also identified SLC25A51 as mammalian mitochondrial NAD^+ transporter, which supports the finding of the collaboration.[181-182] Further research on the metabolic role of SLC25A51 is ongoing, which highlights the significance of the discovery of SLC25A51 (personal communication, not published yet: Cambronne lab, Hottinger lab).

Experiments with the NAD-Snifit only involve the overexpression of potential SLCs as NAD^+ transporter or the knock-down of the more important SLC. A suitable positive control would be the overexpression of a known yeast or plant NAD^+ transporter. These experiments could not be performed, because the cDNA of these NAD^+ transporter has not been available at that time. However, such experiments were performed by the collaborators using a different NAD^+-biosensor.[133]

4.7 Nam and Trp starvation

Culturing U2OS cells in Nam-free, Trp-free or Nam/Trp-free media reveals distinct subcellular effects in free NAD^+. A drastic decrease in NAD^+ upon Nam depletion is to be expected as it is the most important precursor for cultured cells.[183] While Trp starvation has only a little effect on cytosolic and nuclear NAD^+, mitochondrial NAD^+ is significantly increased. Nam/Trp starvation appears to compensate for the effect of Nam depletion. These data are in line with data from the Opitz lab, however the subcellular insights are valuable to elucidate the connection between Trp starvation and NAD^+ biosynthesis. The subcellular effects of both, Trp depletion and Nam/Trp depletion are intriguing and could hint to an unknown compensation mechanism.

5 Summary and outlook

This PhD thesis describes the development of fluorogenic FRET donor substrates for the NAD(P)-Snifits and the subsequent application of the NAD(P)-Snifits in primary neurons.

Prior to this work, the applicability of the NAD(P)-Snifits in complex and more relevant model systems has been limited by the permeability of the FRET donor substrate CP-TMR-C6-SMX and its labelling of the NAD(P)-Snifits. To address these issues, the TMR scaffold was optimized by converting the *ortho*-carboxy moiety into substituted sulfonamides. The three resulting fluorogenic dyes were combined with the SPR inhibitors SMX or PPT to yield six new FRET donor substrates. After evaluation in live cells, CP-MaP555-C6-SMX and CP-MaP555-PPT were selected as substrates with the best permeability and labelling of the NAD(P)-Snifits. The NAD(P)-Snifits were functional when labelled with CP-MaP555-C6-SMX or CP-MaP555-PPT as demonstrated by the response to pharmacological treatments in U2OS cells.

CP-MaP555-C6-SMX and CP-MaP555-PPT were able to label the NAD(P)-Snifits in primary neurons. Due to its superior permeability and labelling, CP-MaP555-PPT could also be used for no-wash labelling, making it suitable for long term experiments. This enabled for the first time subcellular measurements of free NAD^+ levels and $NADPH/NADP^+$ ratios in live primary neurons. Additionally, subcellular fluctuations of free NAD^+ levels and $NADPH/NADP^+$ ratios upon pharmacological treatment in primary neurons could be observed for the first time.

FLIM-FRET measurements revealed clear differences between U2OS cells and primary neurons regarding their subcellular free NAD^+ levels and $NADPH/NADP^+$ ratios. U2OS cells had much higher levels of free mitochondrial NAD^+ than primary neurons. While primary neurons had higher cytosolic and nuclear $NADPH/NADP^+$ ratios, their mitochondria had much lower $NADPH/NADP^+$ ratios than U2OS cells. An explanation could be a different activity of oxidative phosphorylation in both cell types. These findings suggest that free subcellular NAD^+ levels and $NADPH/NADP^+$ ratios can vary significantly between different cell types. They also provide a starting point for a more systematic evaluation of NAD^+ levels and $NADPH/NADP^+$ ratios in different

organelles and cell types. This would greatly contribute to the understanding of metabolism in general and should have implications for drug development (*e.g.* cooperative binding of an inhibitor and NAD(P)(H) would dependent on the free concentration or ratios of the cofactors.)

Multiplexing of the NAD-Snifit with the synthetic calcium indicator Cal520 demonstrated how sensors can be used for multiplexing to investigate metabolic relationships and multiple pathways in the same cell at once. The successful application of the NAD(P)-Snifits in primary neurons opened up the possibility to investigate subcellular free NAD^+ and $NADPH/NADP^+$ levels in other primary cells such as hepatocytes or myoblasts, which are frequently used to study NAD(P)(H) metabolism.[184-185]

Furthermore, the NAD-Snifit has provided valuable subcellular insights in different collaborations. For instance, it contributed to the discovery of the first mammalian mitochondrial NAD^+ transporter. NAD-Snifits are also used to elucidate the subcellular response to Nam and Trp starvation. This highlights the potential of the NAD-Snifit to study complex biological questions.

Current projects in the Johnsson lab include the optimization of the SNAP-tag and its substrates. The permeability and labelling kinetics of the SNAP-tag substrates BG and CP are significantly lower than for the Halo-tag substrate.[186-187] A further engineered SNAP-tag combined with an improved SNAP-tag substrate could further increase permeability and labelling kinetic of the FRET donor substrate. Similar permeabilities and labelling kinetics of SNAP-tag and Halo-tag substrate could decrease the incubation time with fluorescent substrates and reduce unspecific background staining. Engineering of the SNAP-tag could lead in a higher turn-on of the FRET donor substrate, resulting in a higher signal to noise.

As of now, the NAD(P)-Snifits have been mainly evaluated in U2OS cells. Stable cell lines could be easily generated using the Trex-FlpIn system and the flat morphology makes this cell line attractive for imaging. However, all immortalized cell lines used in research have alterations of their metabolism and feature a great metabolic diversity.[188-190] This could also result in variations in NAD(P)(H) metabolism between different immortalized cell lines and limit the significance of findings. Applying the

NAD(P)-Snifits in other immortalized cell lines such as human hepatocellular carcinoma cells (HepG2), mouse insulinoma cells (MIN6) or Jurkat cells could help to select the best model system for a defined biological question.[191-193]

The most physiological model systems apart from *in vivo* (e.g. zebrafish or rodents) are *ex vivo* transplants of organs and human induced pluripotent stem (iPS) derived cells or organoids.[194] Using the NAD(P)-Snifits would offer the possibility to reveal new insights into subcellular NAD(P)(H) metabolism in health and disease. Labelling of the NAD(P)-Snifits with the fluorescent substrates will be the main challenge for applying the sensors in these systems. A more permeable FRET donor substrate might be necessary if CP-MaP555-PPT is not sufficient for labelling. One could envision to shift the spirocyclization equilibrium of TMR even more to the spirocyclic form by modifying the *ortho*-carboxylic acid with more electron-rich moieties than *N*,*N*-dimethylsulfamide.

6 Experimental Procedure

6.1 Reproducibility and statistical analysis

Unless stated otherwise, all experiments were performed in three independent replicates. The number of replicates per experiment are stated in the figure legend. Sample sizes were not predetermined by statistical methods.

Statistical analyses were performed with Prism 9.0 using a one-way ANOVA (multiple comparison to a control group) or unpaired, two-tailed *t*-test (comparison of two groups). For multiple comparison analysis, a Dunnett post-hoc correction was performed. A p value < 0.05 was considered significant.

6.2 Biochemical characterization

6.2.1 Spectral measurements

Absorbance spectra were measured using a quartz glass cuvette (150 µL volume, path length: 10 mm). Spectra were recorded from 400–650 nm at 25 °C. Sample concentration was 5 µM and the DMSO content was kept ≤ 1 vol%.

Fluorescence spectra were measured on using a quartz glass cuvette (150 µL volume, path length: 10 mm). Spectra were recorded from 520–700 nm at 25 °C. Sample concentration was 5 µM and the DMSO content was kept ≤ 1 vol%.

6.2.2 Determination of extinction coefficient

The absorbance spectra were measured in different buffers (0.1% TFA in EtOH, 0.1% SDS in PBS and 10 mM HEPES, pH 7.3) at concentrations of 1 µM, 5 µM, 10 µM and 15 µM. All measurements were performed with UV-Vis spectrometer using a quartz glass cuvette (150 µL volume, path length: 10 mm). Spectra were recorded from 400–650 nm at 25 °C. The absorption maxima were plotted against the concentrations and fitted linearly. According to the Lambert-Beer law (**Equation 3**), the resulting slope is the ε of the respective fluorophore.

$$A_\lambda = \varepsilon \cdot c \cdot d \quad (\mathbf{3})$$

ε = extinction coefficient, c = concentration, d = path length.

6.2.3 Determination of quantum yield

Quantum yields were measured using an integrating sphere to determine the absolute quantum yield. Absorbance was < 0.1 a.u..

6.2.4 Water-dioxane titrations

FRET donor substrates were diluted to 5 µM in different water-dioxane mixtures (DMSO content was ≤ 1 vol%). Dioxane content was from 20/80 (vol%) to 90/10 (vol%). Absorbance spectra were measured on a plate reader using PP F-bottom (chimney well) 96-well plates. Spectra were recorded from 400–650 nm at 25 °C. After background correction, the absorbance maxima were plotted against the dielectric constant of the respective water-dioxane mixture.[195]

6.2.5 Turn-on measurements

FRET donor substrates were diluted to 5 µM in activity buffer containing 10 µM purified SNAP-Halo protein.[116] As a reference, the samples were diluted to 5 µM in activity buffer. After incubation at 25 °C for 3 h, the fluorescence spectra were measured. The fold-change in fluorescence was reported by dividing the maxima of the SNAP-tag sample by the corresponding buffer sample.

6.2.6 Labelling kinetics *in vitro*

The FRET donor substrates were diluted to 40 nM in activity buffer. 100 µL of the diluted sensor substrates were added into a black quartz glass 96-well and incubated at 25 °C for 16 h. The reaction was started by the addition of 100 µL activity buffer containing 800 nM of purified NAD-Snifit protein. Final concentrations: 20 nM FRET donor substrates and 400 nM of purified NAD-Snifit protein. The labelling kinetics were measured by an increase in fluorescence polarization (FP) using the following settings:

Excitation filter: 535 nm (bandwidth: 25 nm), emission filter: 595 nm (bandwidth: 35 nm), mirror: dichroic 560, gain: 53, flashes: 10, g-factor: 1.033 and z-position: 17573 µm. FP values were plotted against the time and the second-order rate constant was derived with **Equation 4**.

$$FP=FP_{max}+\frac{FP_0-FP_{max}}{A_0}\cdot\frac{A_0\,(A_0-B_0)e^{(A_0-B_0)kt}}{A_0e^{(A_0-B_0)kt}-B_0} \qquad (\mathbf{4})$$

t = time, FP_0 = FP at t = 0, FP_{max} = FP at upper plateau, k = second-order rate constant, A_0 = starting concentration of FRET donor substrate (20 nM) and B_0 = starting concentration of purified NAD-Snifit protein (400 nM).

6.2.7 Expression and purification of NAD(P)-Snifits

The NAD(P)-Snifit proteins were produced in *E.coli* BL21-DE3. Bacteria were grown in 1 L LB media containing ampicillin (100 µg/mL) at 37 °C. At OD_{600} = 0.6, the culture was cooled to 16 °C and the protein expression was induced by the addition of 1 mM IPTG. After 16 h, the cells were harvested by centrifugation (4000 *g*, 15 min, 4 °C) and resuspended in 30 mL extraction buffer supplemented with 1 mM PMSF, 0.25 mg/mL lysozyme and 5 mM DTT. The suspension was sonicated on ice (7 min, 50% duty cycle, 70% power) and centrifuged (10000 *g*, 15 min, 4 °C). The clear lysate was purified using a Ni-NTA resin. The applied lysate was washed extensively with 10 column volumes (CV) wash buffer and eluted with 5 CV elution buffer. The purified sensor protein was concentrated using an Amicon® ultra 50k cut off filter and the buffer was exchanged to activity buffer. The concentration was determined by measuring the absorbance at 280 nm using an extinction coefficient of 100,000 $M^{-1}cm^{-1}$ that was calculated with ExPASy.[196] The sensor protein was stored in activity buffer + 5 vol.% glycerol at –20 °C.

6.2.8 Labelling of NAD(P)-Snifits

The sensor protein was diluted to 5 µM in activity buffer and incubated with the respective fluorescent substrates (10 µM) at 25 °C for 3 h (reaction volume: 200 µL). The mixture was centrifuged (10000 *g*, 1 min, 4 °C) and the excess of fluorescent substrates was removed using desalting column according to the manufacturer's instructions. The sensor protein solution was concentrated using an Amicon® ultra 50k

cut off filter and centrifuged (10000 *g*, 1 min, 4 °C). The concentration of the labelled sensor protein was determined by measuring the absorbance at 550 and 650 nm in PBS + 0.1% SDS (ε (SiR) = 100,000 $M^{-1}cm^{-1}$).[88]

6.2.9 Titrations of NAD(P)-Snifits

The labelled NAD(P)-Snifit protein was diluted to 20 nM in activity buffer (supplemented with 0.5 mg/mL BSA) in a 96-well back non-binding plate.

For NAD^+, a 10-fold cofactor dilution was added (final volume: 100 µL/well) and incubated for 30 min at 37 °C. NAD^+ concentrations were ranging from 20 mM to 2 nM using 10-fold dilution steps.

For NADPH/$NADP^+$ ratios, the total cofactor concentration was fixed to 100 µM and the following ratios were used: 199, 99, 49, 32.2, 24, 9, 4, 1 as 5-fold dilution. Commercial NADPH was purified from $NADP^+$ by FPLC using an anion exchange column. The following buffer system was used: 20 mM triethanolamine pH 7.7 and for elution a gradient of 20 mM triethanolamine pH 7.7 + 1 M KCl (0–100%).[197] The concentration of NADPH was determined by measuring the absorbance at 340 nm. If necessary, the concentration of NADPH was corrected for $NADP^+$ by measuring the absorbance at 260 nm and 340 nm and using **Equation 5**.

$$[NADP^+](M) = \frac{\left(\frac{A^{260}}{A^{340}} \cdot \varepsilon^{340,\ NADPH} \cdot [NADPH]\right) - (\varepsilon^{260,\ NADPH} \cdot [NADPH])}{\varepsilon^{260,\ NADP^+}} \quad (\mathbf{5})$$

A_{260}/A_{340} = absorbance at 260 nm or 340 nm, respectively, $\varepsilon^{260\ nm}$ (NADPH) = 14,400 $M^{-1}cm^{-1}$, $\varepsilon^{340\ nm}$ (NADPH) = 6220 $M^{-1}cm^{-1}$, $\varepsilon^{260\ nm}$ ($NADP^+$) = 17,800 $M^{-1}cm^{-1}$.

The emission spectra were measured on Tecan Spark® 80 plate reader using the following settings: Excitation wavelength: 520 nm (bandwidth: 10 nm), emission: 550–740 nm (bandwidth: 10 nm), step size: 2, mirror: dichroic 560, gain: 130, flashes: 20, and z-position: 17573 µm. Ratios of FRET/TMR were plotted against [NAD^+] or [NADPH/$NADP^+$] and the half-maximal sensor responses (c_{50} and r_{50}) were obtained using **Equation 6** or **Equation 7**, respectively. Ratios of FRET/isosbestic point were plotted against [NAD^+] or [NADPH/$NADP^+$] and the apparent affinities ($K_{D,\ app}$ and $K_{50,\ app}$) were obtained using **Equation 8** or **Equation 9**, respectively.

$$R = R_{max} + \frac{R_{min} - R_{max}}{1 + \frac{c_{50}}{[NAD^+]}} \quad (\mathbf{6}) \qquad R = R_{max} + \frac{R_{min} - R_{max}}{1 + \frac{r_{50}}{[NADPH/NADP^+]}} \quad (\mathbf{7})$$

$$R = R_{max} + \frac{R_{min} - R_{max}}{1 + \frac{K_{D,\,app}}{[NAD^+]}} \quad (\mathbf{8}) \qquad R = R_{max} + \frac{R_{min} - R_{max}}{1 + \frac{K_{50,\,app}}{[NADPH/NADP^+]}} \quad (\mathbf{9})$$

R = ratio (FRET/TMR), R_{min} = minimal ratio, R_{max} = maximum ratio, c_{50} = half-maximal sensor response, [NAD^+] = concentration of NAD^+, r_{50} = half-maximal sensor response, [NADPH/$NADP^+$] = ratio of NADPH/$NADP^+$, $K_{D,\,app}$ = apparent affinity for NAD^+, $K_{50,\,app}$ = apparent affinity for NADPH/$NADP^+$.

6.2.10 Cloning and production of AVVs

DNA sequences for SNAP-mEGFP, Halo-mGFP and NAD(P)-Snifits (cytosol, nucleus, mitochondria) were sub-cloned into a pAAV vector with a hSyn promotor using Gibson assembly. Plasmids were transformed into NEB stable *E. coli* cells and amplified plasmids were purified using an endotoxin-free kit. Integrity of both ITRs was verified by sequencing. Cloning was performed by Andrea Bergner.

AVVs were produced in HEK293 cells. Cells were transfected with the respective AAV plasmid vector and the helper plasmid (pAdDeltaF6). Cells were harvested and AVVs were purified by affinity chromatography. AVV production was performed by Annette Herold. Viral titers were determined by qPCR, expressed as genomic copies and calculated to be $0.95–1.02 \cdot 10^{13}$ GC/mL.[198] Determination of viral titers was performed by Magnus Huppertz.

6.3 Live cell characterization

6.3.1 General remarks for mammalian cell culture

Unless stated otherwise, U2OS cells were cultured in Dulbecco's modified Eagle's medium (DMEM) containing 4.5 g/L glucose, 4 mM L-glutamine, 1 mM sodium pyruvate and 10% fetal bovine serum (FBS). Cells were grown at 37 °C with a 5% CO_2 atmosphere in a humidified incubator. Cells were splitted 1:3 at 90–95% confluency and also one day before seeding. Therefore, cells were washed once with phosphate buffered saline (PBS) and then incubated with trypsin or TrypLE for 5 min 37 °C. Trypsin was inactivated with the same amount of DMEM. Cell counting was performed with an automated Countess™ II FL cell counter (Invitrogen) using trypan blue staining (10 µL cell suspension + 10 µL trypan blue). All cell lines were routinely tested for mycoplasma contamination by PCR.

For FACS experiments, cells were seeded at $1x10^5$ cells/mL in a 24-well plate using 500 µL medium per well.

For microscopy experiments, cells were seeded at $5x10^4$ cells/mL in a 96-well glass-bottom plate using 100 µL medium per well.

In case of NAD(P)-Snifit cells, the expression was induced by the addition of doxycycline (200 ng/mL).

24 h after seeding, the cells were labelled with the respective FRET donor substrate (500 nM) and Halo-SiR (200 nM) for 14 h. Fluorescent substrate were diluted in DMEM (at least 1:1000 final dilution from DMSO stock). For microscopy experiments, the cells were washed tree times with Hank's Balanced Salt Solution (HBSS) containing 4.5 g/L glucose, 4 mM L-glutamine, 1 mM sodium pyruvate. Live cell imaging was performed in the same media. For drug treatment, the compounds were diluted in DMEM (at least 1:1000 final dilution from DMSO stock) and the cells were incubated for the indicated time period before the media was exchanged to HBSS. For H_2O_2 treatment, cells were incubated with 1 mM H_2O_2 in HBSS.

6.3.2 General remarks for rat primary hippocampal neurons

Preparation of hippocampal neurons was done by Dr. Birgit Koch, Magnus Huppertz, Clara-Marie Gürth, Jasmine Hubrich, Victor Macarrón Palacios, Angel Rafael Cereceda Delgado and Dr. Elisa D'Este. The rats were sacrificed according to the regulations in §4 Tierschutzgesetz (TierSchG). Scarifying was not an animal experiment and did not require specific authorization (§7 Abs. 2 Satz 3 TierSchG).
24 well glass bottom plates were coated with poly-L-ornithine (100 µg/mL) for 20 min, washed with PBS and coated with laminin (1 µg/mL) for one h. New born pups (WISTAR rats) were sacrificed and the hippocampi were extracted. Tryptic digest was followed by mechanical dissection using a pipette to obtain a homogenous solution. The solution was filtered through a cell strainer (40 µm pore size) the cells were seeded at 55k/well. Laminin was removed before seeding. 2 h after seeding, the medium was removed and fresh phenol-red free neurobasal medium (NB) was added containing antibiotics (pen/strep), Glutamax and B27.
Hippocampal neurons were infected with adeno-associated viruses (AVVs) after seven to ten days in culture (see Appendix for viral titers). 0.4 µL of the respective AAV and 10 µL phenol-red free NB medium was added per well. After 10–13 days, the expressed protein constructs were labelled with the respective FRET donor substrate (500 nM) and Halo-SiR (200 nM) for 14 h. Fluorescent substrate were diluted in phenol-red free NB medium as 50x stock and 10 µL was added per well (at least 1:1000 final dilution from DMSO stock). After labelling, additional 500 µL phenol-red free NB medium was added per well.
For drug treatment, the compounds were diluted in phenol-red free NB medium as 10x stock and 100 µL was added per well (at least 1:1000 final dilution from DMSO stock). For H_2O_2 treatment, cells were incubated with 1 mM H_2O_2 in HBSS.

6.3.3 General remarks for confocal microscopy

Confocal microscopy was performed on a Leica SP8 equipped with a white line laser (WLL) and hybrid photodetector for single molecule detection (HyD SMD detector). Live cell imaging was performed at 37 °C with a 5% CO_2 atmosphere in a humidified chamber. The following settings were used for image acquisition: 20x/0.75 air objective, 40x/1.1 water objective or 63x/1.2 water objective; image size:

581.82 x 581.82 µm; scan speed 600 MHz; pinhole 1 airy unit; four line averages and 16 bit depth. Z-stacks were performed with 2 µm step size.

The following settings were used for the different fluorescent channels: DAPI (excitation: 405 nm, detection: 435–480 nm), Mitotracker green/Cal520 (excitation: 488 nm, detection: 500–550 nm), TMR (excitation: 540 nm, detection: 560–610 nm), FRET (excitation: 540 nm, detection: 650–710 nm), CPY (excitation: 595 nm, detection: 605–650 nm) and SiR/Alexa647 (excitation: 630 nm, detection: 650–710 nm), WLL pulse frequency: 80 MHz.

6.3.4 General remarks for FLIM

Fluorescent lifetime imaging was performed on a Leica SP8 (as described before) equipped with a FALCON FLIM setup. Live cell imaging was performed at 37 °C with a 5% CO_2 atmosphere in a humidified chamber. The following settings were used for image acquisition with NAD(P)$^+$ biosensor: 40x/1.1 water objective, image size: 290.62 x 290.62 µm, scan speed 200 MHz, pinhole 5 airy unit, line repetition (10–16), one frame repetition, a minimum of 1000 photons/pixel were collected, max 1 photon/laser pulse, 16 bit depth. The following settings were used for the fluorescent channel: TMR (excitation: 540 nm, detection: 560–610 nm), WLL pulse frequency: 40 MHz. The following settings were changed for image acquisition with Cal520: image size: 154.77 x 154.77 µm, scan speed 600 MHz, one line repetition, one frame repetition, temporal resolution: 0.437 s.

FLIM data were analyzed with the LAS X Software (Leica). An intensity threshold was used to remove the background (200 photons). A 3rd-order exponential reconvolution was used to fit the fluorescent decays of ROIs (**Equation 10**). The amplitude weighted average lifetimes $\langle\tau\rangle$ were calculated with **Equation 11**. The goodness of fit was determined by the reduced chi-square ($\chi 2 < 1.2$) using a non-linear least-squares analysis.

$$y(t) = \left\{IRF(t + Shift_{IRF}) + Bkgr_{IRF}\right\} \otimes \left\{\sum_{i=0}^{n-1} A[i]\, e^{\left(-\frac{t}{\tau[i]}\right)} + Bkgr\right\} \qquad (\mathbf{10})$$

$$\langle\tau\rangle = \frac{\sum_{i=0}^{n-1} A[i]\, \tau[i]}{A_{Sum}} \qquad (\mathbf{11})$$

6.3.5 General remarks for image analysis

Microscopy images were analyzed with FIJI.[199] If applicable, z-stacks were transformed into maximum projections. Image segmentation was performed using Otsu's threshold clustering algorithm.[200] This binary mask was used to obtain the mean intensity values of the ROIs in each channel. Ratios of FRET/TMR channel were calculated with Microsoft Excel.

6.3.6 General remarks for FACS measurements

Cells were washed once with PBS (500 µL) and incubated with trypsin (25 µL) for 5 min 37 °C. Cells were resuspended in PBS containing 2% FBS (325 µL), filtered through a cell strainer cap and subjected to FACS analysis. Data were recorded on a FACS Melody using the following settings: GFP (ex. 488 nm, em. 530±30 nm), TMR (ex. 561 nm, em. 575±20 nm), FRET (ex. 561 nm, em. 697±58 nm) and SiR (ex. 633 nm, em. 697±58 nm). For each measurement, 10'000 events were recorded. Data were analyzed with FlowJo v10 software (BD Bioscience).

Gating strategy was the following Cells were gated for live cells and singlets to exclude cell debris and cell doublets. Cells with a mEGFP construct were first gated for GFP positive cells and then for a subset of TMR/GFP or SiR/GFP, respectively. Ratios of either TMR/GFP or SiR/GFP were obtained by the derived function in FlowJo v10. Cells with the NAD(P)$^+$-Snifits were gated for a subset of FRET/TMR. Ratios of FRET/TMR were obtained by the derived function in FlowJo v10.

6.3.7 Labelling conditions in U2OS cells

U2OS cells expressing either a cytosolic mEGFP-SNAP or mEGFP-Halo were labelled with different concentrations of the FRET donor substrates or Halo-SiR, respectively for 14 h. The same experiment was performed with the addition of 10 µM verapamil to the labelling substrates. The cells were washed with HBSS (3x) and then analzsed by FACS.

For the time course experiment, U2OS cells expressing a cytosolic mEGFP-SNAP construct were labelled with either CP-TMR-C6-SMX, CP-MAP555-C6-SMX or CP-MaP555-PPT (500 nM) at the different time points. The cells were washed with HBSS (3x) and then analyzed by FACS. Data was fitted with **Equation 12**.

$$y=y_0+(\text{plateau}-y_0)\cdot(1-e^{(-kx)}) \qquad (\mathbf{12})$$

6.3.8 Titration of NAD(P)-Snifits with QM385

U2OS T-Rex™ Flp-In™ cells with an inducible NAD(P)-Snifit were expressed and labelled as described above. After labelling, the cells were washed with HBSS (3x) and then incubated with different concentrations of QM385 in HBSS containing 4.5 g/L glucose, 4 mM L-glutamine, 1 mM sodium pyruvate for 1 h. The cells were analyzed by FACS. IC_{50} values were calculated with **Equation 6**.

6.3.9 LC-MS/MS measurements of NAD^+

U2OS T-Rex™ Flp-In™ cells with an inducible NAD-Sifit in cytosol, nucleus or mitochondria were seeded in a 6 well plate at $1x10^5$ cells/mL (volume: 3 mL/well). Expression and labelling of the sensor were performed as described above. Empty U2OS T-Rex™ Flp-In™ cells were used as control. The cells were washed once with PBS (1 mL), detached with trypsin (500 µL) and centrifuged for 5 min at 5000 *g*. The cell pellet was resuspended in 10 µL PBS and 10 µL IS. ^{13}C labelled yeast extract was used as IS. 80 µL of hot buffered ethanol was added and the resuspended mixture was shaken for 3 min at 1000 *g* (80 °C). The mixture was vortexed for 2 min in and then centrifuged (10 min, 10,000 *g*, 4 °C). The supernatant was diluted 1:100 in 2 mM NH_4OAc (pH 9) and subjected to LC-MS/MS measurement (final IS dilution: 1:1000).

The protein pellet was dissolved in 50 µL PBS and then diluted 1:50 in PBS. The concentration was determined by a Bradford assay using a BSA solution (20 mg/mL) for calibration: 0, 20, 30, 40, 50, 60, 80 and 100 µg/mL.
For the LC-MS/MS calibration curve, a stock solution of NAD and NADP in 2 mM NH_4OAc (pH 9) was prepared at 10 mg/mL and subsequently diluted to get a calibration curve at 250, 175, 100, 50, 25, 10, 5, 2.5 and 1 ng/mL (IS 1:1000).

LC-MS/MS was performed with a Shimadzu Nexera UPLC system coupled to Sciex QTrap 6500+ triple-quadrupole mass spectrometer. The samples (prepared as described above) were injected onto a Waters Atlantis Premier BEH C18 AX column (1.7 µm, 2.1 x 50 mm) and the column temperature was set to 50 °C (injection volume: 7.5 µL). The analytes were eluted using a 0.650 mL/min flow of 10 mM NH_4OAc (pH 7.45) and MeOH. After sample injection, a 1.5 min isocratic flow of 5% MeOH in NH_4OAc was followed by 5 to 30% linear gradient. After 2 min, the column was washed with 98% MeOH and re-equilibrated. The total analysis time per sample was 4.5 min and NAD^+ and its internal standard has a retention time of 0.78 min.
NAD^+ was ionized in the negative mode using the following settings: curtain gas: 40 psi, collision ionization voltage: –4,500 V, temperature: 400 °C, heater gas: 65 psi and nebulizer gas: 80 psi. MS/MS analysis was performed *via* multiple reaction monitoring (MRM) using the following transitions (Table 7). Data analysis was performed with MultiQuant 3.0.2 (Sciex). The peak areas were corrected by the internal standard and a linear or quadratic fit (1/x weighting) was applied. Reproducibility was tested by quadruple injection of a NAD^+ solution (10 ng/mL). Coefficient of variation was < 5%.

Table 7: MRM parameters for NAD^+ quantification

Analyte	MRM	Dwell time (ms)	DP (V)	EP (V)	CE (V)	CXP (V)
NAD^+	661.9→540.0	75.0	–35.0	–10.0	–20.0	–35.0
	661.9→79.0	25.0	–35.0	–10.0	–130.0	–9.0

6.3.10 Multiplexing of NAD-Snifit and Cal520 in primary neurons

Expression and labelling of the NAD^+-Snift in cytosol, nucleus and mitochondria was performed as described above. Cells were incubated with 1 µM Cal520 for 1 h. Basel neuronal activity was recorded before NAD^+ levels were measured. For stimulation, neurons were incubated with 10 µM glutamate and 2.5 µM glycine for 1 h. To inhibit neuronal activity, neurons were incubated with 25 µM AP5 and 10 µM CNQX for 1 h. Neuronal activity after treatment was recorded before NAD^+ levels were measured with FLIM.

6.3.11 SLC25A51 transfection screen

U2OS T-Rex™ Flp-In™ cells with an inducible NAD-Snifit in mitochondria were plated at $5*10^4$ cells/mL in a glass-bottom 96 well plate. Sensor expression was induced by the addition of doxycycline (200 ng/mL). After 24 h, the cells were transfected with SLC25A51 using Fugene 6 with the following conditions: 100 ng DNA/well, Ratio Fugene (µL) : DNA (µg) = 1.5:1. After 24 h, the cells were labelled with Halo-CPY (200 nM) for 2 h.

The cells were washed twice with PBS and fixed with 4% PFA for 10 min at room temperature. Next, the cells were incubated with 0.5% TX-100 in PBS for 10 min, washed with PBS-T (PBS + 0.1% Tween™ 20) and then incubated with 3% BSA in PBS-T for 2 h at room temperature. Labelling with the primary antibody (1.0 µg/mL) in 3% BSA in PBS-T was performed for 16 h at 4 °C. The cells were washed twice with PBS-T and then labelled with the secondary antibody (1:2000) in 3% BSA in PBS-T for 1 h at room temperature. The cells were washed twice with PBS and labelled with Hoechst (1 µg/mL) for 5 min at room temperature. The cells were washed twice with PBS before confocal imaging.

6.3.12 NAD^+ measurements: SLC25A51

U2OS T-Rex™ Flp-In™ cells with an inducible NAD-Snifit in mitochondria were plated at $5*10^4$ cells/mL in a 24-well plate. Sensor expression was induced by the addition of doxycycline (200 ng/mL). After 24 h, the cells were labelled with CP-TMR-C6-SMX

(500 nM) and Halo-SiR (200 nM) for 16 h. The cells were washed twice with media and then transfected with either SLC25A51, SLC25A52 or an empty pcDNA3.1 vector using Fugene 6 and the following conditions: 500 ng DNA/well, Ratio Fugene (µL) : DNA (µg) = 1.5:1. After 24 h, the cells were washed twice with PBS and subjected to FACS analysis.

6.3.13 NAD^+ measurements: Nam and Trp starvation

U2OS T-Rex™ Flp-In™ cells an inducible NAD-Snift (cytosol, nucleus or mitochondria) were cultured in normal DMEM medium before being seeded in 6 well plates using customized media: control media containing 10% dialyzed FBS, Nam free media, Trp free media and Nam/Trp free media. The cells were cultured for 72 h and proliferation and morphology was monitored by brightfield microscopy. After 72 h, the cells seeded at $5x10^4$ cells/mL in 24 well plate and sensor expression was induced by the addition of doxycycline (200 ng/mL). After 24 h, the cells were labelled with CP-MaP555-PPT (500 nM) and Halo-SiR (200 nM) for 16 h and were then analyzed by FACS.

6.4 Chemical synthesis

General remarks

All chemical reagents and anhydrous solvents for synthesis were purchased from commercial suppliers (Sigma-Aldrich, Carl Roth GmbH + Co.KG, Merck KGaA, Acros Organics, TCI Chemicals GmbH, Santa Cruz biotechnology, Thermo Fisher Scientific) and were used without further purification or distillation.

Unless stated otherwise, all reactions were performed in oven-dried glassware and anhydrous solvents were used.

Reaction progress was monitored by thin layer chromatography (TLC) on precoated TLC plates (silica gel 60G F254, Merck KGaA). Reaction spots were visualised by UV illumination (254 nm or 366 nm). Alternatively, reaction progress was monitored using a liquid chromatography-mass spectrometry (LC-MS), which was performed on a Nexerra UHPLC system equipped with a Waters ACQUITY UPLC BEH C18 column (1.7 µm 2.1 x 50 mm) connected to a Shimadzu MS2020. Solvent A: 0.1% formic acid (FA) in MilliQ-H_2O, solvent B: MeCN, flowrate: 1 mL/min, gradient: 10% B in A to 90% B in A over 6 min.

Reaction products were either purified by normal phase flash column chromatography (NP-FCC) on self-packed silica gel (60 Å, 0.04-0.063 mm, Macherey-Nagel GmbH & Co. KG) or with a Biotage Isolera Prime (Detection: 254 nm and 280 nm, flow rate: 10 mL/min), equipped with commercially available Silia Sep-cartridges (4 g to 80 g, 40–63 µm, 60 Å, SiliCycle*).*

Alternatively, preparative reverse phase high-performance liquid chromatography (RP-HPLC) was performed on a Waters Alliance e2695 equipped with a 2998 Photodiode Array Detector and an Ascentis C18 column (5 µm pore size, 20x25 cm, flow rate: 8 mL/min). Additionally, a Thermo Scientific Dionex UltiMate 3000-Series, equipped with a DAD-3000(RS) and MWD-3000(RS) Photodiode Array Detector and an Ascentis C18 column (5 µm pore size, 20x25 cm, flow rate: 8 mL/min) was used. Unless stated otherwise, Buffer A: 0.1% TFA in MQ-H_2O and Buffer B: MeCN were used. A typical gradient was 10% B in A to 90% B in A over 60 min.

NMR spectra were recorded in deuterated solvents on a BRUKER Avance III HD 400 (equipped with a CryoProbe™) instruments and calibrated to residual solvent peaks ($^{1}H/^{13}C$ in ppm): Acetone-D_6 (2.05/29.8), Chloroform-D_1 (7.26/77.00), Acetonitrile-D_3 (1.94/118.3), DMSO-D_6 (2.50/39.5), Methanol-D_4 (3.31/49.0). Multiplicities are abbreviated as follows: s = singlet, d = doublet, t = triplet, q = quartet, p = pentet, m = multiplet. Coupling constants *J* are reported in Hz and were partially obtained by Global Spectral Deconvolution (GSD) with MestReNova 14.1.0 (Metrelab Research S.L.). Spectra are reported based on appearance, not on theoretical multiplicities derived from structural information.

HRMS experiments were performed on maXis ETD II HRMS system coupled to a UPLC system operating in the positive and negative mode. The mass of detected ions is given in dependency of the ionic charge in the form of *m/z*.

Diketone (16)

To a solution of *N,N*-dimethylformamide dimethyl acetal (**15**) (1.7 mL, 12.6 mmol, 1.0 equiv.) in dry 1,4-dioxane (9 mL), methyl acetoacetate (**16**) (1.53 mL, 14.2 mmol, 1.1 equiv.) was added and stirred for 2 h at 80 °C. The reaction was quenched by the addition of water (150 mL) and saturated aqueous $NaHCO_3$ solution (50 mL) and was extracted with CH_2Cl_2 (3 x 100 mL). The combined organic phases were washed with saturated aqueous NaCl solution (100 mL), dried over Na_2SO_4 and concentrated *in vacuo*. The crude product was purified *via* NP-FCC (acetone/EtOAc, 5:95 to 10:90) to give **16** (2.05 g, 12.0 mmol, 95%) as a yellow solid.

^{1}H NMR (400 MHz, DMSO-D_6): δ [ppm] = 7.22 (s, 1H), 3.23 (s, 3H), 1.73 (s, 3H).
^{13}C NMR (100 MHz, DMSO-D_6): δ [ppm] = 193.7, 168.7, 156.5, 102.3, 51.2, 28.5.
HRMS (ESI): calc. for $C_8H_{14}NO_3^+$ $(M+H)^+$: 172.0974, found: 172.0968.
LRMS (ESI, LC-MS): $C_8H_{14}NO_3^+$ $(M+H)^+$: 173.10, found: 171.95.
t_R (LC-MS): 0.276 min.
R_f (Acetone/EtOAc = 5/95): 0.27.

Triazane (18)

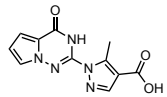

To a suspension of 2-chloropyrrolo[2,1-f][1,2,4]triazin-4(1H)-one (**17**) (1.5 g, 8.85 mmol, 1.0 equiv.) in EtOH (9 mL), hydrazine (1 M solution in EtOH, 88.5 mL, 88.5 mmol, 10.0 equiv.) was added and the reaction mixture was stirred for 72 h at 50 °C. Afterwards the crude product was filtered and washed with cold water to give the product (654.0 mg, 3.96 mmol, 45%) as a yellow solid.

The yellow solid (654.0 mg, 3.96 mmol, 1.0 equiv.) was subsequently dissolved in EtOH (9 mL) and stirred at rt. After 10 min acetic acid (2.2 mL, 38.8 mmol, 9.8 equiv.) and **16** (805.0 mg, 4.7 mmol, 1.2 equiv.) were added and stirred at 50 °C for 4 h. Afterwards the solvent was removed *in vacuo* and the crude product was purified *via* NP-FCC ($MeOH/CH_2Cl_2$ 0:100 to $MeOH/CH_2Cl_2$ 3:97). For subsequent ester hydrolysis, the product (451.0 mg, 1.65 mmol, 1.0 equiv.) and NaOH (193.0 mg in 10 mL water, 3.0 equiv.) in THF (16 mL) were stirred at r.t. for 3 h. The volatiles were removed *in vacuo* and the reaction mixture was acidified with conc. aq. HCl (pH = 1). The precipitate was filtered off, washed with cold water to give **18** (322.0 mg, 1.24 mmol, 31% over two steps) as a colorless solid.

^{1}H NMR (400 MHz, DMSO-D_6): δ [ppm] = 8.10 (s, 1H), 7.68 (dd, J = 2.7, 1.6 Hz, 1H), 7.01 (dd, J = 4.3, 1.6 Hz, 1H), 6.63 (dd, J = 4.3, 2.7 Hz, 1H), 2.73 (s, 3H).

^{13}C NMR (100 MHz, DMSO-D_6): δ [ppm] = ^{13}C NMR (101 MHz, DMSO) δ 163.9, 154.2, 145.8, 143.0, 141.1, 122.2, 118.2, 114.3, 111.1, 108.4, 11.4.

HRMS (ESI): calc. for $C_{11}H_{10}N_5O_3^+$ $(M+H)^+$: 260.0784, found: 260.0778.

LRMS (ESI, LC-MS): $C_{11}H_{10}N_5O_3^+$ $(M+H)^+$: 260.08, found: 259.95.

t_R (LC-MS): 2.266 min.

PPT (19)

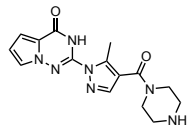

To a solution of **18** (70.0 mg, 270.0 µmol, 1.0 equiv.) in dry DMF (4 mL), PyBOP (155.0 mg, 297.0 µmol, 1.1 equiv.) and piperazine (233 mg, 2.7 mmol, 10.0 equiv.) were added and stirred at 50 °C for 4 h. The reaction was quenched by addition of acetic acid (200 µL) and the crude product was purified *via* RP-HPLC (detection at 254 nm) to give **19** (53.0 mg, 162.0 µmol, 60%) as a colorless solid.

^{1}H NMR (400 MHz, DMSO-D_6): δ [ppm] = 8.01 (s, 1H), 7.66 (dd, J = 2.7, 1.6 Hz, 1H), 7.01 (dd, J = 4.3, 1.7 Hz, 1H), 6.63 (dd, J = 4.3, 2.7 Hz, 1H), 3.73 (d, J = 5.9 Hz, 4H), 3.19 (t, J = 5.3 Hz, 4H), 2.56 (s, 3H).
^{13}C NMR (100 MHz, DMSO-D_6): δ [ppm] = 162.9, 154.1, 142.5, 140.7, 122.1, 118.1, 116.3, 111.0, 108.3, 42.7.
HRMS (ESI): calc. for $C_{15}H_{18}N_7O_2^+$ $(M+H)^+$: 328.1522, found: 328.1516.
LRMS (ESI, LC-MS): $C_{15}H_{18}N_7O_2^+$ $(M+H)^+$: 328.15, found: 328.00.
t_R (LC-MS): 0.277 min.

C6-SMX (23)

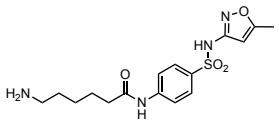

To a solution of Fmoc-6-aminocaproic acid (**20**) (300.0 mg, 849.0 µmol, 1.0 equiv.) in DMF (6.0 mL), EDC·HCl (325.0 mg, 1.7 mmol, 2.0 equiv.) and HOBt (229 mg,1.7 mmol, 2.0 equiv.) were added at r.t.. After full dissolution of the reagents, sulfamethoxazole (**21**) (430.0 mg, 1.7 mmol, 2.0 equiv.) and DIPEA (281 µL, 1.7 mmol, 2.0 equiv.) were added and stirred at r.t. for 12 h. The crude product was purified *via* RP-HPLC (detection at 254 nm). For subsequent deprotection the product (120.0 mg, 204.0 µmol, 1.0 equiv.) was dissolved in piperidine (50 µL, 5 vol%) and DMF (5.0 mL) and stirred at r.t. for 15 min. The crude product was purified *via* RP-HPLC (detection at 254 nm) to give **23** (40.0 mg, 109.0 µmol, 13% over two steps) as a colorless solid.

^{1}H NMR (400 MHz, Methanol-D_4): δ [ppm] = 7.87-7.80 (m, 2H), 7.78-7.74 (m, 2H), 6.14 (q, J = 0.8 Hz, 1H), 2.94 (dd, J = 8.5, 6.8 Hz, 2H), 2.45 (t, J = 7.3 Hz, 2H), 2.32 (d, J = 0.9 Hz, 3H), 1.72 (ddt, J = 17.8, 15.3, 7.5 Hz, 4H), 1.53-1.41 (m, 2H).
^{13}C NMR (100 MHz, Methanol-D_4): δ [ppm] = 165.1, 162.6, 149.73, 135.2, 125.7, 119.9, 110.9, 86.9, 31.0, 28.0, 18.9, 17.5, 16.3, 2.8.
HRMS (ESI): calc. for $C_{16}H_{23}N_4O_4S^+$ $(M+H)^+$: 367.1440, found: 367.1435.
LRMS (ESI, LC-MS): $C_{16}H_{23}N_4O_4S^+$ $(M+H)^+$: 367.14, found: 367.00.
t_R (LC-MS): 1.169 min.
The spectroscopic data were in agreement with previously reported synthesis.[84]

Bisallyl-TMR (25)

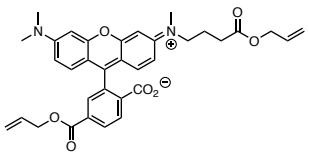

To a solution of 6'-carboxytetramethylrhodamine-C3-COOH (**24**) (307.0 mg, 611.0 µmol, 1.0 equiv.) in DMF (20 mL), triethylamine (682 µL, 4.9 mmol, 8.0 equiv.) and K_2CO_3 (338.0 mg, 2.4 mmol, 4.0 equiv.) were added at r.t.. The reaction mixture was cooled to 0 °C and allyl bromide (317 µL, 3.7 mmol, 6.0 equiv.) was added dropwise. After 12 hours, the reaction was quenched by the addition of acidic acid (500 µL). The crude product was purified *via* NP-FCC (MeOH/CH_2Cl_2 0:100 to 15:85) to yield **25** (143.0 mg, 245.0 µmol, 40%) as a pink powder.

^{1}H NMR (400 MHz, Chloroform-D_1): δ [ppm] = 8.43 (d, J = 8.2 Hz, 1H), 8.33 (dd, J = 8.2, 1.7 Hz, 1H), 7.88 (d, J = 1.6 Hz, 1H), 7.13 (dd, J = 9.5, 1.5 Hz, 2H), 6.89 (dd, J = 9.5, 2.4 Hz, 1H), 6.84–6.75 (m, 2H), 6.73 (d, J = 2.5 Hz, 1H), 6.08–5.98 (m, 1H), 5.98–5.85 (m, 1H), 5.41 (dq, J = 17.2, 1.5 Hz, 1H), 5.33 (dq, J = 7.2, 1.3 Hz, 1H), 5.29 (p, J = 1.3 Hz, 1H), 5.24 (dq, J = 10.4, 1.3 Hz, 1H), 4.84 (dt, J = 5.9, 1.4 Hz, 2H), 4.60 (dt, J = 5.9, 1.4 Hz, 2H), 3.64–3.56 (m, 2H), 3.24 (s, 6H), 3.21 (s, 3H), 2.45 (t, J = 6.6 Hz, 2H,), 1.99 (p, J = 7.0 Hz, 2H).

^{13}C NMR (100 MHz, Chloroform-D_1): δ [ppm] = 172.5166.1, 165.0, 159.1, 157.9, 157.8, 157.3, 156.7, 137.4, 133.7, 132.9, 132.0, 131.8, 131.6, 131.2, 130.3, 119.3, 118.9, 117.8, 114.9, 114.3, 114.2, 114.1, 96.7, 96.7, 66.5, 65.7, 52.5, 41.0, 39.4, 30.7, 22.1.

HRMS (ESI): calc. for $C_{34}H_{35}N_2O_7^+$ $(M+H)^+$: 583.2366, found: 583.2434.

LRMS (ESI, LC-MS): calc. for $C_{34}H_{35}N_2O_7^+$ $(M+H)^+$: 583.24, found: 583.20.

t_R **(LC-MS)**: 3.079 min.

R_f (MeOH/DCM = 5/95): 0.2.

Bisallyl-MaP1 (26)

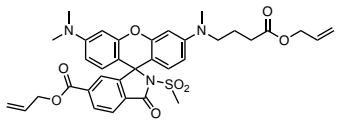

To a solution of **25** (71.0 mg, 122.0 µmol, 1.0 equiv.) in CH_2Cl_2 (10 mL), EDC·HCl (187.0 mg, 975.0 µmol, 8.0 equiv.), DMAP (119.0 mg, 975.0 µmol, 8.0 equiv.) and methanesulfoneamide (92.7 mg, 975.0 µmol, 20.0 equiv.) were added and stirred at 50 °C. After 12 h the reaction was quenched by the addition of acetic acid (200 µL). The crude product was purified *via* RP-HPLC (detection at 540 nm) to give **26** (67.0 mg, 102.0 µmol, 84%) as a pink powder.

^{1}H NMR (400 MHz, Chloroform-D_1): δ [ppm] = 8.29 (dd, J = 8.1, 1.5 Hz, 1H), 8.14 (d, J = 8.1 Hz, 1H), 7.83 (d, J = 1.5 Hz, 1H), 6.97–6.91 (m, 2H), 6.76–6.63 (m, 4H), 6.04–5.86 (m, 2H), 5.43–5.19 (m, 4H), 4.80 (dt, J = 5.9, 1.4 Hz, 2H), 4.59 (dt, J = 5.8, 1.4 Hz, 2H), 3.54-3.45 (m, 2H), 3.14 (s, 6H), 3.10 (s, 3H,), 2.96 (s, 3H), 2.42 (t, J = 6.9 Hz, 2H), 1.96 (p, J = 7.0 Hz, 2H).

^{13}C NMR (100 MHz, Chloroform-D_1): δ [ppm] = 172.5, 166.1, 165.0, 159.8, 157.9, 157.8, 157.3, 156.7, 152.6, 137.4, 133.7, 132.9, 132.0, 131.8, 131.6, 131.2, 130.3, 119.3, 118.9, 117.8, 114.9, 114.3, 114.2, 114.1, 96.7, 96.7, 66.5, 65.7, 52.5, 41.0, 39.4, 30.7, 22.1.

HRMS (ESI): calc. for $C_{35}H_{38}N_3O_8S^+$ $(M+H)^+$: 660.2380, found: 660.2374.

LRMS (ESI, LC-MS): $C_{35}H_{38}N_3O_8S^+$ $(M+H)^+$: 660.24, found: 660.15.

t_R (LC-MS): 3.120 min.

Bisallyl-MaP555 (27)

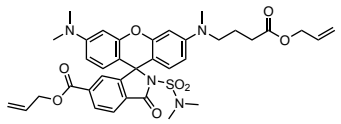

To a solution of **25** (71.0 mg, 122.0 µmol, 1.0 equiv.) in CH_2Cl_2 (10 mL), EDC·HCl (187.0 mg, 975.0 µmol, 8.0 equiv.), DMAP (119.0 mg, 975.0 µmol, 8.0 equiv.) and *N,N*-dimethylsulfamide (303.0 mg, 2.44 mmol, 20.0 equiv.) were added and stirred at 50 °C. After 12 h the reaction was quenched by the addition of acetic acid (200 µL). The crude product was purified *via* RP-HPLC (detection at 540 nm) to give **27** (46.0 mg, 66.8 µmol, 55%) as a pink powder.

^{1}H NMR (400 MHz, Chloroform-D_1): δ [ppm] = 8.23 (dd, J = 8.0, 1.4 Hz, 1H), 8.02 (d, J = 8.0 Hz, 1H), 7.75 (s, 1H), 6.78–6.67 (m, 3H), 6.65 (d, J = 2.5 Hz, 1H), 6.59–6.44 (m, 3H), 6.02–5.85 (m, 2H), 5.39–5.20 (m, 4H), 4.76 (dt, J = 5.9, 1.4 Hz, 2H), 4.58 (dt, J = 5.8, 1.4 Hz, 2H), 3.41 (t, J = 7.6 Hz, 2H), 3.04 (s, 6H), 3.00 (s, 3H), 2.72 (s, 6H), 2.39 (t, J = 7.0 Hz, 2H), 1.93 (p, J = 7.1 Hz, 2H).
^{13}C NMR (100 MHz, Chloroform-D_1): δ [ppm] = 172.8, 166.3, 165.1, 154.1, 154.0, 152.7, 151.2, 136.5, 135.8, 132.2, 131.8, 130.5, 129.4, 128.0, 127.4, 119.3, 118.7, 117.6, 116.3, 114.7, 114.2, 113.8, 110.0, 99.0, 98.9, 66.5, 65.5, 52.2, 41.3, 39.0, 38.04, 31.3, 22.2.
HRMS (ESI): calc. for $C_{36}H_{41}N_4O_8S^+$ $(M+H)^+$: 689.2645, found: 689.2640.
LRMS (ESI, LC-MS): $C_{36}H_{41}N_4O_8S^+$ $(M+H)^+$: 689.26, found: 689.15.
t_R (LC-MS): 3.325 min.

MaP1 (28)

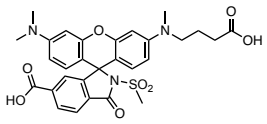

To a solution of **27** (67.0 mg, 101.0 µmol, 1.0 equiv.) and 1,3-dimethylbarbituric acid (95.0 mg, 608.0 µmol, 6.0 equiv.) in MeOH (10 mL) and CH_2Cl_2 (2 mL), tetra-kis(triphenylphosphine)-palladium(0) (117.0 mg, 101.0 µmol, 1.0 equiv.) was added and stirred at r.t. for 12 h. The reaction was quenched by the addition of acetic acid (200 µL) and the crude product was purified *via* RP-HPLC (detection at 540 nm) to give **28** (47.0 mg, 81.1 µmol, 80%) as a pink powder.

^{1}H NMR (400 MHz, Methanol-D_4): δ [ppm] = 8.33 (dd, J = 8.1, 1.6 Hz, 1H), 8.06 (d, J = 8.1 Hz, 1H), 7.92 (d, J = 1.5 Hz, 1H), 7.01 (dd, J = 9.3, 3.9 Hz, 2H), 6.94–6.83 (m, 3H), 6.80 (d, J = 2.5 Hz, 1H), 3.66–3.54 (m, 2H), 3.19 (s, 6H), 3.17 (s, 3H), 2.92 (s, 3H), 2.38 (t, J = 6.9 Hz, 2H), 1.98-1.86 (m, 2H).
^{13}C NMR (100 MHz, Methanol-D_4): δ [ppm] = 176.6, 167.9, 167.7, 157.6, 157.5, 157.1, 156.4, 136.9, 136.5, 132.2, 131.2, 131.1, 130.8, 128.6, 113.9, 113.8, 112.6, 112.4, 104.6, 98.5, 98.4, 53.1, 41.4, 40.9, 39.3, 31.5, 23.2.
HRMS (ESI): calc. for $C_{29}H_{30}N_3O_8S^+$ $(M+H)^+$: 580.1754, found: 580.1748.
LRMS (ESI, LC-MS): $C_{29}H_{30}N_3O_8S^+$ $(M+H)^+$: 580.18, found: 580.10.
t_R (LC-MS): 2.901 min.

MaP555 (29)

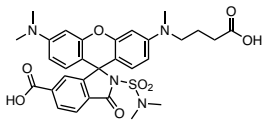

To a solution of **27** (74.0 mg, 107.0 µmol, 1.0 equiv.) and 1,3-dimethylbarbituric acid (101.0 mg, 644 µMol, 6.0 equiv.) in MeOH (10 mL) and CH_2Cl_2 (2 mL), tetra-kis(triphenylphosphine)-palladium(0) (124.0 mg, 107.0 µmol, 1.0 equiv.) was added and stirred at r.t. for 12 h. The reaction was quenched by the addition of acetic acid (200 µL) and the crude product was purified *via* RP-HPLC (detection at 540 nm) to give **29** (36.0 mg, 59.1 µmol, 55%) as a pink powder.

^{1}H NMR (400 MHz, Acetone-D_6): δ [ppm] = 8.24 (s, 1H), 8.05 (s, 1H), 7.64 (s, 1H), 6.90–6.15 (m, J = 64.1 Hz, 6H), 3.44 (s, 3H), 2.99 (s, 9H), 2.71 (s, 6H), 2.39 (t, J = 7.2 Hz, 2H).

^{13}C NMR (100 MHz, Acetone-D_6): δ [ppm] = 174.4, 166.8, 166.3, 159.2, 158.7, 158.4, 153.3, 152.3, 149.8, 136.9, 130.7, 129.2, 127.0, 124.9, 109.6, 109.1, 108.9, 101.0, 99.4, 98.8, 88.6, 52.3, 40.4, 38.5, 38.2, 31.1, 22.7.

HRMS (ESI): calc. for $C_{30}H_{33}N_4O_8S^+$ $(M+H)^+$: 609.2019, found: 609.2014.

LRMS (ESI, LC-MS): $C_{30}H_{33}N_4O_8S^+$ $(M+H)^+$: 609.20, found: 609.15

t_R (LC-MS): 2.146 min.

MaP1-C6-SMX (30)

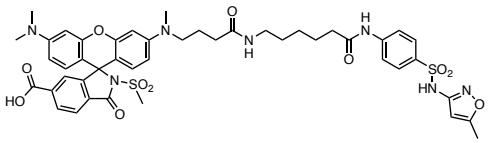

A solution of **28** (23 mg, 39.6 µmol, 1.0 equiv.), TSTU (13 mg, 43.6 µmol, 1.1 equiv.) and DIPEA (52 µL, 317 µmol, 8.0 equiv.) in DMSO (5 mL) was stirred at 35 °C for 45 min. After the presence of the active ester was confirmed by LC-MS, **23** (17 mg, 47.5 µmol, 1.2 equiv.) was added and the reaction mixture was stirred for 6 h at 35 °C. The reaction was quenched by addition of acidic acid (200 µL) and the crude product was purified *via* RP-HPLC (detection at 540 nm) to give **30** (9.0 mg, 9.7 µmol, 25%) as a pink powder.

^{1}H NMR (400 MHz, DMSO-D_6): δ [ppm] = 11.30 (s, 1H), 10.29 (s, 1H), 8.16-8.03 (m, 2H), 7.80 (t, J = 5.5 Hz, 1H), 7.76 (m, 4H), 7.42 (s, 1H), 6.62 (t, J = 8.6 Hz, 2H), 6.44 (d, J = 8.6 Hz, 4H), 6.11 (d, J = 1.2 Hz, 1H), 3.29 (t, J = 7.4 Hz, 2H,), 3.03 (t, J = 6.5 Hz, 2H), 3.00 (s, 3H), 2.94 (s, 6H), 2.89 (s, 3H), 2.32 (t, J = 7.4 Hz, 2H), 2.28 (d, J = 0.8 Hz, 3H), 2.14-2.05 (m, 2H), 1.72 (p, J = 7.2 Hz, 2H), 1.56 (p, J = 7.4 Hz, 2H), 1.39 (dt, J = 6.4, 5.8 Hz, 2H), 1.26 (tq, J = 10.2, 4.3, 3.4 Hz, 2H).
^{13}C NMR (100 MHz, DMSO-D_6): δ [ppm] = 172.0, 171.5, 170.3, 166.0, 165.7, 157.7, 157.6, 152.2, 143.2, 133.6, 130.0, 127.3, 124.9, 124.3, 118.7, 108.1, 98.3, 96.8, 95.4, 51.3, 41.9, 39.9, 38.4, 37.9, 36.4, 32.3, 29.0, 26.1, 24.6, 22.3,12.1.
HRMS (ESI): calc. for $C_{45}H_{50}N_7O_{11}S_2^+$ $(M+H)^+$: 928.3010, found: 928.3004.
LRMS (ESI, LC-MS): $C_{45}H_{50}N_7O_{11}S_2^+$ $(M+H)^+$: 928.30, found: 928.30.
t_R (LC-MS): 2.970 min.

MaP555-C6-SMX (31)

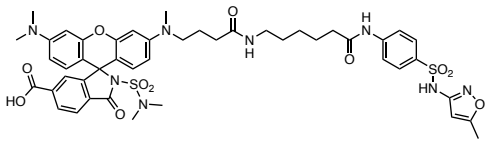

A solution of **29** (18 mg, 29.5 µmol, 1.0 equiv.), TSTU (9.7 mg, 32.5 µmol, 1.1 equiv.) and DIPEA (39 µL, 157.5 µmol, 8 equiv.) in DMSO (5 mL) was stirred at 35 °C for 45 min. After the presence of the active ester was confirmed by LC-MS, **23** (13 mg, 35.4 µmol, 1.2 equiv.) was added and the reaction mixture was stirred for 6 h at 35 °C. The reaction was quenched by addition of acidic acid (200 µL) and the crude product was purified *via* RP-HPLC (detection at 540 nm) to give **31** (8.0 mg, 8.4 µmol, 26%) as a pink powder.

^{1}H NMR (400 MHz, DMSO-D_6): δ [ppm] = 11.30 (s, 1H), 10.28 (s, 1H), 8.11 (d, J = 8.0 Hz, 1H), 8.02 (d, J = 8.1 Hz, 1H), 7.76 (s, 4H), 7.39 (s, 1H), 6.53 (t, J = 9.2 Hz, 2H), 6.45–6.35 (m, 4H), 6.11 (d, J = 1.1 Hz, 1H), 3.28 (q, J = 7.7, 6.1 Hz, 2H), 3.03 (q, J = 6.6 Hz, 2H), 2.92 (s, 6H), 2.88 (s, 3H), 2.63 (s, 6H), 2.31 (t, J = 7.4 Hz, 2H), 2.28 (d, J = 0.9 Hz, 3H), 2.14–2.05 (m, 2H), 1.71 (h, J = 7.2 Hz, 2H), 1.56 (p, J = 7.4 Hz, 2H), 1.40 (p, J = 7.1 Hz, 2H), 1.27 (tt, J = 10.6, 6.4 Hz, 2H).
^{13}C NMR (100 MHz, DMSO-D_6): δ [ppm] = 172.0, 171.5, 170.3, 166.0, 165.6, 158.1, 157.6, 153.7, 152.6, 152.5, 151.1, 150.0, 143.6, 136.7, 132.8, 130.8, 129.9 , 128.6, 128.0, 125.0, 118.7, 108.3, 107.9, 106.2, 105.7, 98.2, 97.7, 95.4, 68.2, 51.2, 39.8, 38.4, 37.9, 37.5, 36.4, 32.4, 29.0, 26.1, 24.6, 22.3, 12.1.
HRMS (ESI): calc. for $C_{46}H_{53}N_8O_{11}S_2^+$ $(M+H)^+$: 957.3275, found: 957.3270.
LRMS (ESI, LC-MS): $C_{46}H_{53}N_8O_{11}S_2^+$ $(M+H)^+$: 957.33, found: 957.20.
t_R (LC-MS): 3.464 min.

CP-MaP1-C6-SMX (32)

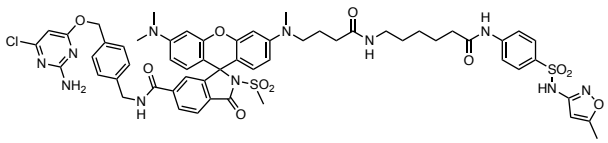

A solution of **30** (9.0 mg, 9.7 µmol, 1.0 equiv.), TSTU (3.2 mg, 10.7 µmol, 1.1 equiv.) and DIPEA (10 µL, 78.0 µmol, 8.0 equiv.) in DMSO (1.5 mL) was stirred at 35 °C for 45 min. After the presence of the active ester was confirmed by LC-MS, CP-NH_2 (**7**) (3.1 mg, 11.6 µmol, 1.2 equiv.) was added and the reaction mixture was stirred overnight at 35 °C. The reaction was quenched by addition of acidic acid (50 µL) and the crude product was purified *via* RP-HPLC (detection at 540 nm) to give **32** (2.3 mg, 1.9 µmol, 20%) as a pink powder.

^{1}H NMR (400 MHz, DMSO-D_6): δ [ppm] = 11.30 (s, 1H), 10.27 (s, 1H), 9.22 (t, J = 5.9 Hz, 1H), 8.16-8.10 (m, 1H), 8.05 (d, J = 8.1 Hz, 1H), 7.76 (s, 4H), 7.50 (s, 1H), 7.34 (d, J = 8.1 Hz, 2H), 7.24 (d, J = 7.9 Hz, 2H), 7.07 (s, 2H), 6.59 (m, 2H), 6.42 (m, 4H,), 6.11 (d, J = 1.0 Hz, 1H), 6.09 (s, 1H), 5.25 (s, 2H), 4.38 (d, J = 5.7 Hz, 2H), 3.28 (s, 2H), 3.03 (q, J = 6.7 Hz, 2H), 2.98–2.85 (m, 12H), 2.31 (t, J = 7.4 Hz, 2H), 2.28 (s, 3H), 2.13–2.05 (m, 2H), 1.71 (p, J = 7.4 Hz, 2H), 1.56 (p, J = 7.5 Hz, 2H), 1.40 (p, J = 7.1 Hz, 2H), 1.27 (ddd, J = 14.3, 8.8, 5.5 Hz, 2H).

^{13}C NMR (100 MHz, DMSO-D_6): δ [ppm] = 172.0, 171.5, 170.3, 170.3, 165.9, 164.5, 162.8, 160.0, 157.6, 143.6, 139.1, 134.8, 132.8, 128.4, 128.0, 127.5, 124.1, 121.6, 118.7, 107.7, 97.9, 95.4, 94.8, 67.2, 51.2, 42.7, 41.9, 39.7, 38.4, 37.9, 36.4, 32.3, 29.0, 26.1, 24.6, 22.3.

HRMS (ESI): calc. for $C_{57}H_{62}ClN_{11}O_{11}S_2^{2+}$ $(M+2H)^{2+}$: 587.6875, found: 587.6875.

LRMS (ESI, LC-MS): $C_{57}H_{61}ClN_{11}O_{11}S_2^{+}$ $(M+H)^{+}$: 1174.36, found: 1174.30.

t_R (LC-MS): 3.974 min.

CP-MaP555-C6-SMX (33)

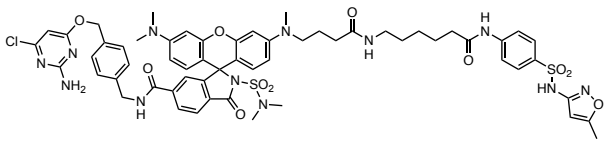

A solution of **31** (12.0 mg, 14.6 µmol, 1.0 equiv.), TSTU (5.3 mg, 17.6 µmol, 1.2 equiv.) and DIPEA (19 µL, 117.0 µmol, 8.0 equiv.) in DMSO (1.5 mL) was stirred at 35 °C for 45 min. After the presence of the active ester was confirmed by LC-MS, CP-NH_2 (**7**) (4.3 mg, 16.1 µmol, 1.1 equiv.) was added and the reaction mixture was stirred overnight at 35 °C. The reaction was quenched by addition of acidic acid (50 µL) and the crude product was purified *via* RP-HPLC (detection at 540 nm) to give **33** (11.0 mg, 9.1 µmol, 63%) as a pink powder.

^{1}H NMR (400 MHz, DMSO-D_6): δ [ppm] = 11.30 (s, 1H), 10.28 (s, 1H), 9.20 (t, J = 6.0 Hz, 1H), 8.15–8.08 (m, 1H), 8.00 (d, J = 8.0 Hz, 1H), 7.77 (s, 4H), 7.49 (s, 1H), 7.34 (d, J = 7.8 Hz, 2H), 7.24 (d, J = 7.8 Hz, 2H), 7.08 (s, 2H), 6.51 (t, J = 8.6 Hz, 2H), 6.47–6.34 (m, 4H,), 6.11 (d, J = 1.0 Hz, 1H), 6.09 (s, 1H), 5.25 (s, 2H), 4.37 (d, J = 5.7 Hz, 2H), 3.27 (t, J = 7.6 Hz, 2H), 3.03 (q, J = 6.6 Hz, 2H), 2.90 (m, 9H), 2.61 (s, 6H), 2.33 (m, 2H), 2.28 (s, 3H), 2.08 (t, J = 7.4 Hz, 2H), 1.70 (p, J = 7.5 Hz, 2H), 1.57 (p, J = 7.5 Hz, 2H), 1.40 (p, J = 7.1 Hz, 2H), 1.33-1.24 (m, 3H).

^{13}C NMR (100 MHz, DMSO-D_6): δ [ppm] = 172.0, 171.5, 170.3, 170.3, 165.7, 164.6, 162.8, 160.0, 157.6, 153.6, 152.6, 152.5, 151.1, 149.9, 143.6, 139.9, 139.1, 134.8, 132.8, 129.7, 128.6, 128.4, 128.0, 127.5, 123.7, 123.0, 118.7, 114.0, 108.2, 107.9, 106.5, 105.9, 98.2, 97.7, 95.4, 94.4, 68.3, 67.2, 51.2, 42.7, 39.8, 38.4, 37.9, 37.5, 36.4, 32.4, 29.0, 26.1, 24.6, 22.3, 12.0.

HRMS (ESI): calc. for $C_{58}H_{65}ClN_{12}O_{11}S2^{2+}$ $(M+H)^{2+}$: 602.1971, found: 602.2007.

LRMS (ESI, LC-MS): $C_{58}H_{64}ClN_{12}O_{11}S2^{+}$ $(M+H)^{+}$: 1203.39, found: 1203.25.

t_R (LC-MS): 3.914 min.

MaP1-PPT (34)

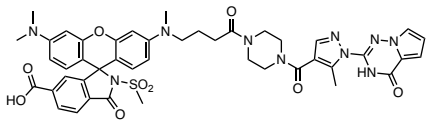

A solution of **28** (23 mg, 39.6 µmol, 1.0 equiv.), PyBOP (23 mg, 43.6 µmol, 1.1 equiv.) and DIPEA (41 µL, 317 µmol, 8.0 equiv.) in DMF (4 mL) was stirred at 35 °C for 20 min. After the presence of the active ester was confirmed by LC-MS, **19** (14 mg, 43.6 µmol, 1.2 equiv.) was added and the reaction mixture was stirred for 6 h at 35 °C. The reaction was quenched by addition of acidic acid (200 µL) and the crude product was purified *via* RP-HPLC (detection at 540 nm) to give **34** (15 mg, 17.0 µmol, 43%) as a pink powder.

^{1}H NMR (400 MHz, DMSO-D_6): δ [ppm] = 8.13 (d, J = 8.0 Hz, 1H), 8.07 (d, J = 8.0 Hz, 1H), 7.92 (d, J = 2.7 Hz, 1H), 7.69–7.58 (m, 1H), 7.42 (s, 1H), 7.04–6.96 (m, 1H), 6.72–6.57 (m, 3H), 6.55–6.31 (m, 4H), 4.01 (s, 4H), 3.58–3.44 (m, 4H), 3.37 (d, J = 12.9 Hz, 2H), 3.03–2.85 (m, 12H), 2.52 (s, 3H), 2.44–2.32 (m, 2H), 1.82–1.72 (m, 2H).

^{13}C NMR (100 MHz, DMSO-D_6): δ [ppm] = 170.5, 166.0, 165.8, 162.8, 154.2, 152.1, 141.8, 141.4, 140.7, 136.63, 130.1, 128.2, 124.3, 122.2, 118.2, 117.2, 111.0, 108.3, 98.3, 97.7, 51.2, 44.7, 41.9, 41.1, 39.3, 37.9, 29.2, 21.7, 11.5.

HRMS (ESI): calc. for $C_{44}H_{45}N_{10}O_9S^+$ $(M+H)^+$: 889.3092, found: 889.3078.

LRMS (ESI, LC-MS): $C_{44}H_{45}N_{10}O_9S^+$ $(M+H)^+$: 889.31, found: 889.25.

t_R (LC-MS): 2.286 min.

MaP555-PPT (35)

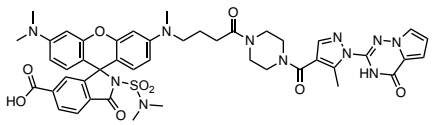

A solution of **29** (18 mg, 29.6 µmol, 1.0 equiv.), PyBOP (17 mg, 32.5 µmol, 1.1 equiv.) and DIPEA (39 µL, 237 µmol, 8.0 equiv.) in DMF (4 mL) was stirred at 35 °C for 20 min. After the presence of the active ester was confirmed by LC-MS, **19** (12 mg, 35.5 µmol, 1.2 equiv.) was added and the reaction mixture was stirred for 6 h. The reaction was quenched by addition of acidic acid (200 µL) and the crude product was purified *via* RP-HPLC (detection at 540 nm) to give **35** (12.2 mg, 13.1 µmol, 44%) as a pink powder.

^{1}H NMR (400 MHz, DMSO-D_6): δ [ppm] = 8.11 (d, J = 8.1 Hz, 1H), 8.03 (d, J = 8.0 Hz, 1H), 7.93 (s, 1H), 7.67–7.63 (m, 1H), 7.38 (s, 1H), 7.00 (dd, J = 4.3, 1.7 Hz, 1H), 6.62 (dd, J = 4.4, 2.7 Hz, 1H), 6.54 (t, J = 9.1 Hz, 2H), 6.43 (d, J = 10.9 Hz, 4H), 3.72 (s, 4H), 3.53 (m, 4H), 3.39–3.28 (m, 2H), 2.91 (s, 9H), 2.63 (s, 6H), 2.52 (s, 3H), 2.38 (q, J = 5.5, 3.9 Hz, 2H), 1.81–1.69 (m, 2H).

^{13}C NMR (100 MHz, DMSO-D_6): δ [ppm] = 170.6, 166.1, 165.7, 162.8, 154.2, 151.2, 150.1, 141.9, 141.4, 140.70, 136.7, 130.8, 129.9, 128.7, 125.0, 124.2, 122.2, 118.2, 117.2, 111.0, 108.3, 108.0, 106.3, 105.7, 98.2, 97.7, 68.2, 51.2, 44.3, 41.4, 39.3, 37.9, 37.5, 30.1, 21.1, 11.5.

HRMS (ESI): calc. for $C_{45}H_{48}N_{11}O_9S^+$ $(M+H)^+$: 918.3357, found: 918.3352.

LRMS (ESI, LC-MS): $C_{45}H_{48}N_{11}O_9S^+$ $(M+H)^+$: 918.34, found: 918.20.

***t*$_R$ (LC-MS)**: 3.258 min.

CP-MaP1-PPT (36)

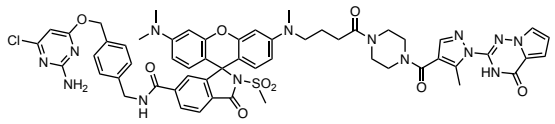

A solution of **34** (15.0 mg, 16.9 µmol, 1.0 equiv.), TSTU (6.1 mg, 20.3 µmol, 1.2 equiv.) and DIPEA (22 µL, 135.0 µmol, 8.0 equiv.) in dry DMSO (1.5 mL) was stirred at 35 °C for 45 min. After the presence of the active ester was confirmed by LC-MS, CP-NH_2 (**7**) (4.9 mg, 18.6 µmol, 1.2 equiv.) was added and the reaction mixture was stirred for 6 h at 35 °C. The reaction was quenched by addition of acidic acid (50 µL) and the crude product was purified *via* RP-HPLC (detection at 540 nm) to give **36** (14.0 mg, 12.3 µmol, 73%) as a pink powder.

^{1}H NMR (400 MHz, DMSO-D_6): δ [ppm] = 12.40 (s, 1H), 9.22 (t, J = 5.9 Hz, 1H), 8.13 (d, J = 8.1 Hz, 1H), 8.06 (d, J = 8.0 Hz, 1H), 7.93 (s, 1H), 7.67 (dd, J = 2.7, 1.7 Hz, 1H), 7.50 (s, 1H, Ar H), 7.38–7.31 (m, 3H), 7.26 (m, 2H), 7.01 (dd, J = 4.3, 1.7 Hz, 1H), 6.66–6.57 (m, 3H), 6.53–6.35 (m, 4H), 6.10 (s, 1H), 5.25 (s, 2H), 4.38 (d, J = 5.7 Hz, 2H), 3.54 (d, J = 15.9 Hz, 8H), 3.36 (d, J = 8.5 Hz, 2H), 2.98 (s, 3H), 2.93 (s, 9H), 2.53 (s, 3H), 2.39 (d, J = 6.9 Hz, 2H), 1.77 (q, J = 7.4 Hz, 2H).
^{13}C NMR (100 MHz, DMSO-D_6): δ [ppm] = 170.5, 170.3, 165.9, 164.5, 162.8, 160.0, 154.1, 141.8, 140.7, 139.1, 134.8, 134.7, 128.4, 128.3, 127.5, 127.3, 127.1, 123.9, 122.9, 122.1, 118.7, 117.16, 116.6, 110.9, 108.8, 97.4, 95.0, 65.5, 50.3, 42.6, 41.9, 39.1, 37.4, 28.4, 21.3, 7.3.
HRMS (ESI): calc. for $C_{56}H_{57}ClN_{14}O_9S^{2+}$ $(M+2H)^{2+}$: 568.3764, found: 568.1916.
LRMS (ESI, LC-MS): $C_{56}H_{56}ClN_{14}O_9S^{+}$ $(M+H)^{+}$: 1135.38, found: 1135.25.
***t_R* (LC-MS)**: 3.718.

CP-MaP555-PPT (37)

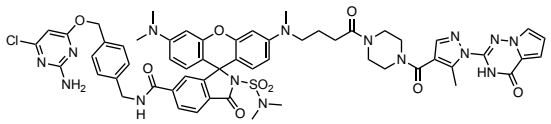

A solution of **35** (14 mg, 15.3 µmol, 1.0 equiv.), TSTU (5.5 mg, 18.3 µmol, 1.2 equiv.) and DIPEA (16 µL, 122.0 µMol, 8.0 equiv.) in dry DMSO (1.4 mL) was stirred at 35 °C for 45 min. After the presence of the active ester was confirmed by LC-MS, CP-NH_2 (**7**) (4.4 mg, 16.7 µmol, 1.1 equiv.) was added and the reaction mixture was stirred for 6 h at 35 °C. The reaction was quenched by addition of acidic acid (50 µL) and the crude product was purified *via* RP-HPLC (detection at 540 nm) to give **37** (11.1 mg, 9.5 µmol, 62%) as a pink powder.

^{1}H NMR (400 MHz, DMSO-D_6): δ [ppm] = 12.40 (s, 1H), 9.20 (t, J = 5.9 Hz, 1H), 8.11 (dd, J = 8.0, 1.5 Hz, 1H), 8.00 (d, J = 8.0 Hz, 1H), 7.93 (s, 1H), 7.66 (dd, J = 2.7, 1.6 Hz, 1H), 7.48 (s, 1H), 7.34 (d, J = 7.9 Hz, 2H), 7.24 (d, J = 7.8 Hz, 2H), 7.10 (d, J = 25.3 Hz, 2H), 7.01 (dd, J = 4.3, 1.7 Hz, 1H), 6.62 (dd, J = 4.4, 2.7 Hz, 1H), 6.52 (t, J = 8.8 Hz, 2H), 6.41 (t, J = 9.7 Hz, 4H), 6.10 (s, 1H), 5.25 (s, 2H), 4.37 (d, J = 5.7 Hz, 2H), 3.53 (m, 8H), 3.34 (d, J = 7.9 Hz, 2H), 2.91 (s, 9H), 2.62 (s, 6H), 2.53 (s, 3H), 2.38 (d, J = 6.8 Hz, 2H), 1.74 (t, J = 7.5 Hz, 2H).

^{13}C NMR (100 MHz, DMSO-D_6): δ [ppm] = 170.5, 170.3, 164.6, 162.8, 162.8, 160.0, 154.2, 152.7, 152.5, 151.1, 150.0, 141.8, 141.4, 140.7, 139.9, 139.1, 134.8, 129.7, 128.7, 128.4, 127.5, 123.7, 123.0, 122.1, 118.2, 117.2, 111.0, 108.3, 107.9, 106.4, 105.9, 98.2, 97.6, 94.4, 68.3, 67.2, 51.1, 44.7, 42.7, 41.2, 39.8, 37.8, 37.5, 29.2, 21.6, 11.5.

HRMS (ESI): calc. for $C_{57}H_{60}ClN_{15}O_9S^{2+}$ $(M+2H)^{2+}$: 582.7049, found: 582.7048.

LRMS (ESI, LC-MS): $C_{57}H_{59}ClN_{15}O_9S^{+}$ $(M+H)^{+}$: 1164.40, found: 1164.25.

***t_R* (LC-MS)**: 3.830 min.

Allyl-TMR (41)

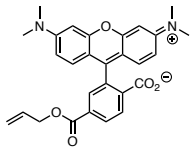

To a solution of 6'-carboxytetramethylrhodamine (**40**) (70.0 mg, 163.0 µmol, 1.0 equiv.) in DMF (10 mL), NEt_3 (181 µL, 1.3 mmol, 8.0 equiv.) and K_2CO_3 (45.0 mg, 325 µmol, 2.0 equiv.) were added at room temperature. The reaction mixture was cooled to 0 °C and allyl bromide (42 µL, 488.0 µmol, 3.0 equiv.) was added dropwise. After 12 h, the reaction was quenched by the addition of acidic acid (500 µL). The crude product was purified *via* NP-FCC ($MeOH/CH_2Cl_2$: 0:100 to 15:85) to yield **41** (34.0 mg, 72.3 µmol, 44%) as a pink powder.[113]

^{1}H NMR (400 MHz, Acetonitrile-D_3): δ [ppm] = 8.41-8.31 (m, 2H), 7.95 (dd, J = 1.6, 0.7 Hz, 1H), 7.11 (d, J = 9.5 Hz, 2H), 6.95 (dd, J = 9.5, 2.5 Hz, 2H), 6.86 (d, J = 2.5 Hz, 2H), 6.09–6.00 (m, 1H), 5.40 (dq, J = 17.3, 1.6 Hz, 1H), 5.28 (dq, J = 10.5, 1.3 Hz, 1H), 4.83 (dt, J = 5.6, 1.4 Hz, 2H), 3.25 (s, 12H).

^{13}C NMR (100 MHz, Acetonitrile-D_3): δ [ppm] = 166.4, 165.5, 158.5, 158.5, 135.5, 135.3, 134.9, 133.2, 132.7, 131.8, 131.6, 119.0, 115.4, 114.6, 97.2, 67.1, 41.3.

HRMS (ESI): calc. for $C_{28}H_{28}N_2O_5^+$ $(M+H)^+$: 471.1842, found: 471.1914.

LRMS (ESI, LC-MS): calc. for $C_{28}H_{28}N_2O_5^+$ $(M+H)^+$: 471.18, found: 471.10.

***t_R* (LC-MS)**: 2.703 min.

R_f ($MeOH/CH_2Cl_2$ = 5/95): 0.1.

The spectroscopic data were in agreement with previously reported synthesis.[113]

Benzyl 4-sulfamoylbutanoate (39)

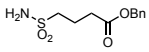

To a solution of 4-sulfamoylbutyric acid (**38**) (1.0 g, 6.0 mmol, 1.0 equiv.) and potassium iodide (298.0 mg, 1.8 mmol, 0.3 equiv.) in DMF (30 mL), DIPEA (989 µL, 6.0 mmol, 1.0 equiv.) and benzyl bromide (715 µL, 6.0 mmol, 1.0 equiv.) were added and stirred at r.t. for 12 h. Afterwards, CH_2Cl_2 (75 mL) and saturated aqueous $NaHCO_3$ solution (75 mL) were added and the organic phase was washed with saturated aqueous NaCl solution (100 mL), concentrated *in vacuo* and purified *via* NP-FCC (EtOAc/hexanes 10:90 to 90:10) to yield **39** (1.2 g, 4.7 mmol, 78%) as a colorless solid.

^{1}H NMR (400 MHz, DMSO-D_6): δ [ppm] = 7.21-7.07 (m, 5H), 4.89 (s, 2H), 2.85-2.76 (m, 2H), 2.33 (t, J = 7.4 Hz, 2H), 1.80-1.68 (m, 2H).

^{13}C NMR (100 MHz, DMSO-D_6): δ [ppm] = 172.4, 136.3, 128.7, 128.3, 128.2, 65.8, 53.7, 31.8, 19.4.

HRMS (ESI): calc. for $C_{11}H_{15}NNaO_4S^+$ $(M+Na)^+$: 280,0619, found: 280.0614.

LRMS (ESI, LC-MS): $C_{11}H_{17}N_2O_4S^+$ $(M+NH_4)^+$: 275.11, found: 275.00.

***t*$_R$ (LC-MS)**: 1.521 min.

***R*$_f$** (EtOAc/Hexane = 10/90): 0.32.

Allyl-benzyl-MaP3 (42)

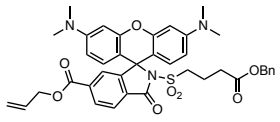

To a solution of **41** (62.0 mg, 132.0 µmol, 1.0 equiv.) in DCM (8 mL), EDC·HCl (202 mg, 1.1 mmol, 8.0 equiv.), DMAP (129.0 mg, 1.1 mmol, 8.0 equiv.) and **39** (678 mg, 2.6 mmol, 20.0 equiv.) were added and stirred at 50 °C. After 12 h the reaction was quenched by the addition of acetic acid (200 µL). The crude product was purified *via* RP-HPLC (detection at 540 nm) to give **39** (50.0 mg, 70.4 mmol, 53%) as a pink powder.

^{1}H NMR (400 MHz, Chloroform-D_1): δ [ppm] = 8.32 (dd, *J* = 8.1, 1.6 Hz, 1H,), 8.16 (d, *J* = 8.1 Hz, 1H), 7.85 (s, 1H), 7.36-7.27 (m, 5H), 7.05 (d, *J* = 9.2 Hz, 2H), 6.80 (d, *J* = 9.1 Hz, 2H), 6.73 (d, *J* = 2.3 Hz, 2H), 6.05-6.00 (m, 1H), 5.38 (d, *J* = 17.2 Hz, 1H), 5.29 (d, *J* = 10.3 Hz, 1H), 5.04 (s, 2H), 4.81 (d, *J* = 5.9 Hz, 2H), 3.24 (t, *J* = 7.4 Hz, 2H), 3.16 (s, 12H,), 2.35 (t, *J* = 7.2 Hz, 2H), 1.92 (p, *J* = 7.3 Hz, 2H).

^{13}C NMR (100 MHz, Chloroform-D_1): δ [ppm] = 172.0, 166.4, 164.8, 155.7, 153.5, 135.9, 134.9, 131.7, 131.2, 130.7, 128.7, 128.4, 128.2, 127.8, 119.4 (*C*H_2CHCH_2O), 117.3, 114.5, 113.0, 112.4, 98.4, 66.6, 66.5, 53.0, 41.4, 32.2, 18.2.

HRMS (ESI): calc. for $C_{28}H_{27}N_2O_5^+$ $(M+H)^+$: 710.2536, found: 710.2528.

LRMS (ESI, LC-MS**)**: $C_{28}H_{27}N_2O_5^+$ $(M+H)^+$: 710.25, found: 710.20.

***t*$_R$ (LC-MS)**: 3.264 min.

Benzyl-MaP3 (43)

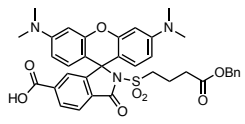

To a solution of **42** (50.0 mg, 70.3 µmol, 1.0 equiv.) and 1,3-dimethylbarbituric acid (66.0 mg, 422 µmol, 6.0 equiv.) in MeOH (10 mL) and CH_2Cl_2 (2 mL), tetra-kis(triphenylphosphine)-palladium(0) (81.0 mg, 70.3 µmol, 1.0 equiv.) was added and stirred at r.t. for 12 h. The reaction was quenched by the addition of acetic acid (200 µL) and the crude product was purified *via* RP-HPLC (detection at 540 nm) to give **43** (35.0 mg, 52.3 µmol, 74%) as a pink powder.

^{1}H NMR (400 MHz, Acetone-D_6): δ [ppm] = 8.28 (dd, J = 8.0, 1.4 Hz, 1H), 8.12 (d, J = 7.7 Hz, 1H), 7.78-7.64 (m, 2H), 7.38–7.27 (m, 5H), 6.86-6.38 (m, 6H), 5.08 (s, 2H), 3.40-3.30 (m, 2H), 3.03 (s, 12H), 2.37 (t, J = 7.3 Hz, 2H), 1.82 (tt, J = 9.1, 6.7 Hz, 2H).

^{13}C NMR (100 MHz, Acetone-D_6): δ [ppm] = 172.4, 166.7, 166.2, 154.0, 152.6, 148.6, 137.4, 134.8, 133.4, 133.3, 131.2, 129.6, 129.5, 129.3, 128.9, 125.9, 125.0, 99.2, 66.6, 54.2, 40.4, 32.4, 19.0.

HRMS (ESI): calc. for $C_{36}H_{36}N_3O_8S^+$ $(M+H)^+$: 670.2223, found: 670.2218.

LRMS (ESI, LC-MS): $C_{36}H_{36}N_3O_8S^+$ $(M+H)^+$: 670.22, found: 670.15.

***t*$_R$ (LC-MS)**: 2.871 min.

MaP3 (44)

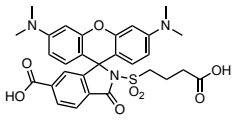

To a solution of **43** (35.0 mg, 52.3 µmol, 1.0 equiv.) in dry THF (3 mL) and dry MeOH (3 mL), under argon atmosphere Pd/C (5.5 mg, 52.3 µmol, 10 mol%) was added. The flask was filled with H_2 and the reaction mixture was stirred at r.t. for 12 h. The reaction was quenched by addition of water (200 µL), filtered and concentrated *in vacuo*. The crude product was purified *via* RP-HPLC (detection at 540 nm) to give **44** (17.0 mg, 29.3 µmol, 56%) as a pink powder.

^{1}H NMR (400 MHz, Acetone-D_6): δ [ppm] = 8.27 (dd, J = 8.0, 1.4 Hz, 1H), 8.10 (d, J = 8.0 Hz, 1H), 7.71 (s, 1H), 6.85–6.44 (m, 6H), 3.39-3.32 (m, 2H), 3.03 (s, 12H), 2.28 (t, J = 7.3 Hz, 2H), 1.84–1.71 (m, 2H).

^{13}C NMR (100 MHz, Acetone-D_6): δ [ppm] = 173.4, 166.8, 166.3, 154.5, 152.9, 137.2, 131.2, 129.6, 125.4, 117.8, 114.9, 110.0, 107.5, 99.2, 54.3, 40.4, 31.9, 18.9.

LRMS (ESI, LC-MS): $C_{29}H_{30}N_3O_8S^+$ $(M+H)^+$: 580.18, found: 580.15.

HRMS (ESI): calc. for $C_{29}H_{30}N_3O_8S^+$ $(M+H)^+$: 580,1754, found: 580.1749.

***t*$_R$ (LC-MS)**: 2.864 min.

MaP3-C6-SMX (45)

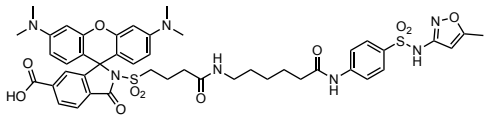

A solution of **44** (8.5 mg, 14.7 µmol, 1.0 equiv.), TSTU (4.9 mg, 16.1 µmol, 1.1 equiv.) and DIPEA (19 µL, 194.0 µmol, 8.0 equiv.) in DMSO (5 mL) was stirred at 35 °C for 45 min. After the presence of the active ester was confirmed by LC-MS, **23** (6.5 mg, 17.6 µmol, 1.2 equiv.) was added and the reaction mixture was stirred for 6 h at 35 °C. The reaction was quenched by addition of acidic acid (200 µL) and the crude product was purified *via* RP-HPLC (detection at 540 nm) to give **45** (6.8 mg, 7.3 µmol, 50%) as a pink powder.

^{1}H NMR (400 MHz, DMSO-D_6): δ [ppm] = 11.30 (s, 1H), 10.28 (s, 1H), 8.16-8.03 (m, 2H), 7.77 (m, 4H), 7.39 (s, 1H), 6.58 (d, J = 8.6 Hz, 2H), 6.40 (m, 4H), 6.11 (d, J = 1.1 Hz, 1H), 3.26–3.17 (m, 2H), 2.98 (m, 2H), 2.93 (s, 12H), 2.32 (dd, J = 8.8, 5.9 Hz, 2H), 2.28 (d, J = 0.8 Hz, 3H), 1.99 (t, J = 7.3 Hz, 2H), 1.59 (m, 4H), 1.43–1.31 (m, 2H), 1.31–1.19 (m, 2H).

^{13}C NMR (100 MHz, DMSO-D_6): δ [ppm] = ^{13}C NMR 172.0, 170.4, 170.3, 166.0, 165.8, 158.0, 157.6, 151.3, 143.6, 137.2, 132.8, 130.5, 130.0, 128.3, 128.0, 125.0, 124.4, 118.3, 108.4, 98.2, 95.4, 53.8, 39.7, 38.3, 36.4, 33.0, 28.9, 26.1, 24.6, 18.3, 12.1.

HRMS (ESI): calc. for $C_{45}H_{50}N_7O_{11}S_2^+$ $(M+H)^+$: 928.3010, found: 928.3004.

LRMS (ESI, LC-MS): $C_{45}H_{50}N_7O_{11}S_2^+$ $(M+H)^+$: 928.30, found: 928.30.

t_R (LC-MS): 3.008 min.

CP-MaP3-C6-SMX (46)

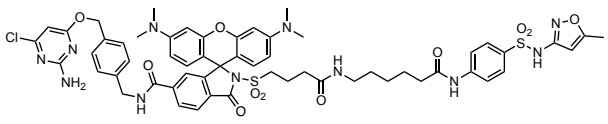

A solution of **45** (6.8 mg, 7.3 µmol, 1.0 equiv.), TSTU (2.6 mg, 8.8 µmol, 1.2 equiv.) and DIPEA (10 µL, 58.6 µmol,75.7 equiv.) in DMSO (1.5 mL) was stirred at 35 °C for 45 min. After the presence of the active ester was confirmed by LC-MS, CP-NH_2 (**7**) (2.1 mg, 8.1 µmol, 1.1 equiv.) was added and the reaction mixture was stirred overnight at 35 °C. The reaction was quenched by addition of acidic acid (50 µL) and the crude product was purified *via* RP-HPLC (detection at 540 nm) to give **46** (2.9 mg, 2.5 µmol, 34%) as a pink powder.

^{1}H NMR (400 MHz, DMSO-D_6): δ [ppm] = 11.30 (s, 1H), 10.28 (s, 1H), 9.21 (t, J = 5.9 Hz, 1H), 8.13 (d, J = 8.1 Hz, 1H), 8.04 (d, J = 8.0 Hz, 1H), 7.77 (s, 4H), 7.38–7.31 (m, 2H), 7.24 (d, J = 7.9 Hz, 2H), 7.07 (s, 2H), 6.56 (d, J = 8.5 Hz, 2H), 6.40 (s, 4H), 6.11 (d, J = 1.0 Hz, 1H), 6.10 (s, 1H), 5.25 (s, 2H), 4.38 (d, J = 5.7 Hz, 2H), 3.20 (t, J = 7.8 Hz, 2H), 2.94 (d, J = 16.2 Hz, 14H), 2.31 (t, J = 7.4 Hz, 2H), 2.28 (d, J = 0.8 Hz, 3H), 1.99 (t, J = 7.3 Hz, 2H), 1.65–1.50 (m, 4H), 1.36 (p, J = 7.0 Hz, 2H), 1.27–1.22 (m, 2H).

^{13}C NMR (100 MHz, DMSO-D_6): δ [ppm] = 172.0, 170.3, 170.3, 170.3, 165.9, 164.5, 162.8, 160.0, 157.6, 151.0, 143.6, 139.1, 135.2, 134.8, 132.8, 128.4, 128.0, 127.5, 122.7, 118.7, 106.3, 98.2, 95.4, 94.4, 66.1, 54.1, 43.1, 39.7, 37.96, 36.4, 31.1, 28.3, 26.1, 24.6, 19.0, 12.0.

HRMS (ESI): calc. for $C_{57}H_{62}ClN_{11}O_{11}S_2^{2+}$ $(M+2H)^{2+}$: 587.3676, found: 587.6875.

LRMS (ESI, LC-MS): $C_{57}H_{61}ClN_{11}O_{11}S_2^{+}$ $(M+H)^{+}$: 1174.37, found: 1174.25.

t_R (LC-MS): 3.779 min.

MaP3-PPT (47)

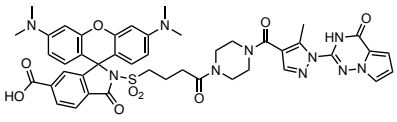

A solution of **44** (8.5 mg, 14.7 µmol, 1.0 equiv.), PYBOP (8.4 mg, 16.1 µmol, 1.1 equiv.) and DIPEA (19 µL, 117.0 µmol, 8.0 equiv.) in DMF (4 mL) was stirred at 35 °C for 20 min. After the presence of the active ester was confirmed by LC-MS, **19** (5.8 mg, 17.6 µmol, 1.2 equiv.) was added and the reaction mixture was stirred for 6 h. The reaction was quenched by addition of acidic acid (200 µL) and the crude product was purified *via* RP-HPLC (detection at 540 nm) to give **47** (5.5 mg, 6.2 µmol, 42%) as a pink powder.

^{1}H NMR (400 MHz, DMSO-D_6): δ [ppm] = 8.14 (d, J = 8.0 Hz, 1H), 8.07 (d, J = 8.0 Hz, 1H), 7.40 (s, 1H), 7.01 (dd, J = 4.3, 1.7 Hz, 1H), 6.62 (dt, J = 7.2, 3.6 Hz, 3H), 6.43 (s, 4H), 3.63–3.42 (m, 6H), 3.39–3.28 (m, 4H), 2.94 (s, 12H), 2.55 (s, 3H), 2.23 (t, J = 6.9 Hz, 2H), 1.66 (p, J = 7.1 Hz, 2H).

^{13}C NMR (100 MHz, DMSO-D_6): δ [ppm] = 169.5, 166.0, 165.8, 162.8, 154.2, 141.9, 141.4, 140.7, 137.1, 130.1, 128.4, 125.2, 122.2, 118.2, 117.1, 111.0, 108.3, 98.2, 54.0, 44.6, 39.7, 30.7, 19.0, 12.8.

HRMS (ESI): calc. for $C_{44}H_{45}N_{10}O_9S^+$ $(M+H)^+$: 889.3092, found: 889.3086.

LRMS (ESI, LC-MS): $C_{44}H_{45}N_{10}O_9S^+$ $(M+H)^+$: 889.31, found: 889.20.

t_R (LC-MS): 3.008 min.

CP-MaP3-PPT (48)

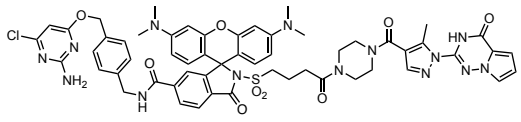

A solution of **47** (14 mg, 15.3 µmol, 1.0 equiv.), TSTU (5.5 mg, 18.3 µmol, 1.2 equiv.) and DIPEA (16 µL, 122.0 µmol, 8.0 equiv.) in dry DMSO (1.4 mL) was stirred at 35 °C for 45 min. After the presence of the active ester was confirmed by LC-MS, CP-NH_2 **(7**) (4.4 mg, 16.7 µmol, 1.1 equiv.) was added and the reaction mixture was stirred overnight at 35 °C. The reaction was quenched by addition of acidic acid (50 µL) and the crude product was purified *via* RP-HPLC (detection at 540 nm) to give **48** (11.1 mg, 9.5 µmol, 62%) as a pink powder.

^{1}H NMR (400 MHz, DMSO-D_6): δ [ppm] = 12.40 (s, 1H), 9.20 (t, J = 5.9 Hz, 1H), 8.11 (dd, J = 8.0, 1.5 Hz, 1H), 8.00 (d, J = 8.0 Hz, 1H), 7.93 (s, 1H), 7.66 (dd, J = 2.7, 1.6 Hz, 1H), 7.48 (s, 1H), 7.34 (d, J = 7.9 Hz, 2H), 7.24 (d, J = 7.8 Hz, 2H), 7.10 (d, J = 25.3 Hz, 2H,), 7.01 (dd, J = 4.3, 1.7 Hz, 1H), 6.62 (dd, J = 4.4, 2.7 Hz, 1H), 6.52 (t, J = 8.8 Hz, 2H), 6.41 (t, J = 9.7 Hz, 4H), 6.10 (s, 1H), 5.25 (s, 2H), 4.37 (d, J = 5.7 Hz, 2H), 3.53 (m, 8H), 3.34 (d, J = 7.9 Hz, 2H), 2.91 (s, 9H), 2.62 (s, 6H), 2.53 (s, 3H), 2.38 (d, J = 6.8 Hz, 2H), 1.74 (t, J = 7.5 Hz, 2H).

^{13}C NMR (100 MHz, DMSO-D_6): δ [ppm] = 170.5, 170.3, 164.6, 162.8, 162.8, 160.0, 154.2, 152.7, 152.5, 151.1, 150.0, 141.8, 141.4, 140.7, 139.9, 139.1, 134.8, 129.7, 128.7, 128.4, 127.5, 123.7, 123.0, 122.1, 118.2, 117.2, 111.0, 108.3, 107.9, 106.4, 105.9, 98.2, 97.6, 94.4, 68.3, 67.2, 51.1, 44.7, 42.7, 41.2, 39.8, 37.8, 37.5, 29.2, 21.6, 11.5.

HRMS (ESI): calc. for $C_{57}H_{60}ClN_{15}O_9S^{2+}$ $(M+2H)^{2+}$: 582.2012, found: 582.7048.

LRMS (ESI, LC-MS): $C_{57}H_{59}ClN_{15}O_9S^{+}$ $(M+H)^{+}$: 1164.40, found: 1164.25.

t_R (LC-MS): 3.830 min.

7 Appendix

7.1 Protein sequences

Annotations: SNAP-tag, Halo-tag, SPR, mEGFP, p30 linker, Strep-tag, His-tag, COX8 sequence, NLS sequence

7.1.1 SNAP-Halo (bacterial expression)

MASWSHPQFEKGADDDDKVPHMDKDCEMKRTTLDSPLGKLELSGCEQGLHEIIFLGKGTSAADAVEVP
APAAVLGGPEPLMQATAWLNAYFHQPEAIEEFPVPALHHPVFQQESFTRQVLWKLLKVVKFGEVISYS
HLAALAGNPAATAAVKTALSGNPVPILIPCHRVVQGDLDVGGYEGGLAVKEWLLAHEGHRLGKPGLGG
RLEVLFQGPKAFLEGSEIGTGFPFDPHYVEVLGERMHYVDVGPRDGTPVLFLHGNPTSSYVWRNIIPH
VAPTHRCIAPDLIGMGKSDKPDLGYFFDDHVRFMDAFIEALGLEEVVLVIHDWGSALGFHWAKRNPER
VKGIAFMEFIRPIPTWDEWPEFARETFQAFRTTDVGRKLIIDQNVFIEGTLPMGVVRPLTEVEMDHYR
EPFLNPVDREPLWRFPNELPIAGEPANIVALVEEYMDWLHQSPVPKLLFWGTPGVLIPPAEAARLAKS
LPNCKAVDIGPGLNLLQEDNPDLIGSEIARWLSTLEISGAPGFSSISAHHHHHHHHHH

7.1.2 NADP⁺-Snifit (bacterial expression)

MASWSHPQFEKGADDDDKVPHMEGGLGRAVCLLTGASRGFGRTLAPLLASLLSPGSVLVLSARNDEAL
RQLEAELGAERSGLRVVRVPADLGAEAGLQQLLGALRELPRPKGLQRLLLINNAGSLGDVSKGFVDLS
DSTQVNNYWALNLTSMLCLTSSVLKAFPDSPGLNRTVVNISSLCALQPFKGWALYCAGKAARDMLFQV
LALEEPNVRVLNYAPGPLDTDMQQLARETSVDPDMRKGLQELKAKGKLVDCKVSAQKLLSLLEKDEFK
SGAHVDFYDKEFGSEIGTGFPFDPHYVEVLGERMHYVDVGPRDGTPVLFLHGNPTSSYVWRNIIPHVA
PTHRCIAPDLIGMGKSDKPDLGYFFDDHVRFMDAFIEALGLEEVVLVIHDWGSALGFHWAKRNPERVK
GIAFMEFIRPIPTWDEWPEFARETFQAFRTTDVGRKLIIDQNVFIEGTLPMGVVRPLTEVEMDHYREP
FLNPVDREPLWRFPNELPIAGEPANIVALVEEYMDWLHQSPVPKLLFWGTPGVLIPPAEAARLAKSLP
NCKAVDIGPGLNLLQEDNPDLIGSEIARWLSTLEISGSGRPPPPPPPPPPPPPPPPPPPPPPPPPPP
PPGGRSRSLEMDKDCEMKRTTLDSPLGKLELSGCEQGLHEIIFLGKGTSAADAVEVPAPAAVLGGPEP
LMQATAWLNAYFHQPEAIEEFPVPALHHPVFQQESFTRQVLWKLLKVVKFGEVISYSHLAALAGNPAA
TAAVKTALSGNPVPILIPCHRVVQGDLDVGGYEGGLAVKEWLLAHEGHRLGKPGLGGAPGFSSISAHH
HHHHHHHH

7.1.3 NAD⁺-Snifit (bacterial expression)

MASWSHPQFEKGADDDDKVPHMEGGLGRAVCLLTGASRGFGRTLAPLLASLLSPGSVLVLSDWNDEAL
RQLEAELGAERSGLRVVRVPADLGAEAGLQQLLGALRELPRPKGLQRLLLINNAGSLGDVSKGFVDLS
DSTQVNNYWALNLTSMLCLTSSVLKAFPDSPGLNRTVVNISSLCALQPFKGWALYCAGKAARDMLFQV
LALEEPNVRVLNYAPGPLDTDMQQLARETSVDPDMRKGLQELKAKGKLVDCKVSAQKLLSLLEKDEFK
SGAHVDFYDKEFGSEIGTGFPFDPHYVEVLGERMHYVDVGPRDGTPVLFLHGNPTSSYVWRNIIPHVA
PTHRCIAPDLIGMGKSDKPDLGYFFDDHVRFMDAFIEALGLEEVVLVIHDWGSALGFHWAKRNPERVK
GIAFMEFIRPIPTWDEWPEFARETFQAFRTTDVGRKLIIDQNVFIEGTLPMGVVRPLTEVEMDHYREP
FLNPVDREPLWRFPNELPIAGEPANIVALVEEYMDWLHQSPVPKLLFWGTPGVLIPPAEAARLAKSLP
NCKAVDIGPGLNLLQEDNPDLIGSEIARWLSTLEISGSGRPPPPPPPPPPPPPPPPPPPPPPPPPPP
PPGGRSRSLEMDKDCEMKRTTLDSPLGKLELSGCEQGLHEIIFLGKGTSAADAVEVPAPAAVLGGPEP
LMQATAWLNAYFHQPEAIEEFPVPALHHPVFQQESFTRQVLWKLLKVVKFGEVISYSHLAALAGNPAA
TAAVKTALSGNPVPILIPCHRVVQGDLDVGGYEGGLAVKEWLLAHEGHRLGKPGLGGAPGFSSISAHH
HHHHHHHH

7.1.4 Cytosolic NADP+-Snifit (mammalian expression)

MEGGLGRAVCLLTGASRGFGRTLAPLLASLLSPGSVLVLSARNDEALRQLEAELGAERSGLRVVRVPA
DLGAEAGLQQLLGALRELPRPKGLQRLLLINNAGSLGDVSKGFVDLSDSTQVNNYWALNLTSMLCLTS
SVLKAFPDSPGLNRTVVNISSLCALQPFKGWALYCAGKAARDMLFQVLALEEPNVRVLNYAPGPLDTD
MQQLARETSVDPDMRKGLQELKAKGKLVDCKVSAQKLLSLLEKDEFKSGAHVDFYDKEFGSEIGTGFP
FDPHYVEVLGERMHYVDVGPRDGTPVLFLHGNPTSSYVWRNIIPHVAPTHRCIAPDLIGMGKSDKPDL
GYFFDDHVRFMDAFIEALGLEEVVLVIHDWGSALGFHWAKRNPERVKGIAFMEFIRPIPTWDEWPEFA
RETFQAFRTTDVGRKLIIDQNVFIEGTLPMGVVRPLTEVEMDHYREPFLNPVDREPLWRFPNELPIAG
EPANIVALVEEYMDWLHQSPVPKLLFWGTPGVLIPPAEAARLAKSLPNCKAVDIGPGLNLLQEDNPDL
IGSEIARWLSTLEISGSGRPPPPPPPPPPPPPPPPPPPPPPPPPGGRSRSLEMDKDCEMKRTT
LDSPLGKLELSGCEQGLHEIIFLGKGTSAADAVEVPAPAAVLGGPEPLMQATAWLNAYFHQPEAIEEF
PVPALHHPVFQQESFTRQVLWKLLKVVKFGEVISYSHLAALAGNPAATAAVKTALSGNPVPILIPCHR
VVQGDLDVGGYEGGLAVKEWLLAHEGHRLGKPGLG

7.1.5 Cytosolic NAD+-Snifit (mammalian expression)

MEGGLGRAVCLLTGASRGFGRTLAPLLASLLSPGSVLVLSDWNDEALRQLEAELGAERSGLRVVRVPA
DLGAEAGLQQLLGALRELPRPKGLQRLLLINNAGSLGDVSKGFVDLSDSTQVNNYWALNLTSMLCLTS
SVLKAFPDSPGLNRTVVNISSLCALQPFKGWALYCAGKAARDMLFQVLALEEPNVRVLNYAPGPLDTD
MQQLARETSVDPDMRKGLQELKAKGKLVDCKVSAQKLLSLLEKDEFKSGAHVDFYDKEFGSEIGTGFP
FDPHYVEVLGERMHYVDVGPRDGTPVLFLHGNPTSSYVWRNIIPHVAPTHRCIAPDLIGMGKSDKPDL
GYFFDDHVRFMDAFIEALGLEEVVLVIHDWGSALGFHWAKRNPERVKGIAFMEFIRPIPTWDEWPEFA
RETFQAFRTTDVGRKLIIDQNVFIEGTLPMGVVRPLTEVEMDHYREPFLNPVDREPLWRFPNELPIAG
EPANIVALVEEYMDWLHQSPVPKLLFWGTPGVLIPPAEAARLAKSLPNCKAVDIGPGLNLLQEDNPDL
IGSEIARWLSTLEISGSGRPPPPPPPPPPPPPPPPPPPPPPPPPGGRSRSLEMDKDCEMKRTT
LDSPLGKLELSGCEQGLHEIIFLGKGTSAADAVEVPAPAAVLGGPEPLMQATAWLNAYFHQPEAIEEF
PVPALHHPVFQQESFTRQVLWKLLKVVKFGEVISYSHLAALAGNPAATAAVKTALSGNPVPILIPCHR
VVQGDLDVGGYEGGLAVKEWLLAHEGHRLGKPGLG

7.1.6 Nuclear NADP+-Snifit (mammalian expression)

MEGGLGRAVCLLTGASRGFGRTLAPLLASLLSPGSVLVLSARNDEALRQLEAELGAERSGLRVVRVPA
DLGAEAGLQQLLGALRELPRPKGLQRLLLINNAGSLGDVSKGFVDLSDSTQVNNYWALNLTSMLCLTS
SVLKAFPDSPGLNRTVVNISSLCALQPFKGWALYCAGKAARDMLFQVLALEEPNVRVLNYAPGPLDTD
MQQLARETSVDPDMRKGLQELKAKGKLVDCKVSAQKLLSLLEKDEFKSGAHVDFYDKEFGSEIGTGFP
FDPHYVEVLGERMHYVDVGPRDGTPVLFLHGNPTSSYVWRNIIPHVAPTHRCIAPDLIGMGKSDKPDL
GYFFDDHVRFMDAFIEALGLEEVVLVIHDWGSALGFHWAKRNPERVKGIAFMEFIRPIPTWDEWPEFA
RETFQAFRTTDVGRKLIIDQNVFIEGTLPMGVVRPLTEVEMDHYREPFLNPVDREPLWRFPNELPIAG
EPANIVALVEEYMDWLHQSPVPKLLFWGTPGVLIPPAEAARLAKSLPNCKAVDIGPGLNLLQEDNPDL
IGSEIARWLSTLEISGSGRPPPPPPPPPPPPPPPPPPPPPPPPPGGRSRSLEMDKDCEMKRTT
LDSPLGKLELSGCEQGLHEIIFLGKGTSAADAVEVPAPAAVLGGPEPLMQATAWLNAYFHQPEAIEEF
PVPALHHPVFQQESFTRQVLWKLLKVVKFGEVISYSHLAALAGNPAATAAVKTALSGNPVPILIPCHR
VVQGDLDVGGYEGGLAVKEWLLAHEGHRLGKPGLGGAPDPKKKRKVDPKKKRKVDPKKKRKELRASP

7.1.7 Nuclear NAD+-Snifit (mammalian expression)

MEGGLGRAVCLLTGASRGFGRTLAPLLASLLSPGSVLVLSDWNDEALRQLEAELGAERSGLRVVRVPA
DLGAEAGLQQLLGALRELPRPKGLQRLLLINNAGSLGDVSKGFVDLSDSTQVNNYWALNLTSMLCLTS
SVLKAFPDSPGLNRTVVNISSLCALQPFKGWALYCAGKAARDMLFQVLALEEPNVRVLNYAPGPLDTD
MQQLARETSVDPDMRKGLQELKAKGKLVDCKVSAQKLLSLLEKDEFKSGAHVDFYDKEFGSEIGTGFP
FDPHYVEVLGERMHYVDVGPRDGTPVLFLHGNPTSSYVWRNIIPHVAPTHRCIAPDLIGMGKSDKPDL
GYFFDDHVRFMDAFIEALGLEEVVLVIHDWGSALGFHWAKRNPERVKGIAFMEFIRPIPTWDEWPEFA
RETFQAFRTTDVGRKLIIDQNVFIEGTLPMGVVRPLTEVEMDHYREPFLNPVDREPLWRFPNELPIAG
EPANIVALVEEYMDWLHQSPVPKLLFWGTPGVLIPPAEAARLAKSLPNCKAVDIGPGLNLLQEDNPDL
IGSEIARWLSTLEISGSGRPPPPPPPPPPPPPPPPPPPPPPPPPPPGGRSRSLEMDKDCEMKRTT
LDSPLGKLELSGCEQGLHEIIFLGKGTSAADAVEVPAPAAVLGGPEPLMQATAWLNAYFHQPEAIEEF
PVPALHHPVFQQESFTRQVLWKLLKVVKFGEVISYSHLAALAGNPAATAAVKTALSGNPVPILIPCHR
VVQGDLDVGGYEGGLAVKEWLLAHEGHRLGKPGLGGAPDPKKKRKVDPKKKRKVDPKKKRKELRASP

7.1.8 Mitochondrial NADP+-Snifit (mammalian expression)

MSVLTPLLLRGLTGSARRLPVPRAKIHSLSVLTPLLLRGLTGSARRLPVPRAKIHSLGGSVLTPLLLR
GLTGSARRLPVPRAKIHSLSVLTPLLLRGLTGSARRLPVPRAKIHSLGGSGGSEGGLGRAVCLLTGAS
RGFGRTLAPLLASLLSPGSVLVLSARNDEALRQLEAELGAERSGLRVVRVPADLGAEAGLQQLLGALR
ELPRPKGLQRLLLINNAGSLGDVSKGFVDLSDSTQVNNYWALNLTSMLCLTSSVLKAFPDSPGLNRTV
VNISSLCALQPFKGWALYCAGKAARDMLFQVLALEEPNVRVLNYAPGPLDTDMQQLARETSVDPDMRK
GLQELKAKGKLVDCKVSAQKLLSLLEKDEFKSGAHVDFYDKEFGSEIGTGFPFDPHYVEVLGERMHYV
DVGPRDGTPVLFLHGNPTSSYVWRNIIPHVAPTHRCIAPDLIGMGKSDKPDLGYFFDDHVRFMDAFIE
ALGLEEVVLVIHDWGSALGFHWAKRNPERVKGIAFMEFIRPIPTWDEWPEFARETFQAFRTTDVGRKL
IIDQNVFIEGTLPMGVVRPLTEVEMDHYREPFLNPVDREPLWRFPNELPIAGEPANIVALVEEYMDWL
HQSPVPKLLFWGTPGVLIPPAEAARLAKSLPNCKAVDIGPGLNLLQEDNPDLIGSEIARWLSTLEISG
SGRPPPPPPPPPPPPPPPPPPPPPPPPPPPPGGRSRSLEMDKDCEMKRTTLDSPLGKLELSGCEQG
LHEIIFLGKGTSAADAVEVPAPAAVLGGPEPLMQATAWLNAYFHQPEAIEEFPVPALHHPVFQQESFT
RQVLWKLLKVVKFGEVISYSHLAALAGNPAATAAVKTALSGNPVPILIPCHRVVQGDLDVGGYEGGLA
VKEWLLAHEGHRLGKPGLG

7.1.9 Mitochondrial NAD+-Snifit (mammalian expression)

MSVLTPLLLRGLTGSARRLPVPRAKIHSLSVLTPLLLRGLTGSARRLPVPRAKIHSLGGSVLTPLLLR
GLTGSARRLPVPRAKIHSLSVLTPLLLRGLTGSARRLPVPRAKIHSLGGSGGSEGGLGRAVCLLTGAS
RGFGRTLAPLLASLLSPGSVLVLSDWNDEALRQLEAELGAERSGLRVVRVPADLGAEAGLQQLLGALR
ELPRPKGLQRLLLINNAGSLGDVSKGFVDLSDSTQVNNYWALNLTSMLCLTSSVLKAFPDSPGLNRTV
VNISSLCALQPFKGWALYCAGKAARDMLFQVLALEEPNVRVLNYAPGPLDTDMQQLARETSVDPDMRK
GLQELKAKGKLVDCKVSAQKLLSLLEKDEFKSGAHVDFYDKEFGSEIGTGFPFDPHYVEVLGERMHYV
DVGPRDGTPVLFLHGNPTSSYVWRNIIPHVAPTHRCIAPDLIGMGKSDKPDLGYFFDDHVRFMDAFIE
ALGLEEVVLVIHDWGSALGFHWAKRNPERVKGIAFMEFIRPIPTWDEWPEFARETFQAFRTTDVGRKL
IIDQNVFIEGTLPMGVVRPLTEVEMDHYREPFLNPVDREPLWRFPNELPIAGEPANIVALVEEYMDWL
HQSPVPKLLFWGTPGVLIPPAEAARLAKSLPNCKAVDIGPGLNLLQEDNPDLIGSEIARWLSTLEISG
SGRPPPPPPPPPPPPPPPPPPPPPPPPPPPPGGRSRSLEMDKDCEMKRTTLDSPLGKLELSGCEQG
LHEIIFLGKGTSAADAVEVPAPAAVLGGPEPLMQATAWLNAYFHQPEAIEEFPVPALHHPVFQQESFT
RQVLWKLLKVVKFGEVISYSHLAALAGNPAATAAVKTALSGNPVPILIPCHRVVQGDLDVGGYEGGLA
VKEWLLAHEGHRLGKPGLG

7.1.10 SNAP-mEGFP (mammalian expression)

MDKDCEMKRTTLDSPLGKLELSGCEQGLHEIIFLGKGTSAADAVEVPAPAAVLGGPEPLMQATAWLNA
YFHQPEAIEEFPVPALHHPVFQQESFTRQVLWKLLKVVKFGEVISYSHLAALAGNPAATAAVKTALSG
NPVPILIPCHRVVQGDLDVGGYEGGLAVKEWLLAHEGHRLGKPGLGMVSKGEELFTGVVPILVELDGD
VNGHKFSVSGEGEGDATYGKLTLKFICTTGKLPVPWPTLVTTLTYGVQCFSRYPDHMKQHDFFKSAMP
EGYVQERTIFFKDDGNYKTRAEVKFEGDTLVNRIELKGIDFKEDGNILGHKLEYNYNSHNVYIMADKQ
KNGIKVNFKIRHNIEDGSVQLADHYQQNTPIGDGPVLLPDNHYLSTQSKLSKDPNEKRDHMVLLEFVT
AAGITLGMDELYK

7.1.11 Halo-mEGFP (mammalian expression)

MGSEIGTGFPFDPHYVEVLGERMHYVDVGPRDGTPVLFLHGNPTSSYVWRNIIPHVAPTHRCIAPDLI
GMGKSDKPDLGYFFDDHVRFMDAFIEALGLEEVVLVIHDWGSALGFHWAKRNPERVKGIAFMEFIRPI
PTWDEWPEFARETFQAFRTTDVGRKLIIDQNVFIEGTLPMGVVRPLTEVEMDHYREPFLNPVDREPLW
RFPNELPIAGEPANIVALVEEYMDWLHQSPVPKLLFWGTPGVLIPPAEAARLAKSLPNCKAVDIGPGL
NLLQEDNPDLIGSEIARWLSTLEISGMVSKGEELFTGVVPILVELDGDVNGHKFSVSGEGEGDATYGK
LTLKFICTTGKLPVPWPTLVTTLTYGVQCFSRYPDHMKQHDFFKSAMPEGYVQERTIFFKDDGNYKTR
AEVKFEGDTLVNRIELKGIDFKEDGNILGHKLEYNYNSHNVYIMADKQKNGIKVNFKIRHNIEDGSVQ
LADHYQQNTPIGDGPVLLPDNHYLSTQSKLSKDPNEKRDHMVLLEFVTAAGITLGMDELYK

7.1.12 SLC25A51 (mammalian expression)

MMDSEAHEKRPPILTSSKQDISPHITNVGEMKHYLCGCCAAFNNVAITFPIQKVLFRQQLYGIKTRDA
ILQLRRDGFRNLYRGILPPLMQKTTTLALMFGLYEDLSCLLHKHVSAPEFATSGVAAVLAGTTEAIFT
PLERVQTLLQDHKHHDKFTNTYQAFKALKCHGIGEYYRGLVPILFRNGLSNVLFFGLRGPIKEHLPTA
TTHSAHLVNDFICGGLLGAMLGFLFFPINVVKTRIQSQIGGEFQSFPKVFQKIWLERDRKLINLFRGA
HLNYHRSLISWGIINATYEFLL

7.1.13 SLC25A52 (mammalian expression)

MIDSEAHEKRPPILTSSKQDISPHITNVGEMKHYLCGCCAAFNNVAITYPIQKVLFRQQLYGIKTRDA
VLQLRRDGFRNLYRGILPPLMQKTTTLALMFGLYEDLSCLLRKHVRAPEFATHGVAAVLAGTAEAIFT
PLERVQTLLQNHKHHDKFTNTYQAFKALKCHGIGEYYRGLVPILFRNGLSNVLFFGLRGPIKEHLPTA
TTHSAHLVNDFIGGGLLGAMLGFLCFPINVVKTRIQSQIGGEFQSFPKVFQKIWLERDRKLINLFRGA
HLNYHRSLISWGIINATYEFLL

7.2 NAD(P)-Snifits constructs

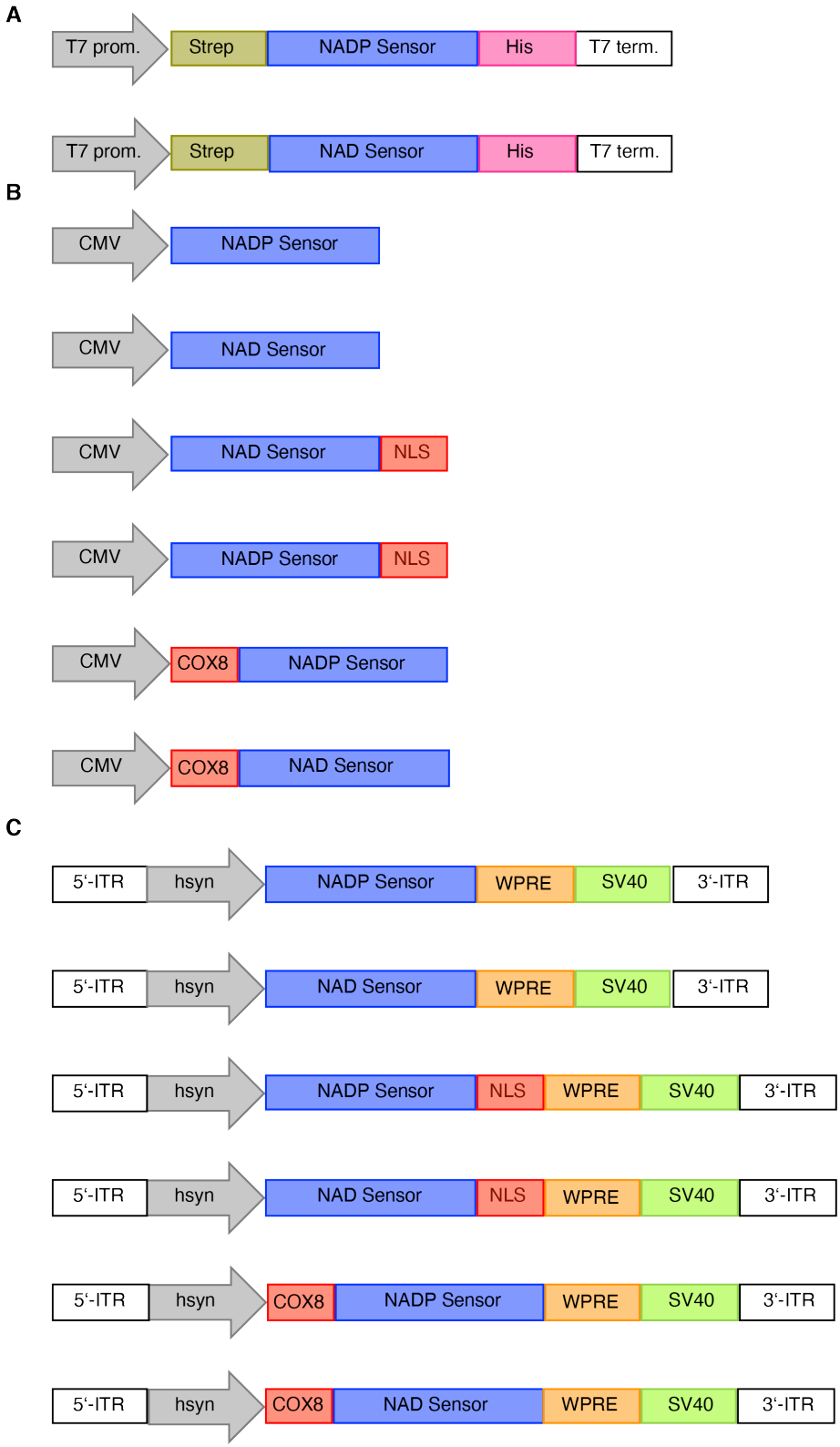

Figure 36: NAD(P)-Snifits constructs for bacterial expression (A), expression in U2OS cells (B) and expression in neurons (C).

7.3 Key resource table

Table 8: key resources that were used in this thesis.

Reagent or resource	Source	Identifier
Machines and equipment		
V-770 spectrophotometer	Jasco	n/a
V-8600 spectrofluorometer	Jasco	n/a
Quantusaurus C11347	Hamamatsu	n/a
Spark® 80 plate reader	Tecan	n/a
PP F-bottom 96 well plates	Greiner bio-one	#655201
black quartz glass 96 well plate	Hellma Analytics	#730009-B-44
HisPur™ Ni-NTA Superflow	Thermo Scientific	#25217
Amicon® ultra 50 k	Merck Millipore	#UFC5050B
Zebra™ Spin 40 k cut off	Thermo Scientific	#87766
96 well back non-binding plate	Corning	#3993
24-well plate cell culture	TPP	#92024
6-well plate cell culture	TPP	#92006
96-well glass-bottom plate	Eppendorf	#0030741030
24-well glass bottom plate	Cellvis	#P24-1.5H-N
cell strainer cap	Corning	#352235
FACS Melody	BD Bioscience	n/a
SP8 Confocal Microscope	Leica	n/a
FALCON FLIM	Leica	n/a
Software		
LAS X Software	Leica	n/a
FlowJo	BD Bioscience	n/a
Fiji	National Institutes of Health	doi:10.1038/nmeth.2019
Prism 9.0	GraphPad	n/a
Cells		
WISTAR rats	Janvier	n/a
Hippocampal neurons	MPImF	n/a
U2OS	ATCC	HTB-96™
U2OS: SNAP-mEGFP	Johnsson lab	n/a
U2OS: Halo-mEGFP	Johnsson lab	n/a
U2OS: NAD-Snifit	Johnsson lab	this thesis
U2OS: NADP-Snifit	Johnsson lab	this thesis
E. coli BL21 (DE3)-pLysS	Millipore	#694513
Cell culture reagents		
DMEM	Gibco	#31966-021
DMEM, phenol-red free	Gibco	#21053-028
Neurobasal medium, phenol-red free	Gibco	#12348-017
FBS	Gibco	#10500-064
PBS	Gibco	#10010-015
HBSS	Corning	#21-023-CV
Trypsin	Gibco	#252000
TrypLE	Gibco	#12604-013
Glucose solution	Gibco	#A24940-01
Sodium pyruvate	Gibco	#31966-021

Glutamax	Gibco	#35050-087
B27	Gibco	#17504044
Doxycycline	TCI	#D4126
Hoechst	Sigma	#94403
Mitotracker green	Invitrogen	#M7514
FK866	Sigma	#F8557
NR	Sigma	#SMB00907
Vincristine	Sigma	#V8879
Thapsigargin	Sigma	#T9033
Oligomycin	Sigma	#579-13-5
QM385	Quartet Medicine	n/a
^{13}C labelled yeast extract	Cambridge Isotopes	#ISO1
Cal520 AM-ester	Sigma	#148505-34-1
Fugene 6	Promega	#E269A
Rabbit Anti-FLAG	Sigma Aldrich	#F742T
Goat-Anti Rabbit IgG Alexa647	Invitrogen	#A21248,

Chemicals		
Halo-CPY	Johnsson lab	n/a
Halo-SiR	Johnsson lab	10.1038/nchem.1546
CP-TMR-C6-SMX	Johnsson lab	10.7554/eLife.32638
CP-MaP1-C6-SMX	Johnsson lab	this thesis
CP-MaP1-PPT	Johnsson lab	this thesis
CP-MaP555-C6-SMX	Johnsson lab	this thesis
CP-MaP555-PPT	Johnsson lab	this thesis
CP-MaP3-C6-SMX	Johnsson lab	this thesis
CP-MaP3-PPT	Johnsson lab	this thesis
NAD^+	Sigma	#10127965001
$NADP^+$	Alfa Aesar	#44126
NADPH	Carl Roth	#AE14.3
BSA solution	Sigma	#B8667

7.4 List of buffers

Table 9: Composition of buffers used in this thesis.

name	composition
activity buffer	50 mM HEPES, 50 mM NaCl, pH 7.4, 1 mM DTT
His extraction	50 mM KH2PO4, 300 mM NaCl, 5 mM imidazole, pH 8.0, 1 mM PMSF, 0.25 mg/mL lysozyme, 1 mM DTT
His wash	50 mM KH2PO4, 300 mM NaCl, 10 mM imidazole, pH 7.5
His elution	50 mM KH2PO4, 300 mM NaCl, 500 mM imidazole, pH 7.5

7.5 Analytical data

Diketone (16)

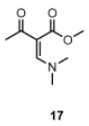

17

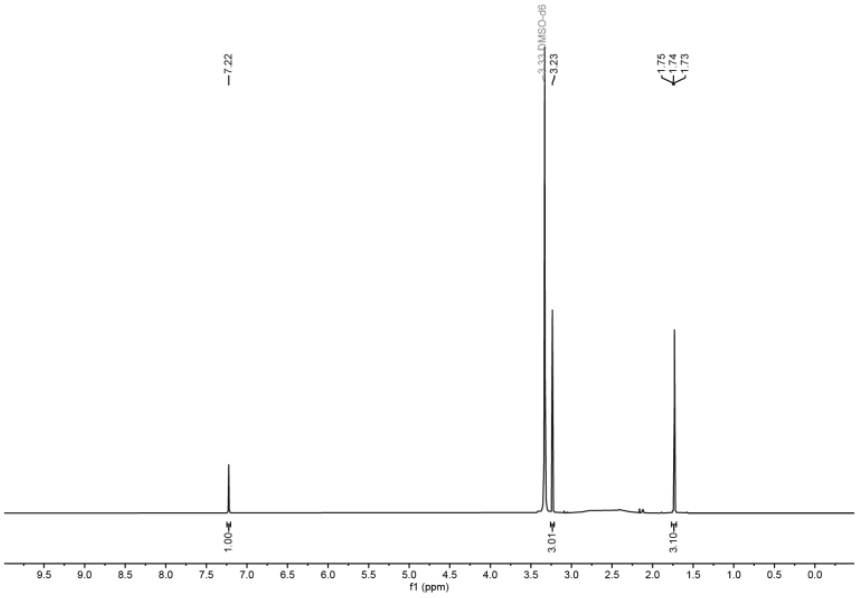

400 MHz
Solvent: DMSO-D_6
Nucleus: ^{1}H

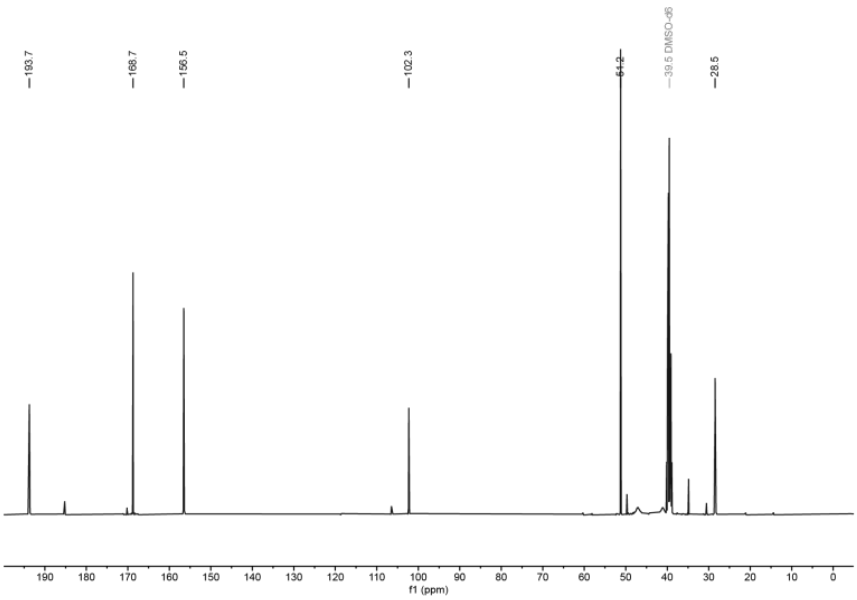

100 MHz
Solvent: DMSO-D_6
Nucleus: ^{13}C

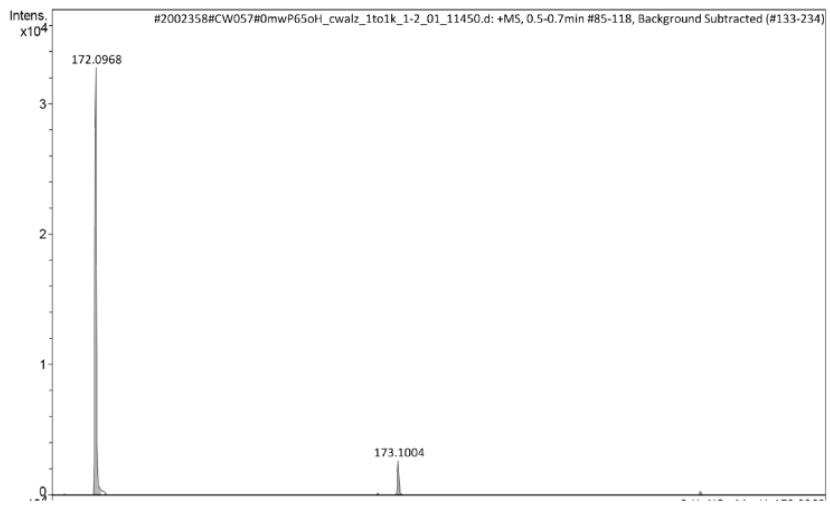

Triazine (18)

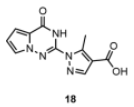

18

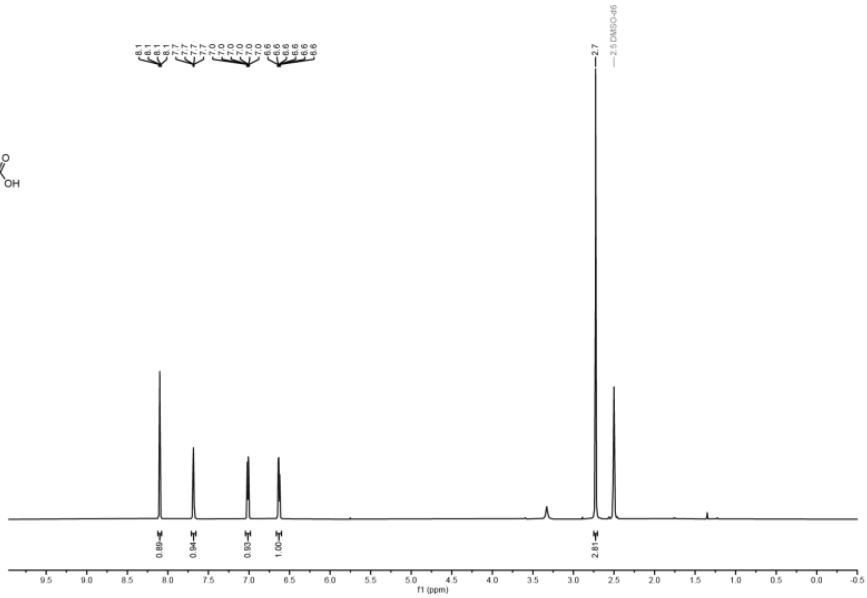

400 MHz
Solvent: DMSO-D_6
Nucleus: ^{1}H

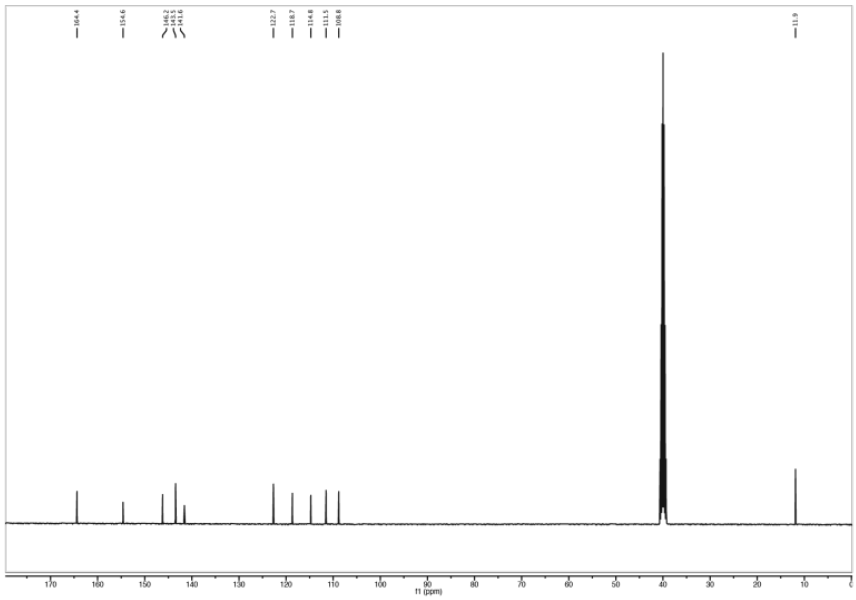

100 MHz
Solvent: DMSO-D_6
Nucleus: ^{13}C

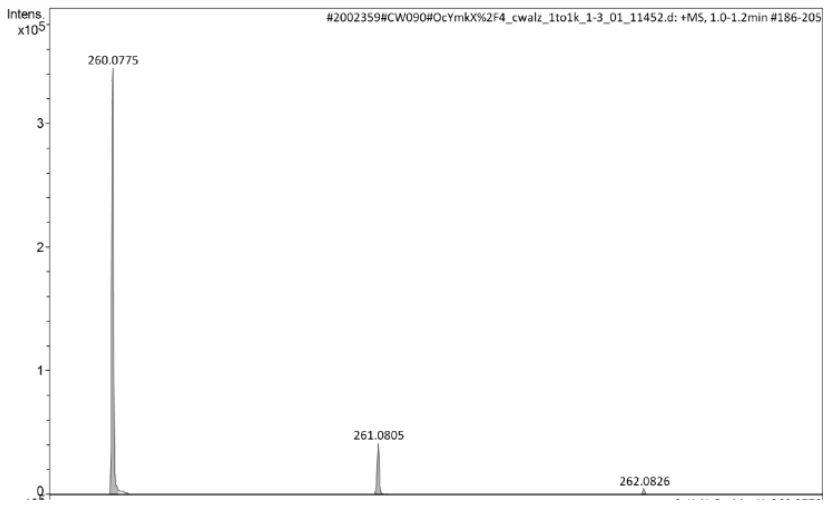

PPT (19)

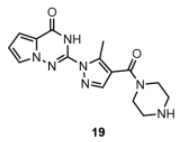

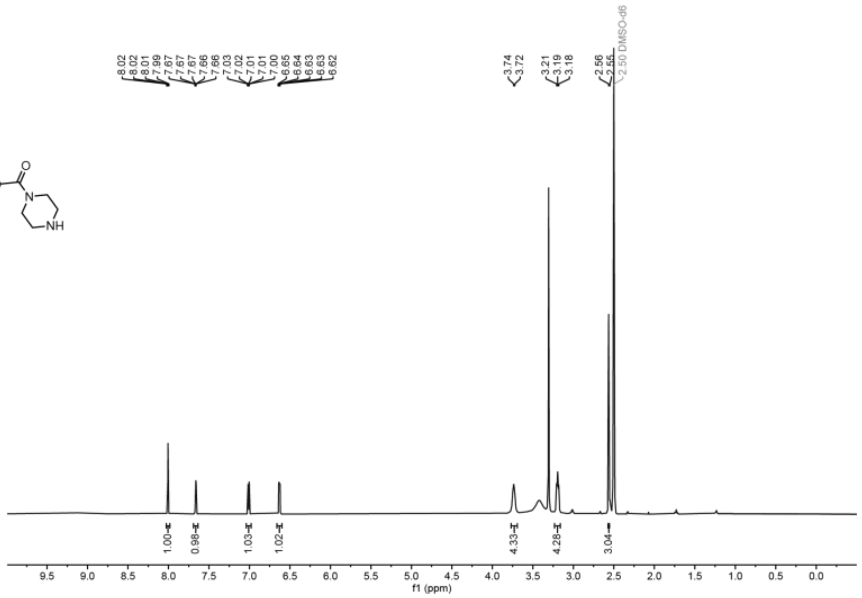

400 MHz
Solvent: DMSO-D_6
Nucleus: ^{1}H

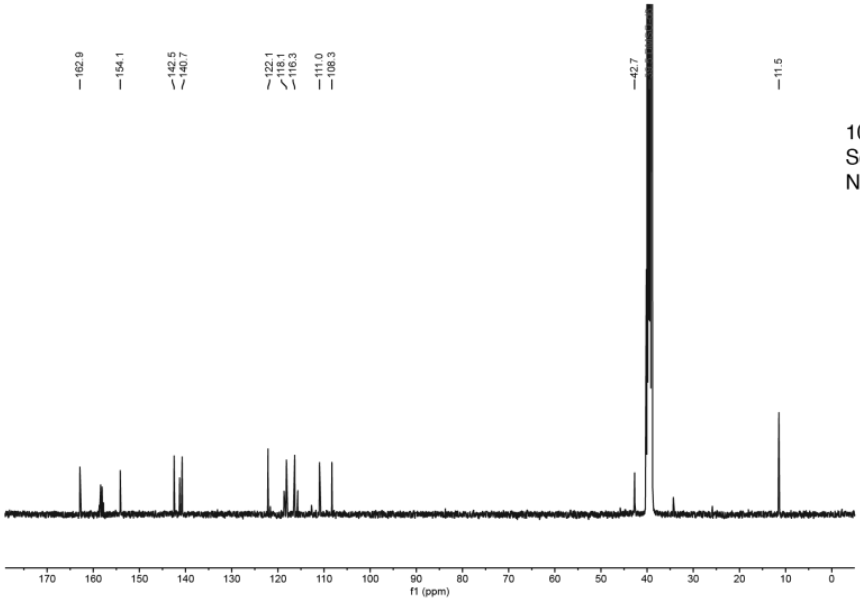

100 MHz
Solvent: DMSO-D_6
Nucleus: ^{13}C

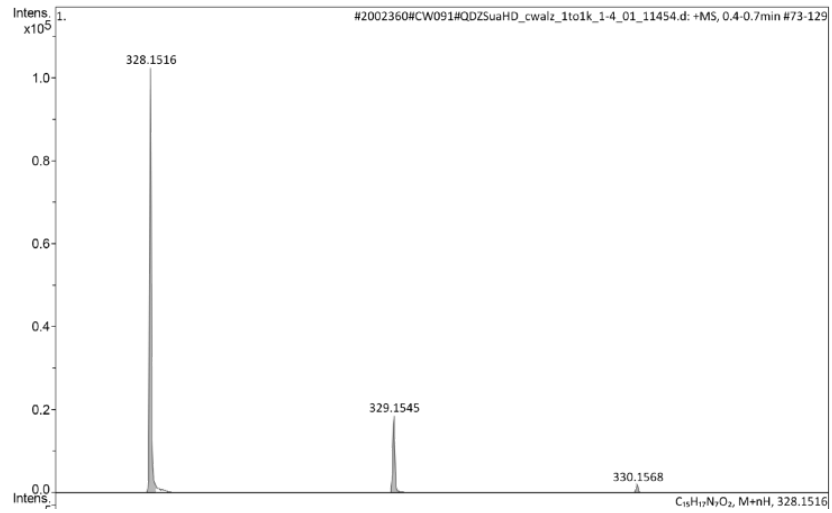

C6-SMX (23)

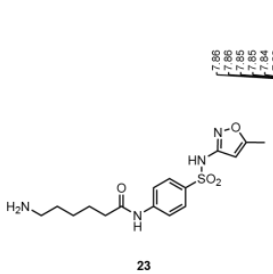

400 MHz
Solvent: MeOH-D_4
Nucleus: ^{1}H

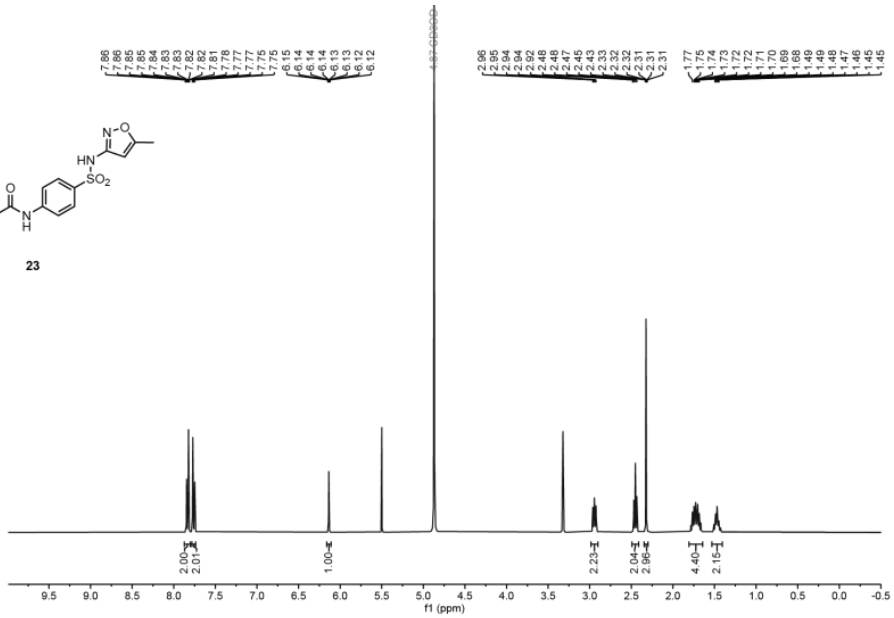

100 MHz
Solvent: MeOH-D_4
Nucleus: ^{13}C

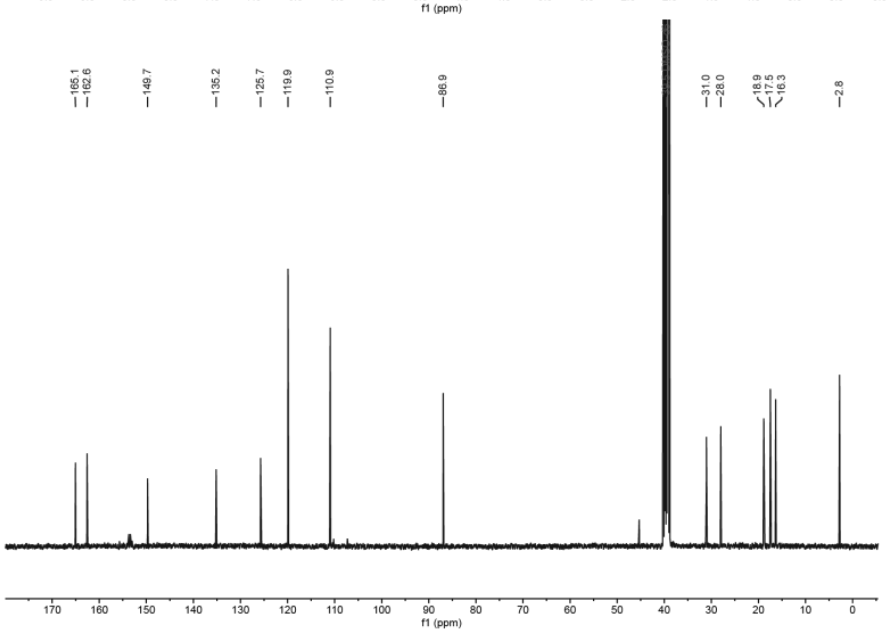

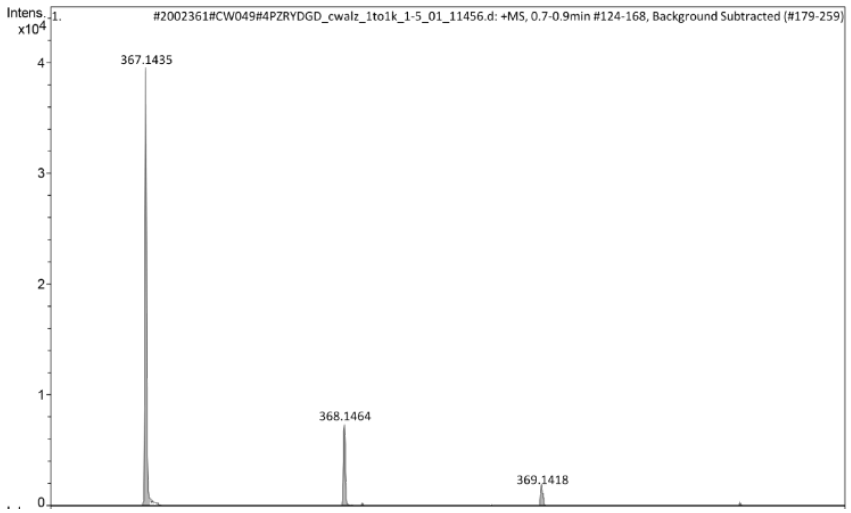

Bisallyl-TMR (25)

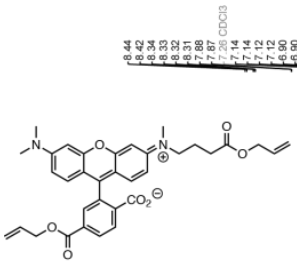

25

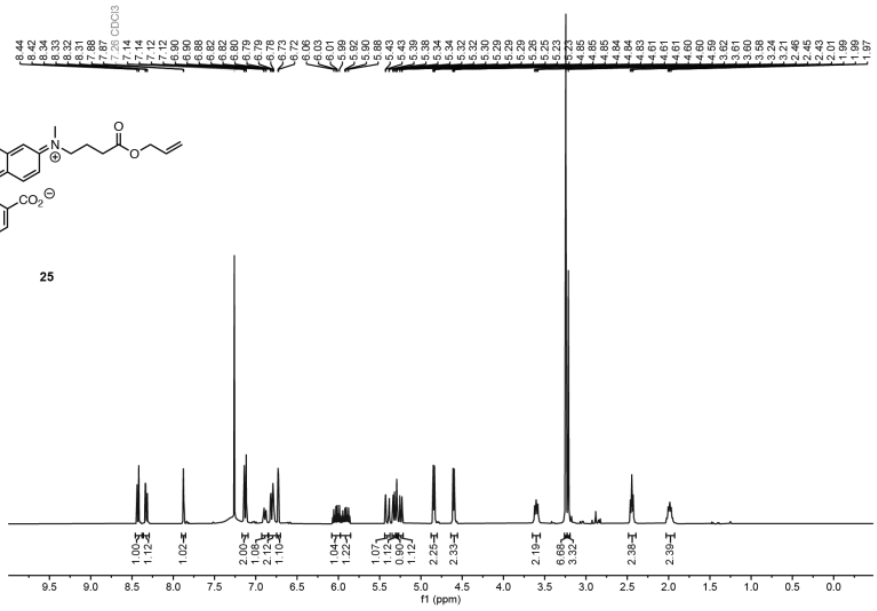

400 MHz
Solvent: $CHCl_3$-D_1
Nucleus: ^1H

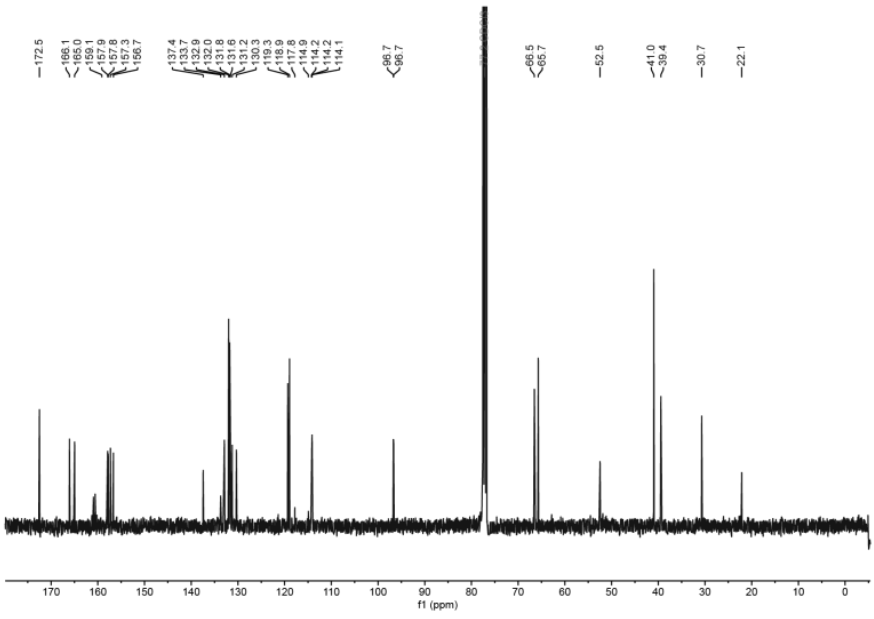

100 MHz
Solvent: $CHCl_3$-D_1
Nucleus: ^{13}C

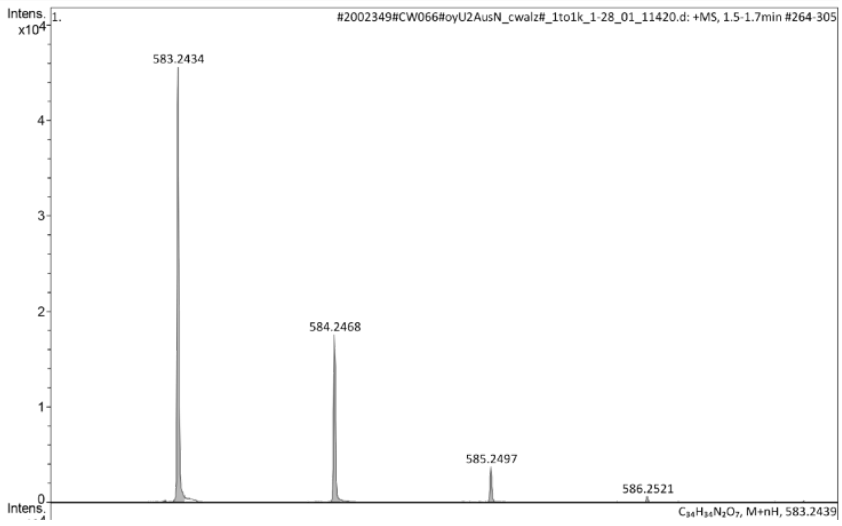

Bisallyl-MaP1 (26)

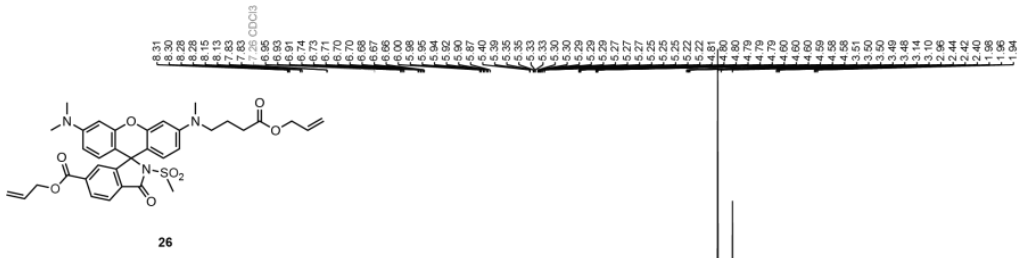

26

400 MHz
Solvent: $CHCl_3$-D_1
Nucleus: ^1H

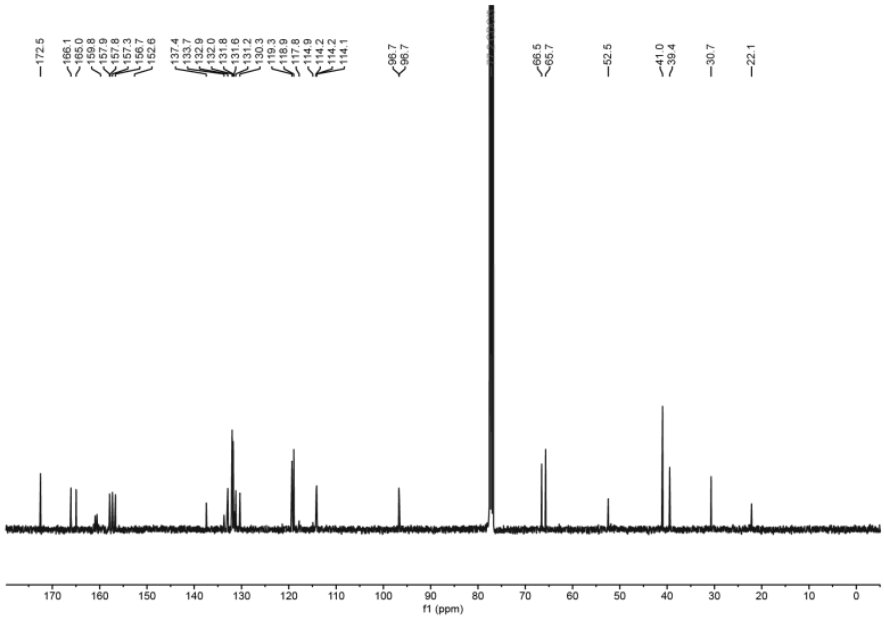

100 MHz
Solvent: $CHCl_3$-D_1
Nucleus: ^{13}C

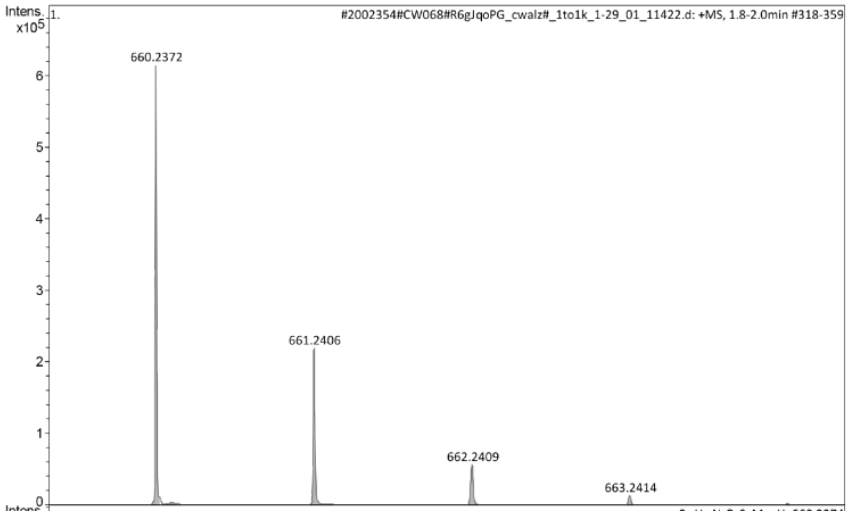

MaP1 (28)

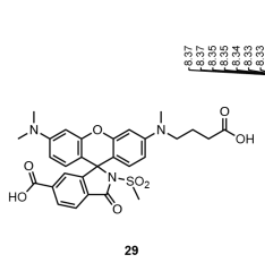

29

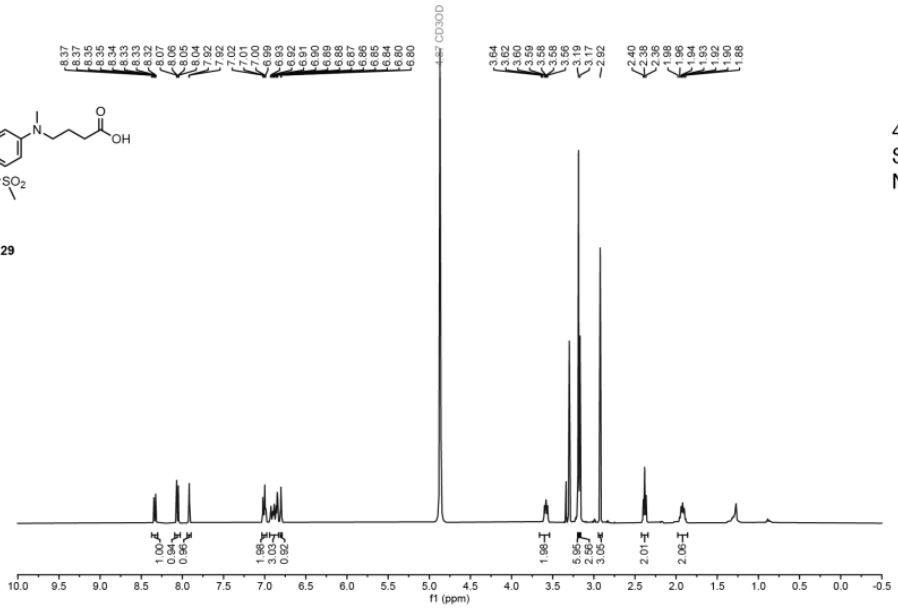

400 MHz
Solvent: MeOH-D_4
Nucleus: ^{1}H

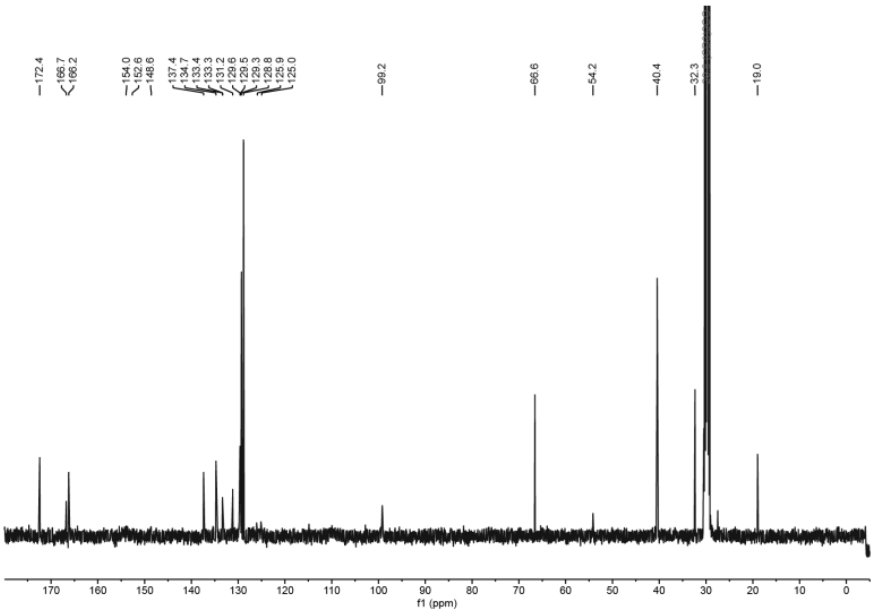

100 MHz
Solvent: MeOH-D_4
Nucleus: ^{13}C

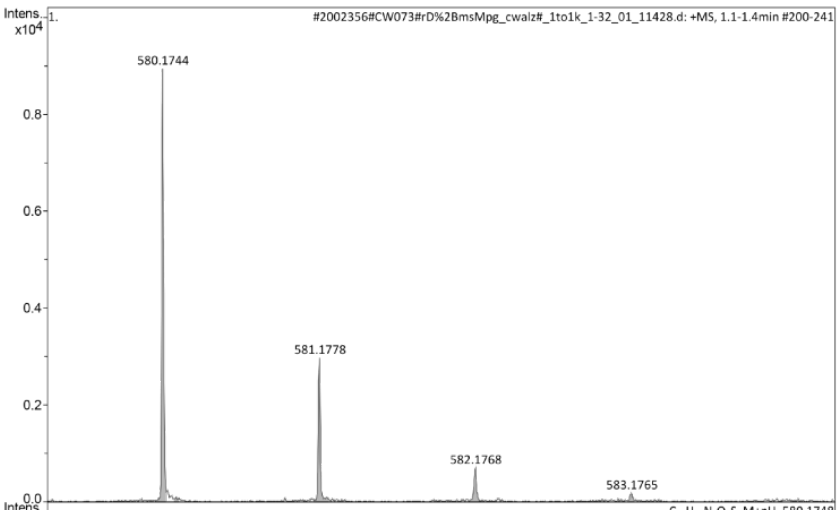

Bisallyl-MaP555 (27)

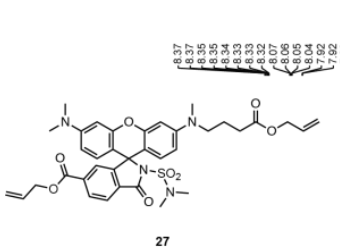

27

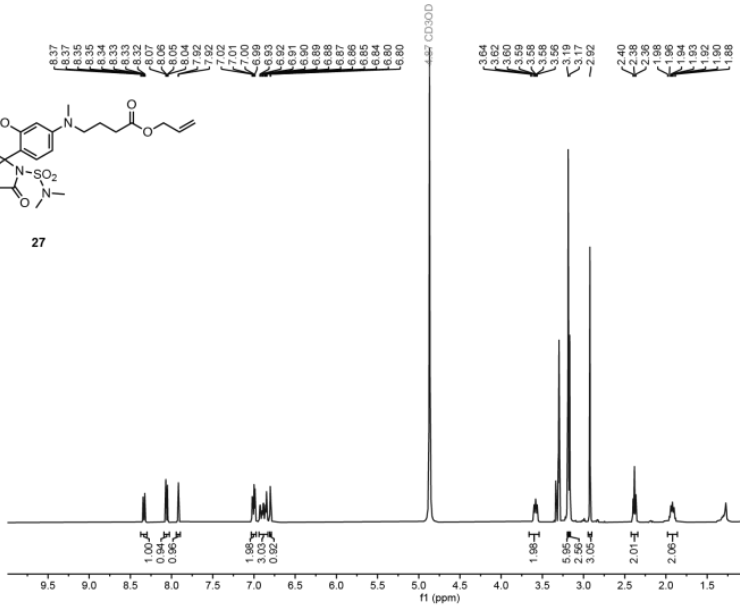

400 MHz
Solvent: $CHCl_3$-D_1
Nucleus: ^1H

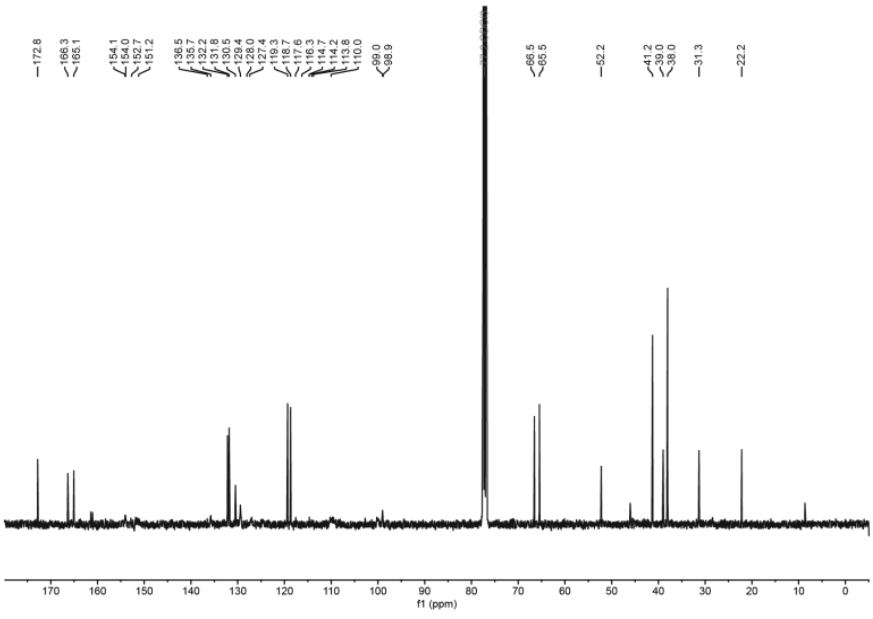

100 MHz
Solvent: $CHCl_3$-D_1
Nucleus: ^{13}C

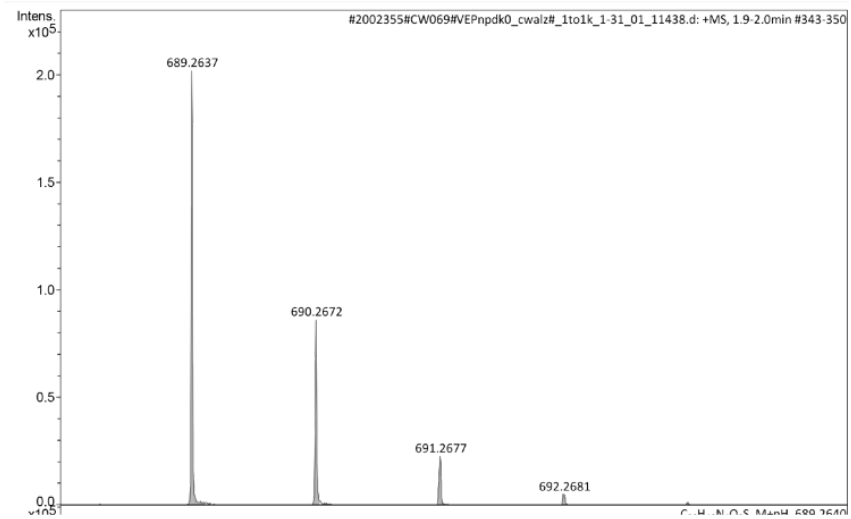

MaP555 (29)

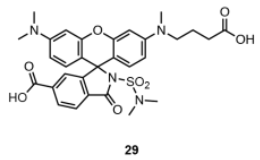

29

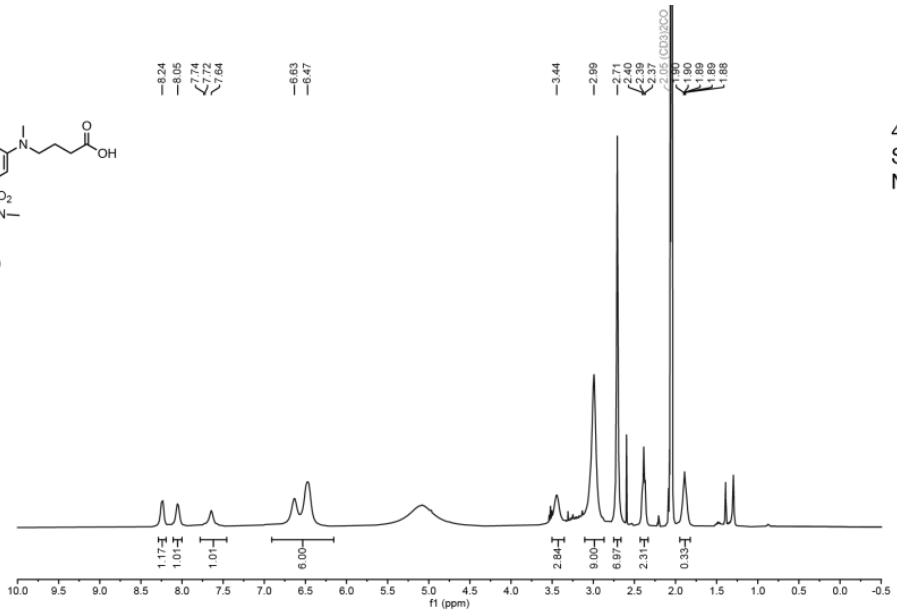

400 MHz
Solvent: Acetone-D_6
Nucleus: ^{1}H

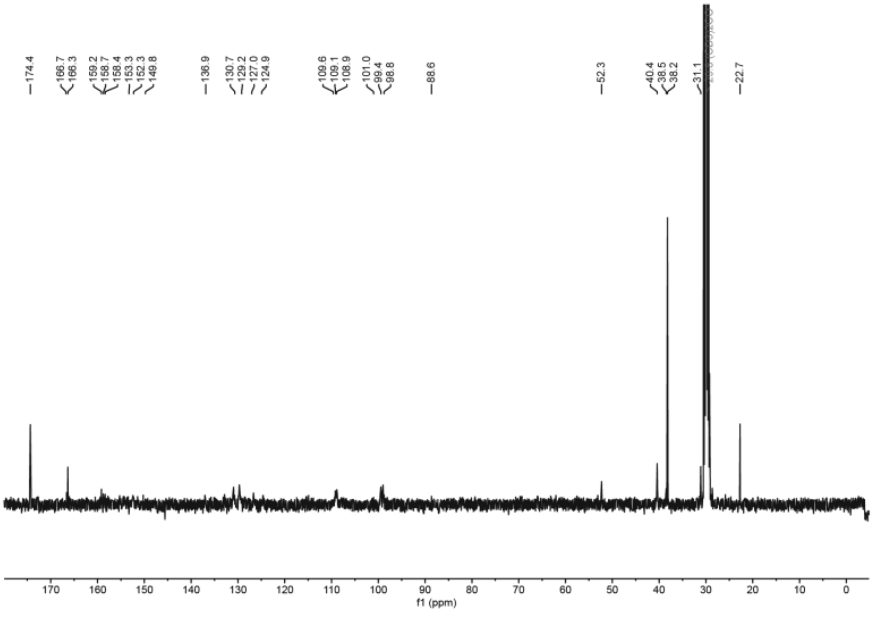

100 MHz
Solvent: Acetone-D_6
Nucleus: ^{13}C

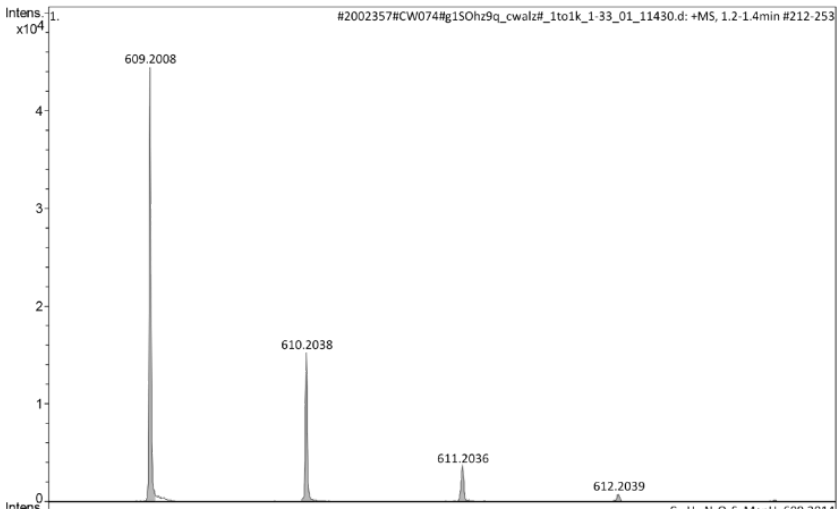

MaP1-C6-SMX (30)

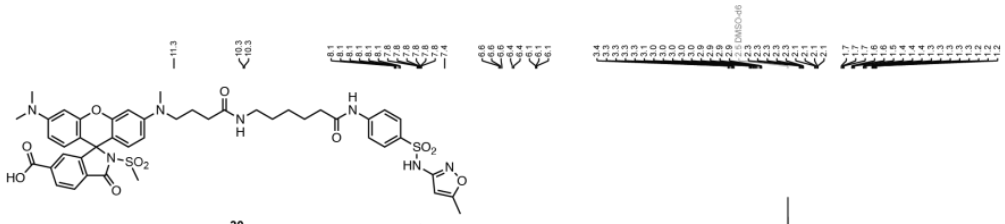

30

400 MHz
Solvent: DMSO-D_6
Nucleus: ^{1}H

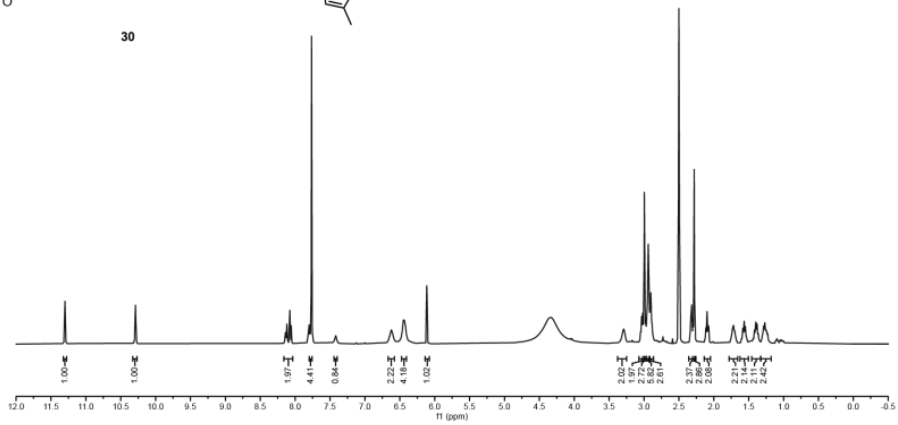

100 MHz
Solvent: DMSO-D_6
Nucleus: ^{13}C

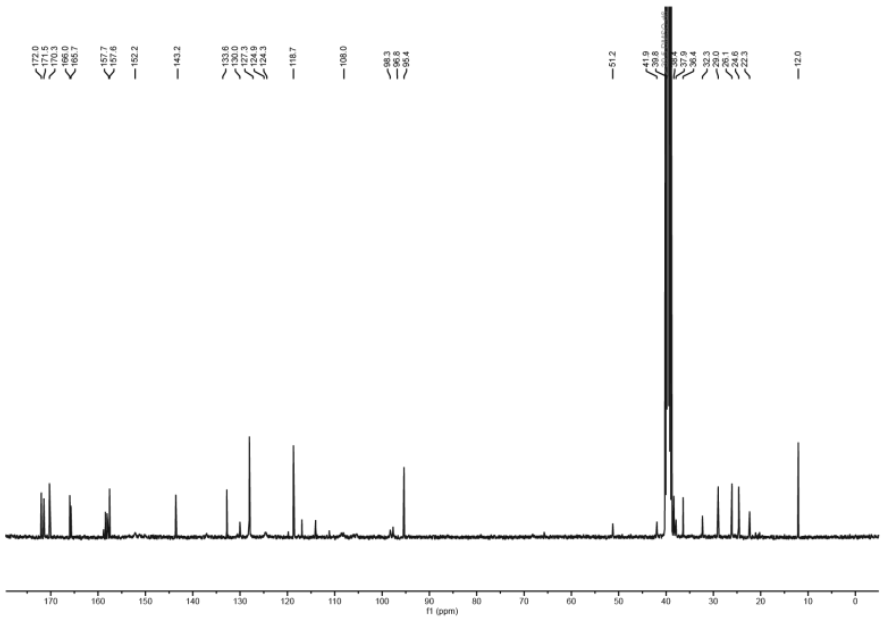

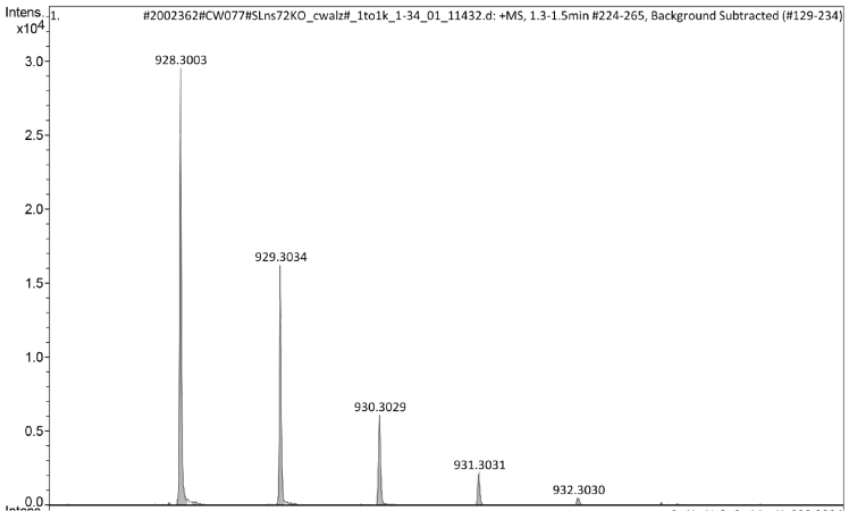

MaP555-C6-SMX (31)

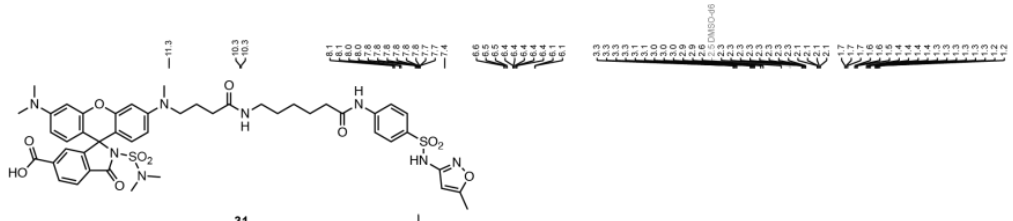

31

400 MHz
Solvent: DMSO-D_6
Nucleus: ^{1}H

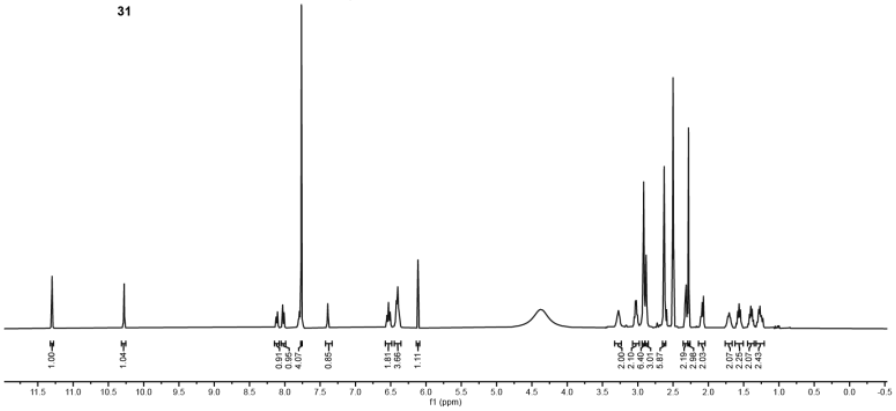

100 MHz
Solvent: DMSO-D_6
Nucleus: ^{13}C

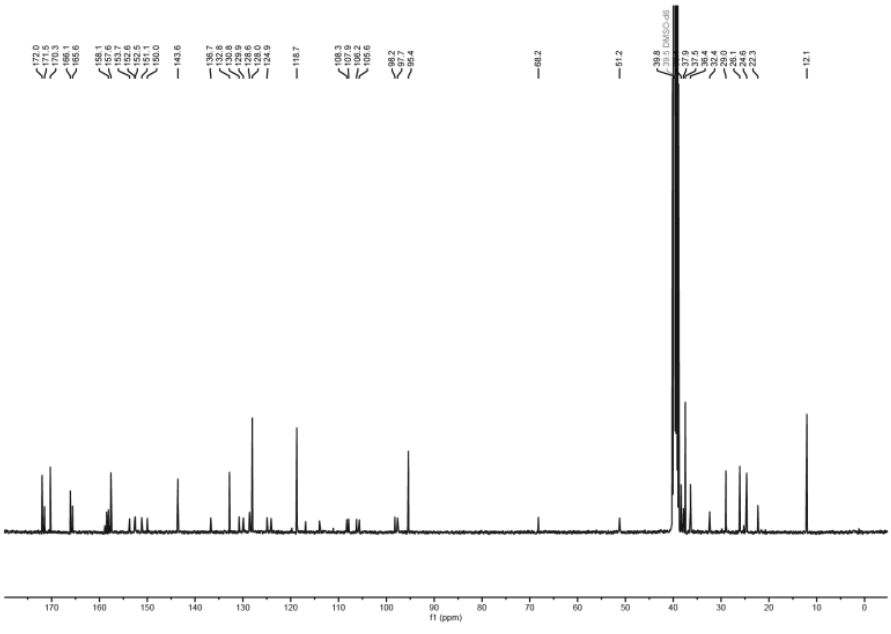

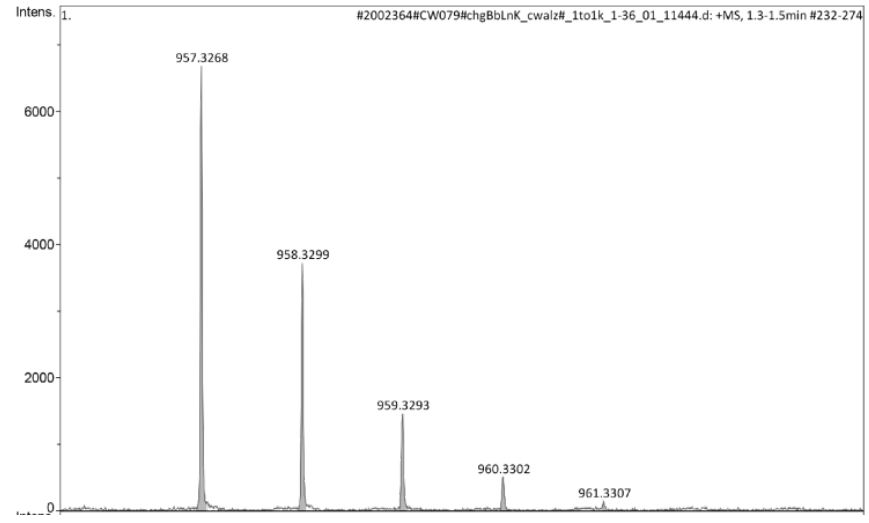

CP-MaP1-C6-SMX (32)

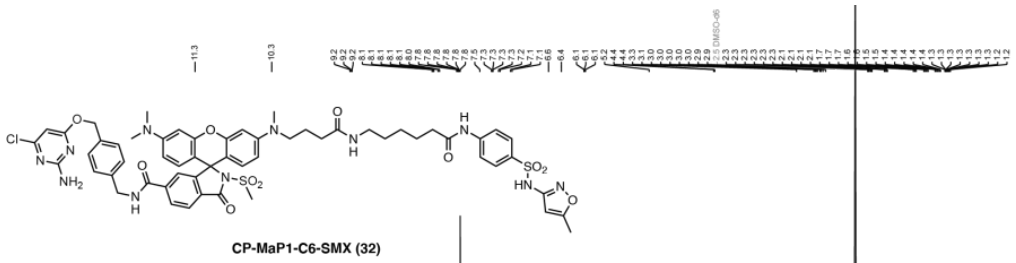

400 MHz
Solvent: DMSO-D_6
Nucleus: ^{1}H

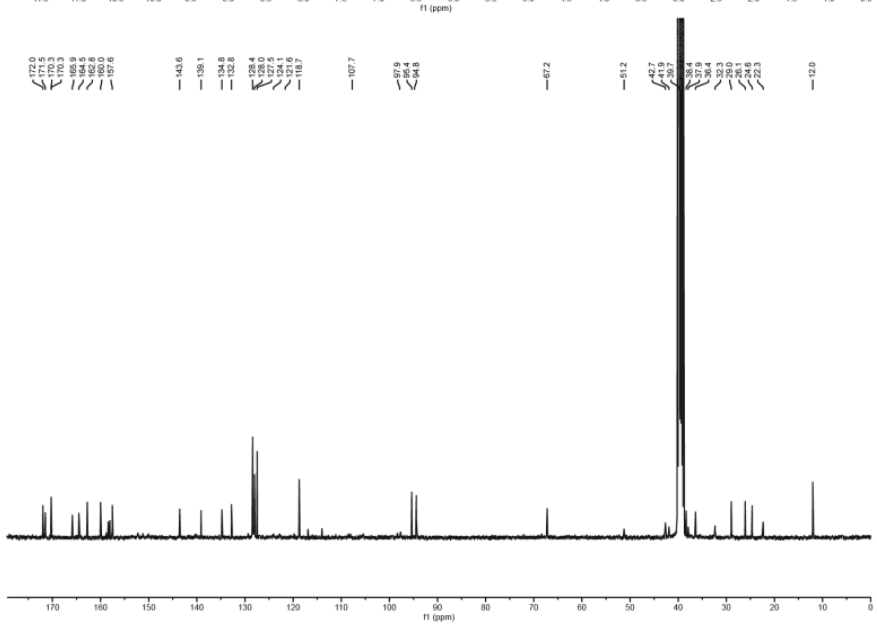

100 MHz
Solvent: DMSO-D_6
Nucleus: ^{13}C

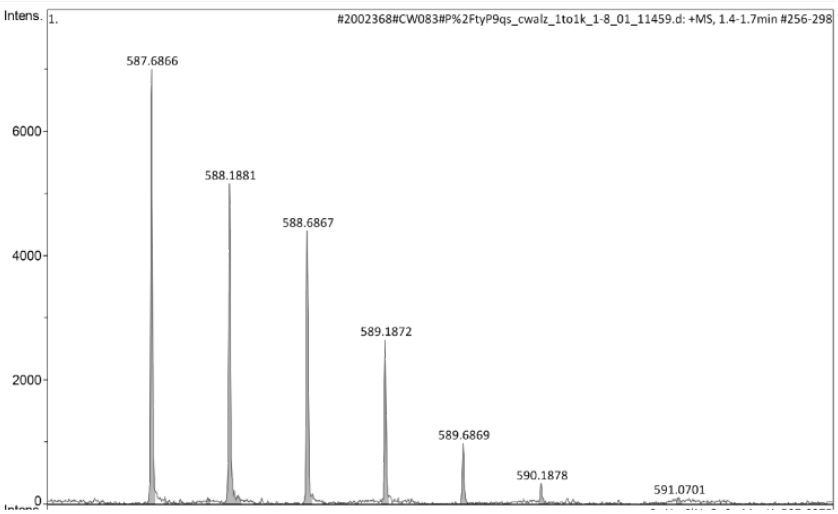

CP-MaP555-C6-SMX (33)

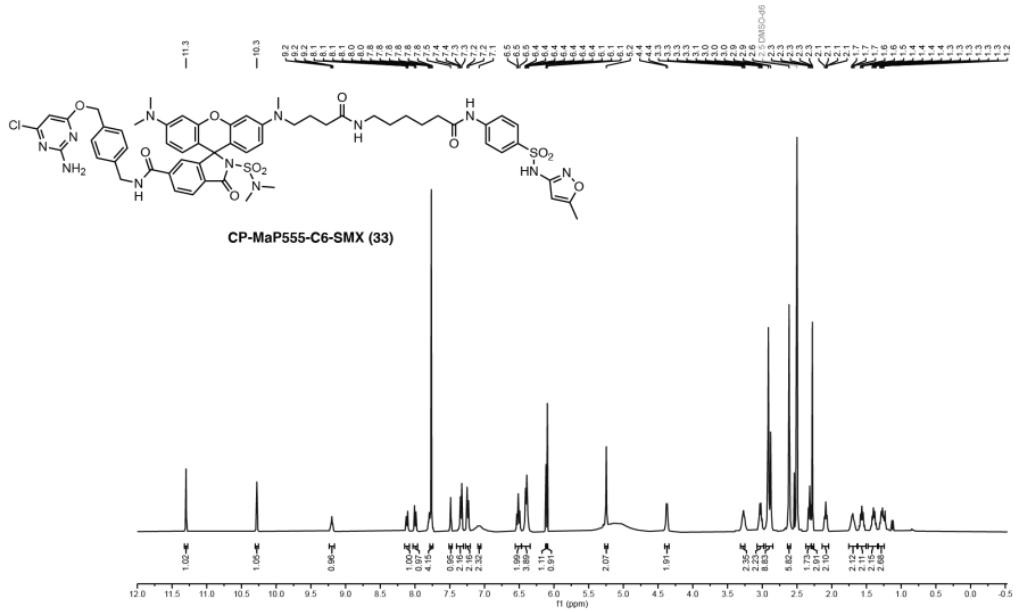

400 MHz
Solvent: DMSO-D_6
Nucleus: ^{1}H

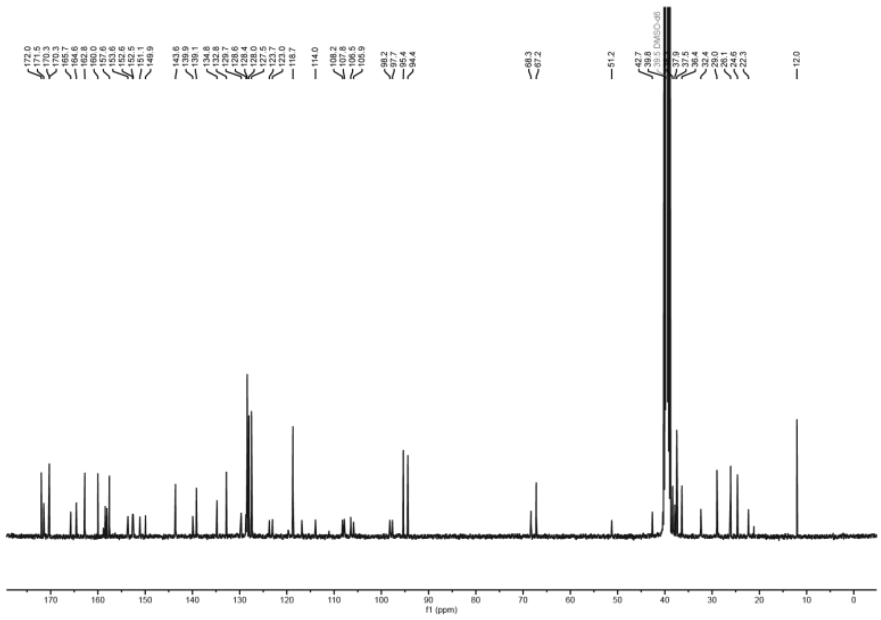

100 MHz
Solvent: DMSO-D_6
Nucleus: ^{13}C

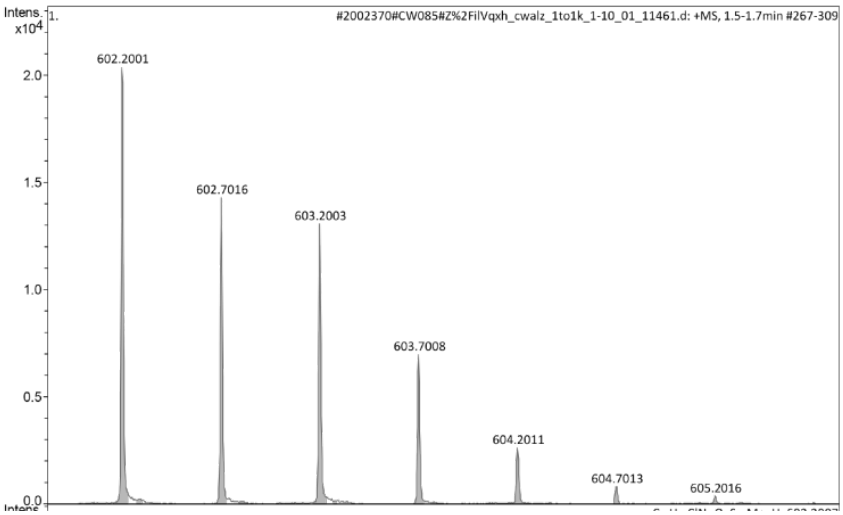

MaP1-PPT (34)

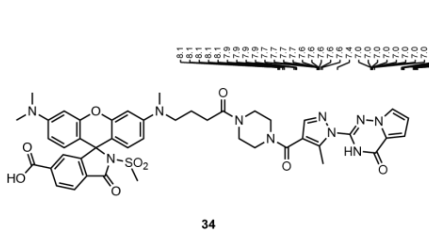

34

400 MHz
Solvent: DMSO-D_6
Nucleus: ^{1}H

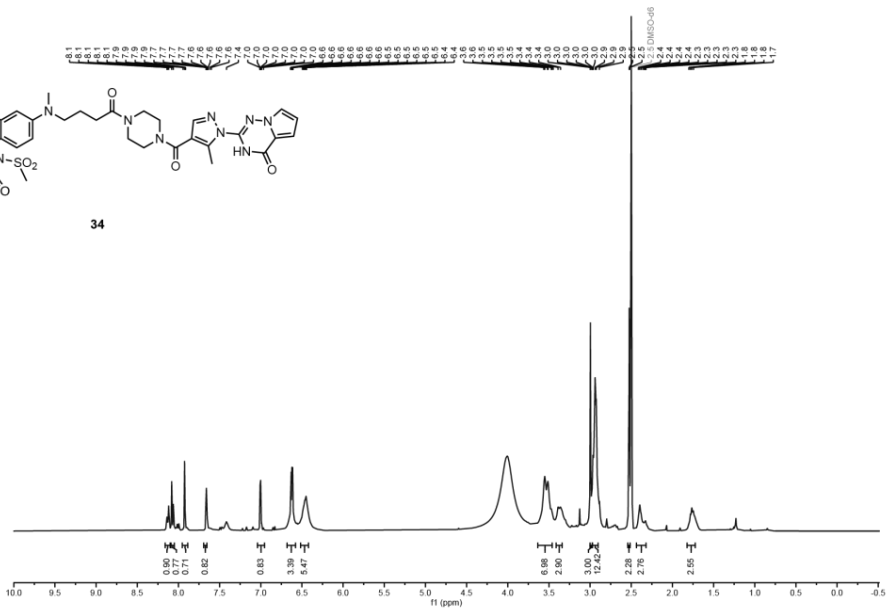

100 MHz
Solvent: DMSO-D_6
Nucleus: ^{13}C

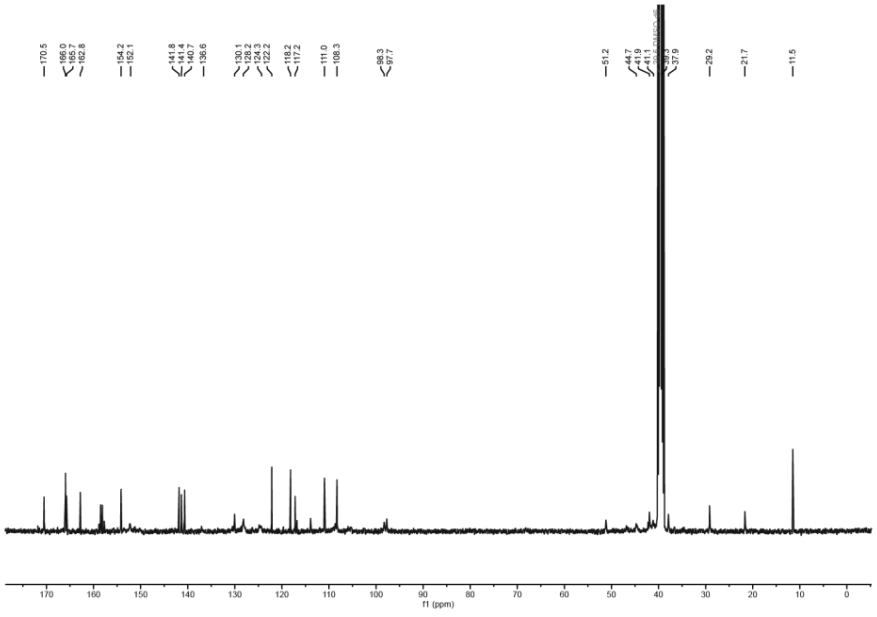

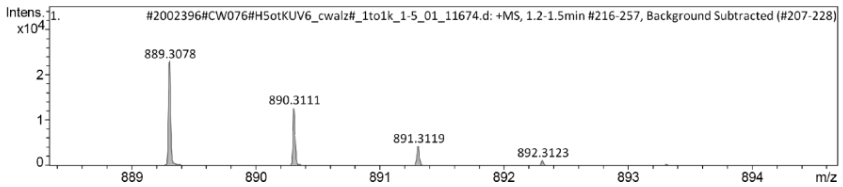

MaP555-PPT (35)

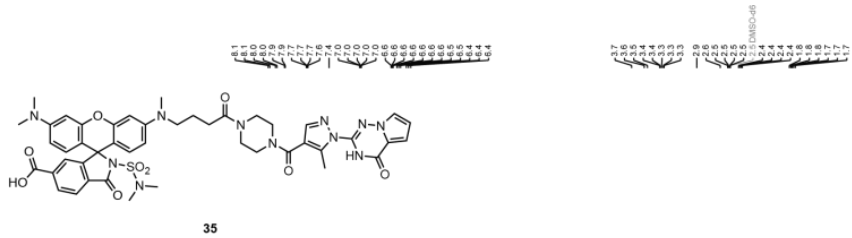

35

400 MHz
Solvent: DMSO-D_6
Nucleus: ^{1}H

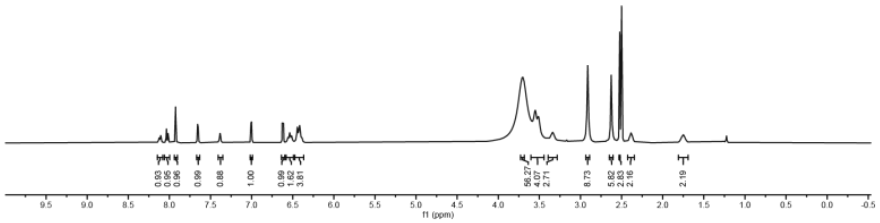

100 MHz
Solvent: DMSO-D_6
Nucleus: ^{13}C

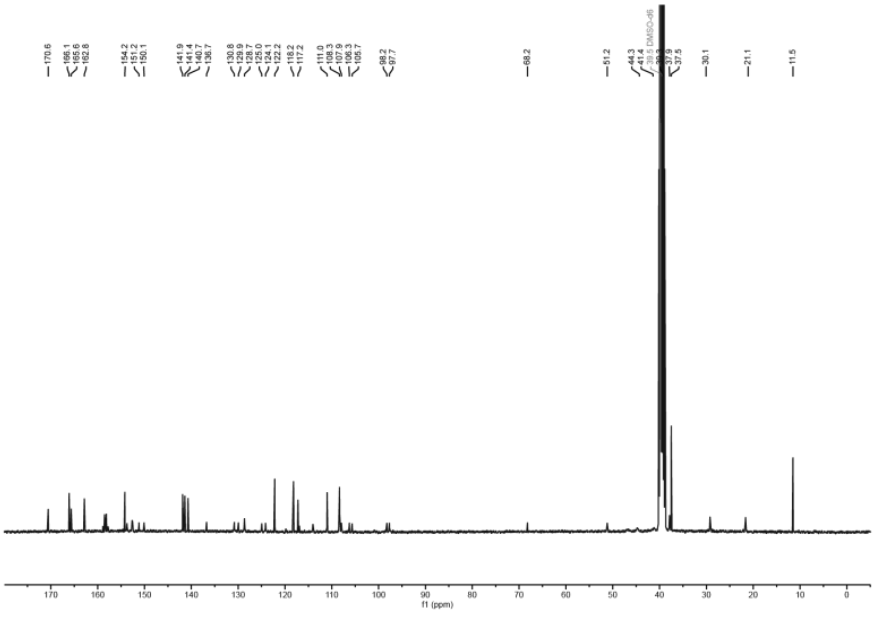

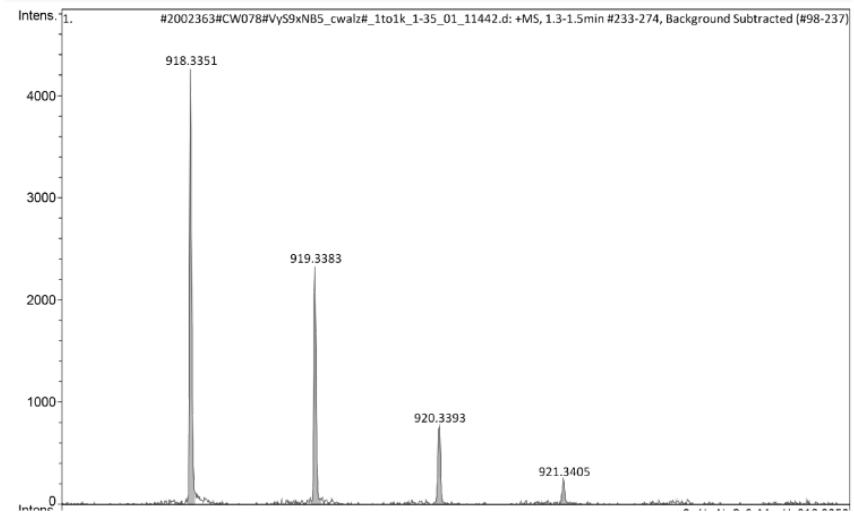

CP-MaP1-PPT(36)

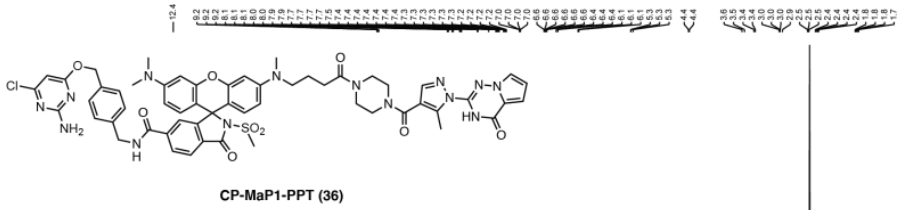

400 MHz
Solvent: DMSO-D_6
Nucleus: ^{1}H

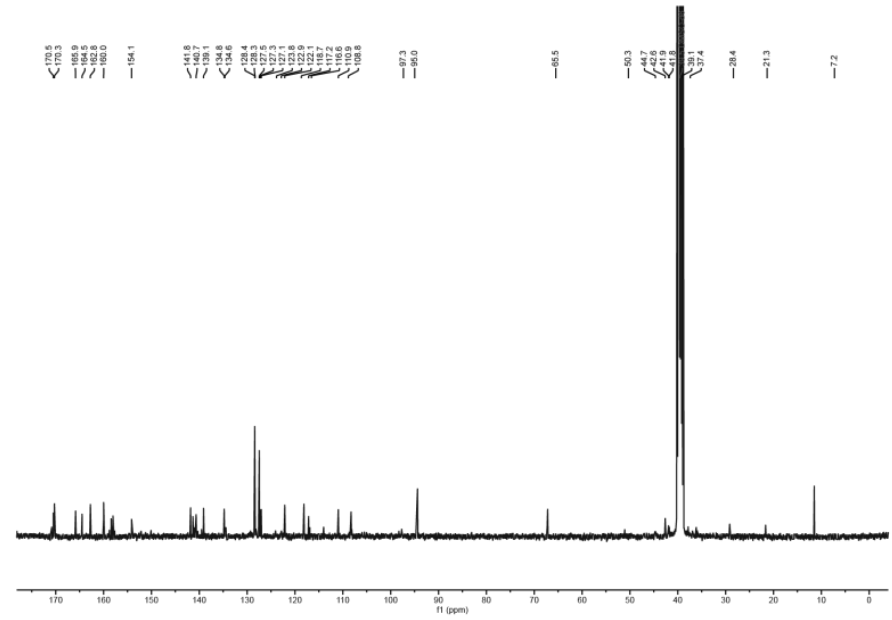

100 MHz
Solvent: DMSO-D_6
Nucleus: ^{13}C

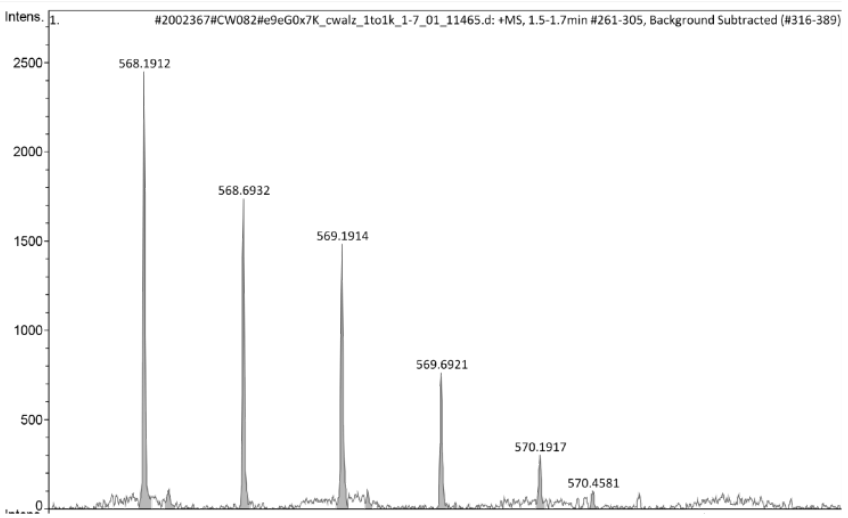

CP-MaP555-PPT (37)

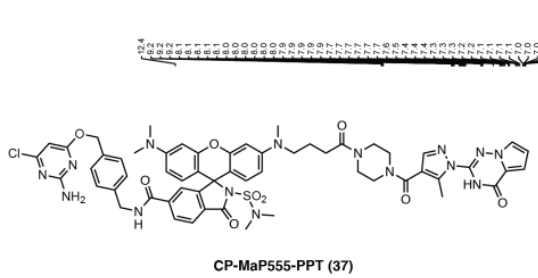

400 MHz
Solvent: DMSO-D_6
Nucleus: ^{1}H

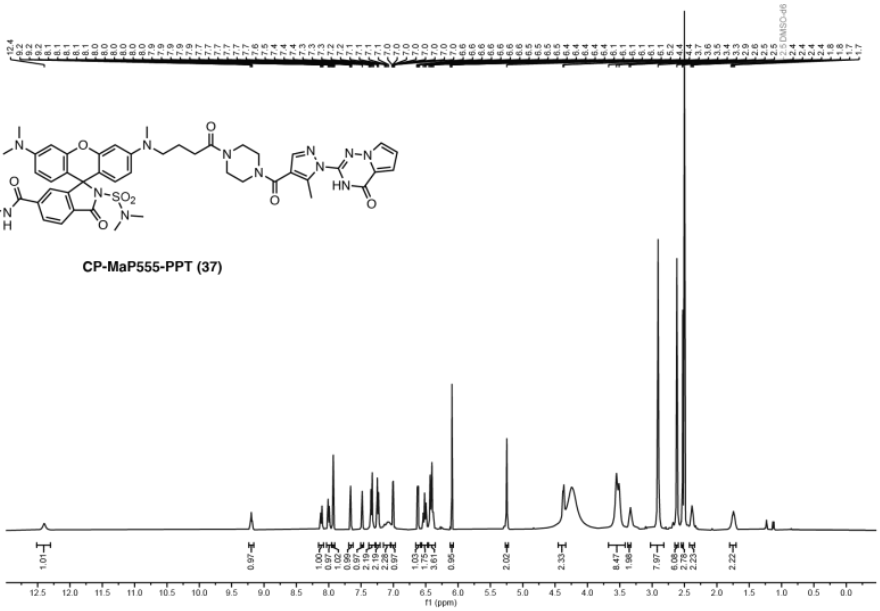

100 MHz
Solvent: DMSO-D_6
Nucleus: ^{13}C

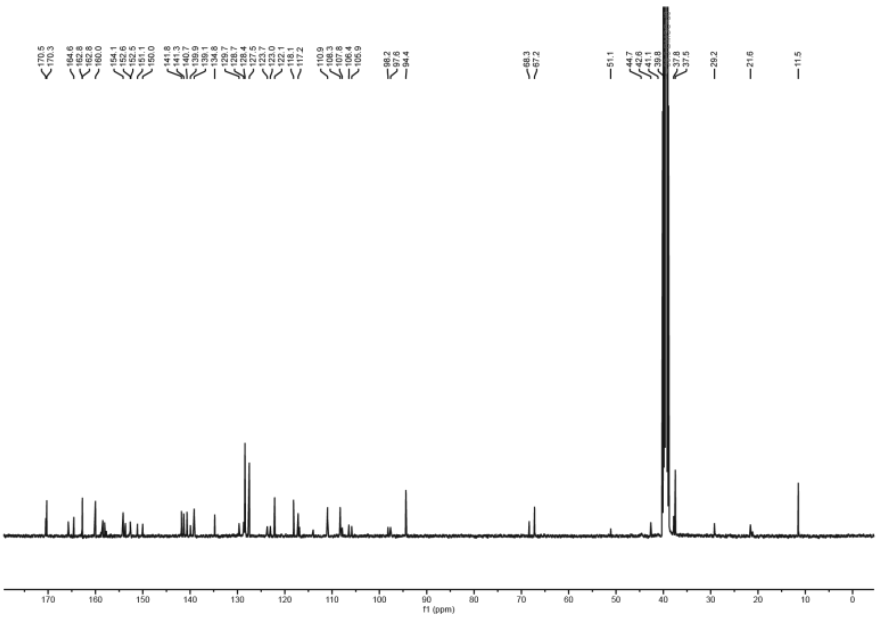

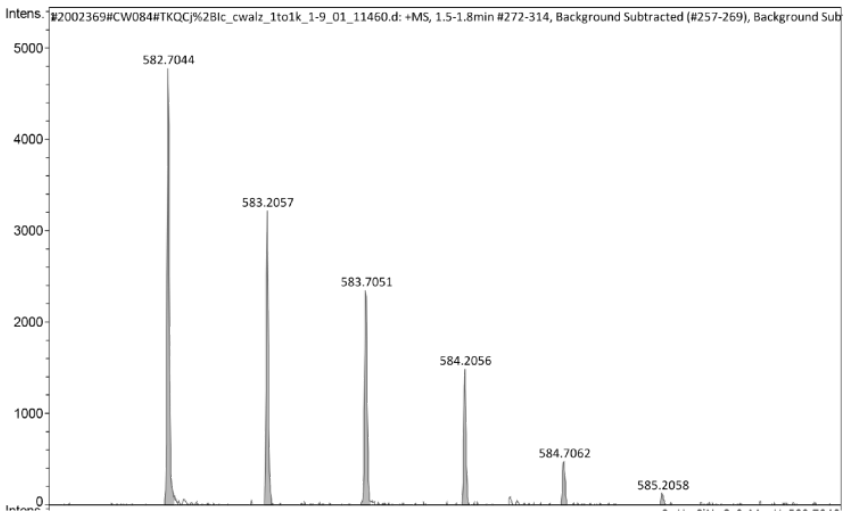

Allyl-TMR (41)

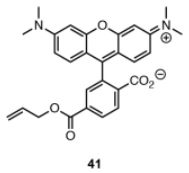

41

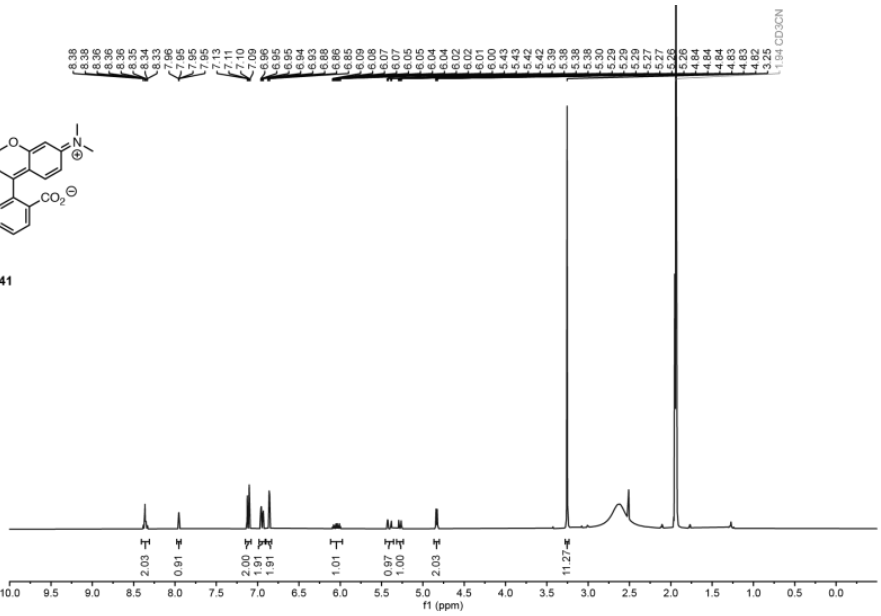

400 MHz
Solvent: MeCN-D_3
Nucleus: ^{1}H

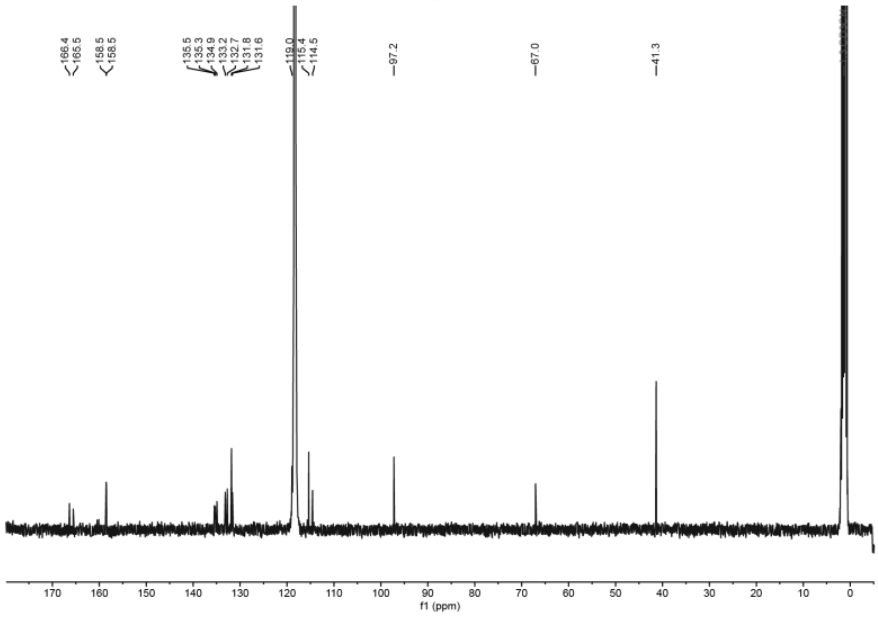

100 MHz
Solvent: MeCN-D_3
Nucleus: ^{13}C

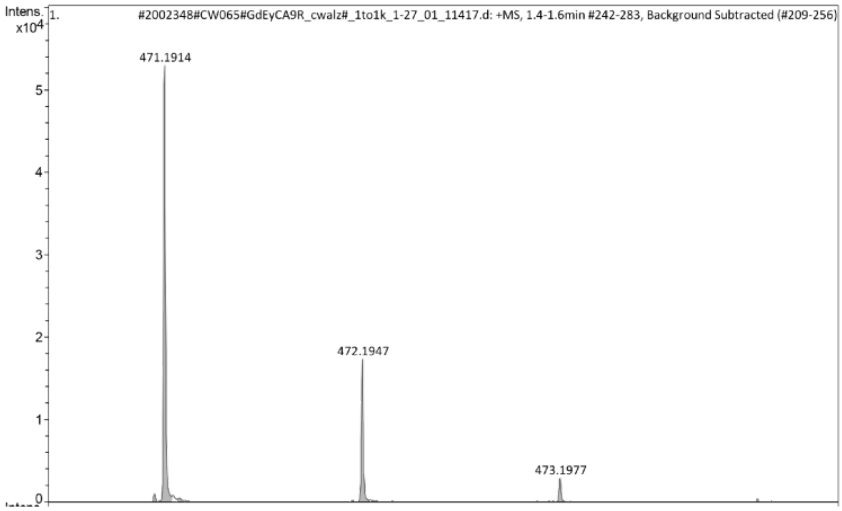

Benzyl butanoate (39)

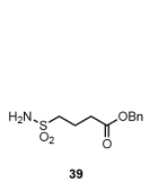

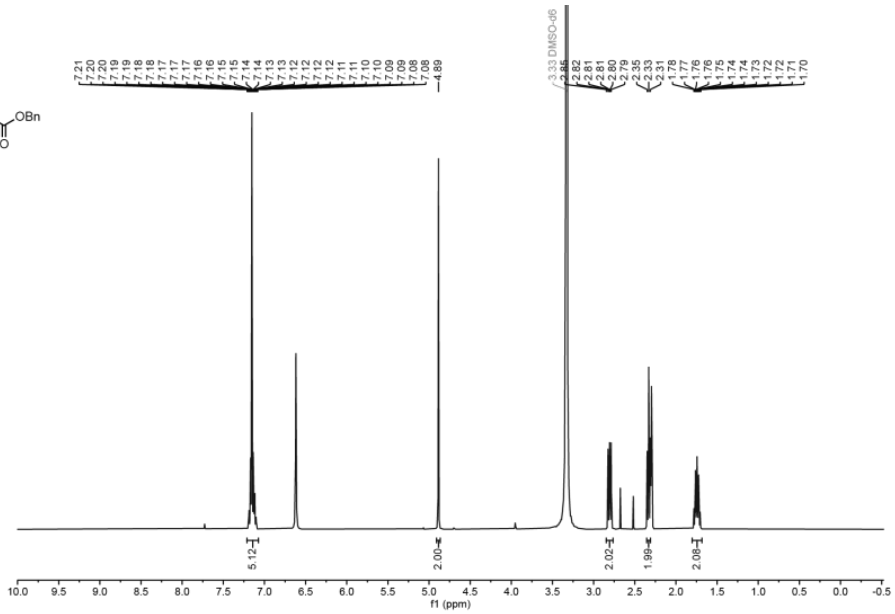

400 MHz
Solvent: DMSO-D_6
Nucleus: ^{1}H

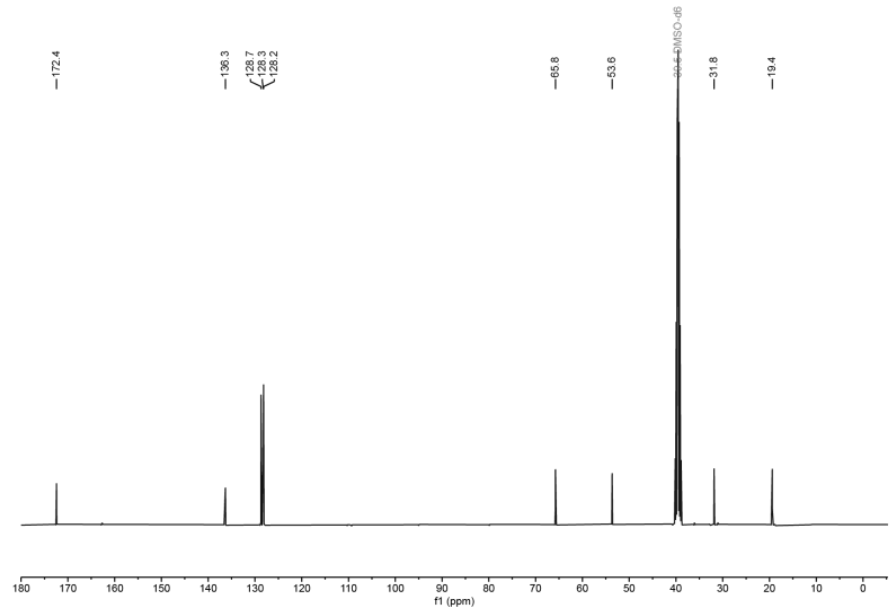

100 MHz
Solvent: DMSO-D_6
Nucleus: ^{13}C

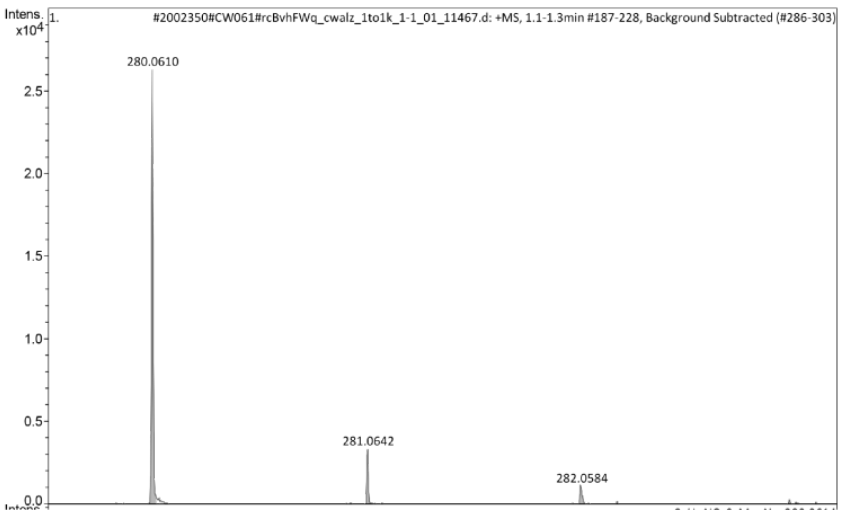

Allyl-benzyl-TMR (42)

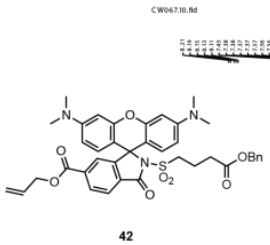

42

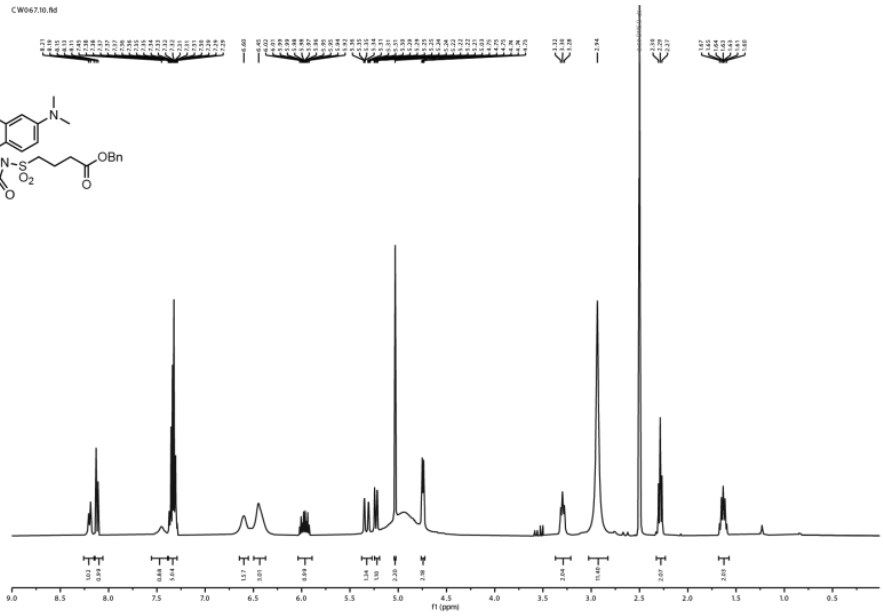

400 MHz
Solvent: DMSO-D_6
Nucleus: ^{1}H

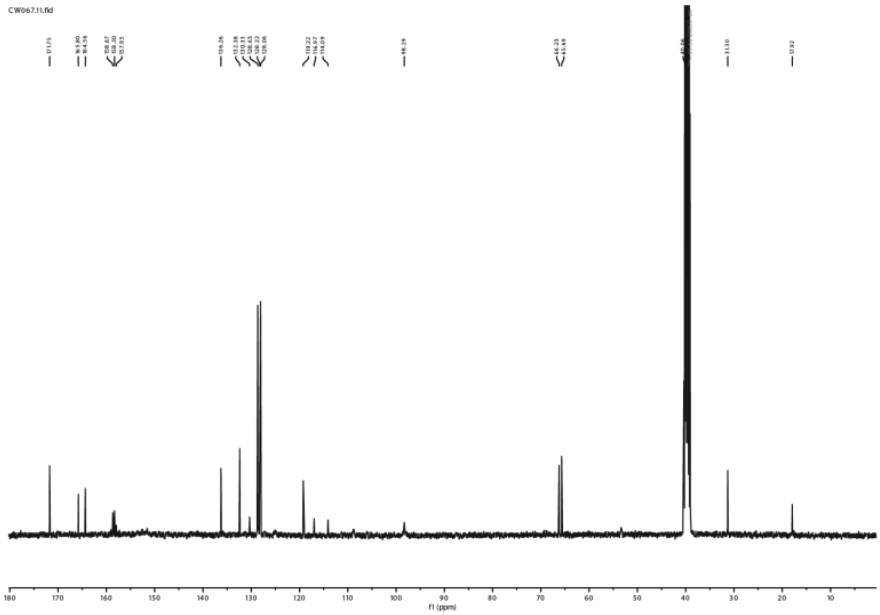

100 MHz
Solvent: DMSO-D_6
Nucleus: ^{13}C

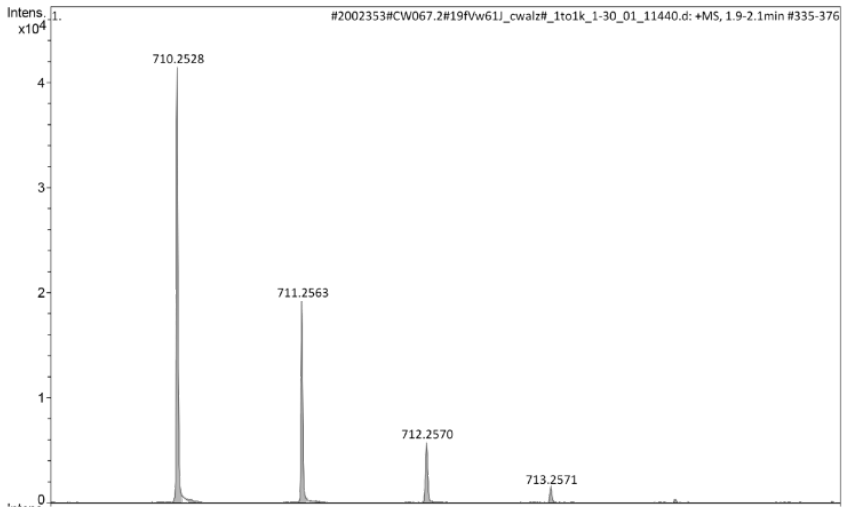

Benzyl-MaP3 (43)

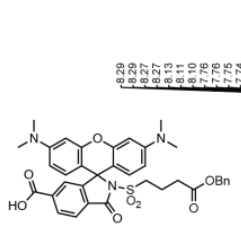

43

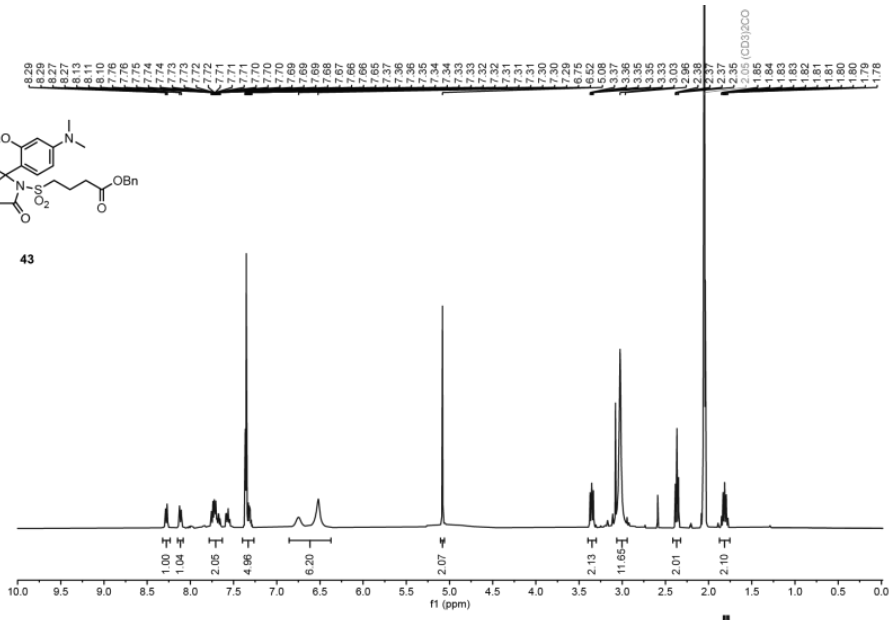

400 MHz
Solvent: Acetone-D_6
Nucleus: ^{1}H

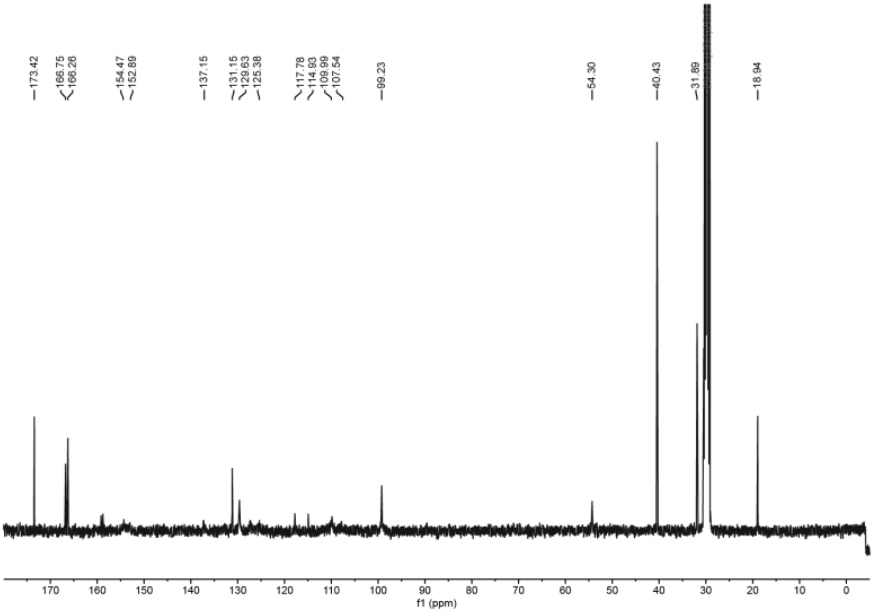

100 MHz
Solvent: Acetone-D_6
Nucleus: ^{13}C

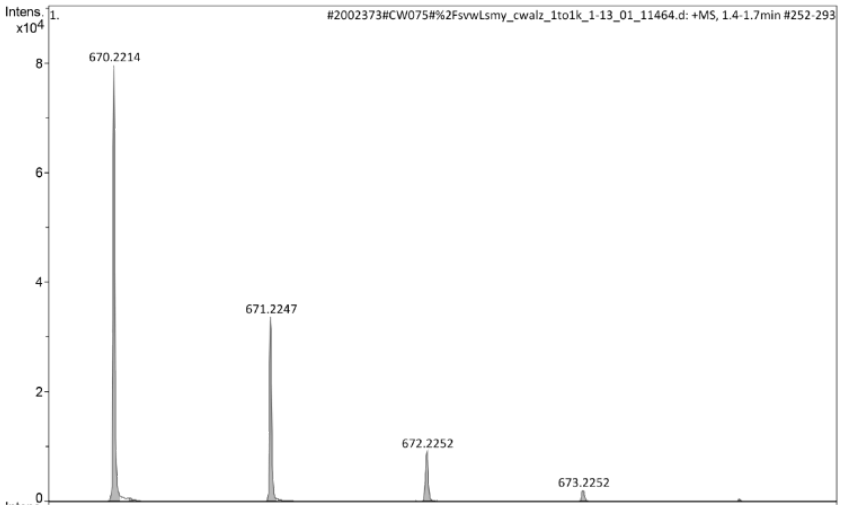

MaP3 (44)

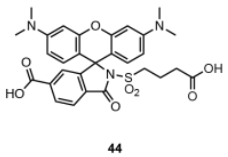

44

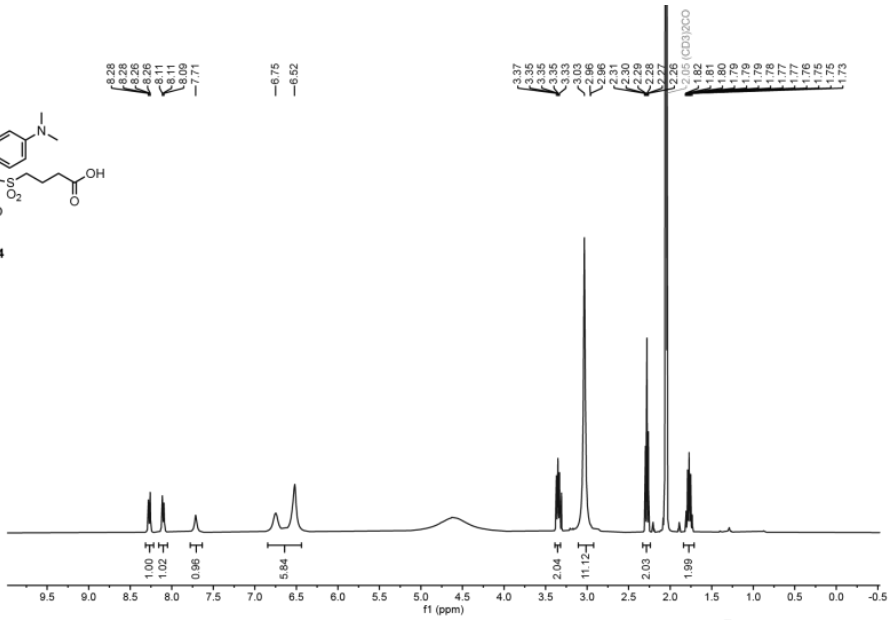

400 MHz
Solvent: Acetone-D_6
Nucleus: ^{1}H

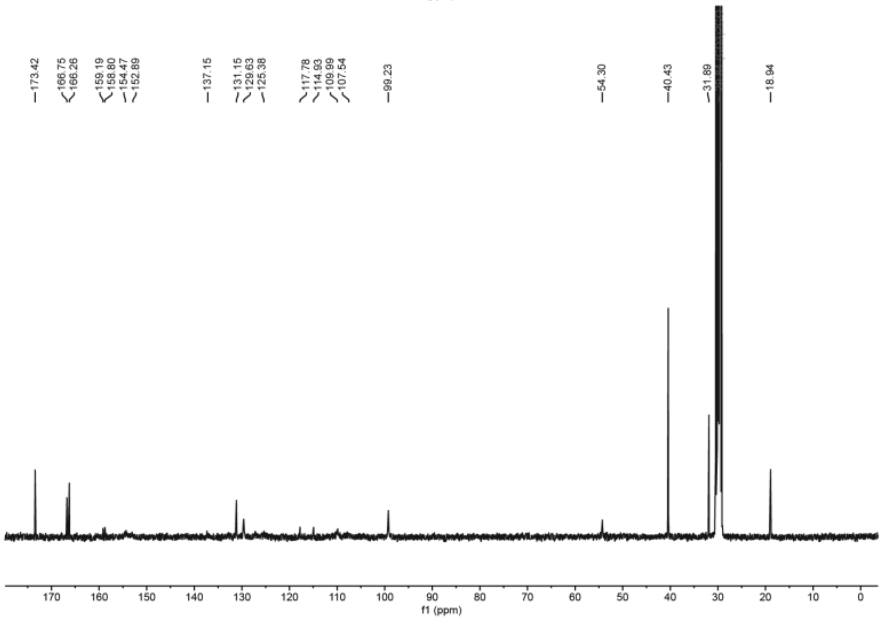

100 MHz
Solvent: Acetone-D_6
Nucleus: ^{13}C

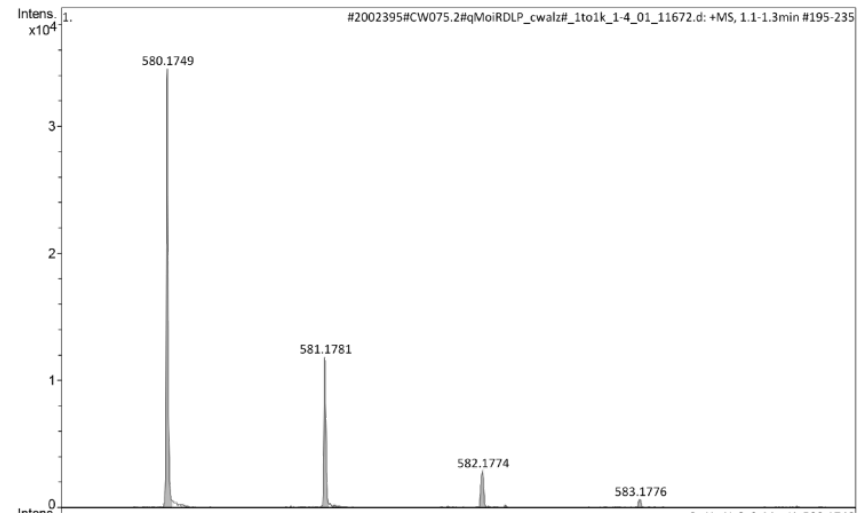

MaP3-C6-SMX (45)

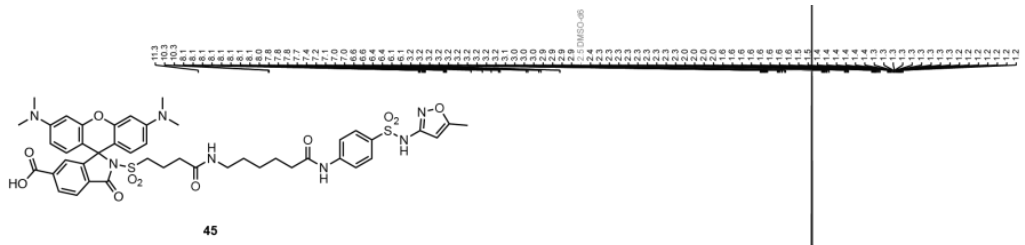

45

400 MHz
Solvent: DMSO-D_6
Nucleus: ^{1}H

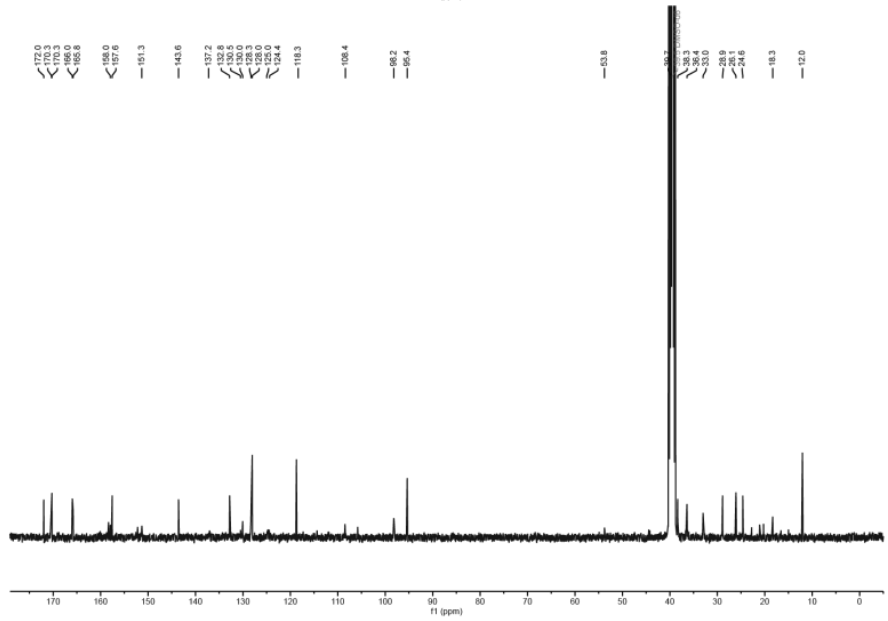

100 MHz
Solvent: DMSO-D_6
Nucleus: ^{13}C

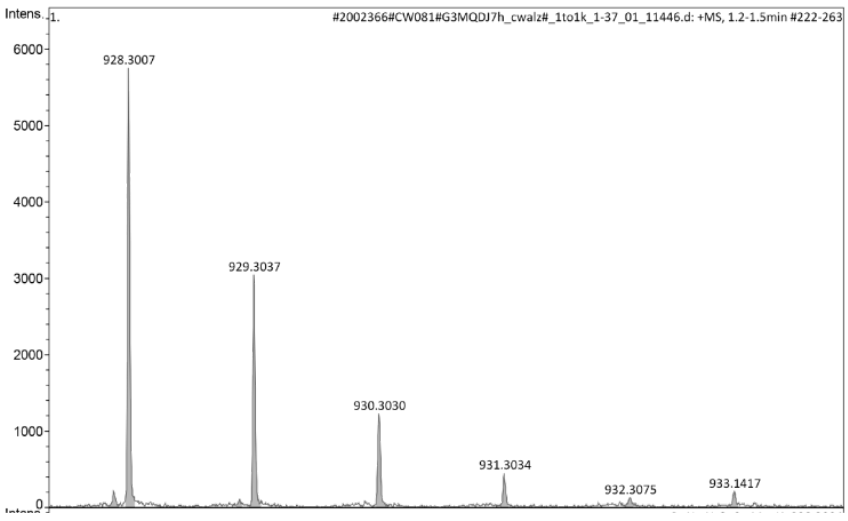

CP-MaP3-C6-SMX (46)

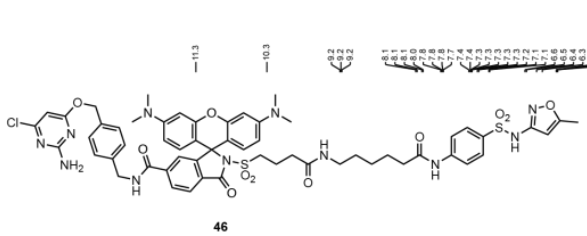

46

400 MHz
Solvent: DMSO-D_6
Nucleus: ^{1}H

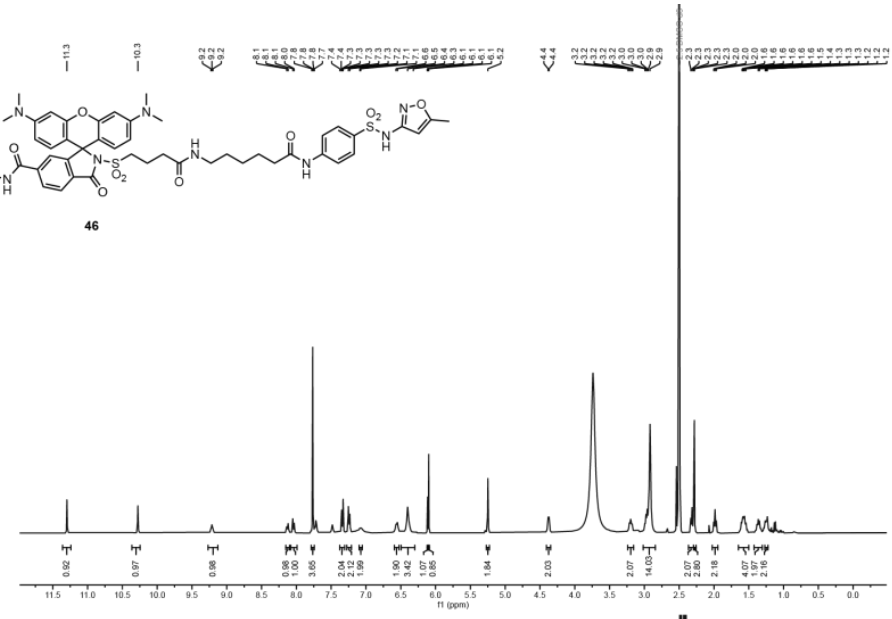

100 MHz
Solvent: DMSO-D_6
Nucleus: ^{13}C

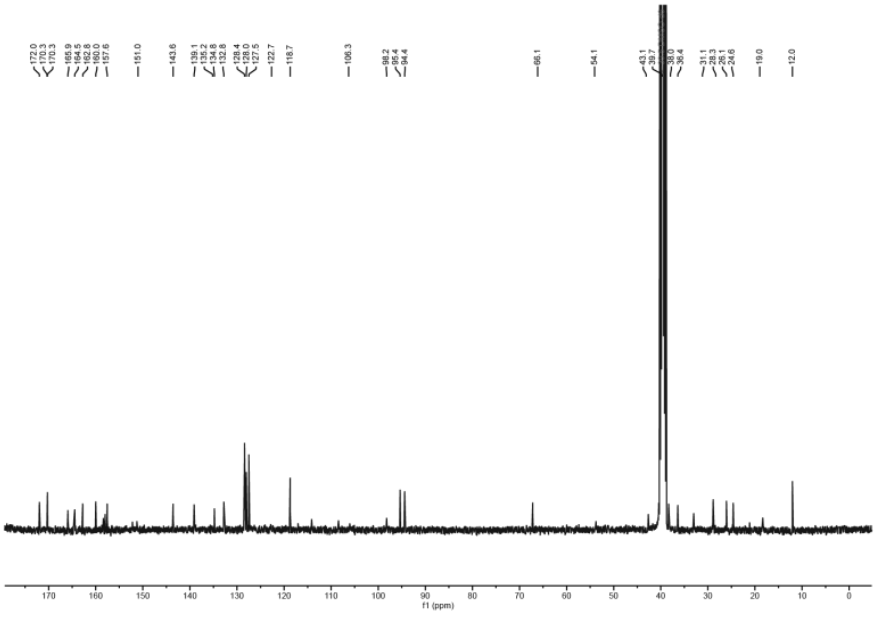

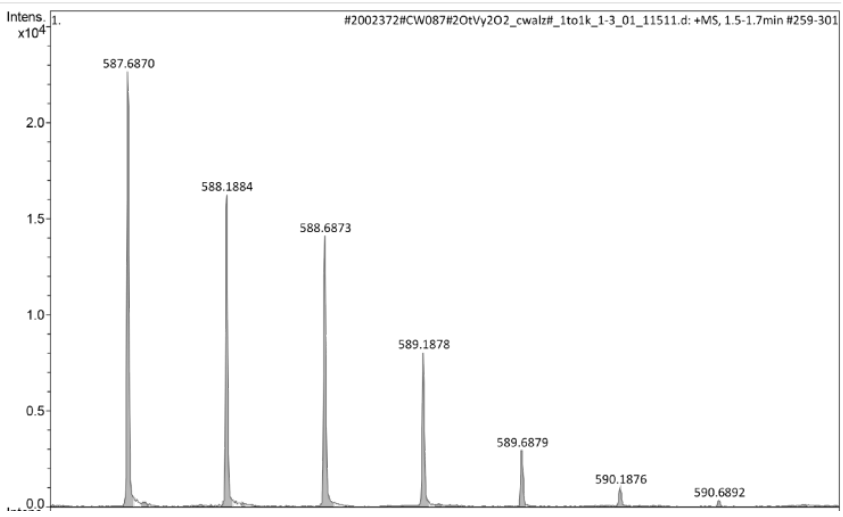

MaP3-PPT (47)

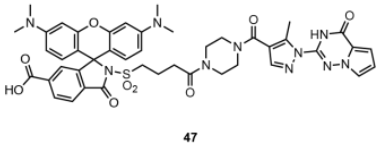

47

400 MHz
Solvent: DMSO-D_6
Nucleus: ^{1}H

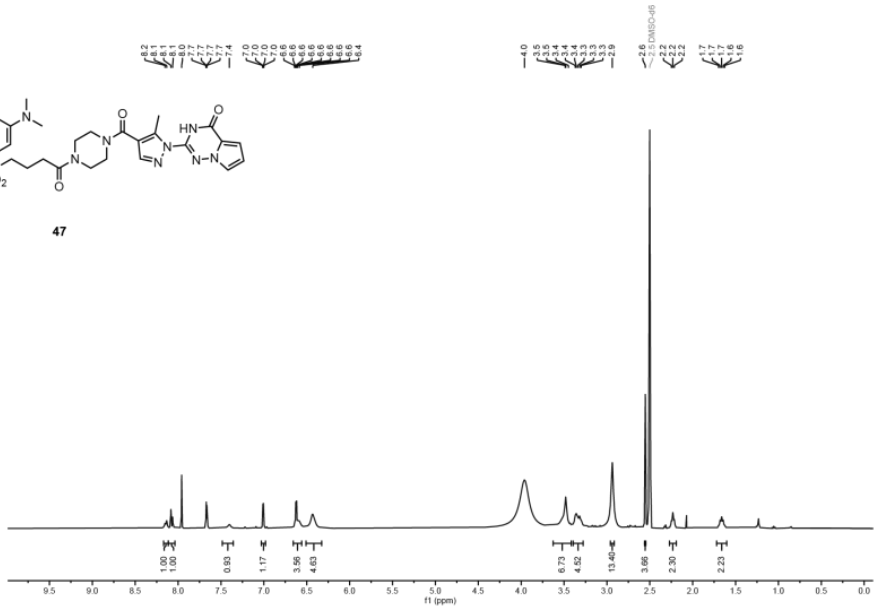

100 MHz
Solvent: DMSO-D_6
Nucleus: ^{13}C

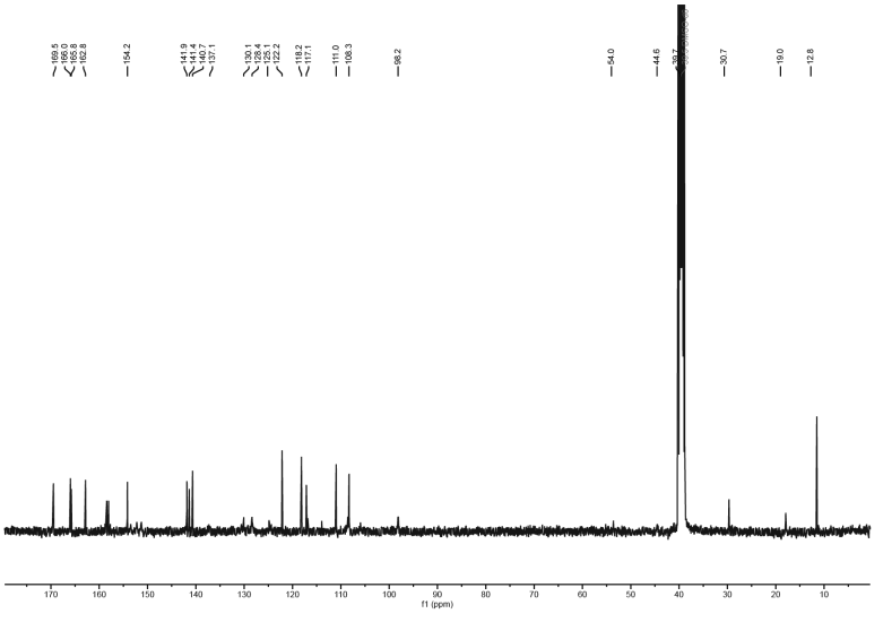

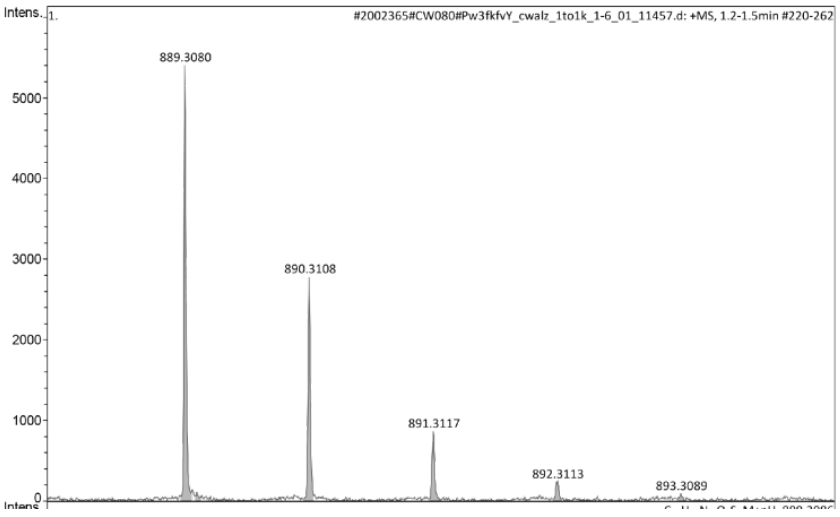

CP-MaP3-PPT (48)

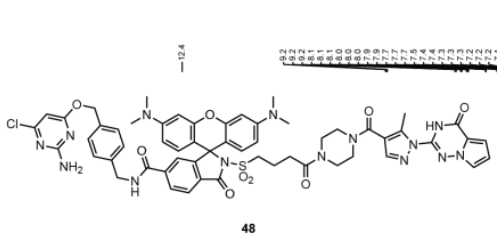

48

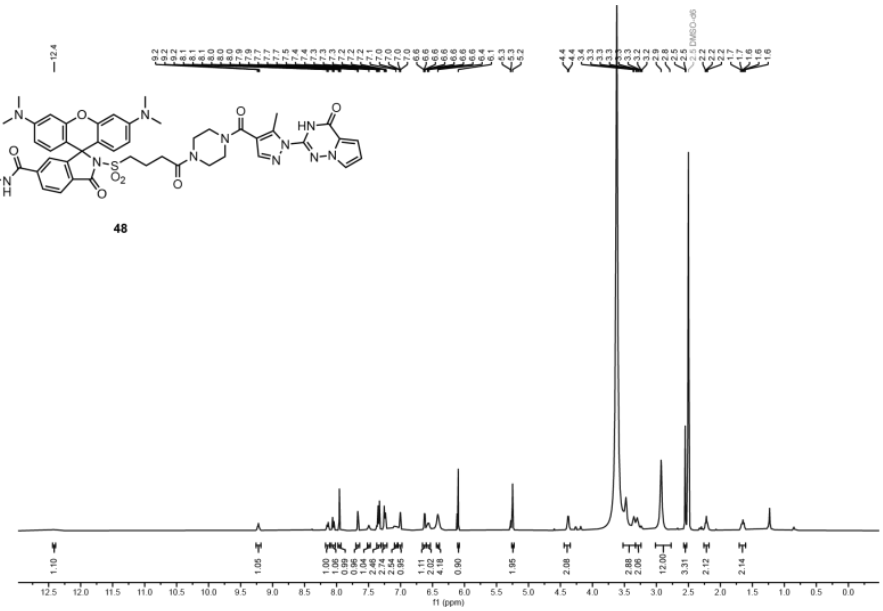

400 MHz
Solvent: DMSO-D_6
Nucleus: ^{1}H

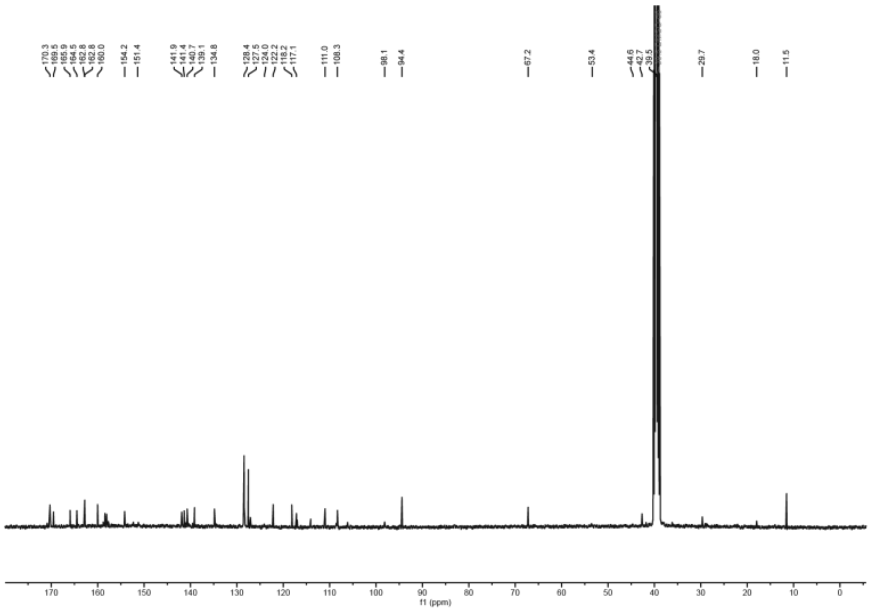

100 MHz
Solvent: DMSO-D_6
Nucleus: ^{13}C

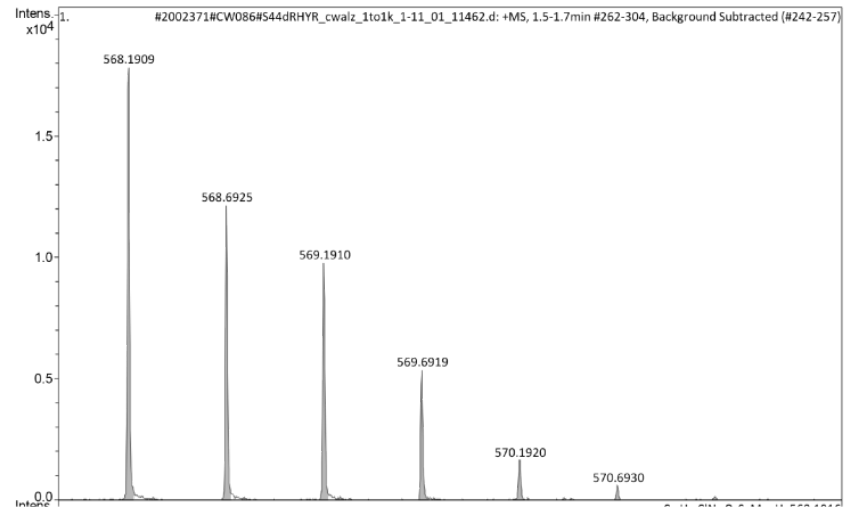

8 References

[1] A. Zecchin, P. C. Stapor, J. Goveia, P. Carmeliet, *Curr. Opin. Biotechnol.* **2015**, *34*, 73-81.

[2] M. R. Depaoli, H. Bischof, E. Eroglu, S. Burgstaller, J. Ramadani-Muja, T. Rauter, M. Schinagl, M. Waldeck-Weiermair, J. C. Hay, W. F. Graier, R. Malli, *Pharmacol. Ther.* **2019**, *202*, 98-119.

[3] K. Huber, P. Khamehgir-Silz, T. Schramm, V. Gorshkov, B. Spengler, A. Römpp, *Anal. Bioanal. Chem.* **2018**, *410*, 5825-5837.

[4] M. Y. Berezin, S. Achilefu, *Chem. Rev.* **2010**, *110*, 2641-2684.

[5] E. C. Greenwald, S. Mehta, J. Zhang, *Chem. Rev.* **2018**.

[6] B. Nagel, H. Dellweg, L. M. Gierasch, *Pure Appl. Chem.* **1992**, *64*, 143-168.

[7] J. G. Park, A. E. Palmer, in *Fluorescent Protein-Based Biosensors: Methods and Protocols* (Eds.: J. Zhang, Q. Ni, R. H. Newman), Humana Press, Totowa, NJ, **2014**, pp. 29-47.

[8] A. Bolbat, C. Schultz, *Biol. Cell.* **2017**, *109*, 1-23.

[9] B. Wallace, P. J. Atzberger, *PLOS ONE* **2017**, *12*, e0177122.

[10] B. T. Bajar, E. S. Wang, S. Zhang, M. Z. Lin, J. Chu, *Sensors* **2016**, *16*.

[11] B. Hellenkamp, S. Schmid, O. Doroshenko, O. Opanasyuk, R. Kühnemuth, S. Rezaei Adariani, B. Ambrose, M. Aznauryan, A. Barth, V. Birkedal, M. E. Bowen, H. Chen, T. Cordes, T. Eilert, C. Fijen, C. Gebhardt, M. Götz, G. Gouridis, E. Gratton, T. Ha, P. Hao, C. A. Hanke, A. Hartmann, J. Hendrix, L. L. Hildebrandt, V. Hirschfeld, J. Hohlbein, B. Hua, C. G. Hübner, E. Kallis, A. N. Kapanidis, J.-Y. Kim, G. Krainer, D. C. Lamb, N. K. Lee, E. A. Lemke, B. Levesque, M. Levitus, J. J. McCann, N. Naredi-Rainer, D. Nettels, T. Ngo, R. Qiu, N. C. Robb, C. Röcker, H. Sanabria, M. Schlierf, T. Schröder, B. Schuler, H. Seidel, L. Streit, J. Thurn, P. Tinnefeld, S. Tyagi, N. Vandenberk, A. M. Vera, K. R. Weninger, B. Wünsch, I. S. Yanez-Orozco, J. Michaelis, C. A. M. Seidel, T. D. Craggs, T. Hugel, *Nat. Methods* **2018**, *15*, 669-676.

[12] L. B. McGown, K. Nithipatikom, *Appl. Spectrosc. Rev.* **2000**, *35*, 353-393.

[13] P. G. Wu, L. Brand, *Anal. Biochem.* **1994**, *218*, 1-13.

[14] C. Deo, L. D. Lavis, *Curr. Opin. Neurobiol.* **2018**, *50*, 101-108.

[15] L. D. Lavis, R. T. Raines, *ACS Chem. Biol.* **2008**, *3*, 142-155.

[16] R. Y. Tsien, *Annu. Rev. Neurosci.* **1989**, *12*, 227-253.

[17] A. K. Stout, I. J. Reynolds, *Neuroscience* **1999**, *89*, 91-100.

[18] P. Liu, V. Grenier, W. Hong, V. R. Muller, E. W. Miller, *J. Am. Chem. Soc.* **2017**, *139*, 17334-17340.

[19] A. E. Palmer, Y. Qin, J. G. Park, J. E. McCombs, *Trends Biotechnol.* **2011**, *29*, 144-152.

[20] J. Nakai, M. Ohkura, K. Imoto, *Nat. Biotechnol.* **2001**, *19*, 137-141.

[21] V. Liss, B. Barlag, M. Nietschke, M. Hensel, *Sci. Rep.* **2015**, *5*, 17740.

[22] G. V. Los, L. P. Encell, M. G. McDougall, D. D. Hartzell, N. Karassina, C. Zimprich, M. G. Wood, R. Learish, R. F. Ohana, M. Urh, D. Simpson, J. Mendez, K. Zimmerman, P. Otto, G. Vidugiris, J. Zhu, A. Darzins, D. H. Klaubert, R. F. Bulleit, K. V. Wood, *ACS Chem. Biol.* **2008**, *3*, 373-382.

[23] A. Keppler, S. Gendreizig, T. Gronemeyer, H. Pick, H. Vogel, K. Johnsson, *Nat. Biotechnol.* **2003**, *21*, 86-89.

[24] C. Deo, S.-H. Sheu, J. Seo, D. E. Clapham, L. D. Lavis, *J. Am. Chem. Soc.* **2019**, *141*, 13734-13738.

[25] C. Deo, A. S. Abdelfattah, H. K. Bhargava, A. J. Berro, N. Falco, H. Farrants, B. Moeyaert, M. Chupanova, L. D. Lavis, E. R. Schreiter, *Nat. Chem. Biol.* **2021**, *17*, 718-723.

[26] S. Abdelfattah Ahmed, T. Kawashima, A. Singh, O. Novak, H. Liu, Y. Shuai, Y.-C. Huang, L. Campagnola, C. Seeman Stephanie, J. Yu, J. Zheng, B. Grimm Jonathan, R. Patel, J. Friedrich, D. Mensh Brett, L. Paninski, J. Macklin John, J. Murphy Gabe, K. Podgorski, B.-J. Lin, T.-W. Chen, C. Turner Glenn, Z. Liu, M. Koyama, K. Svoboda, B. Ahrens Misha, D. Lavis Luke, R. Schreiter Eric, *Science* **2019**, *365*, 699-704.
[27] M. a. Brun, R. Griss, L. Reymond, K.-T. Tan, J. Piguet, R. J. R. W. Peters, H. Vogel, K. Johnsson, *J. Am. Chem. Soc.* **2011**, *133*, 16235-16242.
[28] M. a. Brun, K.-T. Tan, E. Nakata, M. J. Hinner, K. Johnsson, *J. Am. Chem. Soc.* **2009**, *131*, 5873-5884.
[29] H. Farrants, J. Hiblot, R. Griss, K. Johnsson, in *Synthetic Protein Switches: Methods and Protocols* (Ed.: V. Stein), Springer New York, New York, NY, **2017**, pp. 101-117.
[30] L. Xue, I. A. Karpenko, J. Hiblot, K. Johnsson, *Nat. Chem. Biol.* **2015**, *11*, 917-923.
[31] W. Ying, *Antioxid. Redox Signal.* **2007**, *10*, 179-206.
[32] C. Cantó, Keir J. Menzies, J. Auwerx, *Cell Metab.* **2015**, *22*, 31-53.
[33] R. H. Houtkooper, C. Cantó, R. J. Wanders, J. Auwerx, *Endocr. Rev.* **2010**, *31*, 194-223.
[34] K. W. Ryu, T. Nandu, J. Kim, S. Challa, R. J. DeBerardinis, W. L. Kraus, *Science* **2018**, *360*, eaan5780.
[35] R. Zapata-Pérez, R. J. A. Wanders, C. D. M. van Karnebeek, R. H. Houtkooper, *EMBO Mol. Med.* **2021**, *13*, e13943.
[36] E. Katsyuba, A. Mottis, M. Zietak, F. De Franco, V. van der Velpen, K. Gariani, D. Ryu, L. Cialabrini, O. Matilainen, P. Liscio, N. Giacchè, N. Stokar-Regenscheit, D. Legouis, S. de Seigneux, J. Ivanisevic, N. Raffaelli, K. Schoonjans, R. Pellicciari, J. Auwerx, *Nature* **2018**, *563*, 354-359.
[37] D. A. Bender, *Molecular Aspects of Medicine* **1983**, *6*, 101-197.
[38] J. R. Revollo, A. A. Grimm, S.-i. Imai, *J. Biol. Chem.* **2004**, *279*, 50754-50763.
[39] A. Rongvaux, R. J. Shea, M. H. Mulks, D. Gigot, J. Urbain, O. Leo, F. Andris, *Eur. J. Immunol.* **2002**, *32*, 3225-3234.
[40] P. Bieganowski, C. Brenner, *Cell* **2004**, *117*, 495-502.
[41] L. Agledal, M. Niere, M. Ziegler, *Redox Rep.* **2010**, *15*, 2-10.
[42] L. Chen, Z. Zhang, A. Hoshino, H. D. Zheng, M. Morley, Z. Arany, J. D. Rabinowitz, *Nat. Metab.* **2019**, *1*, 404-415.
[43] S.-H. Jo, M.-K. Son, H.-J. Koh, S.-M. Lee, I.-H. Song, Y.-O. Kim, Y.-S. Lee, K.-S. Jeong, W. B. Kim, J.-W. Park, B. J. Song, T.-L. Huhe, *J. Biol. Chem.* **2001**, *276*, 16168-16176.
[44] S. Murai, A. Ando, S. Ebara, M. Hirayama, Y. Satomi, T. Hara, *Oncogenesis* **2017**, *6*, e329-e329.
[45] M. Di Stefano, L. Conforti, *FEBS J.* **2013**, *280*, 4711-4728.
[46] E. Verdin, *Science (New York, N.Y.)* **2015**, *350*, 1208-1213.
[47] P. Jagtap, C. Szabó, *Nat. Rev. Drug Discov.* **2005**, *4*, 421-440.
[48] H. Zhu, Y.-D. Tang, G. Zhan, C. Su, C. Zheng, *Front. Immunol.* **2021**, *12*.
[49] M.-C. Caron, A. K. Sharma, J. O'Sullivan, L. R. Myler, M. T. Ferreira, A. Rodrigue, Y. Coulombe, C. Ethier, J.-P. Gagné, M.-F. Langelier, J. M. Pascal, I. J. Finkelstein, M. J. Hendzel, G. G. Poirier, J.-Y. Masson, *Nat. Commun.* **2019**, *10*, 2954.
[50] R. H. Houtkooper, E. Pirinen, J. Auwerx, *Nat. Rev. Mol. Cell Biol.* **2012**, *13*, 225-238.
[51] Z. Radak, K. Suzuki, A. Posa, Z. Petrovszky, E. Koltai, I. Boldogh, *Redox Biol.* **2020**, *35*, 101467.
[52] Y. Zhu, Y. Yan, D. R. Gius, A. Vassilopoulos, *Curr. Opin. Oncol.* **2013**, *25*.
[53] L. Zhong, R. Mostoslavsky, *Cell Metab.* **2011**, *13*, 621-626.
[54] Y. Nakahata, S. Sahar, G. Astarita, M. Kaluzova, P. Sassone-Corsi, *Science* **2009**, *324*, 654-657.
[55] J. M. Ribeiro, J. Canales, A. Cabezas, J. R. Rodrigues, R. M. Pinto, I. López-Villamizar, M. J. Costas, J. C. Cameselle, *Sci. Rep.* **2018**, *8*, 1036.
[56] H. C. Lee, *Annu. Rev. Pharmacool. Toxicol.* **2001**, *41*, 317-345.

[57] S. Banerjee, T. F. Walseth, K. Borgmann, L. Wu, K. R. Bidasee, M. S. Kannan, A. Ghorpade, *J. Neuroimmune Pharmacol.* **2008**, *3*, 154.
[58] W. Xiao, R.-S. Wang, D. E. Handy, J. Loscalzo, *Antioxid. Redox Signal.* **2017**, *28*, 251-272.
[59] R. Franco, J. A. Cidlowski, *Cell Death Differ.* **2009**, *16*, 1303-1314.
[60] J. Fernandez, R. A. Wilson, *PLOS ONE* **2014**, *9*, e87300.
[61] A. Panday, M. K. Sahoo, D. Osorio, S. Batra, *Cell. Mol. Immunol.* **2015**, *12*, 5-23.
[62] F. Magnani, S. Nenci, E. Millana Fananas, M. Ceccon, E. Romero, M. W. Fraaije, A. Mattevi, *Proc. Natl. Acad. Sci.* **2017**, *114*, 6764.
[63] G. T. Nguyen, E. R. Green, J. Mecsas, *Front. Cell. Infect. Microbiol.* **2017**, *7*, 373.
[64] M. Sedeek, R. Nasrallah, R. M. Touyz, R. L. Hébert, *J. Am. Soc. Nephrol.* **2013**, *24*, 1512.
[65] E. Georgieva, D. Ivanova, Z. Zhelev, R. Bakalova, M. Gulubova, I. Aoki, *Anticancer Res.* **2017**, *37*, 5373.
[66] I. García-Ruiz, P. Solís-Muñoz, D. Fernández-Moreira, M. Grau, T. Muñoz-Yagüe, J. A. Solís-Herruzo, *Sci. Rep.* **2016**, *6*, 23664.
[67] T. Ge, J. Yang, S. Zhou, Y. Wang, Y. Li, X. Tong, *Front. Endocrinol.* **2020**, *11*, 365.
[68] M. W. Ma, J. Wang, Q. Zhang, R. Wang, K. M. Dhandapani, R. K. Vadlamudi, D. W. Brann, *Mol. Neurodegener.* **2017**, *12*, 7.
[69] S. Lautrup, D. A. Sinclair, M. P. Mattson, E. F. Fang, *Cell Metab.* **2019**, *30*, 630-655.
[70] S. A. J. Trammell, B. J. Weidemann, A. Chadda, M. S. Yorek, A. Holmes, L. J. Coppey, A. Obrosov, R. H. Kardon, M. A. Yorek, C. Brenner, *Sci. Rep.* **2016**, *6*, 26933.
[71] Y. Lu, Y. Liu, Y. Pang, K. Pacak, C. Yang, *Pharmacol. Ther.* **2018**, *188*, 168-175.
[72] U. Galli, G. Colombo, C. Travelli, G. C. Tron, A. A. Genazzani, A. A. Grolla, *Front. Pharmacol.* **2020**, *11*, 656.
[73] N. Pollak, C. Dölle, M. Ziegler, *Biochem. J* **2007**, *402*, 205-218.
[74] X. A. Cambronne, W. L. Kraus, *Trends Biochem. Sci* **2020**, *45*, 858-873.
[75] T. O. Metz, Q. Zhang, J. S. Page, Y. Shen, S. J. Callister, J. M. Jacobs, R. D. Smith, *Biomark. Med.* **2007**, *1*, 159-185.
[76] S. A. J. Trammell, C. Brenner, *Comput. Struct. Biotechnol.* **2013**, *4*, e201301012.
[77] P. M. Schaefer, S. Kalinina, A. Rueck, C. A. F. von Arnim, B. von Einem, *Cytom. A* **2019**, *95*, 34-46.
[78] J. T. Sharick, P. F. Favreau, A. A. Gillette, S. M. Sdao, M. J. Merrins, M. C. Skala, *Sci. Rep.* **2018**, *8*, 5456.
[79] X. A. Cambronne, M. L. Stewart, D. Kim, A. M. Jones-Brunette, R. K. Morgan, D. L. Farrens, M. S. Cohen, R. H. Goodman, *Science (New York, N.Y.)* **2016**, *352*, 1474-1477.
[80] Y. Zou, A. Wang, L. Huang, X. Zhu, Q. Hu, Y. Zhang, X. Chen, F. Li, Q. Wang, H. Wang, R. Liu, F. Zuo, T. Li, J. Yao, Y. Qian, M. Shi, X. Yue, W. Chen, Z. Zhang, C. Wang, Y. Zhou, L. Zhu, Z. Ju, J. Loscalzo, Y. Yang, Y. Zhao, *Dev. Cell* **2020**, *53*, 240-252.e247.
[81] Y. P. Hung, J. G. Albeck, M. Tantama, G. Yellen, *Cell Metab.* **2011**, *14*, 545-554.
[82] Y. Zhao, Q. Hu, F. Cheng, N. Su, A. Wang, Y. Zou, H. Hu, X. Chen, H.-M. Zhou, X. Huang, K. Yang, Q. Zhu, X. Wang, J. Yi, L. Zhu, X. Qian, L. Chen, Y. Tang, J. Loscalzo, Y. Yang, *Cell Metab.* **2015**, *21*, 777-789.
[83] Y. Zhao, J. Jin, Q. Hu, H.-M. Zhou, J. Yi, Z. Yu, L. Xu, X. Wang, Y. Yang, J. Loscalzo, *Cell Metab.* **2011**, *14*, 555-566.
[84] O. Sallin, L. Reymond, C. Gondrand, F. Raith, B. Koch, K. Johnsson, *eLife* **2018**, *7*, e32638.
[85] R. Tao, Y. Zhao, H. Chu, A. Wang, J. Zhu, X. Chen, Y. Zou, M. Shi, R. Liu, N. Su, J. Du, H.-m. Zhou, L. Zhu, X. Qian, H. Liu, J. Loscalzo, Y. Yang, *Nat. Methods* **2017**, *14*, 720-728.
[86] W. D. Cameron, C. V. Bui, A. Hutchinson, P. Loppnau, S. Gräslund, J. V. Rocheleau, *Nat. Methods* **2016**, *13*, 352-358.

[87] H. Haruki, M. G. Pedersen, K. I. Gorska, F. Pojer, K. Johnsson, *Science* **2013**, *340*, 987.
[88] G. Lukinavičius, K. Umezawa, N. Olivier, A. Honigmann, G. Yang, T. Plass, V. Mueller, L. Reymond, I. R. Corrêa Jr, Z.-G. Luo, C. Schultz, E. a. Lemke, P. Heppenstall, C. Eggeling, S. Manley, K. Johnsson, *Nat. Chem.* **2013**, *5*, 132-139.
[89] Y. Geng, A. Pertsinidis, *Sci. Rep.* **2021**, *11*, 12220.
[90] C. J. Hedeskov, K. Capito, P. Thams, *Biochem. J.* **1987**, *241*, 161-167.
[91] J. Zhang, A. ten Pierick, H. M. van Rossum, R. M. Seifar, C. Ras, J.-M. Daran, J. J. Heijnen, S. A. Wahl, *Sci. Rep.* **2015**, *5*, 12846-12846.
[92] Y. Kallberg, U. Oppermann, B. Persson, *FEBS J.* **2010**, *277*, 2375-2386.
[93] N. Tanaka, T. Nonaka, M. Nakanishi, Y. Deyashiki, A. Hara, Y. Mitsui, *Structure* **1996**, *4*, 33-45.
[94] S. O'Hagan, D. B. Kell, *Mar. Drugs* **2020**, *18*.
[95] I. Patik, D. Kovacsics, O. Német, M. Gera, G. Várady, B. Stieger, B. Hagenbuch, G. Szakács, C. Özvegy-Laczka, *Biochem. Pharmacol.* **2015**, *98*, 649-658.
[96] T. De Bruyn, G. J. P. van Westen, A. P. Ijzerman, B. Stieger, P. de Witte, P. F. Augustijns, P. P. Annaert, *Mol. Pharmacol.* **2013**, *83*, 1257.
[97] E. Jouan, M. Le Vee, C. Denizot, G. Da Violante, O. Fardel, *Fundam. Clin. Pharmacol.* **2014**, *28*, 65-77.
[98] C. W. Cunningham, A. Mukhopadhyay, G. H. Lushington, B. S. J. Blagg, T. E. Prisinzano, J. P. Krise, *Mol. Pharm.* **2010**, *7*, 1301-1310.
[99] M. D. Shultz, *J. Med. Chem.* **2019**, *62*, 1701-1714.
[100] C. A. Lipinski, F. Lombardo, B. W. Dominy, P. J. Feeney, *Adv. Drug Deliv. Rev.* **2001**, *46*, 3-26.
[101] C. A. Lipinski, *J. Pharmacol. Toxicol. Methods* **2000**, *44*, 235-249.
[102] L. Z. Benet, C. M. Hosey, O. Ursu, T. I. Oprea, *Adv. Drug Deliv. Rev.* **2016**, *101*, 89-98.
[103] Bradley C. Doak, B. Over, F. Giordanetto, J. Kihlberg, *Chem. Biol.* **2014**, *21*, 1115-1142.
[104] A. Daina, O. Michielin, V. Zoete, *Sci. Rep.* **2017**, *7*, 42717.
[105] J. B. Grimm, A. K. Muthusamy, Y. Liang, T. A. Brown, W. C. Lemon, R. Patel, R. Lu, J. J. Macklin, P. J. Keller, N. Ji, L. D. Lavis, *Nat. Methods* **2017**, *14*, 987.
[106] J. B. Grimm, B. P. English, J. Chen, J. P. Slaughter, Z. Zhang, A. Revyakin, R. Patel, J. J. Macklin, D. Normanno, R. H. Singer, T. Lionnet, L. D. Lavis, *Nat. Methods* **2015**, *12*, 244.
[107] L. Wang, M. S. Frei, A. Salim, K. Johnsson, *J. Am. Chem. Soc.* **2019**, *141*, 2770-2781.
[108] S. Schuster, M. Penke, T. Gorski, S. Petzold-Quinque, G. Damm, R. Gebhardt, W. Kiess, A. Garten, *PLOS ONE* **2014**, *9*, e91045.
[109] M. Hasmann, I. Schemainda, *Cancer Research* **2003**, *63*, 7436.
[110] R. Grant, *Nat. Prec.* **2010**.
[111] S. J. F. Cronin, C. Seehus, A. Weidinger, S. Talbot, S. Reissig, M. Seifert, Y. Pierson, E. McNeill, M. S. Longhi, B. L. Turnes, T. Kreslavsky, M. Kogler, D. Hoffmann, M. Ticevic, D. da Luz Scheffer, L. Tortola, D. Cikes, A. Jais, M. Rangachari, S. Rao, M. Paolino, M. Novatchkova, M. Aichinger, L. Barrett, A. Latremoliere, G. Wirnsberger, G. Lametschwandtner, M. Busslinger, S. Zicha, A. Latini, S. C. Robson, A. Waisman, N. Andrews, M. Costigan, K. M. Channon, G. Weiss, A. V. Kozlov, M. Tebbe, K. Johnsson, C. J. Woolf, J. M. Penninger, *Nature* **2018**, *563*, 564-568.
[112] A. N. Butkevich, M. L. Bossi, G. Lukinavičius, S. W. Hell, *J. Am. Chem. Soc.* **2019**, *141*, 981-989.
[113] L. Wang, M. Tran, E. D'Este, J. Roberti, B. Koch, L. Xue, K. Johnsson, *Nature Chemistry* **2020**, *12*, 165-172.
[114] A. L. Boreen, W. A. Arnold, K. McNeill, *Environ. Sci. Technol.* **2004**, *38*, 3933-3940.
[115] M.-K. Yun, Y. Wu, Z. Li, Y. Zhao, M. B. Waddell, M. Ferreira Antonio, E. Lee Richard, D. Bashford, W. White Stephen, *Science* **2012**, *335*, 1110-1114.

[116] N. Lardon, L. Wang, A. Tschanz, P. Hoess, M. Tran, E. D'Este, J. Ries, K. Johnsson, *J. Am. Chem. Soc.* **2021**, *143*, 14592-14600.
[117] K. R. Huber, W. F. Schmidt, E. A. Thompson, A. M. Forsthoefel, R. W. Neuberg, R. S. Ettinger, *British Journal of Cancer* **1989**, *59*, 714-718.
[118] S. Meister, B. Frey, V. R. Lang, U. S. Gaipl, G. Schett, U. Schlötzer-Schrehardt, R. E. Voll, *Neoplasia* **2010**, *12*, 550-IN553.
[119] S. M. McMahon, M. B. Jackson, *Trends Neurosci.* **2018**, *41*, 880-884.
[120] J. A. Levitt, S. P. Poland, N. Krstajic, K. Pfisterer, A. Erdogan, P. R. Barber, M. Parsons, R. K. Henderson, S. M. Ameer-Beg, *Sci. Rep.* **2020**, *10*, 5146.
[121] S. A. J. Trammell, M. S. Schmidt, B. J. Weidemann, P. Redpath, F. Jaksch, R. W. Dellinger, Z. Li, E. D. Abel, M. E. Migaud, C. Brenner, *Nat. Commun.* **2016**, *7*, 12948.
[122] P. Sehgal, P. Szalai, C. Olesen, H. A. Praetorius, P. Nissen, S. B. Christensen, N. Engedal, J. V. Møller, *J. Biol. Chem.* **2017**, *292*, 19656-19673.
[123] L. Li, G.-k. Hu, *Biosci. Rep.* **2015**, *35*.
[124] E. A. Veal, A. M. Day, B. A. Morgan, *Mol. Cell* **2007**, *26*, 1-14.
[125] C. W. Hui, Y. Zhang, K. Herrup, *PLOS ONE* **2016**, *11*, e0147134.
[126] C. Bardy, M. van den Hurk, T. Eames, C. Marchand, R. V. Hernandez, M. Kellogg, M. Gorris, B. Galet, V. Palomares, J. Brown, A. G. Bang, J. Mertens, L. Böhnke, L. Boyer, S. Simon, F. H. Gage, *Proc. Natl. Acad. Sci.* **2015**, *112*, E2725.
[127] D. Liu, M. Pitta, M. P. Mattson, *Ann. N.Y. Acad. Sci.* **2008**, *1147*, 275-282.
[128] H. Guo, L. M. Camargo, F. Yeboah, M. E. Digan, H. Niu, Y. Pan, S. Reiling, G. Soler-Llavina, W. A. Weihofen, H.-R. Wang, Y. G. Shanker, T. Stams, A. Bill, *Sci. Rep.* **2017**, *7*, 11608.
[129] J. Davies, A. A. Francis, A. W. Jones, J. C. Watkins, *Neurosci. Lett.* **1981**, *21*, 77-81.
[130] G. Matsumoto, M. Kawatani, C. Takeshige, *Neurosci. Lett.* **1991**, *133*, 211-214.
[131] C. M. Díaz-García, R. Mongeon, C. Lahmann, D. Koveal, H. Zucker, G. Yellen, *Cell Metab.* **2017**, *26*, 361-374.e364.
[132] I. Pérez-Liébana, I. Juaristi, P. González-Sánchez, L. González-Moreno, E. Rial, M. Podunavac, A. Zakarian, J. Molgó, B. Pardo, J. Satrústegui, A. del Arco, *bioRxiv* **2021**, 2021.2002.2002.429391.
[133] T. S. Luongo, J. M. Eller, M.-J. Lu, M. Niere, F. Raith, C. Perry, M. R. Bornstein, P. Oliphint, L. Wang, M. R. McReynolds, M. E. Migaud, J. D. Rabinowitz, F. B. Johnson, K. Johnsson, M. Ziegler, X. A. Cambronne, J. A. Baur, *Nature* **2020**, *588*, 174-179.
[134] C. C. Alano, A. Tran, R. Tao, W. Ying, J. S. Karliner, R. A. Swanson, *J. Neurosci. Res.* **2007**, *85*, 3378-3385.
[135] F. Di Lisa, R. Menabò, M. Canton, M. Barile, P. Bernardi, *J. Biol. Chem.* **2001**, *276*, 2571-2575.
[136] Laura A. Sena, Navdeep S. Chandel, *Mol. Cell* **2012**, *48*, 158-167.
[137] F. Palmieri, B. Rieder, A. Ventrella, E. Blanco, P. T. Do, A. Nunes-Nesi, A. U. Trauth, G. Fiermonte, J. Tjaden, G. Agrimi, S. Kirchberger, E. Paradies, A. R. Fernie, H. E. Neuhaus, *J. Biol. Chem.* **2009**, *284*, 31249-31259.
[138] F. Berger, C. Lau, M. Dahlmann, M. Ziegler, *J. Biol. Chem.* **2005**, *280*, 36334-36341.
[139] A. Nikiforov, C. Dölle, M. Niere, M. Ziegler, *J. Biol. Chem.* **2011**, *286*, 21767-21778.
[140] M. Pittelli, L. Formentini, G. Faraco, A. Lapucci, E. Rapizzi, F. Cialdai, G. Romano, G. Moneti, F. Moroni, A. Chiarugi, *J. Biol. Chem.* **2010**, *285*, 34106-34114.
[141] A. Davila, L. Liu, K. Chellappa, P. Redpath, E. Nakamaru-Ogiso, L. M. Paolella, Z. Zhang, M. E. Migaud, J. D. Rabinowitz, J. A. Baur, *eLife* **2018**, *7*, e33246.
[142] T. Wang, K. Birsoy, N. W. Hughes, K. M. Krupczak, Y. Post, J. J. Wei, E. S. Lander, D. M. Sabatini, *Science* **2015**, *350*, 1096.
[143] T. Bertomeu, J. Coulombe-Huntington, A. Chatr-aryamontri, K. G. Bourdages, E. Coyaud, B. Raught, Y. Xia, M. Tyers, *Mol. Cell. Biol.* **2018**, *38*, e00302-00317.
[144] G. Masson, D. Gomez Pardo, J. Cossy, *Chirality* **2021**, *33*, 5-21.
[145] T. Gleede, L. Reisman, E. Rieger, P. C. Mbarushimana, P. A. Rupar, F. R. Wurm, *Polym. Chem.* **2019**, *10*, 3257-3283.

[146] S. K. Dwivedi, S. Gandhi, N. Rastogi, V. K. Singh, *Tetrahedron Lett.* **2007**, *48*, 5375-5377.
[147] G. Bai, T. N. O'Connell, M. A. Brodney, C. R. Butler, L. C. Czabaniuk, A. M. Gilbert, E. A. LaChapelle, C. Li, L. A. McAllister, K. Ogilvie, L. Philippe, R. Salomon-Ferrer, M. J. Shapiro, J. T. Starr, D. P. Uccello, J. M. Withka, J. Yan, M. F. Brown, *ACS Medicinal Chemistry Letters* **2021**, *12*, 1585-1588.
[148] A. Čikoš, S. Dragojević, A. Kubiček, *J. Pharm. Biomed. Anal.* **2021**, *203*, 114232.
[149] Y. Nisimoto, S. Motalebi, C.-H. Han, J. D. Lambeth, *J. Biol. Chem.* **1999**, *274*, 22999-23005.
[150] M. J. Tebbe, H. V. Atton, C. Avery, S. M. Bromidge, M. Kerry, A. K. Kotey, N. J. Monck, M. Meniconi, M. P. Ridgill, H. Tye, E. Saiah, K. P. Johnsson, K. I. Gorska, H. Peng, J. M. McCall.
[151] G. D. Fasman, *CRC Handbook of Biochemistry and Molecular Biology, Vol. 3*, CRC Press, **2017**.
[152] *https://www.thermofisher.com/de/de/home/technical-resources/media-formulation.176.html*, *DMEM, high glucose, GlutaMAX(TM), pyruvate, Media Formulations, accessed: 22.09.2021*.
[153] E. S. Hwang, S. B. Song, *Biomolecules* **2020**, *10*.
[154] D. C. Schöndorf, D. Ivanyuk, P. Baden, A. Sanchez-Martinez, S. De Cicco, C. Yu, I. Giunta, L. K. Schwarz, G. Di Napoli, V. Panagiotakopoulou, S. Nestel, M. Keatinge, J. Pruszak, O. Bandmann, B. Heimrich, T. Gasser, A. J. Whitworth, M. Deleidi, *Cell Rep.* **2018**, *23*, 2976-2988.
[155] R. S. Fletcher, G. G. Lavery, *Journal of Molecular Endocrinology* **2018**, *61*, R107-R121.
[156] B. Sutcliffe, J. Ng, T. O. Auer, M. Pasche, R. Benton, G. S. X. E. Jefferis, S. Cachero, *Genetics* **2017**, *205*, 1399-1408.
[157] J.-M. Masch, H. Steffens, J. Fischer, J. Engelhardt, J. Hubrich, J. Keller-Findeisen, E. D'Este, N. T. Urban, S. G. N. Grant, S. J. Sahl, D. Kamin, S. W. Hell, *Proc. Natl. Acad. Sci.* **2018**, *115*, E8047.
[158] K. A. Anderson, A. S. Madsen, C. A. Olsen, M. D. Hirschey, *Biochim. Biophys. Acta Bioenerg.* **2017**, *1858*, 991-998.
[159] J. M. Berthiaume, J. G. Kurdys, D. M. Muntean, M. G. Rosca, *Antioxid. Redox Signal.* **2017**, *30*, 375-398.
[160] I. Lopez-Fabuel, J. Le Douce, A. Logan, A. M. James, G. Bonvento, M. P. Murphy, A. Almeida, J. P. Bolaños, *Proc. Natl. Acad. Sci.* **2016**, *113*, 13063.
[161] L. Adler, C. Chen, Y. Koutalos, *J. Biol. Chem.* **2014**, *289*, 1519-1528.
[162] I. Martínez-Reyes, N. S. Chandel, *Nat. Commun.* **2020**, *11*, 102.
[163] Q. Zhang, P. S. Padayatti, J. H. Leung, *Front. Physiol.* **2017**, *8*, 1089.
[164] R. Oeggl, T. Neumann, J. Gätgens, D. Romano, S. Noack, D. Rother, *Front. bioeng. biotechnol.* **2018**, *6*, 196.
[165] R. L. Pongratz, R. G. Kibbey, G. I. Shulman, G. W. Cline, *J. Biol. Chem.* **2007**, *282*, 200-207.
[166] A.-K. Bouzier-Sore, J. P. Bolaños, *Frontiers in Aging Neuroscience* **2015**, *7*, 89.
[167] P. Rodriguez-Rodriguez, E. Fernandez, J. P. Bolaños, *Journal of Cerebral Blood Flow & Metabolism* **2013**, *33*, 1843-1845.
[168] K. N. Niforou, A. K. Anagnostopoulos, K. Vougas, C. Kittas, V. G. Gorgoulis, G. T. Tsangaris, *Cancer Genomics - Proteomics* **2008**, *5*, 63.
[169] W. J. Israelsen, M. G. Vander Heiden, *Cell* **2010**, *143*, 669-671.
[170] L. Diebold, N. S. Chandel, *Free Radical Biol. Med.* **2016**, *100*, 86-93.
[171] O. Warburg, *Science* **1956**, *123*, 309-314.
[172] Michael P. Murphy, *Biochem. J* **2008**, *417*, 1-13.
[173] L. R. Stein, S.-i. Imai, *Trends Endocrinol. Metab.* **2012**, *23*, 420-428.
[174] J. Gordon, S. Amini, M. K. White, in *Neuronal Cell Culture: Methods and Protocols* (Eds.: S. Amini, M. K. White), Humana Press, Totowa, NJ, **2013**, pp. 1-8.

[175] M. Agostini, F. Romeo, S. Inoue, M. V. Niklison-Chirou, A. J. Elia, D. Dinsdale, N. Morone, R. A. Knight, T. W. Mak, G. Melino, *Cell Death Differ.* **2016**, *23*, 1502-1514.
[176] L. Boquist, I. Ericsson, *FEBS Lett.* **1984**, *178*, 245-248.
[177] D. Nolfi-Donegan, A. Braganza, S. Shiva, *Redox Biol.* **2020**, *37*, 101674.
[178] A. Verkhratsky, M. Nedergaard, *Physiol. Rev.* **2017**, *98*, 239-389.
[179] J. W. Deitmer, S. M. Theparambil, I. Ruminot, S. I. Noor, H. M. Becker, *Front. Neurosci.* **2019**, *13*, 1301.
[180] V. Dvorak, T. Wiedmer, A. Ingles-Prieto, P. Altermatt, H. Batoulis, F. Bärenz, E. Bender, D. Digles, F. Dürrenberger, L. H. Heitman, A. P. Ijzerman, D. B. Kell, S. Kickinger, D. Körzö, P. Leippe, T. Licher, V. Manolova, R. Rizzetto, F. Sassone, L. Scarabottolo, A. Schlessinger, V. Schneider, H. J. Sijben, A.-L. Steck, H. Sundström, S. Tremolada, M. Wilhelm, M. Wright Muelas, D. Zindel, C. M. Steppan, G. Superti-Furga, *Front. Pharmacol.* **2021**, *12*, 1968.
[181] N. Kory, J. uit de Bos, S. van der Rijt, N. Jankovic, M. Güra, N. Arp, A. Pena Izabella, G. Prakash, H. Chan Sze, T. Kunchok, A. Lewis Caroline, M. Sabatini David, *Sci. Adv.*, *6*, eabe5310.
[182] E. Girardi, G. Agrimi, U. Goldmann, G. Fiume, S. Lindinger, V. Sedlyarov, I. Srndic, B. Gürtl, B. Agerer, F. Kartnig, P. Scarcia, M. A. Di Noia, E. Liñeiro, M. Rebsamen, T. Wiedmer, A. Bergthaler, L. Palmieri, G. Superti-Furga, *Nat. Commun.* **2020**, *11*, 6145.
[183] L. Liu, X. Su, W. J. Quinn, 3rd, S. Hui, K. Krukenberg, D. W. Frederick, P. Redpath, L. Zhan, K. Chellappa, E. White, M. Migaud, T. J. Mitchison, J. A. Baur, J. D. Rabinowitz, *Cell Metab.* **2018**, *27*, 1067-1080.e1065.
[184] A. Sambeat, J. Ratajczak, M. Joffraud, J. L. Sanchez-Garcia, M. P. Giner, A. Valsesia, J. Giroud-Gerbetant, M. Valera-Alberni, A. Cercillieux, M. Boutant, S. S. Kulkarni, S. Moco, C. Canto, *Nat. Commun.* **2019**, *10*, 4291.
[185] David W. Frederick, E. Loro, L. Liu, A. Davila, Jr., K. Chellappa, Ian M. Silverman, William J. Quinn, III, Sager J. Gosai, Elisia D. Tichy, James G. Davis, F. Mourkioti, Brian D. Gregory, Ryan W. Dellinger, P. Redpath, Marie E. Migaud, E. Nakamaru-Ogiso, Joshua D. Rabinowitz, Tejvir S. Khurana, Joseph A. Baur, *Cell Metab.* **2016**, *24*, 269-282.
[186] J. Wilhelm, S. Kühn, M. Tarnawski, G. Gotthard, J. Tünnermann, T. Tänzer, J. Karpenko, N. Mertes, L. Xue, U. Uhrig, J. Reinstein, J. Hiblot, K. Johnsson, *Biochemistry* **2021**, *60*, 2560-2575.
[187] R. S. Erdmann, S. W. Baguley, J. H. Richens, R. F. Wissner, Z. Xi, E. S. Allgeyer, S. Zhong, A. D. Thompson, N. Lowe, R. Butler, J. Bewersdorf, J. E. Rothman, D. St Johnston, A. Schepartz, D. Toomre, *Cell Chem. Biol.* **2019**, *26*, 584-592.e586.
[188] J. H. Joly, B. T. L. Chew, N. A. Graham, *PLOS Comput. Biol.* **2021**, *17*, e1008942.
[189] K. Ortmayr, S. Dubuis, M. Zampieri, *Nat. Commun.* **2019**, *10*, 1841.
[190] P.-H. Chen, L. Cai, K. Huffman, C. Yang, J. Kim, B. Faubert, L. Boroughs, B. Ko, J. Sudderth, E. A. McMillan, L. Girard, D. Chen, M. Peyton, M. D. Shields, B. Yao, D. S. Shames, H. S. Kim, B. Timmons, I. Sekine, R. Britt, S. Weber, L. A. Byers, J. V. Heymach, J. Chen, M. A. White, J. D. Minna, G. Xiao, R. J. DeBerardinis, *Mol. Cell* **2019**, *76*, 838-851.e835.
[191] A. Molinaro, B. Becattini, G. Solinas, *Sci. Rep.* **2020**, *10*, 12031.
[192] M. Prentki, Franz M. Matschinsky, S. R. M. Madiraju, *Cell Metab.* **2013**, *18*, 162-185.
[193] A. A. Fernández-Ramos, C. Marchetti-Laurent, V. Poindessous, S. Antonio, C. Petitgas, I. Ceballos-Picot, P. Laurent-Puig, S. Bortoli, M.-A. Loriot, N. Pallet, *Sci. Rep.* **2017**, *7*, 10550.
[194] I. C. McLean, L. A. Schwerdtfeger, S. A. Tobet, C. S. Henry, *Lab on a Chip* **2018**, *18*, 1399-1410.
[195] F. E. Critchfield, J. A. Gibson, J. L. Hall, *J. Am. Chem. Soc.* **1953**, *75*, 1991-1992.
[196] E. Gasteiger, A. Gattiker, C. Hoogland, I. Ivanyi, R. D. Appel, A. Bairoch, *Nucleic Acids Res.* **2003**, *31*, 3784-3788.
[197] G. A. Orr, J. S. Blanchard, *Anal. Biochem.* **1984**, *142*, 232-234.

[198] C. Aurnhammer, M. Haase, N. Muether, M. Hausl, C. Rauschhuber, I. Huber, H. Nitschko, U. Busch, A. Sing, A. Ehrhardt, A. Baiker, *Hum. Gene Ther. Methods* **2011**, *23*, 18-28.
[199] J. Schindelin, I. Arganda-Carreras, E. Frise, V. Kaynig, M. Longair, T. Pietzsch, S. Preibisch, C. Rueden, S. Saalfeld, B. Schmid, J.-Y. Tinevez, D. J. White, V. Hartenstein, K. Eliceiri, P. Tomancak, A. Cardona, *Nat. Methods* **2012**, *9*, 676-682.
[200] N. Otsu, *IEEE Trans. Syst. Man Cybern. Syst.* **1979**, *9*, 62-66.

9 List of Figures

Figure 1: Fundamentals of fluorescent biosensors. 4
Figure 2: Biosynthesis of NAD^+ and $NADP^+$. 6
Figure 3: Design of NAD(P)-Snifits. 11
Figure 4: Spirocyclization equilibria of TMR derivatives. 14
Figure 5: Design and synthesis of CP-Rhod540-C6-SMX. 16
Figure 6: Characterization of CP-Rhod540-C6-SMX in vitro 18
Figure 7: Labelling and response of NAD-Snifit in live cells 19
Figure 8: Characterization of NAD-Snifit in live cells. 21
Figure 9: Investigation of CP-Rhod540-C6-SMX degradation. 23
Figure 10: Design and rational of MaP dye-based FRET donor substrates 25
Figure 11: Synthesis of PPT and C6-SMX 26
Figure 12: Synthesis of CP-MaP1-C6-SMX, CP-MaP1-PPT, CP-MaP555-C6-SMX and CP-MaP555-PPT. 27
Figure 13: Synthesis of CP-MaP3-C6-SMX and CP-MaP3-PPT. Reagents and conditions: 28
Figure 14: Characterization of MaP dye-based FRET donor substrates in vitro. 31
Figure 15: Determination of labelling conditions of MaP dye-based FRET donor substrates. 33
Figure 16: Live cell labelling with MaP dye-based FRET donor substrates. 34
Figure 17: Benchmark of CP-TMR-C6-SMX with CP-MaP555-C6-SMX and CP-MaP555-PPT. 35
Figure 18: Artifical opeing of NAD(P)-Snifit in live cells. 37
Figure 19: LC-MS/MS measurements of total NAD^+ in lysates from U2OS cells. 39
Figure 20: FLIM-FRET measurements of the NAD-Snifit labelled with CP-MaP555-C6-SMX/Halo-SiR in U2OS cells. 41
Figure 21: FLIM-FRET measurements of the NAD-Snifit labelled with CP-MaP555-PPT/Halo-SiR in U2OS cells. 43
Figure 22: FLIM-FRET measurements by the NADP-Snifit labelled with CP-MaP555-C6-SMX/Halo-SiR in U2OS cells. 45
Figure 23: FLIM-FRET measurements by the NADP-Snifit labelled with CP-MaP555-PPT/Halo-SiR in U2OS cells. 47
Figure 24: Labelling of SNAP- and Halo-tag in primary neurons. 49
Figure 25: Labelling of NAD-Snifit in primary neurons. 50
Figure 26: No wash labelling in primary neurons. 51

Figure 27: FLIM-FRET measurements of the NAD-Snifit labelled ..... with CP-MaP555-PPT/Halo-SiR in primary neurons. 53

Figure 28: FLIM-FRET measurements of the NADP-Snifit labelled ..... with CP-MaP555-PPT/Halo-SiR in primary neurons. 55

Figure 29: Comparison of subcellular NAD^+ levels and NADPH/$NADP^+$ ratios in ..... U2OS cells and primary neurons. 56

Figure 30: Subcellular levels of NAD^+ and neuronal activity. 58

Figure 31: Transfection screen for SLC25A51 using different ratios of ..... Fugene6 reagent to DNA. 60

Figure 32: Measurements of mitochondrial NAD^+ levels. 61

Figure 33: Subcellular NAD^+ levels upon Nam and Trp starvation. 64

Figure 34: Degradation pathways of azetidine containing molecules. 66

Figure 35: Major pathways for energy production in cancer cells and ..... primary neurons. 75

Figure 36: NAD(P) -Snifits constructs for bacterial expression (A), expression ..... in U2OS cells (B) and expression in neurons (C). 126

10 List of Tables

Table 1: Fluorescent biosensors for NAD(H). 9

Table 2: Fluorescent biosensors for NADP(H). 9

Table 3: Spectral properties of FRET donor substrates CP-TMR-C6-SMX ..... and CP-Rhod540-C6-SMX. 17

Table 4: Key physicochemical properties of FRET donor substrates in the open[a] ..... and spirocyclic[b] form, respectively. 26

Table 5: Spectroscopic data of FRET donor substrates and titration of purified ..... NAD(P)-Snifits with NAD^+ or NADPH/$NADP^+$. 30

Table 6: Titration of NAD-Snifit and NADP-Snifit with QM385 in U2OS cells. 36

Table 7: MRM parameters for NAD^+ quantification 91

Table 8: key resources that were used in this thesis. 127

Table 9: Composition of buffers used in this thesis. 128

11 List of Publications

Publications in peer-reviewed journals

- "*Improved NAD(P)$^+$-Snifits reveal differences of mitochondrial nicotinamide adenine dinucleotides in primary neurons and U2OS cells"*
  Fabio Raith, Lars Hellweg, Carlo Walz, Sebastian Fabritz, Kai Johnsson, *manuscript in preparation*.

- *"Mitochondrial NAD$^+$ controls nuclear ARTD1-induced ADP-ribosylation"*
  Ann-Katrin Hopp; Federico Teloni; Corentin Condrand; Fabio Raith; Lavinia Bisceglie; Kathrin Nowak; Anna Howald; Patrick G.A. Pedrioli; Kai Johnsson; Matthias Altmeyer; Deena M. Leslie Pedrioli; Michael O Hottiger; *Mol. Cell*; **2021**, *81*, 340-354.

- *"SLC25A51 is a mammalian mitochondrial NAD$^+$ transporter"*
  Timothy S. Luongo, Jared M. Eller, Mu-Jie Lu, Marc Niere, Fabio Raith, Caroline Perry, Marc R. Bornstein, Paul Oliphint, Lin Wang, Melanie R. McReynolds, Marie E. Migaud, Joshua D. Rabinowitz, F. Brad Johnson, Kai Johnsson, Mathias Ziegler, Xiaolu A. Cambronne, Joseph A. Baur; *Nature* **2020**; *588*, 174-179.

- *"Semisynthetic biosensors for mapping cellular concentrations of nicotinamide adenine dinucleotides"*
  Oliver Sallin, Luc Reymond, Corentin Gondrand, Fabio Raith, Birgit Koch, Kai Johnsson; *eLife* **2018**; 7; e32638.

Conference Posters

- *"An improved semisynthetic biosensor for the investigation of neuronal NAD$^+$ metabolism"*
  Fabio Raith, Kai Johnsson; *The NAD$^+$ Metabolism and Signaling Conference*; **2021**; online meeting.

- *"A NAD$^+$-Biosensor with improved labelling and affinity in live cells"*
  Fabio Raith, Carlo Walz, Kai Johnsson; *EMBO Workshop: Chemical Biology*; **2020**; online meeting.

12 Eidesstattliche Versicherung

Eidesstattliche Versicherung gemäß §8 der Promotionsordnung für die Naturwissenschaftlich-Mathematische Gesamtfakultät der Universität Heidelberg

Bei der eingereichten Dissertation zu dem Thema „*development of fluorogenic substrates for NAD(P)-Snifits enables the investigation of nicotinamide adenine dinucleotide metabolism in primary neurons*" handelt es sich um meine eigenständig erbrachte Leistung.

Ich habe nur die angegebenen Quellen und Hilfsmittel benutzt und mich keiner unzulässigen Hilfe Dritter bedient. Insbesondere habe ich wörtlich oder sinngemäß aus anderen Werken übernommene Inhalte als solche kenntlich gemacht.

Die Arbeit oder Teile davon habe ich bislang nicht an einer Hochschule des In- oder Auslands als Bestandteil einer Prüfungs- oder Qualifikationsleistung vorgelegt.

4. Die Richtigkeit der vorstehenden Erklärungen bestätige ich.

5. Die Bedeutung der eidesstattlichen Versicherung und die strafrechtlichen Folgen einer unrichtigen oder unvollständigen eidesstattlichen Versicherung sind mir bekannt.

Ich versichere an Eides statt, dass ich nach bestem Wissen die reine Wahrheit erklärt und nichts verschwiegen habe.

Heidelberg, 28.10.2021 _____

Fabio Raith